Characterisation of the MIRI Spectrometer, an instrument for the James Webb Space Telescope

MICHAEL BRIGGS

Institute for Astronomy

School of Physics & Astronomy

University of Edinburgh

Doctor of Philosophy

February 2010

Abstract

The MIRI-MRS is a future space based Medium Resolution Spectrometer and one of four instruments to be integrated onto The James Webb Space Telescope. The Medium Resolution Spectrometer is designed to be diffraction limited across its entire passband of 5 - 28.3 microns. It achieves this through the spectral filtering of the passband into four channels with each one containing an integral field unit optimised for minimal diffraction losses. The integral field unit enables the simultaneous measurement of the spectral data across the entire field of view.

The design of the Medium Resolution Spectrometer is outlined with particular reference to the choice of slice widths used for each channel to minimise the diffraction losses from the slicing mechanism. The slice widths are also used to derive the extent of the field of view and combined with the along slice plate scale at the detector the technique required for complete spatial sampling of the spectrometer is outlined. The operation of the Channel 1 image slicer component was tested cryogenically at 5 microns for diffraction losses due to the slicing of the point spread function. This was so that the actual diffraction losses could be measured and compared with the optical model. From the resulting analysis I concluded that the operation of the image slicers were well understood for diffraction losses.

Performance tests were required on the instrument because of its novel design. This was the first implementation of an integral field unit operating between 5 - 28.3 microns and it was necessary to ensure that the operation of the image slicer did not induce unacceptable diffraction losses into the instrument. Tests were required on the assembled instrument to verify the optical design. A Verification Model of MIRI was built to enable test verification of the optical design. This testing was carried out in advance of the MIRI Flight Model assembly so that changes could be made to the Flight Model design if necessary. This testing phase was also designed to define the calibration process necessary to prepare the MIRI Flight Model for scientific operations. For the testing

phase it was necessary to create an astronomical source simulator. This MIRI Telescope Simulator was constructed in Madrid where I spent two months ensuring the point source movement across the field of view would be sufficient to investigate the Medium Resolution Spectrometer.

My contribution was to help assemble both the Verification and Flight Models. I also participated in the Verification Model testing phase from the test design phase to the test implementation and data analysis. My role in the analysis was to investigate the field of view of the Medium Resolution Spectrometer Verification Model and whether the field of view requirements for the spectrometer were met. During this analysis I also verified that the diffraction effects of the end-to-end instrument were well understood by the optical model.

The Medium Resolution Spectrometer Verification Model field of view compromised the field of view requirement for the spectrometer. A similar analysis for the Flight Model showed that there would be a low probability that the field of view requirement would be met. As a result of the analysis I defined a new slit mask design that would align the field of view sampled by Channel 1 to increase the aligned field of view. As a result there is a high probability that the field of view requirement for the Flight Model will be exceeded.

The test analysis discovered a magnification effect within the spectrometer which must be properly characterised to enable accurate field of view reconstruction. I designed a test necessary for the calibration phase of the Flight Model to enable full spatial alignment of the Medium Resolution Spectrometer. I also measured an excess flux level in the Channel 1 observations at the detector and there was a ghost detected in the Channel 1 images. Whilst the origin of either the excess flux or the ghost could not be completely determined I investigated the possibility that they will not be present in the Flight Model due to the slight design differences. If present however they will not increase the background level of an observation above the requirement outlined for Channel 1.

Declaration

I hereby declare that this thesis entitled *Characterisation of the MIRI Spectrometer, an instrument for the James Webb Space Telescope* is not substantially the same as any that I have submitted for a degree or diploma or other qualification at any other University. I further state that no part of my thesis has already been or is being concurrently submitted for any such degree, diploma or other qualification.

This thesis is the outcome of my own work except where specifically indicated in the text.

Michael Briggs,
Edinburgh,
August 2009.

Acknowledgements

There have been so many people who during my tenure at Edinburgh have aided in my understanding of the MIRI spectrometer and the background knowledge required to understand its operation and appreciate its significance to science. I would firstly like to thank my primary supervisor Gillian Wright for all her help and encouragement over the years. I would also like to thank my secondary supervisor Peter Brand for those many insightful coffee break discussions. Alistair Glasse, David Lee and Martyn Wells all deserve a special mention for their willingness share their knowledge about the spectrometer design and their advice whilst reducing the test data. I would also thank the remaining members of the MIRI team at Edinburgh who were always very helpful when I came knocking on their door, namely Philip Parr-Burman, Angus Gallie, Tom Baillie and John Murray. Suzie Ramsay-Howat also deserves a mention as she was great in helping me to understand the data reduction procedure of an integral field unit. During my time at Edinburgh I was also fortunate enough to work alongside Tim Hawarden on an investigation into molecular hydrogen regions in nearby galaxies. Tim had a great insight into the processes involved in these galaxies and his enthusiasm into this subject and others was infectious. Unfortunately Tim is no longer with us and I believe the world is a lesser place for this.

Looking further afield I would like to take this opportunity to thank Luis Gonzales, Eva Diaz and the rest of the MIRI team at the Instituto Nacional de Técnica Aeroespacial for making me feel a part of the team (despite the initial language barrier) whilst I was on attachment in Madrid. I would also like to thank the members of the MIRI Test Team for their help during the Verifica-

tion Model testing phase and resultant data analysis, in particular Tim Grundy, Paul Eccleston, Helen Walker and Brian O'Sullivan.

A big thank you is also due to all my friends and colleagues at Edinburgh for making sure that I always had extra curricular activities to take my mind off more pressing matters. In particular I would like to thank my housemates over the years that include Matthew Hollister, Benjamin Edelshain, James Roditi, Helen Dumigan, Christopher Montgomery and also Michael Campbell who has had the dubious pleasure of living with me in Edinburgh as well as during our undergraduate days in Leicester. I would also like to thank Erik Gerwick and Henry Pearce for what was simultaneously my most horrible and enjoyable experience in Edinburgh. A weekly quartet of 7.30am weight lifting sessions at the CSE, one of the Scotsman's top 5 gyms in Scotland, was one of the highlights of my week which at one point required me to go on a shopping spree for some slightly larger clothes. A big thank you also goes to Galaxy for making the most amazing post workout chocolate milk I have ever tasted then putting it into 500ml bottles. I would like to thank the American football teams at Edinburgh University and Dundee for all the fun I had playing during my four years in Scotland. I would also like to thank Under Armour for making the cold weather sportswear which enabled me to actually enjoy playing American football outdoors in Scotland. I would like to thank all my office mates and others for all their help, good chat and bad jokes over the years namely Anita Schell, Barnaby Rowe, Rachael Smith, Eduardo Ibar, Yasin Memari, Stuart Lynn, Jenny Richardson, Simon Reynolds, Sarah Buehler, Nick Rowell, Neil Phillips and everyone else who has contributed to my mental wellbeing during my years at Edinburgh. I would like to thank my amazing girlfriend Mayen for putting up with and looking after me whilst I was finishing my thesis, all the tasty dinners definitely helped me cope with what was a very stressful time. Finally I would like to thank my parents who have been very supportive of me not only during my university career but throughout my life. I believe that my upbringing played a large part in me deciding to continue my studies to this level and I would like to dedicate this thesis to them.

Contents

List of Figures

List of Tables

CHAPTER 1

Introduction

The James Webb Space Telescope is a passively cooled future space based platform that will provide diffraction limited infrared optimised observations. The primary mirror diameter is approximately 6.5 m which is more than twice that of Hubble. It is to orbit around Lagrange Point 2 (1.5 million km from the Earth in the opposite direction from The Sun). As well as using the Earth as a shield from the Sun, The James Webb Space Telescope will have a sunshield the size of a tennis court. This is to further reduce the background level at the instruments. It is intended that the James Webb Space Telescope will operate in a region of very low background making for observations with minimal background noise. The lifetime requirement of the James Webb Space Telescope is to be a minimum of five years, after the commissioning of the instrument, with an extension of up to ten years (Sonneborn, 2007; Wright et al., 2004).

MIRI or the Mid-Infrared Instrument will be one of four instruments to be integrated onto The James Webb Space Telescope, to be launched in 2013. Being developed as a 50-50 partnership between the USA and Europe it will provide imaging, coronagraphy and low and medium resolution spectroscopy over 5 - 28.3 μm (Wright et al., 2004). MIRI is the only instrument on the James Webb Space Telescope with a dedicated cooler (Wright et al., 2008). It contains a single stage, solid hydrogen cryostat which keeps the optics and detectors at approximately 7K which is necessary to minimise

the mid-infrared thermal emission component of the instrument (Wright et al., 2003). The background of the observations will consist of low levels of in-field Zodiacal light, scattered thermal emission from the sunshield and telescope, scattered starlight and scattered zodiacal light (Sonneborn, 2007).

Historically space telescopes have been designed to investigate wavelengths that were previously difficult to observe due to the atmospheric absorbtion features, ie UV, X-Ray and Gamma Ray telescopes. At present the largest gaps in our knowledge occur in the understanding the universe at high redshifts in an area called the "Dark Zone" and also in the formation and evolution of galaxies, stars and planetary systems.

Ground based observations at wavelengths greater than about 2 microns begin to be background contaminated by thermal emissions from within the telescope and from the hot atmosphere (Dressler, 1998). This reduces their ability to measure faint signals from distant objects. For the observation of such objects at large redshifts this background contamination must be removed. Placing a well shielded space telescope at a large distance from the Earth and cooling it to $\sim$ 50 K will greatly increase the sensitivity of the telescope in the near to mid-infrared region from that achievable in ground based installations (Dressler, 1998). It is along these lines that the design of the James Webb Space Telescope and the Mid-Infrared Instrument was constructed.

The unobserved "Dark Zone" is bounded by the observations of the Cosmic Background Explorer and the Hubble Space Telescope. The light from stars and galaxies in this region is redshifted to z $\sim$ 6 - 20 (Rees, 1998). The deepest observations of galaxies indicate that the colours can only be explained using a combination of evolved stellar populations and dust (Caputi et al., 2004). Assuming this dust is also prevalent at a higher redshift implies that local dust extinction will be a factor of concern for observations of these types of galaxies. As such the optimum bandwidth for their observation would be in the near to mid-infrared as dust is relatively transparent at these wavelengths. Observing at these wavelengths is also advantageous as the optical spectrum of objects at such high redshifts is shifted into the near to mid-infrared bandwidth due to the Doppler Effect. For example at a redshift of z = 15 the optical range of 380 - 750 nm is redshifted to 6 - 12 microns which due to the spectral coverage of the MIRI Imager of 5.6 - 25.5 microns will enable a measurement of the rest frame optical spectrum from these high redshift objects.

1.1 The Science Requirements

The James Webb Space Telescope has been principally designed to enable the investigation and measurement of several as yet unobserved processes in the Universe. These are: The formation of the very first stars in the Universe and the subsequent reionisation of the intergalactic medium; The formation and evolution of the first stars into galaxies and the subsequent evolution of these galaxies into the structures that we observe in our local neighborhood; The formation and evolution of both low and high mass stars from a protoplanetary system; The formation of gas giants and terrestrial planets in protoplanetary systems and the subsequent evolution of habitable planets.

The Medium Resolution Spectrometer will be used for each of these investigations except for the formation of the very first stars and reionisation as these sources will be too faint to observe. The features of the spectrometer are best utilised when observing extended objects as it will provide spectroscopic data from across the entire field of view. This can be used to ascertain the distribution, interaction and kinematics of materials within the object. The Medium Resolution Spectrometer will be used to investigate galaxies at different epochs to determine the evolution processes that form the galaxies that we observe in our local neighborhood. It will be used to observe protoplanetary systems to determine the processes involved in the formation of stars and how stars of large masses are formed. The formation of planetary systems will be investigated to determine how the terrestrial and gas giant planets are formed to enable an understanding of the processes involved in the creation of the Solar System. The information contained within this section has been taken from the James Webb Space Telescope Science Requirements Documents (NASA, 2004).

1.1.1 The Assembly of Galaxies

The z = 1 Universe is very much like that seen in our local neighborhood in that there is a similar distribution of Hubble Type spiral and elliptical galaxies. By observation the optical and near-infrared wavelengths of these z = 1 galaxies are also very similar however there are many more regions of very high star formation activity observed in the ultraviolet at z = 1 than in the local Universe.

Looking at higher redshifts there is a marked change in the distribution of galaxies within the Hubble Type sequence as galaxies at z = 3 are generally blue with more irregular morphologies. These galaxies however have generally been selected in ultraviolet which may indicate that this is just a selection effect and there is an as yet unobserved population of redder galaxies present at this epoch also. Beyond this redshift there are very limited observations of galaxies out to the epoch of reionisation. The Hubble Ultra Deep Field image gave an indication that galaxies at very high redshift were not just of exotic shapes but that there were also galaxies present that are similar to those observed in our local neighborhood.

The Medium Resolution Spectrometer will enable a measurement of galaxies at varying redshifts which will be used to investigate the evolution of galaxies. As it measures both spectral and spatial data of a target it will enable a detailed survey into the distribution of metals and kinematics of matter around typical galaxies which will further help to investigate the processes behind galaxy formation and evolution.

1.1.2 The Birth of Stars and Protoplanetary Systems

The formation of planetary systems is a product of the formation of stars. Currently it is accepted that the stars form from small dense regions embedded within a much larger molecular cloud which accrete material to grow in size. Eventually the central star will become so large that its radiation pressure will dominate over the accretion hence ending the growth phase of the central star. This effect implies that there is a problem in the formation of high mass stars as there is an obvious limit to the mass achievable of a star which is formed by accretion. It is possible however that high mass stars can form when a large accretion rate dominates over the radiation pressure.

The Medium Resolution Spectrometer will enable observations during the initial stages of the protostellar collapse whilst these protoplanetary systems are completely enveloped by large opaque molecular clouds. Through many observations of such systems an investigation into these star forming regions and in particular the formation method of high mass stars is possible.

1.1.3 Planetary Systems and the Origins of Life

It is thought that many young protoplanetary systems have gas giants which migrate towards the parent star and eventually merge with it. Gas giants of a Saturnian Mass or greater have been measured from surveys at a radius of the parent star where the terrestrial planets are found in an evolved system. As it is expected that any gas giant migration towards the parent star will remove the material from the circumstellar disk these gas giants would remove all material from the Habitable Zone. This is a problem for the subsequent formation of habitable planets.

It is possible that the gas giants which migrate towards the parent star is indicative of an early stage in planetary formation and there is a subsequent formation of gas giant planets in the outer Solar System which initiates the formation of the terrestrial planets. The process by which this is possible is due to tidal interactions of the gas giants with planetesimals which increases the eccentricity of their orbits so that they enter the Habitable Zone where they collide to form planets. This tidal interaction could also be responsible for populating these planets with water as the planetesimals delivered from the outer Solar System would contain ice.

By using the Medium Resolution Spectrometer to perform a detailed survey of nearby stars with protoplanetary disks the typical processes involved in the formation of a planetary system can be determined observationally. This will help to understand the formation of the Solar System. By measuring the physical and chemical properties of these planetary systems it will be possible to investigate their potential for the origins of life. The holy grail in the study of protoplanetary systems is a system that is on the pathway to creating terrestrial planets in the Habitable Zone or one that already exists. If such a find was achieved that would be a great step in quantifying the probability that other life exists in the Universe as it would enable a derivation of the number of such systems in the Universe. An evolved planetary system like the Solar System would also present a good target at which to point a radio receiver.

1.2 The Design of a Long Slit Spectrometer

Because of the large distances to the high redshift objects which the Medium Resolution Spectrometer (MRS) is required to observe their signal will be very faint. To

increase the sensitivity of the instrument the MRS is optimised for low diffraction losses and to deliver a high throughput of signal. As a result of these science drivers the design of the MRS is complicated. Before considering the design of the MRS that of a long slit spectrometer will first be considered.

The design of a basic long slit spectrometer is shown in Figure 1.1. The incident light is focussed onto an entrance slit which is placed at an image plane. The entrance slit selects a slice of the incident field of view for transmission through the spectrometer. The collimator forms the light from each point at the entrance slit into a parallel beam of rays. Without a grating present the camera would create a single image of the entrance slit on the detector.

The "Side View" in Figure 1.1 shows the along slice direction of the spectrometer, due to the orientation of the grating there is no wavelength dispersion in this direction. The colours are used to denote different positions in the along slice field of view.

The "Top View" depicts the wavelength dispersion of the spectrometer in the across slice direction. Due to the orientation of the grating, the collimated beam at the grating experiences an angular dispersion dependant upon the wavelength. As a result of this distribution the camera produces a series of monochromatic entrance slit images across the detector. It is in this way that the spectrum of an astronomical region can be measured.

Note that the long slit spectrometer detailed in Figure 1.1 uses transmission optics. This was done to simplify the ray diagrams. In practice infrared telescopes such as MIRI utilise reflection optics as the throughput of such systems can be kept high. The throughput refers to the efficiency of an optical system ie $\frac{Flux_{out}}{Flux_{in}}$.

In the along slice direction the spatial information of the field of view slice is retained. As a result long slit spectrometers are commonly used to investigate the spectral changes across extended sources.

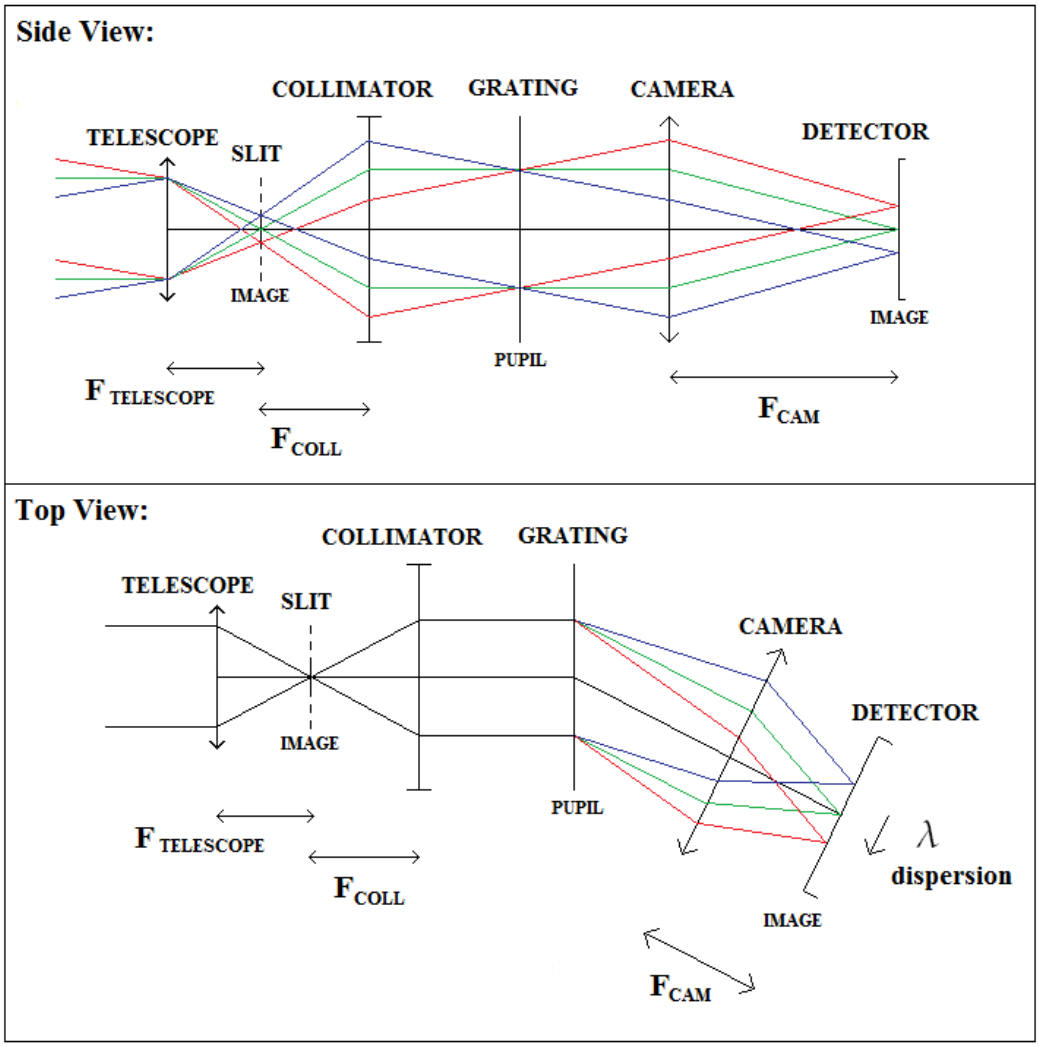

Figure 1.1: Optical diagram of a basic long slit spectrometer

Note that the different colours in the "Side View" represent light incident from different off axis angles and are not wavelength dependant

1.2.1 The Telescope and the Entrance Slit

When designing a long slit spectrometer the typical width of an entrance slit is set to be smaller than the point spread function of the wavelength to be investigated. However reducing the slit width too much will increase the diffraction losses which will reduce the throughput of the instrument.

The typical length of an entrance slit will normally extend the entire length of the field image created by the telescope at the entrance slit aperture, this is to maximise the along slice on-sky coverage.

The telescope element produces an output beam, for example, of a focal ratio f/20 and an effective focal length $F_{telescope}$ of the primary telescope diameter times the focal ratio. The plate scale produced at the slit is $\frac{1}{F_{telescope}}$ which is commonly measured in arcseconds per mm. Note that the plate scale is reduced by increasing the focal length of a lens (telescope) causing a simultaneous reduction in the field of view transmitted through the slit. This trade-off has to be considered alongside the science aspirations when designing a long slit spectrometer.

The Point Spread Function

The point spread function which is used to define the width of the the entrance slit in a long slit spectrometer (and the width of the image slicers in the Medium Resolution Spectrometer) is a measure of the response of an imaging system to a point source. It defines the size of the best focus spot of light produced in a telescope by a point source. When applied to telescope design, due to the large distances to an object, the incident rays can be approximated as parallel. This is referred to as Fraunhofer Diffraction.

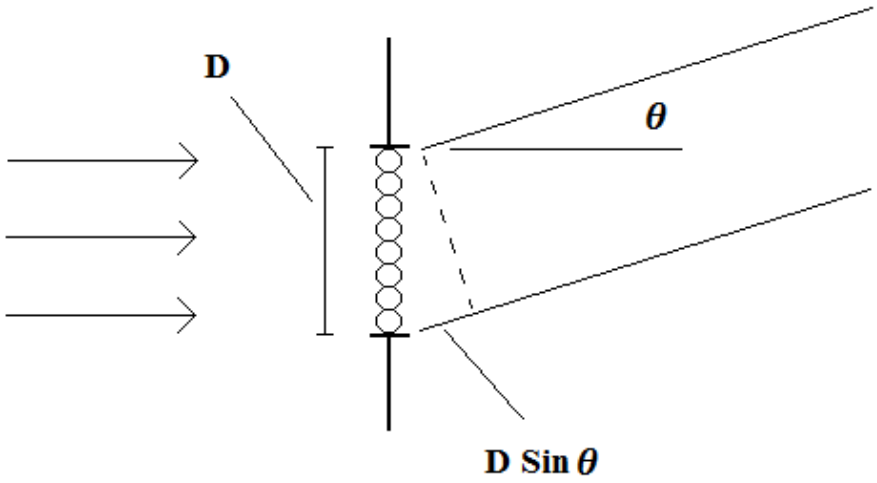

Figure 1.2: The Diffraction at an Attenuating Aperture

Consider Figure 1.2 which shows the light incident from a point source onto an aperture of diameter D. As the incident light is parallel Huygens' Principle can be applied which allows the incident wavefront to be approximated by a row of sources at the aperture. We shall consider eight such sources as shown in the diagram. The angle θ which causes a path difference $DSin\theta = \lambda$ will see constructive interference between the top and bottom sources. However the first and the fifth sources will cause destructive interference at this angle, as will each subsequent pair including the fourth and the eighth sources. As a result $DSin\theta = \lambda$ describes the angular radius of the 1st minimum from the incident beam.

The point spread function of a telescope can be similarly calculated because the telescope primary mirror is in effect an aperture as it attenuates the incident light. For a telescope of primary mirror diameter D, the radius of the point spread function to 1st minimum (considering small angles) has the form shown in Equation 1.1 where the factor of 1.22 arises from the mathematical analysis of a circular aperture. This relationship defines a diffraction pattern that follows a first order Bessel Function.

$$\theta = 1.22\frac{\lambda}{D} \tag{1.1}$$

It can be seen that increasing the diameter of the telescope will reduce the size of the point spread function as will reducing the wavelength observed. A reduction in the size of the point spread function means that the size of best focus of a point source is reduced. This will improve the resolution of an image created by the telescope. As such telescopes are normally designed with as large a primary mirror as possible.

1.2.2 The Collimator

The collimator must have the same focal ratio as the telescope output beam. It operates by forming the light from any point on the entrance slit aperture into a collimated beam. It produces a collimated image of the pupil at a distance v from the collimator where $\frac{1}{u} + \frac{1}{v} = \frac{1}{F_{coll}}$ and $u = \frac{1}{F_{telescope}+F_{coll}}$. A grating is placed at this pupil image. Consider the equation for the spectral resolution delivered by a grating (Equation 1.2) where R is the resolution, n is the order to be observed and N the total number of rulings illuminated on the grating.

$$R = nN \tag{1.2}$$

The grating is placed at a pupil image as the footprint at the pupil is the same for each position on the field of view. This reduces the required size of the grating and ensures that the off axis beams will see the same irregularities in the rulings if any are present.

Increasing the focal length of the collimator will increase the size of the pupil footprint on the grating which in turn will increase the spectral resolution of the instrument through the illumination of additional rulings. As such it is ideal to make the pupil dimension at the grating as large as possible, the balancing factors being the space available and the size of the grating to be illuminated.

1.2.3 The Grating

A dispersion element is vital to any spectrometer. The operation of a reflection grating can be seen in Figure 1.3. The wavelength dispersion occurs because the angle of reflection necessary for constructive interference varies depending on the wavelength being observed. In effect the angle at which constructive interference occurs is that which sets the path difference CD-AB equal to a complete wavelength interval (or a multiple thereof).

This interference is described by the 2D Grating Equation, shown in Equation 1.3 which defines the angular distribution of constructive interference where d is the distance between adjacent rulings, λ is the wavelength of incident light, n is the order of diffracted light observed from the grating and θ_i and θ_r denote the angles of incidence and reflection.

$$d(Sin\theta_i - Sin\theta_r) = n\lambda \tag{1.3}$$

When designing an instrument the grating defines the spectral resolution of the instrument. Looking at higher order fringes increases the spectral resolution as the wavelength dispersion is more spread out over angle. There is however a complication with overlapping fringes at higher orders.

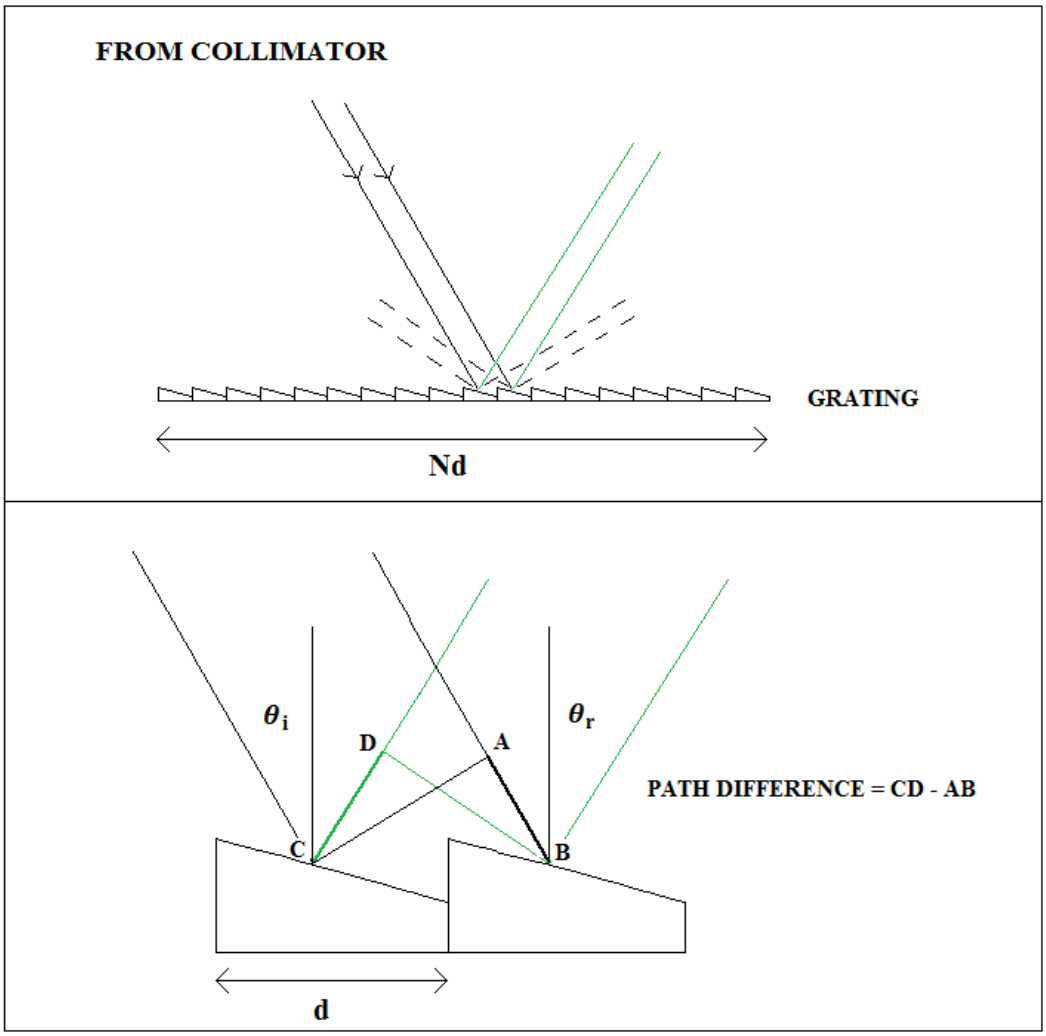

Figure 1.3: A Reflection Grating

1.2.4 The Spectral Resolution of the Spectrometer

It has been noted that increasing the number of rulings illuminated at the grating will increase the resolution as will looking at higher order fringes. Now consider the actual spectral resolution delivered by a long slit spectrometer. Using the 2D Grating Equation the angular dispersion towards the detector can be described by Equation 1.4.

$$\frac{\delta\theta_r}{\delta\lambda} = \frac{n}{dCos\theta_r} \tag{1.4}$$

and hence the linear scale at the detector can be described as per Equation 1.5.

$$\frac{\delta L}{\delta \lambda} = \left(\frac{\delta \theta_r}{\delta \lambda} \right) F_{cam} \tag{1.5}$$

The diffraction limit of the minimum angular width at the detector $\delta\theta_r$ can be described as per Equation 1.6.

$$\delta\theta_r = \frac{\lambda}{NdCos\theta_r} \tag{1.6}$$

where $NdCos\theta_r$ denotes the angular size that the grating subtends at the detector. Combining Equations 1.4 and 1.6 enables the measurement of the resolving power or spectral resolution of the instrument shown in Equation 1.7. Note that this derivation reproduces the grating equation shown in Equation 1.2.

$$\frac{\lambda}{\delta\lambda} = nN \tag{1.7}$$

However as this resolution is derived from the minimum angular width resolvable at the detector this is a best case analysis for the spectral resolution. In practice due to the non zero size of the slit width the spectral resolution does not reach this lower limit. Therefore in order to calculate the delivered spectral resolution the slit width must also be considered. As such the resolvable wavelength at the detector is defined by the linear scale at the detector and the slit width w. The slit width at the detector which is related to the size of the entrance slit aperture and the focal ratios of the camera and collimator via $w_{det} = \frac{w_{slit} f_{cam}}{f_{coll}}$ where $\frac{f_{cam}}{f_{coll}}$ defines the magnification of the slit image within the spectrometer. Equation 1.8 shows the actual minimum angular width resolvable at the detector.

$$\delta\lambda_{det} = \left(\frac{\delta\lambda}{\delta L} \right) \delta w_{det} = \frac{dCos\theta_r w_{slit}}{nD_{cam} f_{coll}} \tag{1.8}$$

where the $f/ratio$ of a lens defines $f_{cam} = \frac{F_{cam}}{D_{cam}}$. As such the delivered spectral resolution of a spectrometer can be described by Equation 1.9

$$\frac{\lambda}{\delta\lambda} = \frac{\lambda n f_{coll} W}{dw_{slit}} \tag{1.9}$$

where $W = \frac{D_{cam}}{Cos\theta_r}$ refers to the width of the part of the grating illuminated by the beam.

1.3 The Medium Resolution Spectrometer and the Image Slicers

The primary innovation of MIRI to maximise the science return is the image slicers that form part of the Medium Resolution Spectrometer. These image slicers, whilst not an entirely new technology, have never been shown to work over the entire bandwidth and cryogenic temperatures at which the Medium Resolution Spectrometer will operate. An image slicer operates by spatially slicing an input field and aligning the slices end to end for input into a long slit spectrometer, this is illustrated in Figure 1.4 (Ramsay-Howat et al., 2003). At the input to the spectrometer the spatial information of the object of interest is retained resulting in spatial and spectral knowledge across the entire field of view. In effect an image slicer provides the user with a simultaneous measurement of the spectra from each spatial position.

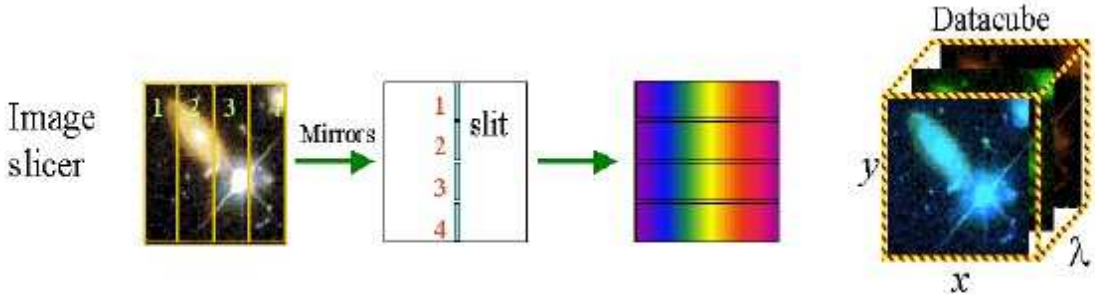

Figure 1.4: The Image Slicing Process

The advantage of an image slicer over a traditional long slit spectrometer is maximised when spectroscopic data is required from an extended source. In such a case a single observation using an image slicer would return the spectral data from across several slices of the extended source whilst several observations would be required with a long slit spectrometer to achieve the same spatial coverage. As a result the image slicer provides a reduction in total integration time by a factor of n for such an observation, where n is the number of slices in the image slicer.

Due to the large distances and high spectral resolution at which the Medium Resolution Spectrometer (MRS) is required to operate the design is optimised to maximise the incident flux. To increase the sensitivity of the instrument the MRS is diffraction

limited and is optimised for low diffraction losses and to deliver a high throughput of signal.

1.4 Areas of Concern of the Medium Resolution Spectrometer Design

In an instrument such as the Medium Resolution Spectrometer there are several areas of concern that the instrument will operate as it has been designed. The first area is regarding the increase in scattered light within the instrument. This scattered light originates primarily from the imperfections in the mirrors used in the optics of the instrument and as such the effects of scattered light become more important as the wavelength of the light becomes of the same order as the size of the imperfections. The typical surface roughness of the imperfections of the gold coated aluminium optical surfaces in the Medium Resolution Spectrometer were approximately 25nm root mean squared. At the low wavelength cut-off for the Medium Resolution Spectrometer of 5 microns this surface roughness should not induce much scattered light at an optical surface. However the 30 reflections necessary to image the incident light in its correct form onto the detector might create a cumulative scattered light effect which would increase the scattered light to a measurable level. This scattered light will reduce the useful transmission of the Medium Resolution Spectrometer and if it were presented to the detector it would further reduce the signal to noise of an observation by creating a heightened background level. If present the quantification of such scattered light is necessary to calculate the reduction in the signal to noise of an observation and the increased observation time required to observe an object to the signal to noise of the unscattered case. I measured and quantified such scattered light in the Channel 1 observations (5 - 7.7 microns) and showed that the intensity of such scattered light did not exceed the requirements for the Medium Resolution Spectrometer.

There was also the potential the scattered light is in the form of a ghost in the reconstructed field of view. I investigated this for Channel 1 which did show a ghost offset from the compact source. Using a systems analysis I managed to narrow the source of the ghost down to a region within the Spectrometer Pre-Optics however the offset of the ghost from the compact source on the field of view could not be completely explained.

The second area of concern regards the alignment of the image slices in the reconstructed image. Without delving too deeply into the design at this stage it shall be noted that there will be small differences in the along slice plate scale between the slices due to the differing optics of each slice in the spectrometer. The reconstructed field of view of the Medium Resolution Spectrometer also shows many spatial slice offsets creating a jagged edge along the field of view. As a result of these issues the spatial calibration of the reconstructed field of view is not a simple task. I devised a method to enable the full spatial calibration of the Medium Resolution Spectrometer from the investigation of a verification model such that a suitable calibration could be achieved for flight. Additionally the along slice offsets which result in the jagged edge of the reconstructed field of view will reduce the field of view of a channel below the instrument requirement. I investigated this during the construction of the Flight Model and devised a change of a Channel 1 component to increase the probability that the Medium Resolution Spectrometer field of view requirement would be met.

1.5 Thesis Outline

A large project such as MIRI involves the collaboration of many institutions and individuals. At the time I entered the project the design of the MIRI Medium Resolution Spectrometer had been completed and a large amount of the components had already been fabricated. I aided in the alignment, integration and verification stages of both a Verification Model and the Flight Model which helped my understanding of the operation of the Medium Resolution Spectrometer. To perform the Verification Model test campaign it was necessary to create a team responsible for the characterisation of the complete MIRI instrument. The function of this test team was to create a complete suite of tests designed to investigate the performance and characterise the Mid-Infrared Instrument. I was heavily involved in the test team during the script development stage, the actual testing phase at the Rutherford Appleton Laboratories and in the subsequent test analysis.

Introduction to the Project

Being such a large project the introduction to this thesis is split over three chapters. This chapter has outlined the science requirements of the James Webb Space Telescope, MIRI and the Medium Resolution Spectrometer which had a large influence on the design. It has also looked at the design of a basic long slit spectrometer and compared this with the basic operation of an image slicer and the Medium Resolution Spectrometer. Areas of concern for the design of such instruments have also been highlighted. These areas will be further investigated later in this thesis.

Chapter 2 will look at the design of the Medium Resolution Spectrometer where possible drawing comparisons to the long slit spectrometer. It will also outline the operational considerations behind the choice of slice width for each channel and will look at the spatial and spectral sampling and resolution of the instrument. Finally this chapter will outline a test on a prototype image slicer which was done to measure the diffraction losses due to slicing. This details the first measurement of the diffraction losses in practice which were required to verify that the optical model was correct. I performed the analysis on the results to show the diffraction losses due to slicing were at about the levels described by the optical model.

The previously mentioned Verification Model was built to enable test verification of the optical design. For this testing phase it was necessary to create an astronomical source simulator. This simulator was constructed in Madrid. I spent two months on attachment in Madrid ensuring the point source movement across the field of view could be achieved to the required precision to investigate the operation of the Medium Resolution Spectrometer. This work is outlined in Chapter 3. This chapter will also review the test campaign carried out at the Rutherford Appleton Laboratories during August and September 2009 and the role I performed within the test team.

My function in the subsequent test analysis had been to investigate the field of view of the MIRI Medium Resolution Spectrometer because due to my involvement with the assembly of the image slicing components at the UK Astronomy Technology Center I was best equipped to analyse the data. The test analysis will be detailed across the remaining chapters of this thesis with the conclusions being drawn in the final chapter. To aid the presentation of the results the analysis has been divided into three chapters.

Chapter 4 outlines the data reduction technique required to reconstruct the Verification Model field of view and compares the measured on-sky extents with the instrument requirements and the optical model. This chapter also details an amendment I made to a component in the Flight Model to increase the probability that the Flight Model field of view would exceed the instrument requirements.

Chapter 5 outlines a magnification of the slice lengths that was measured across the detector. This magnification induces an error into the spatial alignment of the reconstructed Verification Model field of view. This chapter also details a performance test that I devised which must be carried out on the Flight Model to enable a full spatial calibration of the field of view.

Chapter 6 outlines the measurement of additional light at the Verification Model detector. In considering each case separately it enables a systematic analysis of the Medium Resolution Spectrometer to investigate the origin. The resultant reduction in the signal to noise of the instrument due to the additional light is calculated and compared to the requirement.

CHAPTER 2

The JWST MIRI-MRS Spectrometer

To minimise the integration time that the Medium Resolution Spectrometer requires for observations its design was optimised for low and well understood diffraction losses as a higher throughput reduces the integration time required for an object to achieve a specified signal to noise. The Medium Resolution Spectrometer design has similarities to that of the long slit spectrometer outlined in Section 1.2 though due to the field being sliced and the high throughput required there are several additional features. A systems diagram of the Medium Resolution Spectrometer is outlined in Figure 2.1. Each of the systems described in this section will be covered in detail later in this chapter.

MIRI is composed of four instruments: the MIRI Imager Sub-system, Medium Resolution Spectrometer Sub-system, Low Resolution Spectrometer Sub-system and the Coronagraphic Imager Sub-system. In this thesis they shall be referred to as the MIRI Imager, Medium Resolution Spectrometer, Low Resolution Spectrometer and the Coronagraphic Imager.

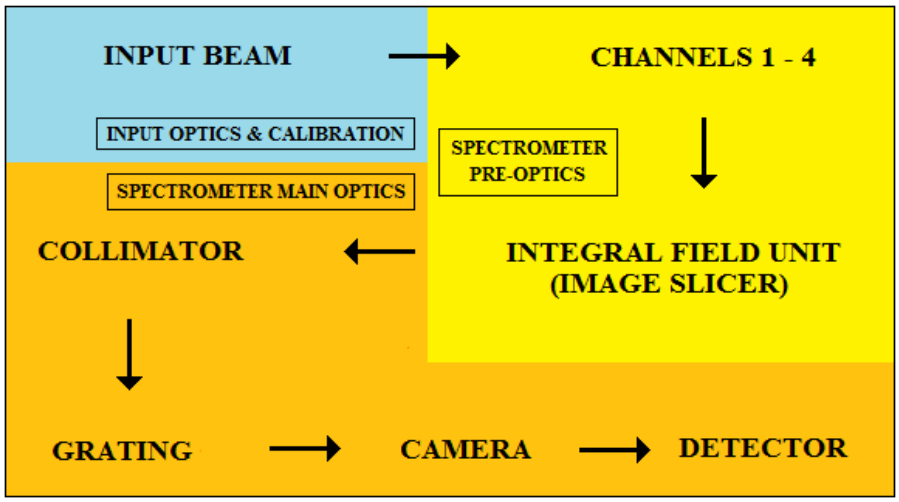

Figure 2.1: Medium Resolution Spectrometer Systems Diagram

An input beam is supplied to the Spectrometer Pre-Optics from the Input Optics and Calibration (IOC). The input beam enters the Spectrometer Pre-Optics and is divided into four wavelength channels in a section called the Dichroic Level. These channels exit the Dichroic Level separately and are input into an Integral Field Unit. Each Integral Field Unit acts like the entrance slit of the long slit spectrometer in that they define the on-sky dimensions of a slice (slit) in the Medium Resolution Spectrometer. The purpose of an Integral Field Unit is to divide up the incident field of view into many slices and align them end to end for input into the Spectrometer Main Optics. The Spectrometer Main Optics produces the wavelength dispersion and re-images the slices with the correct magnification onto the detector. Its operation is identical to that of the dispersion and re-imaging section of the long slit spectrometer (the collimator, grating, camera & detector) outlined in Section 1.2. It was the Spectrometer Pre-Optics which were designed and constructed at the UK Astronomy Technology Center.

The bandwidth of the spectral channels and the slice width used for the image slicer in each channel are designed such that the diffraction losses are minimised over the entire spectral coverage. This analysis will be presented along with the operational method to achieve full spatial sampling which is dependant upon the slice width. The expected spectral resolution of the Medium Resolution Spectrometer will also be considered.

The derivation of the field of view from the available detector area for each channel will also be outlined. It will be shown that there was a minimum spacing required between adjacent slices at the detector so that there would be no reduction in the signal to noise of a spectrum due to pollution from adjacent spectra.

The testing of a prototype image slicer at operational wavelengths will also be described. Its purpose was to enable the direct measurement of the diffraction losses induced by image slicing. It will be seen that the measured losses closely match those expected from the diffraction modelling. All of the design information contained within this chapter was taken from Renouf (2006) unless stated otherwise.

2.1 The MIRI Input Optics and Calibration

The MIRI Input Optics and Calibration receives the Medium Resolution Spectrometer input beam from the James Webb Space Telescope (JWST) telescope element. The JWST primary mirror is of diameter 6595mm. The MIRI Input Optics and Calibration takes the F/20 beam produced by JWST and converts it to an F/39.37 beam for input into the Spectrometer Pre-Optics. This beam conversion was necessary because a large amount of optics was required to be inserted between the input pupil and and the field image. The beam conversion was carried out using a combination of flat and powered mirrors.

The MIRI Input Optics and Calibration produces a pupil image at the input aperture to the Spectrometer Pre Optics where the spectrometer cold stop is placed. The pupil image is of diameter 13.59mm creating a field image a further 535mm beyond the cold stop. Between the pupil image and the field image the field of view is divided into four channels. This region is called The Dichroic Level.

The MIRI Input Optics and Calibration contains a contamination control cover which when closed isolates the Medium Resolution Spectrometer from the outside environment. This ability was included due to requirement specification OBA-0654 (Bean, 2008) which states that ”the OBA shall provide a means of dark current measurement for the spectrometer at monthly intervals”. It is necessary to provide the means for a dark measurement of the detectors as an accurate dark observation is required during the data reduction.

The spectrometer calibration unit is housed in a separate assembly from the MIRI Input Optics and Calibration. Its function is to enable a uniform illumination over the Medium Resolution Spectrometer field of view useful for the calibration of the spectrometer.

2.2 The MIRI Spectrometer Pre-Optics

The purpose of the Spectrometer Pre Optics is to split the light both spectrally and spatially into a pre-defined form for input into the Spectrometer Main Optics. Spectrally the field of view is divided into four channels of equal bandwidth. This is done in a region called the Dichroic Level using dichroic filters in both transmission and reflection. Spatially the Spectrometer Pre-Optics divides each field of view transmitted through the four channels into slices. It does this using four image slicers each optimised for its operational passband. Each image slicer is housed in an Integral Field Unit. We will consider each of the Spectrometer Pre-Optics components and their operation in turn. In each case we will make reference to any requirements of the instrument and how they are met through the design. For the case of the image slicers we will cover the design and operation in detail in Section 2.4.

The Spectrometer Pre-Optics was designed as a well baffled system intended to reduce scattered light intensity at the detector. Straylight analysis shows the baffle system consisting of five aperture masks combined with low scattering non-optical surfaces reduces unwanted light to levels which meet the requirements by at least a factor of 10.

2.2.1 The Dichroic Level

The Dichroic Level is located between the pupil image created by the MIRI Input Optics and Calibration and the image plane a further 535mm downstream. The Dichroic Level is the region in which the input beam is split into four wavelength channels necessitated because the diffraction associated with image slicing is wavelength dependant and a single slicer could not be constructed to operate effectively over the range of 5 - 28.3 μm. This is because the diffraction effects would be too variable over the entire passband resulting in an inability of the instrument to be optimised for low

and well understood diffraction losses across its entire spectral coverage.

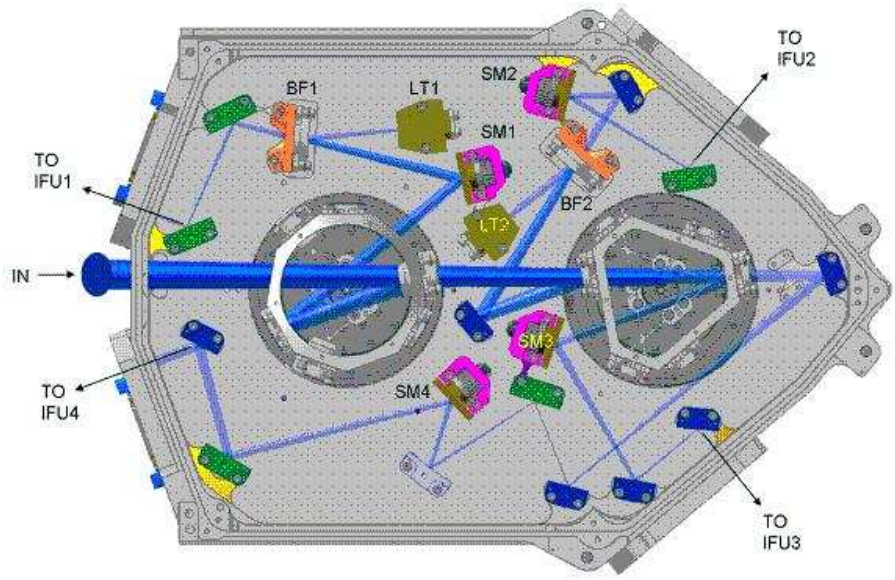

Figure 2.2: Layout of the dichroic and the folding mirrors in the dichroic level of the SPO; SM depicts an adjustable mirror, BF a blocking filter and LT a light trap.

The Dichroic Level is shown in Figure 2.2 (Wells et al., 2006). The wavelength splitting is achieved using three sets of three dichroics in series. Three dichroics represents the minimum number required to re-direct the input light into four channels. They are housed on two Dichroic Wheel Assemblies located towards the center of the Dichroic Level. Each set of dichroic filters is referred to as a different instrument configuration. The use of three sets of dichroics means that for each instrument configuration a different wavelength range is defined for each channel. This removes the need to form parts of the sub-spectra from wavelength regions of dichroic filters that quickly change from high reflectivity to high transmission which would be more difficult to properly characterise. In effect this relaxes the transmission and reflection requirements to be placed on the individual filters achieving a higher and more constant signal transmission across the spectral coverage of the instrument than could be achieved by trying to have a single set of filters operational from 5 - 28.3 μm.

Consider the reflection and transmission requirements of Channel 1 which is required to reflect 5 - 7.7 microns and transmit longer wavelengths (as per Figure 2.3). To achieve this with a single filter will require a very sharp transition between reflection

and transmission with wavelength however using three different filters will relax the requirements for each filter. It does mean however that to obtain an objects spectrum over the complete wavelength range of the instrument three sub-spectra observations have to be taken each utilising a different instrument configuration for each channel.

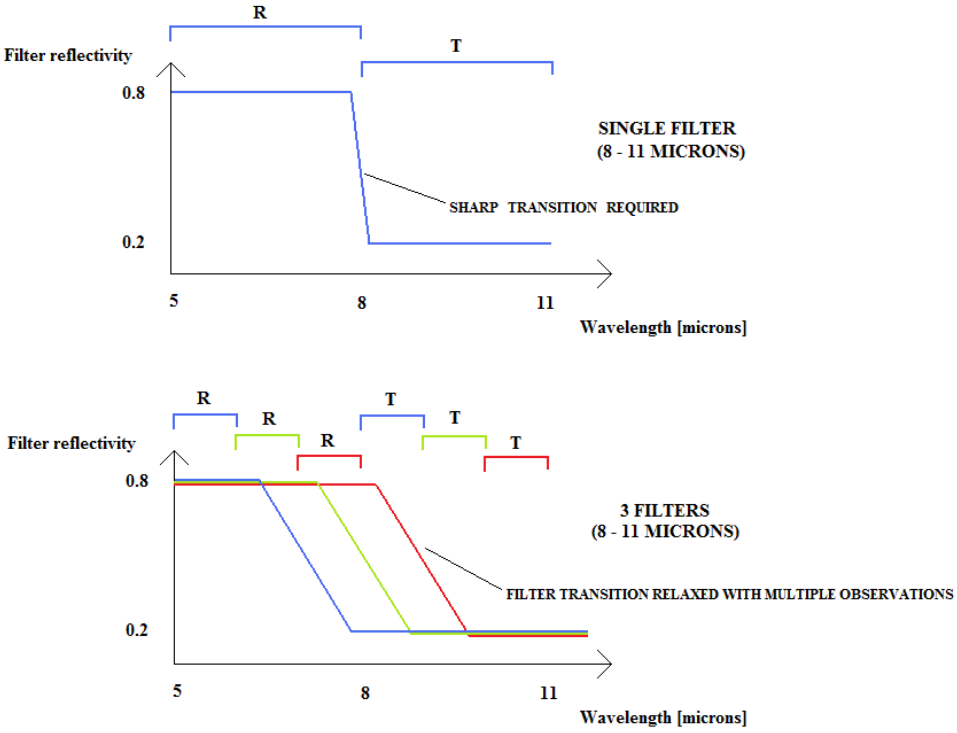

Figure 2.3: The Relaxed Dichroic Properties using Multiple Filters

It is also noteworthy that having a single operational dichroic set would require the presentation of a channels entire spectrum to the detector in a single observation. This would approximately reduce the spectral resolution of the Medium Resolution Spectrometer by an approximate factor of 3 as the entire wavelength data would need to be imaged onto the same detector area in a single observation as opposed to three sub-spectra increments.

In Figure 2.2 the purpose of the adjustable mirror was to ensure that the field image created by the MIRI Input Optics and Calibration was directed towards the field stop at the exit of the Dichroic Level. The blocking filters were included in Channels 1 & 2 to provide further spectral filtering of the beams incident on the gratings. This was to ensure that there were no higher order spectra from lower wavelengths incident

upon the detector as this would reduce the signal to noise of the observation. The light traps are placed in pairs with the blocking filters which filter the unwanted light in reflection. Due to their relative orientation to the beam the reflected light is directed towards the light trap. The light traps are expected to reflect less than 1% of the input flux. Their operation will be considered in Section 6.1.2 at Figure 6.15.

Wavelength Coverage

The full wavelength coverage of the Medium Resolution Spectrometer ranges from 5 - 28.3 microns the separation of which into four passbands of equal bandwidth defines the cut-off points for each of the channels. Dividing the channels into equal bandwidth was done because the size of the Point Spread Function (PSF) will increase by the same factor between the smallest and largest transmitted wavelength of each channel. This is important to achieve low diffraction losses as the diffraction effects induced by image slicing are dependant upon the relative size of the slice width and the PSF. With a well designed image slicer the diffraction losses for each channel can be minimised.

The short wavelength cut-off for each channel is given by Equation 2.1 where *i* denotes the channel number (1-4) and k is the bandwidth of a channel (given by Equation 2.2). The resulting wavelength coverage of the four spectrometer channels is shown in Table 2.1.

$$\lambda_{short(i)} = \lambda_{short(1)} k^{(i-1)} \tag{2.1}$$

$$k = \frac{28.3}{5}^{(0.25)} = 1.54 \tag{2.2}$$

Channel	λ -range [μ m]
1	5.00 - 7.70
2	7.70 - 11.86
3	11.86 - 18.26
4	18.26 - 28.30

Table 2.1: MIRI-Medium Resolution Spectrometer Channel Passbands

The Dichroic Filters

It was noted that each channel requires three sub-spectra observations to obtain complete wavelength coverage. The passband for each channel is divided equally between the three sub-spectra so that the spectral resolution for the sub-spectra will scale linearly with wavelength as each must must fit into a constant detector length. The dichroic configurations are named A, B and C. For each configuration Dichroic 1A needs to reflect Channel 1A and transmit Channels 2A, 3A and 4A. In general dichroic nX has to reflect Channel nX and transmit Channels (n+1)X up to 4X where X = A,B or C (Glasse, 2003).

The sub-spectra of each channel for all dichroic configurations are shown in Figure 2.4 (Wells et al., 2006). There is an slight overlap between each region where the wavelength coverage shifts to a different instrument configuration. This enables a smooth transition to be achieved when combining the data from different configurations into a single spectrum. There are several requirements that must be met for these transition regions.

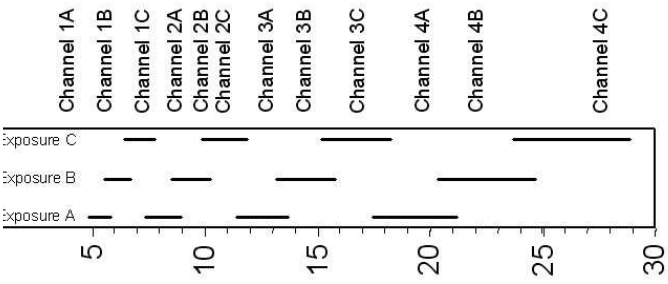

Figure 2.4: Wavelength coverage for each dichroic configuration

OBA-0646 states that ”if any MIRI spectrometer is physically divided into partitions covering different portions of the spectral range, spectra obtained in all sub-bands that are contiguous shall overlap in wavelength coverage by at least 100 pixels, to allow smooth joining”.

OBA-0647 states that ”In the overlap region the throughput needs to be $>$ 70% of transmittance in the middle of the segment”.

OBA-0648 states that "The wavelength overlap must be the same for all sub-bands to within $\pm$ 40 pixels".

Each of these requirements is concerned with creating a smooth transition between sub-spectra. They define both the length of spectrum and the necessary signal to achieve this.

The dichroic filters utilise a multilayered coating deposited onto a 21mm diameter, 5mm thick optical grade CVD cadmium telluride (CdTe). It is the differing widths of the multilayer coating which provides the different transmission profiles of each filter through back reflective interference. They are designed to operate under cryogenic temperatures of 7K and a tilt angle of 10 degrees. The tilt angle is necessary so that the reflection from the front surface does not retrace the incident optical path as the front reflected light from all dichroic wheel mounted filters form part of the instrument transmission requirements.

2.2.2 The Integral Field Units

The Integral Field Unit divides up the incident field of view into many slices and aligns them end to end for input into the Spectrometer Main Optics. They enable the simultaneous measurement of spectroscopic data from across the entire field of view and avoid the need to accurately center point sources on a narrow slit as would have been necessary with a long slit spectrometer. There are four Integral Field Units each optimised for operation over a specific bandwidth. Each Integral Field Unit utilises an anamorphic pre-optics, image slicer, two re-imaging mirrors and an output slit mask. As well as defining the size of the on-sky field of view an Integral Field Unit defines the beam ratio required at the detector for full spectral sampling. The Integral Field Units are an essential part of the Spectrometer Pre-Optics which was designed and constructed at the UK Astronomy Technology Center.

The Anamorphic Pre-Optics

The anamorphic pre-optics provide a differential magnification in two axes to image the square input field of view onto the rectangular image plane at the image slicer. This was done to provide the image field dimensions required for full spectral sampling at

the detector. Each anamorphic pre-optic consists of four toroidal mirrors and a flat output fold mirror. Designed to accept a square input field they create an output beam with a pupil image at the input pupil mask of the Integral Field Unit and a field image of the required dimensions at the slicer. The Channel 2 anamorphic pre-optics are shown in Figure 2.5. Note the anamorphic output pupil can also be seen in the image of the Integral Field Unit shown in Figure 2.8.

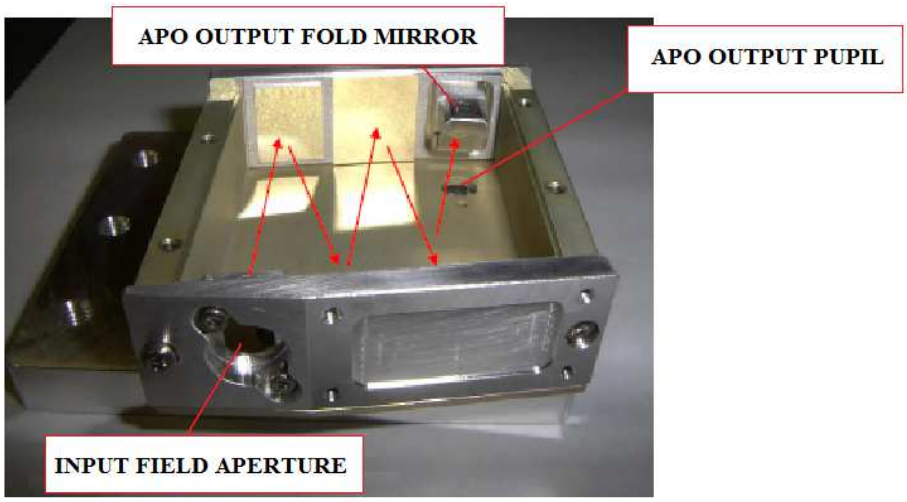

Figure 2.5: The Channel 2 Anamorphic Pre-Optics

We will now consider the Channel 1 beam at the detector at 5 microns. It will be shown later that the plate scale in the along slice direction at the detector is 0.196 arcseconds per pixel where each pixel is of side 25 microns. The reason behind such a choice will be discussed later during the consideration of spatial sampling in Section 2.5.

If the same plate scale were to apply in the across slice direction at the detector then the slice width of 0.176 arcseconds would extend less than a pixel on the detector. The dimension of a slice width is preferred to extend across two pixels in the across slice direction so that each spectral line is fully sampled (this will be considered further in Section 2.6). To achieve this extension it is required that the slice must be magnified in the across slice direction by a factor of 2.25.

The anamorphic pre-optics provides the differential magnification before image slicing has occurred. This was done as it is much simpler to magnify the field as a single unit than as many individual slices. The f/ratios of the beams produced by the

anamorphic pre-optics at each image slicer are noted in Table 2.2.

	Channel 1	Channel 2	Channel 2	Channel 4
Spectral f/ratio at Slicer	177.7	135.7	105.0	82.4
Spatial f/ratio at Slicer	79.0	101.8	78.8	61.8

Table 2.2: Attributes of the Anamorphic Pre-Optics

The Channel 1 slice width extends 1 mm on the image slicer. This results in a slice width on the sky of 0.176 arcseconds via the plate scale $\frac{1}{fD} = 0.176$ arcseconds per mm where f is the across slice focal ratio and D the telescope diameter of 6595mm. Similarly 1mm of the Channel 1 slice length extends 0.379 arcseconds. The factor of 2.25 magnification of the field image in the across slice direction has been achieved. Note that the anamorphic factor used for Channels 2, 3 & 4 was 1.33. The anamorphic factors were requested by the members of the MIRI design team responsible for the Spectrometer Main Optics.

The magnitude of anamorphism in the re-magnified field of view is also seen in the pupil image however the longest and shortest axes are swopped. In an optical system the product of the maximum off axis angle on the sky and the diameter of the beam at the pupil stop is conserved. This is called Éntendue. Consider Figure 2.6 which depicts the Channel 1 anamorphism. $D_{along}\theta_{along} = D_{across}\theta_{across}$, where θ is the maximum off axis angle on the sky and D is the diameter of the pupil. Consider the Channel 1 beam incident on the image slicer. θ_{across} increases by a factor of 2.25 due to the magnification. By Éntendue the pupil diameter in the across slice direction is reduced by the same factor.

The input field aperture to the anamorphic pre-optics is conjoined with the field image produced by the MIRI Input Optics and Calibration (as per Section 2.1) for Channels 1,2 & 3. It was noted that this field image was 535mm downstream from the pupil image created at the cold stop. The Channel 4 optics were not able to be compressed into this 535mm envelope and as a result Channel 4 has a slightly different design. It has two additional powered mirrors in the relay optics which along with the anamorphic pre-optics create a pupil at the entrance pupil aperture to the Integral Field Unit and transpose the field image directly onto the rectangular Channel 4 image slicer.

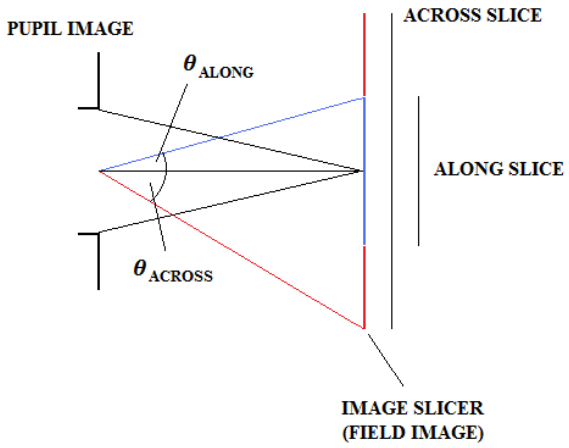

Figure 2.6: Relationship of Éntendue within a Telescope

The Image Slicers

The image slicer is the principal component that enables spectroscopy to be done across the entire field of view simultaneously. This is achieved through the slicing of the image. It was noted that each image slicer was housed in an Integral Field Unit which is optimised for operation over the transmitted passband. The slice width of an image slicer was set to equal the full width half maximum of the minimum wavelength diffraction limited point spread function in that channel (as per Equation 2.3). This was done to minimise diffraction losses across the operational wavelengths.

$$W = \frac{\lambda_{min}}{D} \tag{2.3}$$

W is the slice width in radians, λ_{min} the minimum wavelength of the spectral coverage of a channel and D the diameter of the JWST primary telescope mirror (6595mm). The analysis used to determine the exact operational design of the image slicers will be looked at in detail in Section 2.4.

The Channel 2 image slicer is shown in Figure 2.7. It can clearly be seen how the field image is sliced by its projection onto the slicer. The image slicers are constructed out of a single piece of aluminium. This serves to avoid any alignment complications that could arise when constructing the instrument or under vibration during launch.

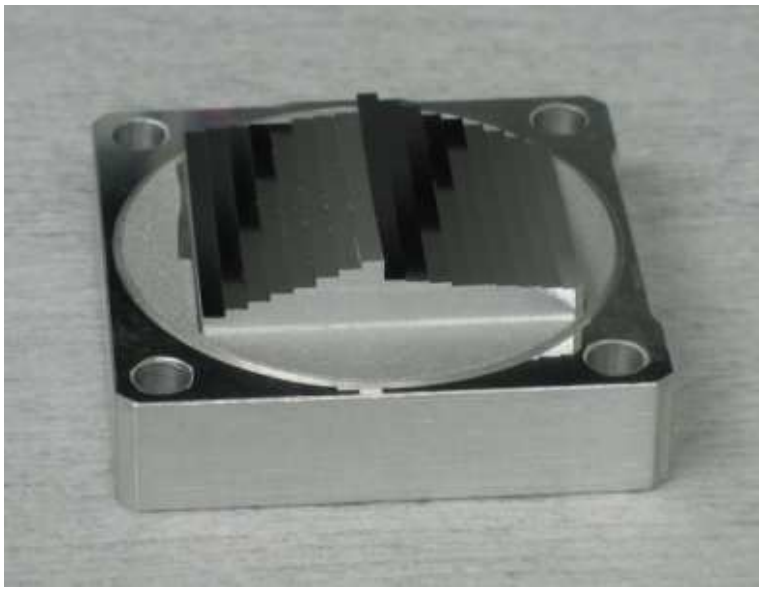

Figure 2.7: The Channel 2 Image Slicer

Table 2.3 shows the slice width and the complete field of view coverage of each channel. The on-sky slice widths are derived from the spectral focal ratio of the beam at the slicer and the width of a slice on the image slicer. The derivation of the number of slices in a channel and the length of each slice (the field of view) will be considered further in Section 2.7. Note that spectral refers to the across slice and spatial the along slice direction.

Figure 2.8 shows the optical model of the Channel 1 Integral Field Unit from the top and side views (Lee, 2007a). The image slicer separates the sliced field image into two sets of slices and directs each set out of the IFU via a re-imaging mirror. Conceptually the design is the same for each channel with only the number of slices varying. The image slicer creates an image of the input pupil for each slice at the line of pupil images indicated in the diagram (there is a corresponding line of pupil images for the bottom slices also). Because of the path differences from the slicer to this plane not all of the pupil images will be in perfect focus.

	Channel 1	Channel 2	Channel 2	Channel 4
Spectral f/ratio at Slicer	177.7	135.7	105.0	82.4
Slice Width [arcsecs]	0.176	0.276	0.387	0.645
Slice Width [mm]	1.0	1.2	1.3	1.7
Number of Slices	21	17	16	12
Spectral Field of View [arcsecs]	3.7	4.7	6.2	7.7
Spatial Field of View [arcsecs]	3.7	4.5	6.1	7.9

Table 2.3: Slice Widths and Total Field of View

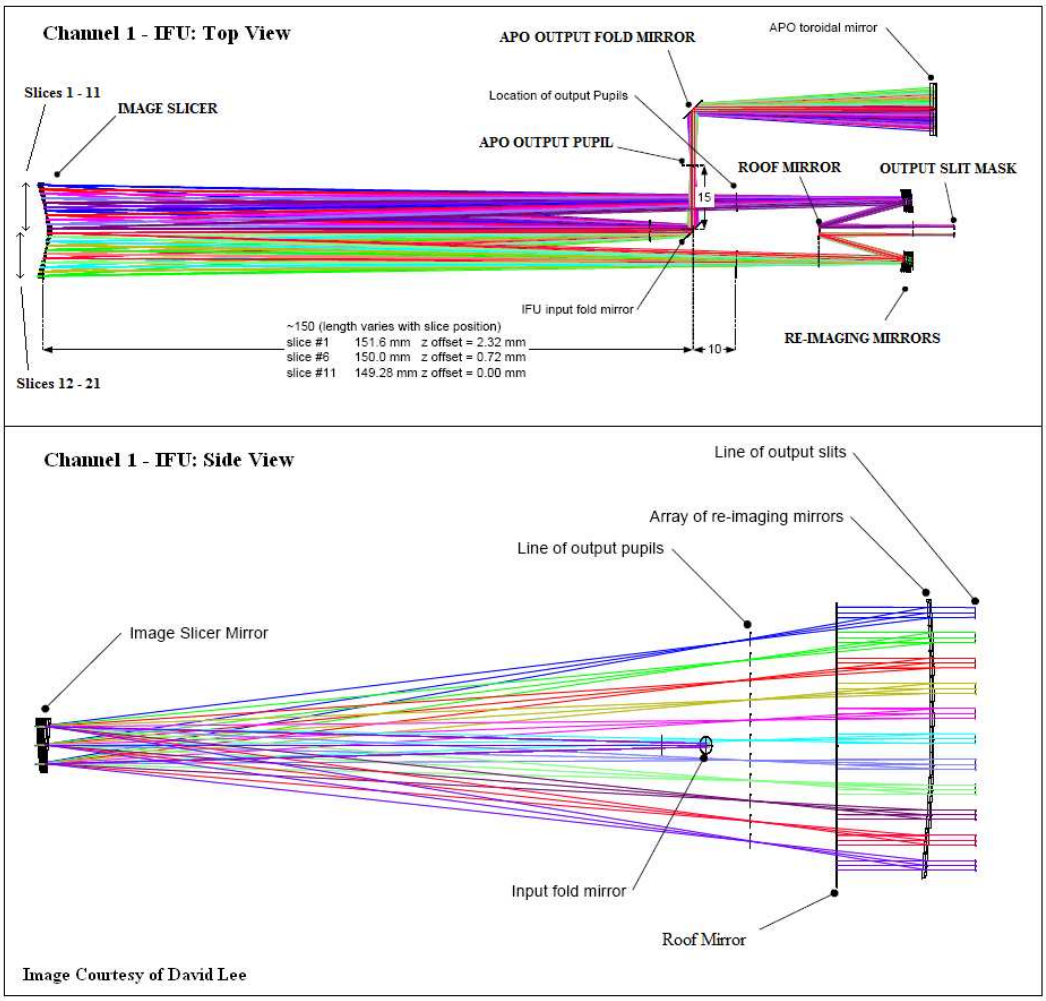

Figure 2.8: The Channel 1 Zemax model of the IFU

The Re-Imaging Mirrors

There are two re-imaging mirrors in an Integral Field Unit one for each line of pupil images created by each side of the image slicer. The re-imaging mirrors output telecentric slice images at the output slit mask and create an image at infinity of each pupil created by the image slicers. Telecentric denotes that the chief rays for each slit image are parallel. As a result the pupil images formed by the collimator will all be aligned and overlap at the grating. The combined optical aberrations of the Integral Field Unit cause the exit pupil to be deviated from being perfectly telecentric. Optical analysis has shown an effective pupil at the grating $\sim$6% larger than nominal. This increased illumination area on the grating has been taken into account when creating the rulings on the grating.

The mechanical drawing of a Channel 2 re-imaging mirror is shown in Figure 2.9. Each contains n off-axis spherical mirrors where n is 11, 9, 8 & 6 for Channels 1, 2, 3 & 4 respectively. It was designed that the two re-imaging mirrors used in a channel are identical to reduce the cost of the fabrication. Note that the re-imaging mirrors in the Integral Field Unit can also be seen in Figure 2.8. Each re-imaging mirror directs the incident beams towards a flat fold mirror. This mirror is called the roof mirror due to the angle that the two fold mirrors subtend (as per Figure 2.8). After reflection from the fold mirror the field images of each slice are directed towards the output slit mask of the Integral Field Unit.

Figure 2.9: Mechanical Drawing of a Channel 2 Re-Imaging Mirror

The Output Slit Mask

The Channel 2 output slit mask (as per Figure 2.10) is placed at the image plane of the slices produced by the re-imaging mirrors. This plane is subsequently imaged by the Spectrometer Main Optics onto the detector. The output slit mask defines the field of view in the along slice direction via the length of the slices that are transmitted through the Integral Field Unit.

The slit mask also defines the slice spacing on the detector. This is an important instrument design parameter because the spacing must be sufficient to avoid overlap between adjacent slices but also small enough not to waste detector area (to be detailed fully in Section 2.4). The slice spacing was defined at the output slit mask because this image plane is imaged directly onto the detector and as such there are no possible alignment errors that could change the gap size between adjacent slices on the detector.

Figure 2.10: The Channel 2 Output Slit Mask

The f/ratios of the beams at the output slit mask are detailed in Table 2.4. The larger slice width for Channel 4 is due to the beam produced by the anamorphic pre-optics. It would have been possible to reduce this slice width at the output slit mask by changing the across slice magnification applied by the anamorphic pre-optics however the anamorphism provided for each channel was that requested by our colleagues in the Netherlands.

	Channel 1	Channel 2	Channel 2	Channel 4
Spectral f/ratio at Mask	46.08	28.8	23.0	19.6
Spatial f/ratio at Mask	20.48	21.6	17.3	14.7
Slit Length [mm]	2.42	3.12	3.39	3.73
Gap Length [mm]	0.51	0.62	0.77	1.01
Slice Width [mm]	0.258	0.254	0.285	0.404

Table 2.4: Slice Widths and Total Field of View

Consider the along slice extent of the Channel 1 output slit mask. The along slice f/ratio is 20.48. Combining this with the telescope diameter D = 6595mm gives a plate scale of 1.52 arcseconds per mm. The along slice dimension of a slit on the output silt mask is 2.42 mm which combines to create an along slice coverage of 3.7 arcseconds which is in agreement with the designed along slice field of view (noted in Table 2.3). The length of the gap between adjacent slices for Channel 1 is 4 pixels at 0.196 arcseconds per pixel on the detector. The derivation of gap size will be considered in Section 2.7.

The design of the Spectrometer Pre-Optics requires that the slice images should be telecentric upon leaving the Integral Field Unit ie the chief rays for all images at all positions along all slits are parallel. As a result the pupil images formed by the collimator will all be aligned and overlap at the grating. The combined optical aberrations of the anamorphic pre-optics and Integral Field Unit cause the exit pupil to be deviated from being perfectly telecentric. Optical analysis has shown an effective pupil at the grating $\sim$6% larger than nominal. This increased illumination area on the grating has been taken into account when creating the rulings on the grating. Between the Integral Field Unit output slit masks and the collimator is the Output Fold Level. This level of the Spectrometer Pre-Optics simply consists of four flat fold mirrors which each direct an output slit image toward the collimator of the Spectrometer Main Optics.

2.3 The Spectrometer Main Optics

The Spectrometer Main Optics has the function of collimating the outputs of the Spectrometer Pre-Optics and relaying them onto their correct grating. Its operation is identical to that of the dispersion and re-imaging section of the long slit spectrometer (the

collimator, grating, camera & detector) outlined in Section 1.2. After the wavelength dispersion the camera system re-images the light with the correct magnification onto two detector arrays.

2.3.1 The Collimator and Grating

The geometry of the collimator and grating shown in Figure 2.11 is approximately constant for each channel. Note that the additional fold mirror between the Integral Field Unit output slit mask and the collimating mirror is not included. The collimator is a powered mirror which produces a pupil image for each slice at the grating. Because the output slit mask produces a telecentric output the pupil images from each slice will overlap at the grating. The pupil image footprint on the grating is an ellipse covering an area of approximately 25 x 41 mm spectrally and spatially respectively.

The gratings are designed to reflect solely in the zeroth and first order with $\sim 55\%$ of the light incident being reflected into the 1^{st} order. The majority of the light is directed into this order as the grating is blazed to an angle of $(29 + \frac{26}{2})$. The 1^{st} order light is reflected towards the camera optics of the Spectrometer Main Optics which relay it to the detector. The zeroth order light is directed towards a light trap in the Spectrometer Pre Optics which is designed to effectively remove it from the system. To accommodate the three sub-spectra there are three gratings for each channel. Each grating is mounted within the Spectrometer Pre-Optics on the reverse side of the dichroic wheel.

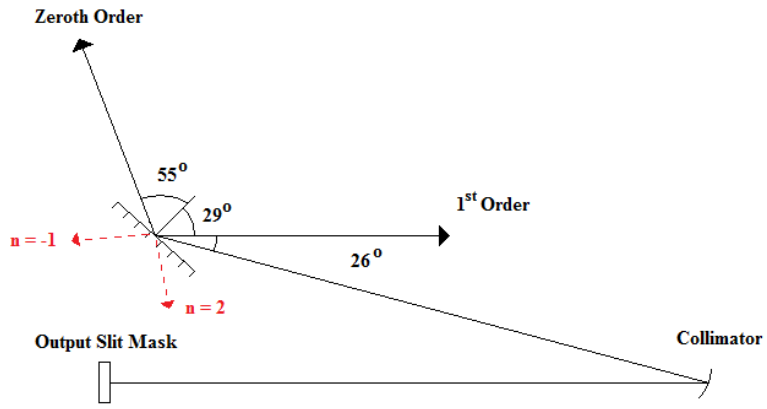

Figure 2.11: The Collimator Interface to the Gratings

2.3.2 The Camera Optics and Detector

The camera optics are divided into two sections each relaying the data from two channels to a detector. The camera optics for Channels 3 & 4 are shown in Figure 2.12 is a mirror image to that of Channels 1 & 2. Channels 1 & 4 utilise four reflections to project the slice images onto the detector array and Channels 2 & 3 utilise three. Each pair of channels is designed to use two common powered mirrors to reduce the complexity of the camera optics and more importantly the weight. The complete system is shown in Figure 2.13 where the positions of the three sets of gratings on the wheels can be seen. Note that they are situated on the opposite side of the same rotational stages as the dichroic filters which removes the possibility of selecting an incorrect dichroic-grating configuration. It also reduces the weight of the instrument and the number of mechanical parts hence the risk of a mechanical failure during flight.

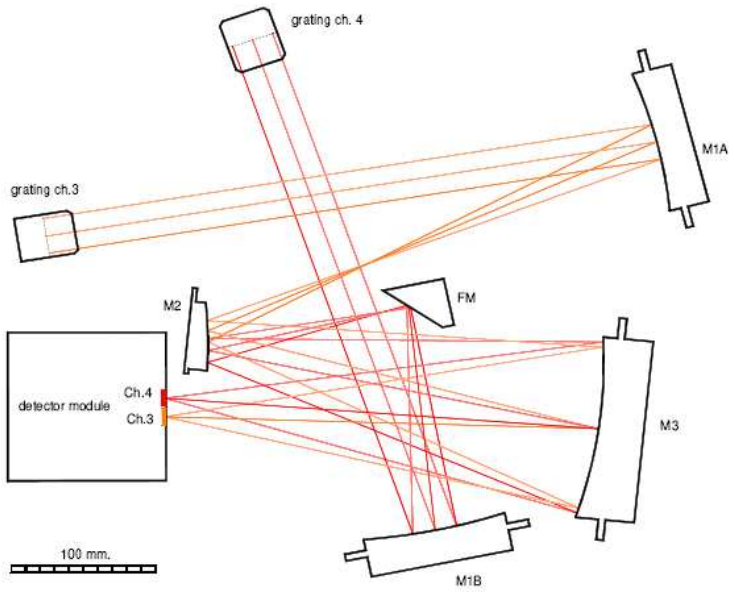

Figure 2.12: The Spectral Imager of Channels 3 & 4. M1A/B, M2 & M3 depict powered mirrors and FM a fold mirror.

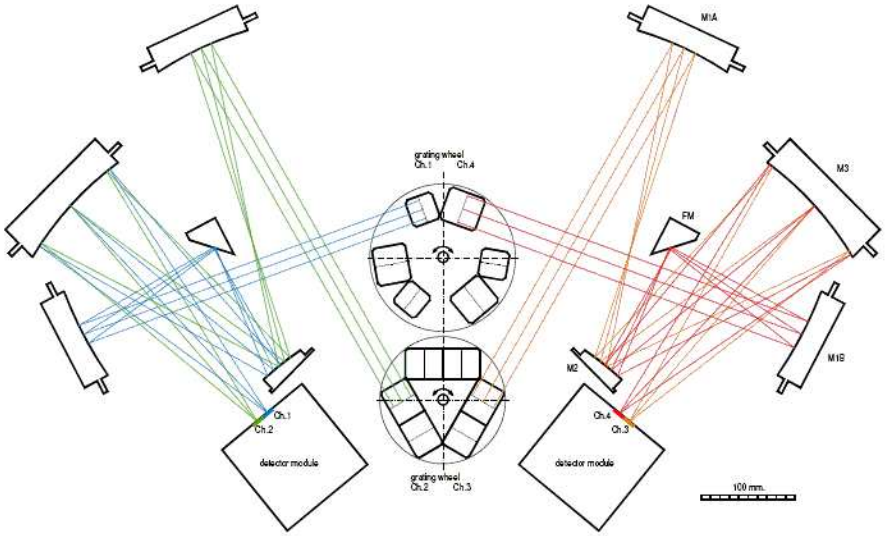

Figure 2.13: The Spectrometer Main Optics Complete Spectral Imager

The magnification of the slice image at the output slit mask onto the detector is defined by the ratio of the focal lengths of the camera to the collimator. This magnification is approximately 0.196 for each channel.

2.4 The MIRI-MRS Slice Widths

The slice widths have to be optimised for each channel so that the diffraction losses incurred by slicing are minimised. As the losses are due to diffraction which is wavelength dependant the channel bandwidths are the basis from which the slice widths are calculated.

Consider light incident on a circular aperture. A large aperture in comparison to the wavelength of light will see the light travel through the aperture with a minimal amount of diffraction. Reducing the aperture to the approximate wavelength of the incident light will result in a diffracted beam which can be considered as a point source. Reducing the size of the limiting aperture increases the amount of diffraction at the aperture.

It is the same with image slicing where the comparative size of the slice width and the point spread function (PSF) to be sliced determines the amount of diffraction that

is incurred due to slicing. A slice width that is smaller that the PSF will cause more diffraction in the across slice direction than a slice width that is larger.

Requirement OBA-0940 states that "higher diffraction will reduce the throughput of the Spectrometer Pre-Optics which is required to achieve, at the start of life, an optical transmission of 0.39" (Bean, 2008). The optical transmission must be maximised for the instrument to reduce the integration time required for an observation as this will enable more observations over the lifetime of the instrument. The choice of slice width is therefore an important parameter for the effectiveness of the instrument.

The Boundary Case Slice Widths

In the initial design phase, the MIRI slice width for a channel was defined to be between 0.5 and 2.4 $\frac{\lambda_{min}}{D}$, where $\frac{\lambda_{min}}{D}$ is the full width half maximum (FWHM) of the minimum wavelength point spread function (PSF) for each channel (as per Section 1.2.1 Figure 1.2). It will be shown in Section 2.5 that the number of telescope pointings required for fully spatially sampled data increases with increasing slice width whilst simultaneously the throughput loss due to diffraction decreases. The final choice of slice width must strike a balance between these two conflicting effects.

The lower limit of 0.5 $\frac{\lambda_{min}}{D}$ corresponds to the slice width equalling the half width half maximum of the minimum wavelength PSF in the channel. This was set as the lower boundary because at this limit the FWHM of the PSF is dissected into two pixels at the detector. This means that full spatial sampling has already been achieved in the across slice direction in one single observation. The problem with this slice width is the relatively high diffraction losses associated with it. These will be looked at shortly.

The upper limit of 2.4 $\frac{\lambda_{min}}{D}$ is more closely related to the diameter of the minimum wavelength PSF out to 1st min. This upper limit was set in order to keep the spectral resolution of the instrument constant. Consider the slice width being larger than this upper limit. A point source would not illuminate the whole of the slice whilst an extended source would. As the extended source illuminates more of the slice it would create thicker spectral lines than a point source leading to a change in the spectral resolution depending on the source type.

In terms of the diffraction, a slice width of size 2.4 $\frac{\lambda_{min}}{D}$ would barely slice into the minimum wavelength PSF out to 1st minimum. This causes significantly less diffraction loss than the previous case however to achieve full spatial sampling in the across slice direction an observational dither would have to be carried out. For full spatial sampling in a single dither the offset would have to be such that it shifts the observed structure by N + $\frac{1}{2}$ slice widths (where N is an integer amount of slice widths). For a larger slice width this requires a larger offset reducing the fully sampled field of view.

The other obvious slice width to consider is that where the slice width equals the FWHM of the min wavelength PSF or 1.0 $\frac{\lambda_{min}}{D}$. It is a compromise between the two boundary widths and as such has intermediate properties. This slice width is the one used in flight and the diffraction losses associated with it will be looked at in the next section.

Diffraction Analysis of the Boundary Case Slice Widths

The derivation of the operational slice width for the Medium Resolution Spectrometer will be considered using a basic analogy of the system to calculate the diffraction losses due to the attenuation of the point spread function by the image slicer. Diffraction of light through slicing at an image plane in a telescope will not be evident at subsequent image planes as they are real images of one another. It will however be evident at a pupil plane as the light has been dispersed. The diffraction losses due to slicing relate the amount of light incident on a subsequent image plane from that incident on the image plane where the slicing occurs. The diffraction loss occurs because some of the signal is not transmitted through the pupil aperture as it is diffracted too much into the system. The diffraction losses can be reduced by oversizing the pupil apertures and the rest of the optics.

The proposed method was to take the fast fourier transform of the MIRI point spread function at both the shortest and longest wavelengths with the slice widths previously defined in Section 2.4. We consider a perfect optical system with no aberrations included in the analysis. Note that this investigation is relevant for all channels because each channel has the same bandwidth and the slice widths are selected from the bandwidth in the same way.

The procedure used to analyse the diffraction losses due to a slicing event is outlined in Figure 2.14. The aim of the investigation was to derive the diffraction losses associated with slicing into the point spread function of an approximately slice centered point source image. There are higher diffraction losses associated with slicing point spread functions that are not slice centered. This is because more diffraction is produced by attenuating the PSF at a position closer to the central maximum.

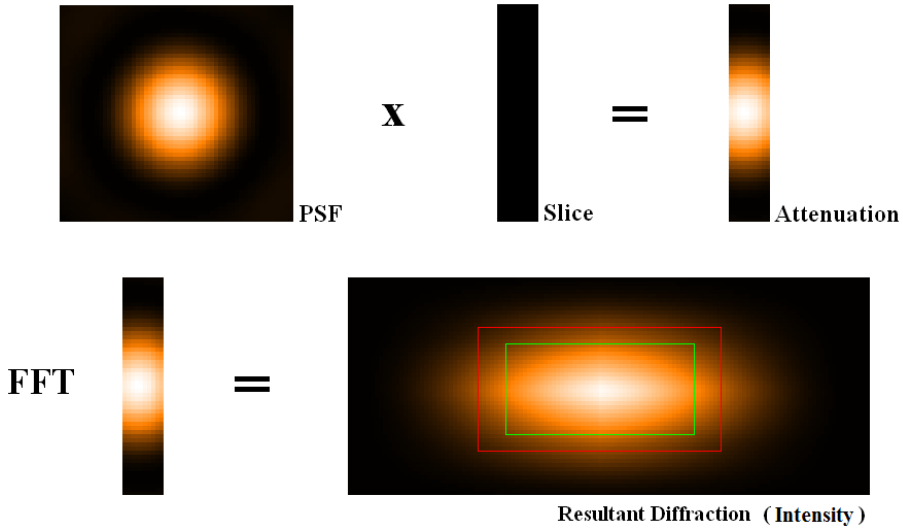

Figure 2.14: Slice Diffraction Loss Modelling

The point source image and the relative slice width combine to create an attenuation at the edges of the point spread function by the slice. This attenuation can be seen in Figure 2.14 labelled Attenuation. By taking a fast fourier transform of this attenuation the resultant diffraction at the pupil can be derived. The amount of signal transmitted through the system is dependant on the size of the aperture at the pupil plane where an oversizing of this aperture will result in less diffraction losses. This analysis is possible because the imaging optics in a telescope act as a fourier transform device.

From this basic model the diffraction losses for all three proposed slice widths at both $\lambda_{min} = 5\mu m$ and $\lambda_{max} = 7.7\mu m$ were calculated from the fraction of the attenuated flux at a pupil aperture to the total flux incident on the slice. The results are presented in Table 2.5 as % losses.

Slice Width	Optics Oversizing	λ_{min}	λ_{max}
$0.5\frac{\lambda_{min}}{D}$	2.0	31	53
$1.0\frac{\lambda_{min}}{D}$	2.0	6	14
$2.4\frac{\lambda_{min}}{D}$	2.0	5	12

Table 2.5: Percentage Diffraction Losses for Proposed Slice Widths

One of the top level design parameters states that the Medium Resolution Spectrometer should operate with a high throughput of signal. This instantly rules out the lower slice width as the diffraction losses increase above 50% at longer wavelengths. Remembering the earlier paradigm about the trade off between slice width and full spatial sampling it is concluded that the 1.0 $\frac{\lambda_{min}}{D}$ width for the slice is the best choice as it has a high throughput of signal and the offset required for full spatial sampling will be shown to be quite small (see Section 2.5).

In an early analysis of the instrument design the slice diffraction of MIRI showed losses of 4% and 10% for the slice width 1.0 $\frac{\lambda_{min}}{D}$ which decreased to 3% and 7% when changing the optics oversizing from 1.5 to 2 (Glasse, 2003). The actual optics oversizing and the diffraction losses for the Flight Model are shown in Table 2.6. Optics oversizing refers to the size of the pupil apertures with respect to the nominal beam profile. Larger apertures will transmit more diffracted light leading to a reduction in diffraction losses.

Channel	Optics Oversizing	Slice Losses (λ_{min})	Slice Losses (λ_{max})
1	2.5	3	9
2	2.5	4	8
3	2.0	6	12
4	1.7	5	13

Table 2.6: Optics Oversizing & Percentage Diffraction Losses for the Slice Widths

The diffraction analysis which I performed in this section had 2 times optics oversizing and measured diffraction losses of 6% and 14%. This model is closely related to that of Channel 3 which also has optics oversizing of 2 and diffraction losses of 6% and 12%. Due to the good agreement it can be concluded that the diffraction analysis using a

simple model is a good approximation to understand the more complex operation of the optical model of the spectrometer.

2.5 Full Spatial Sampling with the MIRI-MRS

It has been shown how the Medium Resolution Spectrometer slice widths have been chosen to minimise the diffraction losses in each channel. The slice width of 1.0 $\frac{\lambda_{min}}{D}$ will be furthermore referred to as 1.0 a_{diff}. An investigation into the operational method to achieve full spatial sampling will now be outlined.

Along Slice Direction

First consider the simpler case of the along slice direction. The along slice pixel scale at the detector in arcseconds per pixel is 0.196 for Channels 1 and 2, 0.245 for Channel 3 and 0.273 for Channel 4. If a feature falls within a single pixel it is unknown where the center of the feature resides spatially. By scanning the telescope in the along slice direction by roughly n + $\frac{1}{2}$ amount of pixels (where n is an integer number of detector pixels) and making another observation this feature will now be split between two pixels and from comparing the signal in each pixel it is possible to calculate the centroid of the feature assuming it is symmetric about the peak.

Due to the varying pixel scales of the channels at the detector it will be difficult to offset each channel by n + $\frac{1}{2}$ pixels simultaneously. An offset of 0.9 arcseconds would offset Channels 1 & 2 by 4.6 pixels, Channel 3 by 3.67 pixels and Channel 4 by 3.29 pixels. As each channel sees an along slice offset of approximately n + $\frac{1}{2}$ this offset could be used during flight. However performing a larger telescope offset will reduce the fully sampled field of view from that achieved with a smaller offset.

Across Slice Direction

The spatial sampling in the across slice direction is achieved in the same manner. By offsetting each slice by N + $\frac{1}{2}$ slice widths (where N is an integer number of slice widths) what would previously fallen on a single slice is now divided between two adjacent slices. Achieving this offset simultaneously for all four channels will enable

fully spatially sampled data to be acquired with a minimum telescope observation time (as only one across slice dither and observation is required).

The theoretical slice widths derived from the FWHM of the λ_{min} PSF in each channel are 0.176, 0.271, 0.417 and 0.643 arcseconds. It will be shown that a slight deviation from these values enables high sampling quality to be achieved for all slices in a single telescope offset. Consider the offset needed to move each slice by N + $\frac{1}{2}$ slice widths on the sky. Keeping N to a minimum will mean for each channel there will be a maximum fraction of the field of view that is fully sampled.

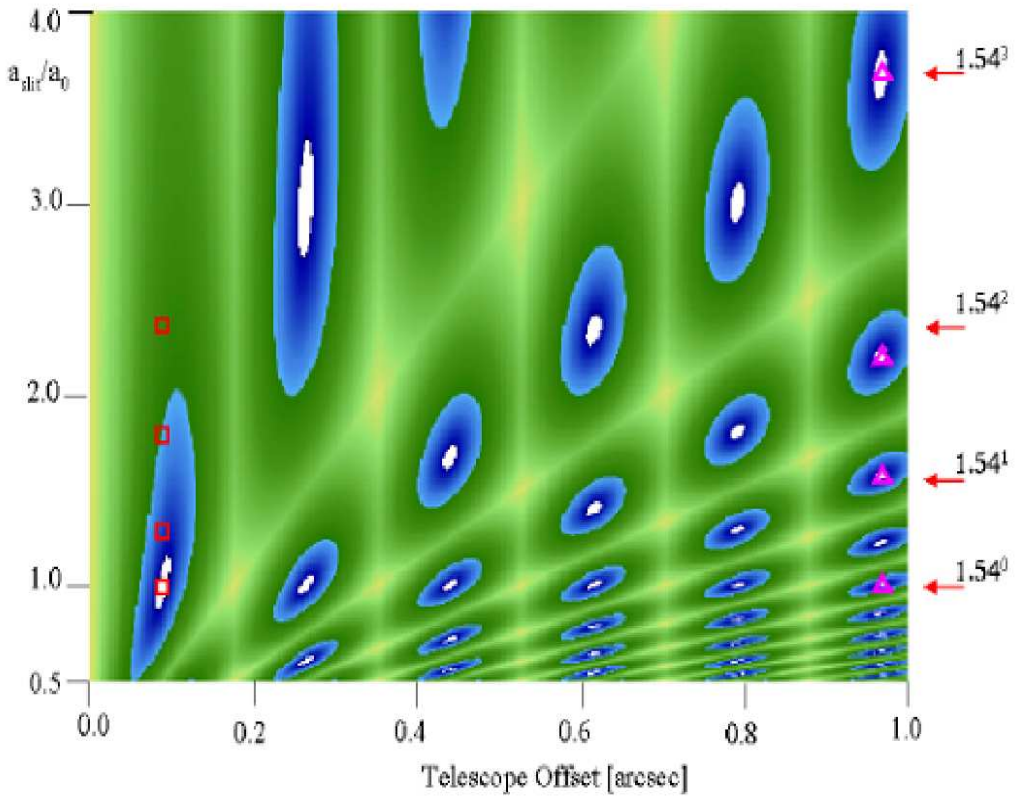

Figure 2.15: Sampling Quality for an Across Slice Dither

Figure 2.15 (Glasse, 2003) shows the across slice sampling as a function of telescope offset. $\frac{a_{slit}}{a_o}$ refers to the slice width being considered (a_{slit}) as a fraction of the Channel 1 slice width (a_o). The slice width ratios which give perfect sampling (telescope dither = N + $\frac{1}{2}$ slice widths) appear within the white regions of the image. The yellow regions define the case where the telescope dither has moved N slice widths. This offset does

not produce any increase in sampling as any features are still in the same across slice position (however they have been transferred to a different slice). The intermediate cases are coloured blue to green.

Table 2.7 contains the parameters that define the pink triangles found along the line x = 0.95 arcseconds. Note the red squares define an early proposal to generate the slit widths which was deemed inadequate due to the reduction in sampling quality at longer wavelength channels. N_{slit} refers to the integer number of slice widths that are offset for each channel at 0.95 arcseconds.

Channel	$slit$	N_{slit}	Slice Width a_{slit}	$\frac{a_{slit}}{a_o}$	$\frac{a_{slit}}{a_{slit-1}}$
1	0	5	0.176	1	-
2	1	3	0.276	1.57	1.57
3	2	2	0.387	2.20	1.40
4	3	1	0.644	3.67	1.67

Table 2.7: Across Slice Spatial Sampling Offsets

The $\frac{a_{slit}}{a_{slit-1}}$ column shows the fractional increase between the slice widths of adjacent channels. For the theoretical slice widths this is always 1.54 which is the same as the fractional change in minimum wavelength of adjacent channels. In practice the channel wavelength transmission is unchanged from theoretical meaning that only the slice widths are varied to achieve the optimum sampling. The largest deviation is for Channel 3 which uses a slice width which is ∼7% smaller in practice than that theoretically derived from the bandwidth. These deviations in slice width do not place the operational slice width outside the 0.5 - 2.44 a_{diff} limits.

The across slice offset required to achieve full spatial sampling for all channels in the across slice direction was 0.95 arcseconds. This corresponds to an on-sky dither of 5.39, 3.44, 2.45 & 1.47 slice widths for Channels 1, 2, 3 & 4 respectively. This dither was intended to minimise the on-sky offset whilst creating the required offsets hence maximising the fully spatially sampled field of view.

2.6 Spectral Sampling and Resolution

It is not possible to offset a telescope to change the sampling of a spectrum as it is purely wavelength dependant. Full spectral sampling must instead be achieved through the design of the instrument. As such the slice width for each channel should cover two pixels on the detector.

Consider the case for Channel 1. The dimension of the detector along which the spectrum will be imaged is 1024 pixels and the size of each overlap between channel dichroic observations is 100 pixels (so that sub-spectra can be joined together seamlessly). For configurations A and C there are 924 pixels over which the wavelength coverage is imaged and 824 for B. As such the number of spectroscopic resolution elements in a sub-spectrum observation is $\frac{924}{2}$ for Dichroics A & C and $\frac{824}{2}$ for B.

The resolving power of an observation can be estimated using Equation 2.4. It is derived from the operational wavelength (λ) divided by the transmitted bandwidth of the dichroic observation ($\Delta\lambda$) times the number of resolution elements (which is the number of pixels divided by the size of a slice width). The transmitted bandwidth $\Delta\lambda$ for the dichroic observation is simply $\frac{(7.7-5)}{3}$ for Channel 1.

$$ResolvingPower = \frac{\lambda}{\Delta\lambda}\frac{824}{2} \tag{2.4}$$

The spectral resolution of the Medium Resolution Spectrometer for the nominal case of a slice width extending across two pixels on the detector is shown in Table 2.8 (Renouf, 2006). In reality the slice width in each channel does not cover two pixels on the detector. This will be considered next.

Channel	Spectral Resolution (λ_{min})	Spectral Resolution (λ_{max})
1	2400	3700
2	2400	3600
3	2400	3600
4	2000	2400

Table 2.8: The Anticipated MIRI-MRS Spectral Resolution

The Operational Spectral Sampling

There is an additional anamorphism applied to the beam in the Spectrometer Main Optics which reduces the slice width on the detector to less than 2 pixels. This reduces the spectral sampling delivered by the spectrometer. It originates in the angle that the grating subtends to both the collimated beam and the camera optics. Consider Figure 2.16. The diameter of the pupil incident on the camera optics is of a factor $\frac{Cos\mathbf{r}}{Cos\mathbf{i}}$ bigger than the pupil size incident on the grating. This is along the spectral direction of the beam in the Medium Resolution Spectrometer.

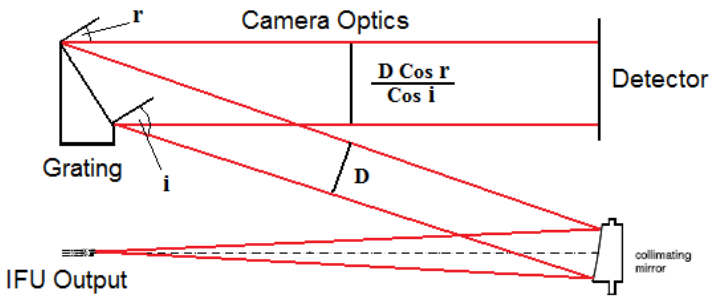

Figure 2.16: The Pupil Anamorphism Applied at the Grating

By Éntendue increasing the diameter of a pupil will reduce the maximum off axis angle on the sky (as per Section 2.2.2 Figure 2.6). As a result the slice width at the detector is reduced by the same magnitude as the across slice pupil dimension is increased leading to a reduction in the spectral sampling of the instrument.

Consider the Channel 1 across slice direction without the grating anamorphism. The Spectrometer Main Optics applies a magnification of the slice image onto the detector of $M = \frac{F_{cam}}{F_{coll}} = 0.196$ and the pixel scale is 25 microns (as per Section 2.3.2). The across slice plate scale of a slice at the output slit mask is 0.679 arcseconds per mm (as per Section 2.2.2 Table 2.4). As such the plate scale at the detector is 0.088 arcseconds or half a slice width per pixel as required for full spatial sampling.

Now consider the across slice direction with the grating anamorphism. The angles of incidence and reflection of the beams at the grating are **i** = 55 & **r** = 29 degrees. This induces a magnification of the pupil in the along slice direction of 1.52. Remember by Éntendue a pupil dimension increase relates to a field dimension decrease of the same

factor. As a result the delivered across slice plate scale at the detector = 0.13 arcseconds per pixel. This reduces the slice width of 0.176 arcseconds to 1.35 pixels resulting in a spectral undersampling of the slice width.

The slice width extent at the detector is shown in Table 2.9. There is a variation between λ_{min} and λ_{max} because the angle of reflection **r** changes due to the wavelength dependant constructive interference. The increase of the Channel 4 spectral line width above 2 pixels is due to the size of the slice in the across slice direction at the output slit mask (noted in Table 2.4) determined by the amount of anamorphism in the beam defined by the anamorphic pre-optics. The anamorphic factor supplied for each channel was that requested by our colleagues in the Netherlands.

Channel	Slice Width at Detector (λ_{min})	Slice Width at Detector (λ_{max})
1	1.40	1.79
2	1.45	1.82
3	1.63	2.04
4	2.25	2.82

Table 2.9: Spectral Sampling at the Detector (in pixels)

The operational spectral resolution for the Medium Resolution Spectrometer considering the spectral sampling at the detector are shown in Table 2.10. They were derived by taking the product of the anticipated spectral resolution in Table 2.8 with ratio of the nominal to the new slice width at the detector.

Channel	Spectral Resolution (λ_{min})	Spectral Resolution (λ_{max})
1	3400	4100
2	3300	3900
3	2900	3400
4	1700	1700

Table 2.10: The MIRI-MRS Spectral Resolution

Requirement OBA-0638 states that "MIRI shall provide integral field spectroscopy with spectral resolving power R $>$ 2400 between 5 and 10 μm, R $>$ 1600 between

10 and 15 μm and R $>$ 800 between 15 and 27 μm". The requirement is met across the entire wavelength coverage of the instrument with a resolution much greater than the requirement at the longest wavelengths. This requirement was described to ensure that the emission lines expected to be observed by the Medium Resolution Spectrometer can be separately resolved.

It has been shown that whilst the spectral resolution of the instrument has been achieved there is spectral undersampling in Channels 1 & 2 and also at the shorter wavelength end of Channel 3. There is nothing that can be done about this at this stage as it is inherent in the design. It may however be possible to recoup some of the information lost through the spectral undersampling. This can be achieved through dithering an observation onto a different slice which may re-sample the wavelength on a sub-pixel scale. Whether the spectral offset achieved between two given slices will be stable or variable depends on the opto-mechanical stability of the spectrometer.

2.7 The MIRI-MRS Fields of View

There are two more factors to consider with the design of the image slicers. These are the number of slices and the length of each slice within a channel. These determine the field of view that each channel samples on the sky. The main constraint for these factors is the space available on the detector as each slice has to be imaged upon it.

Slice Spacing on the Detector

When determining the design of the image slicers the detector area must be considered because it defines a finite space within which the complete channel data must be imaged. For each channel it was required that the field of view be approximately square as this is most useful for observing. As such increasing the number of slices also requires an increase in the length of the slices. An important consideration is the spacing of the slices on the detector.

Requirement OBA-0652 (Bean, 2008) states that "spectra from different spectral/spatial ranges that are imaged on the same two-dimensional detector array shall

be separated by a gap of at least the diameter of the first dark diffraction rings determined from the PSF generated by the segmented telescope, at the longest wavelength in the spatial direction, to avoid overlap of spectra at different orders".

Effectively there is a necessity that the slices on the detector must be separated by 2.44 $\frac{\lambda_{max}}{D}$ or 4 pixels, whichever is largest. This is required so there is no cross talk between the slices. Consider again Channel 1 with its wavelength range of 5 - 7.7 microns. Consider a point source at the edge of a slice whose 1st minimum will be diffracted away from the slice by an amount equal to $1.22\frac{\lambda}{D}$ arcseconds on the detector. Now consider another point source incident on the neighboring slice which will also show the same diffraction. We want to image these slices onto the detector so that the point spread functions created by these neighboring sources do not overlap before their 1st minimum. As such the required separation on the detector is $2.44\frac{\lambda}{D}$ or the diameter of the PSF out to 1st minimum. As this separation needs to hold for all wavelengths in each channel the gap size is calculated for the maximum wavelength of a channel.

This implies that for n slices there are n-1 strips of dead pixels on the detector. These strips are minimised in size to maximise the amount of the detector area available for observations. Consider Channel 1 which has 512 x 1024 pixels of a detector available for use (as per Chapter 4 Figure 4.1). The slices must be laid end to end with the required spacing within the 512 pixel budget (with the wavelength data to be spread over 1024 pixels). In reality the 512 pixel budget defines the total length of the Channel 1 detector area, the actual extent of the Channel 1 data along the detector must be less than this because the Channel 1 and Channel 2 data must be separated from one another to avoid crosstalk between channels. Requirement OBA-0655 (Bean, 2008) states that "sufficient areas of the array shall be left un-illuminated to allow for monitoring and measurement of the scattered light/detector dark current". This is necessary to fully calibrate each observation. In effect this reduces the detector length available for data capture to $<$490 pixels.

A Channel 1 slice width covers 0.176 arcsecs and in the along slice direction the pixel scale is 0.194 arcsecs. The required gap between slices on the detector for this channel is 4 pixels. Equation 2.5 shows the detector equation where n is the number of slices and l is the length of each dimension. For Channel 1 the slice length corresponding to 3.7 arcsecs (the approximate extent of 21 slices in the across slice direction) is approximately 18.85 pixels per slice.

$$[n * l(slice)] + [(n-1) * l(gap)] < 490 \tag{2.5}$$

For Channel 1 the total spatial extent that the slices extend across the detector is 479 pixels. This means that there will be 33 x 1024 unilluminated pixels in the Channel 1 area of the detector. That of Channels 2, 3 & 4 are 464, 485 & 434 pixels respectively. It is evident that there are additional dark unilluminated pixels for each channel though it was not possible to include another slice without exceeding the limit set by Equation 2.5. In each case the achieved field of view was approximately square.

The Fields of View

Using the above equation the Channel 1 design is derived to be one of 21 slices each of length 3.7 arcsecs covering a field of view of 3.7 by 3.7 arcsecs. This exceeds requirement OBA-0641 (Bean, 2008) which states that "The Integral Field Units shall have a common field of view of at least 3.5 by 3.5 arcsecs for all subsections of the spectrograph wavelength range". This field of view requirement was described with the intention that it would enable the fully sampled observation of typical spiral galaxies at z = 1 in a single exposure.

In the across slice direction the detector is larger than the 1024 x 1024 pixels that each pair of channels are imaged upon. This is due to requirement OBA-0655 (Bean, 2008) which states that "sufficient areas of the array shall be left un-illuminated to allow for monitoring and measurement of the scattered light/detector dark current". This is necessary to provide the means for a scattered light and dark measurement of the detectors as an accurate observations of each will be required during the analysis to optimise the data reduction techniques.

Following from this are requirements OBA-0649 and OBA-0650 which deal with the requirements of the spectra position on the detector at both minimum and maximum wavelength. The objective of these requirements are again to ensure there are sufficient dark areas for calibration.

OBA-0649 states that "a spectral line with a wavelength of 5 μm, imaged by that Integral Field Unit slice which places it closest in the dispersion direction to the edge of the array, should fall between 75 and 100 pixels from the edge of the array".

OBA-0650 states that "a spectral line with a wavelength of 28.3 μm, imaged by that Integral Field Unit slice which places it closest in the dispersion direction to the edge of the array, should fall between 50 and 90 pixels from the edge of the array".

As a result of the design of the Medium Resolution Spectrometer the field of view of the instrument is expected to fall within the requirements defined for both the total extent of the field of view and also the amount of non illuminated area on the detector for calibration of the observations.

2.8 Transmission Measurement of a Prototype IFU

2.8.1 Introduction and Test Set-up

The following test was carried out using a Channel 1 Prototype Integral Field Unit to show that the level at which the point spread function is sliced induces those diffraction losses expected by the optical modelling. As this slicing technique is unproven over the complete Medium Resolution Spectrometer spectral coverage this testing is required to ensure the function of the image slicer is well understood for low diffraction losses. The prototype slicer was of the same design as the nominal Channel 1 slicer except that where slices 15 to 21 should be there was instead one flat comparison mirror designed to output where slice 17 outputs (as per Figure 2.17. Note that the image is not to scale). The purpose of the prototype slicer was to enable a direct comparison of the transmission through the Integral Field Unit of the sliced point spread function to that of the unsliced case.

Optical Design of the Prototype IFU

It was expected that further diffraction losses would occur in the across slice or spectral direction due to slicing as the size of the slice width attenuates the point spread function incident on the slicer. The purpose of having the comparison mirror was so that the image of the point source could be centered on it and being much larger in the spectral direction would output an unsliced image. This could be compared with that of a sliced image to give a direct measurement of the amount of light lost due

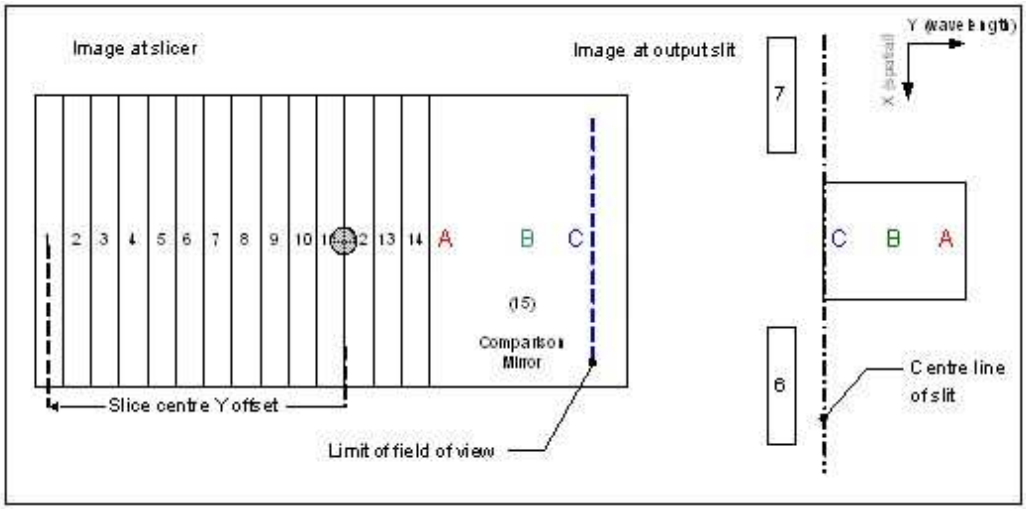

Figure 2.17: Channel 1 Prototype IFU

to diffraction at the slices. The light source could be driven across the slicer enabling the image to be placed on slice or between slices as desired. The footprint of the PSF in a slice centered image extended visibly across three slice widths on the detector. This agrees with the optical model which shows that ∼90% of the incident light, when centered on a slice, falls on that slice and the slices immediately adjacent to it.

Prototype Set-up Pre and Post Optics

The test assembly prior to cooling is shown in Figure 2.18. The pre-optics consisted of a beam splitter, enabling the use of the point and extended sources in the same setup, and some lenses to produce an image of the source at the slicer. A steerable mirror was used to drive the image of a source across the slicer. This was achieved using a LabView interface and could be driven in both the vertical and horizontal directions. The post-optics consisted of three re-imaging lenses which were designed to re-image the output pupil plane of the Integral Field Unit, i.e. the individual slices, directly onto the detector. The flat field source directly illuminated the detector. The test set-up was placed in a cryostat and cooled to its operating temperature of 35K which was the required operating temperature of the detector.

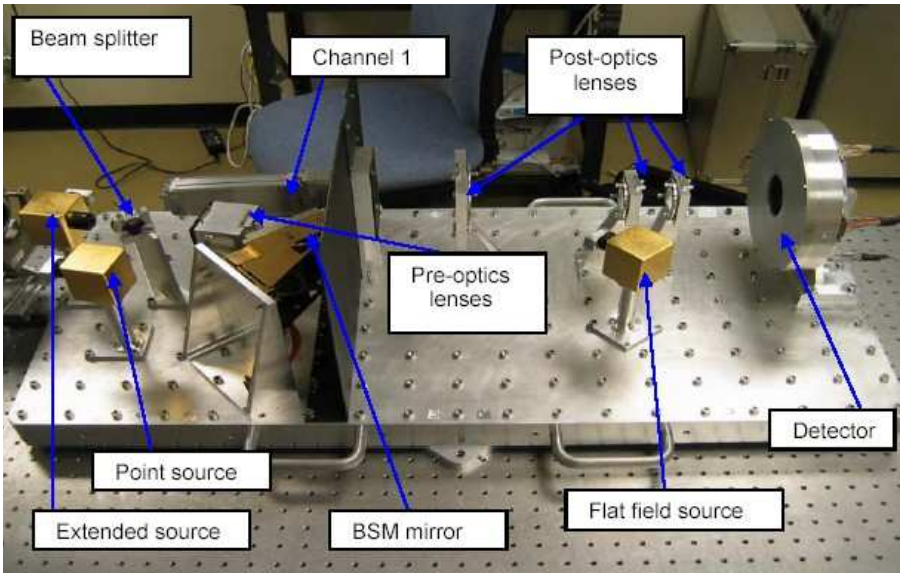

Figure 2.18: Prototype Test Assembly

The Detector

The detector used in the testing was a UIST Engineering Grade Detector of InSb for use at 1 - 5 microns. The detector was large enough to capture slices 4 through 9 with a partial capture of slice 10 and also slices 14 and 17 (the comparison mirror) as shown in Figure 2.19.

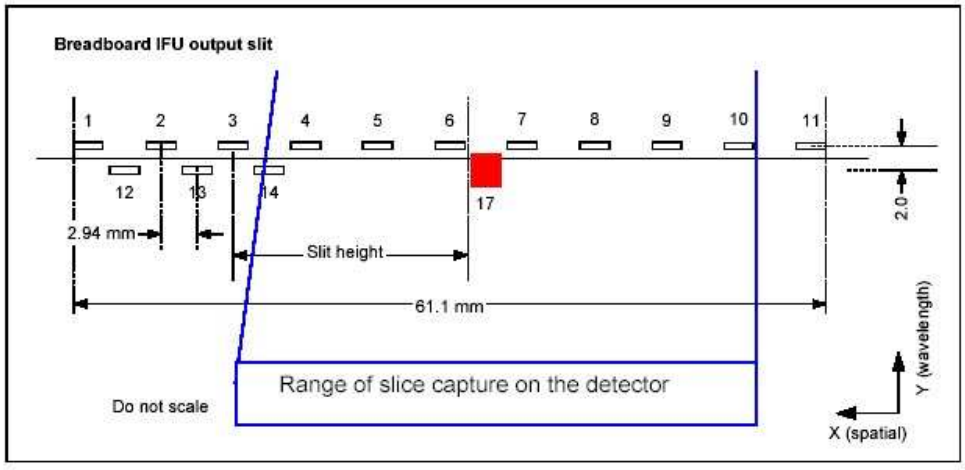

Figure 2.19: Range of Slices captured on the Detector

2.8.2 Test Method and Data Reduction

The premise behind the test was to incrementally drive the point source across the whole slicer in the spectral direction of the slices in order to describe the useful transmission of the prototype Integral Field Unit as a function of across slice position. The spatial position was kept constant at the middle of the slices. The loss in transmission due to slicing was taken as the sum of the three maximum signal outputs divided by the output from the image centered comparison observation. The maximum signal outputs were generally the primary illuminated slice and the two neighboring slices on the slicer though when the source was at a boundary between two slices a small proportion of the signal was pretty evenly shared between a third and fourth slice sandwiching the central two.

Data Analysis

An IDL program was set-up to read in multiple images. On these images several regions of interest were defined at the positions where the slice outputs were found. These regions were defined as circular and slightly oversized to ensure that all of the slice output would fall within them. A taurus or concentric circle was defined outside the first the size of which was defined by the surface area of the taurus being equal to the area inside the first circle. Subtracting the outer taurus from the inner circle resulted in a basic background subtraction. The program scanned through all of the images and created an array of slice output intensity for slices 4 through 9 as a function of primary position of the point source illumination on the slicer.

A flat field image of the detector is shown in Figure 2.20, the dark regions of the image are regions of the detector that are broken (they return a very low intensity of approximately -50 to -200 counts). A trend of increasing intensity across the detector was observed. The increasing intensity could be approximated as linear across the extent of the outer diameter of the a slice analysis taurus. As such the method of background subtraction effectively removed any influence of the intensity change on the slice measurement because the average pixel value of the unilluminated taurus was approximately the same as that of the measurement circle.

By design the Channel 1 slice width was designed to be the same size as the full width half maximum of the point spread function at 5 microns. It has been shown by optical

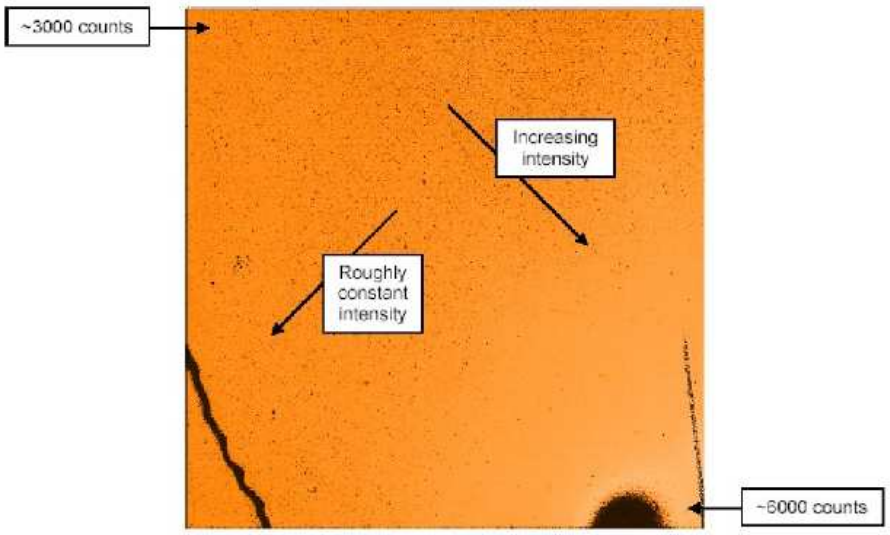

Figure 2.20: Flat Field Image of Prototype Detector

modelling that ∼90% of the incident light falls on three adjacent slices with the point spread function centered on the middle slice at 5 microns. For any across slice position only the three most intense slices were used in the analysis. Whilst this was a good method to model the slice centered case there was a discrepancy at the between slice case where the third and fourth slices were of approximately the same intensity. However due to the low intensity of these slices in comparison to the two central slices the additional loss of ∼ a percent was not deemed significant. The source centered on the comparison mirror was used to scale the flux of the investigation. As such the fraction of flux through three slices to the 90% of the comparison mirror flux was a direct measurement of the diffraction losses due to attenuation of the PSF at the slices.

Two different data sets were taken with the test set-up. One was taken with a fine scan through the across slice position with each increment in the position of the point source being of ∼0.25 slice widths. The second was coarser scan point source scan of ∼1 slice width.

2.8.3 Results and Discussion

The images show a noticeable difference between the pupil image from a sliced and an unsliced point spread function. The sliced images were all approximately the same

size but that produced by the comparison mirror was smaller in the spectral direction than the sliced images as shown in Figure 2.21. The extension in the spectral direction of the pupil images is due to the diffraction which occurs because of the attenuation of the point spread function (as per Section 2.4).

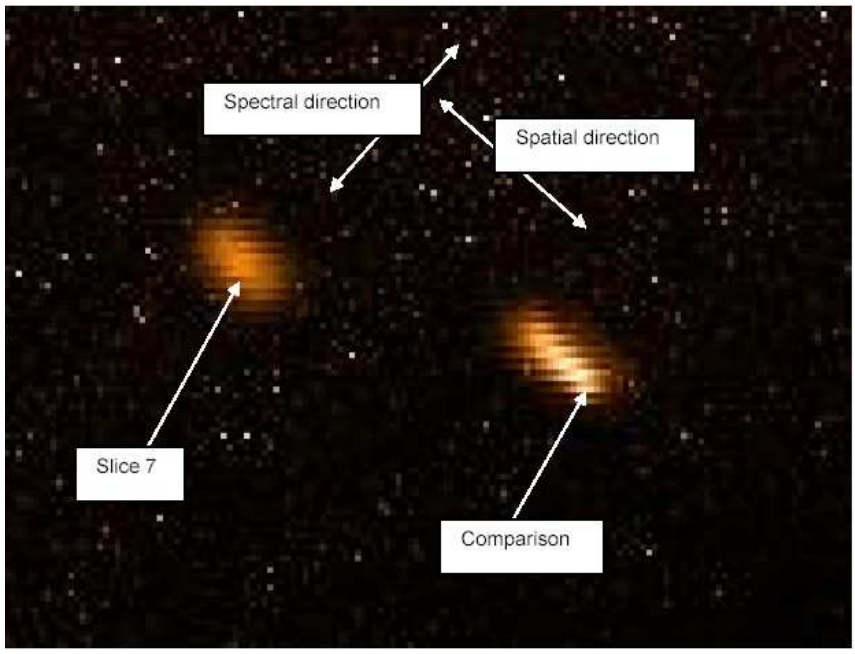

Figure 2.21: Tiled image of Slice 7 and COM Mirror at 12X magnification

The graph in Figure 2.22 shows the transmission from three slices as a fraction of that from the comparison plotted as a function of the primary position of the point source on the slicer. It also shows the total transmission of all the slices (4 through 9) as a function of slice number for the fine data set (again as a fraction of the comparison transmission).

The small blue diamonds show the results of the fine scan and the large red squares that of the coarse scan. The solid yellow line shows the total intensity of all slices (4 through 9). The error bar shown at slice 6 depicts the 3 sigma noise level of a transmitted slice measured at the detector. This was calculated from several images at the same spatial position taken over several days. It should be noted that the slice number is a general indication of the primary position of illumination on the slicer. The exact position could be ascertained to such a high degree of accuracy.

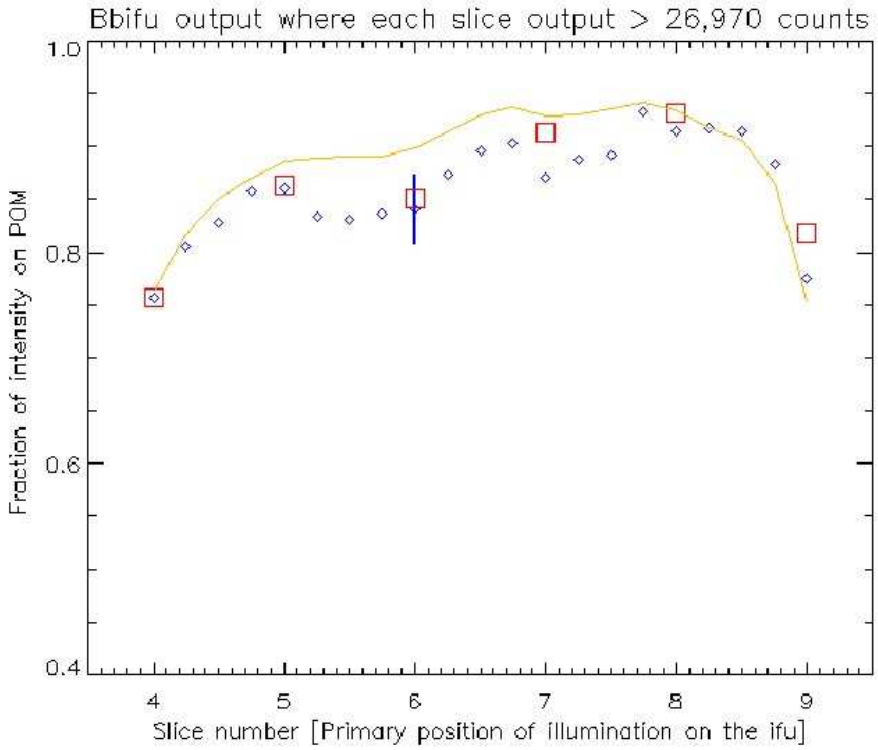

Figure 2.22: A Graph of Prototype Throughput as a Function of Primary Slice Illumination. The blue diamonds and red squares depict the total intensity measured across the three primary illuminated slices and the yellow line depicts the total light transmitted through slices 4 - 9

The useful data is between slices 5 and 8 on the graph. Outside of this range it can be seen that the sliced transmission compared to the comparison transmission starts to decline quite rapidly. This is not a characteristic of the instrument but rather an effect due to an increasingly larger amount of the light being incident on a slice that does not output onto the detector. The same is the case for the other data sets on the graph.

The solid yellow line depicts the total flux transmitted through slices 4 to 9 of the IFU as a fraction of the transmitted comparison image flux ($\sim 0.93 \pm 0.04$). This shows that the image slicer transmits a large fraction of the light incident on it and the diffraction losses are not overwhelming the useful transmission. Due to the baffling system in place in the Integral Field Unit (the input pupil, the pupil mask and the output slit mask) it can be assumed that the fraction of scattered light included in this transmission is relatively small.

From the fine data set the useful transmission through the three principal illuminated slices is measured to be $\sim$0.86 $\pm$ 0.06 of that transmitted through the comparison mirror however only $\sim$90% of the intensity of a slice centered point spread function will fall on the central slice and its two neighboring slices whilst the comparison mirror will transmit the entire point spread function.

In effect the transmission between three slices must be compared with 90% of the light transmitted through the comparison mirror. This gives an approximate diffraction loss in the transmission due to slicing of $\sim$4%. The expected diffraction loss due to image slicing expected from the optical model of Channel 1 at 5 microns is $\sim$3% (as per Table 2.6). This shows that the measured slice diffraction losses for the Prototype Integral Field Unit are approximately the same as those expected from the optical model. It is concluded that the image slicer design is conformant with the transmission requirements of the instrument as understood by the optical model.

2.9 The MIRI Medium Resolution Spectrometer

The design of the Medium Resolution Spectrometer has been reviewed concentrating mainly on the Spectrometer Pre-Optics which were assembled at the UK Astronomy Technology Center. It is the Spectrometer Pre-Optics which enables simultaneous spectra to be taken across the entire field of view. It also defines the extent of the field of view and is optimised to minimise diffraction losses.

The operational slice widths for each channel were analysed using diffraction analysis to show how each slice width was derived. The observational dithers required to achieve full spatial sampling in both the along and across slice direction have also been derived, the latter from a consideration of the slice widths across all channels.

There is an anamorphic magnification applied to the spectrometer field of view so that the sampling in the across slice direction at the detector will be such that a slice width extends two pixels. However due to an error in the design there is an additional beam anamorphism in the Spectrometer Main Optics which reduces the slice width to less than 2 pixels for Channels 1, 2 & the lower wavelengths of Channel 3. This results in a spectral undersampling at the detector. It has been proposed that further information about the positions of the spectral lines could be derived from dithering between

slices as this may sample the spectrum at different across slice positions. The reduced spectral sampling does not degrade the spectral resolution of the spectrometer below the requirements.

The testing of a prototype Channel 1 image slicer at operational wavelengths was carried out to measure the diffraction losses induced by image slicing. It was necessary as the diffraction losses expected by the optical model had to be verified in practice. The test enabled the transmission of the Integral Field Unit for a sliced point spread function (PSF) to be compared with that of an unsliced PSF. It was shown that the measured diffraction loss of 4% was consistent with the optical model expectation of 3%. As such it can be concluded that the optical model does understand the operation of the image slicer at 5 microns.

Further Investigation Required

This analysis of the image slicer operation was a basic test to verify that the diffraction from slicing into the point spread function would be as the models predicted. There is a more detailed test which must be undertaken to fully understand the diffraction of a point spread function in the Integral Field Units when they are integrated onto the complete Mid Infra-red Instrument. This test involves the measurement of the diffraction losses due to a point source being at different across slice positions ie centered on a slice, between slices and at different increments between.

It is expected the diffraction losses vary when the PSF is centered at different across slice positions. This effect must be characterised as it is expected that during observations there will be targets at various across slice positions. This test was to be carried out during the testing of the MIRI Verification Model. To investigate this a certain accuracy in the positioning of the point source on the image slicer is required. During the Verification Model test campaign the point source was to be delivered to the MIRI Verification Model by a telescope simulator. To ensure that this MIRI Telescope Simulator would enable a the required positional accuracy of the point source on the Medium Resolution Spectrometer image slicers I performed a test on the MIRI Telescope Simulator. This test was performed in Madrid in the summer of 2007 where I spent two months on attachment. The design of the MIRI Telescope Simulator which

is relevant to the scanning of the point source across the image slicer will be outlined in the next chapter along with the test procedure and subsequent analysis.

CHAPTER 3

The MIRI Telescope Simulator

The MIRI Telescope Simulator is part of the optical ground support equipment for the Mid-Infrared Instrument. It was constructed out of the necessity to simulate an astronomical source to enable the test verification of the optical design of both the MIRI Verification Model and the Flight Model without the necessity that it be integrated onto a functional model of the James Webb Space Telescope. It facilitates the delivery of an f/20 test beam under cryogenic conditions similar to that supplied by The James Webb Space Telescope. The operational set-up during the calibration phase is shown in Figure 3.1 (Wells et al., 2004).

The primary objective of the MIRI Telescope Simulator is to reproduce the flight functionality of the James Webb Space Telescope under controlled conditions to enable testing of the operation of the entire Mid-Infrared Instrument. This is necessary to ensure the instrument will function correctly during flight and will enable design modifications to the Flight Model to correct any serious deficiencies. The design details contained within this chapter unless otherwise stated have been taken from Aricha et al. (2006).

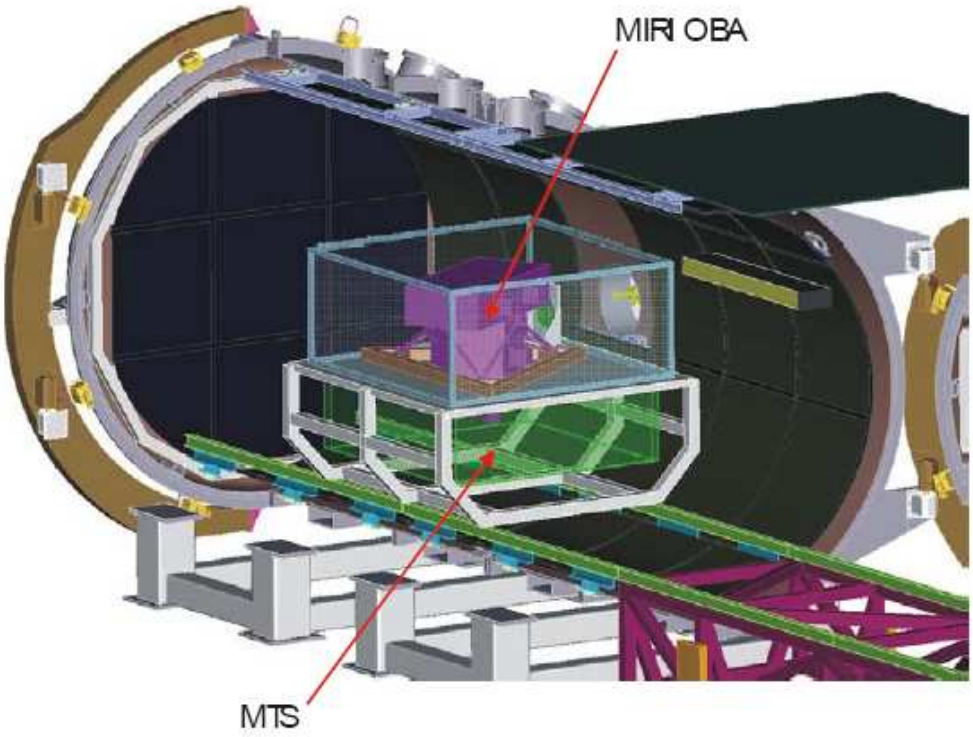

Figure 3.1: MIRI and The MTS in the Cryostat during the Test Campaign

The ability of the MIRI Telescope Simulator to simulate an astronomical source is due to the Main Optical System which provides the illumination and the Source Scanning System which enables the scanning of the simulated source across the MIRI field of view. The source can be selected either as a point source or an extended source which illuminates the entire MIRI field of view.

Image Slicer Test Requirements

The design of the Medium Resolution Spectrometer was developed using optical modelling and has been detailed in Chapter 2. Whilst much of the design is low risk there are some components that have not yet been shown to operate over the entire wavelength and at the cryogenic conditions at which MIRI will operate. One of these as yet unproven components are the image slicers. The testing of the prototype image slicer detailed in Section 2.8 enabled the first measurement of the diffraction losses which were approximately that predicted by the optical model. The next phase of this test is to quantify the diffraction losses for a point source being sliced at varying across

slice positions as it is expected that the point source will undergo diffraction losses depending upon its across slice position. It is necessary to evaluate these diffraction losses as during flight operation it is expected that there will be observations of sources at varying across slice positions.

In order to quantify the diffraction losses it was necessary to ensure that the accuracy of the point source positioning on the image slicer would be sufficient to perform an incremental scan of the point source across a slice. In the MIRI Telescope Simulator the scanning of the simulated source is achieved using a combination of three linear stages. These linear stages were tested in Madrid in 2006 before their integration onto the MIRI Telescope Simulator. I spent two months in Madrid during which time I devised the test procedure to investigate the performance of the linear stages and assisted with the performance test in the cleanroom. In Section 3.2 I will present the test procedure and subsequent analysis to investigate the accuracy of the linear stage movement. I conclude that the stage accuracy is more than adequate to achieve the point source positional accuracy required on the image slicer.

3.1 The Imaging Sub-system

The Imaging Sub-system is responsible for the imaging of the point and extended sources over the entire MIRI field of view. This encompasses the MIRI Imager, Coronagraphic Imager and the Low and Medium Resolution Spectrometers. The Imaging Sub-system contains the Main Optical System and Source Scanning System. The Main Optical System defines an object plane within the MIRI Telescope Simulator and projects this object plane onto the MIRI field of view. The Source Scanning System enables the accurate positioning of an aperture on the object plane to create a point source or extended source image at the MIRI field of view.

3.1.1 The Main Optical System

The Main Optical System defines an object surface within the MIRI Telescope Simulator which can be thought of as the focal plane of the illumination source which is housed in an integrating sphere (as per Figure 3.2).

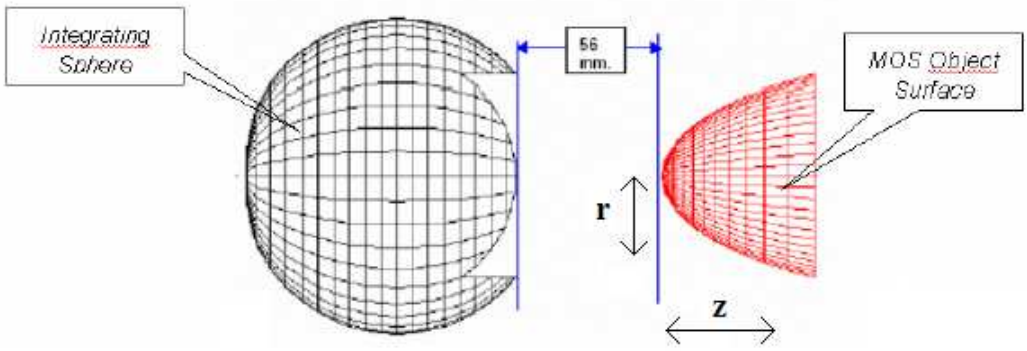

Figure 3.2: The Integrating Sphere and the MOS Object Surface. r depicts the radius and z the depth of any position on the MOS Object Surface

The principal component of the Main Optical System is shown in Figures 3.3 & 3.4. Its purpose is to project the curved object surface shown in Figure 3.2 onto the image plane at the MIRI field of view aperture. It is a centered cassegrian formed by a concave primary mirror, central obscuration and a convex secondary mirror producing a diffraction limited imaging system across the entire spectral coverage of the Medium Resolution Spectrometer. The pupil mask which mimics the shape of the JWST primary mirror is located at the exit pupil at the back of the secondary mirror.

3.1.2 The Source Scanning System

The Source Scanning System controls the selection and positioning of the target source onto the MIRI field of view. It achieves this by positioning a target aperture at the Main Optical System object surface which allows transmission of flux through the MIRI Telescope Simulator towards the MIRI field of view. The target aperture is scannable across the object surface enabling the source position to be scannable across the MIRI field of view. The Source Scanning System is comprised of two elements: The Target Assembly and The Linear Stages.

The Target Assembly shown in Figure 3.5 comprises a sheet of aluminium which has a 100μm pinhole and can also be commanded to create an extended source. It does this through being driven against the actuation sub-assembly which kinematically rotates the extended source sub-assembly (as per Figure 3.6) exposing the Main

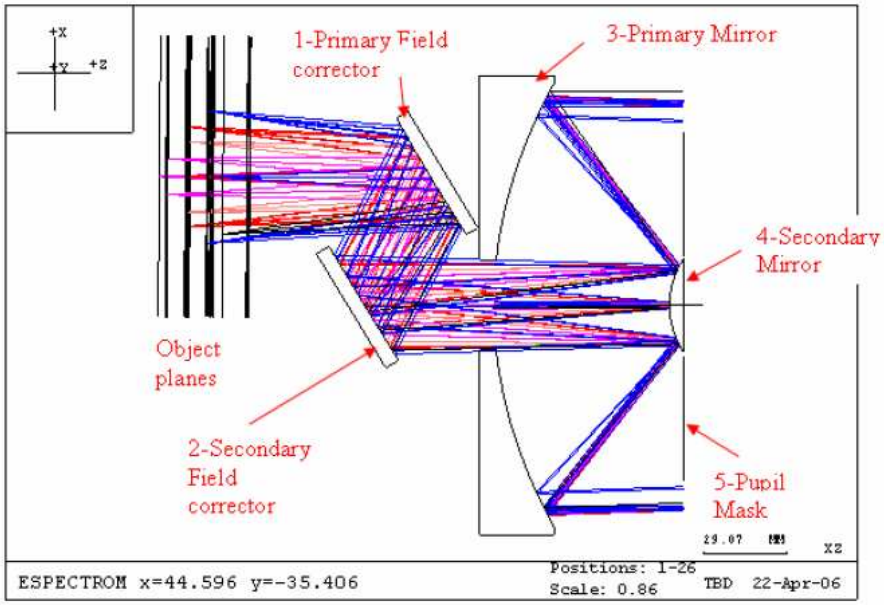

Figure 3.3: The Main Optical System Design

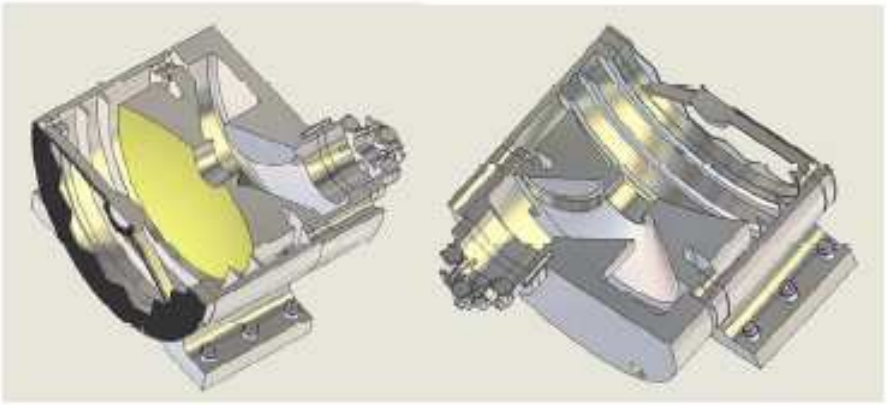

Figure 3.4: Cross-sectional view of Main Optical System

Optical System object surface to the entire MIRI field of view. The extended source does not need to be scanned as it fully illuminates the MIRI field of view. Note that the extended source simply reveals the Main Optical System object surface. It does not need to be placed at the correct position on the object surface as required for the pinhole to create a focussed point source.

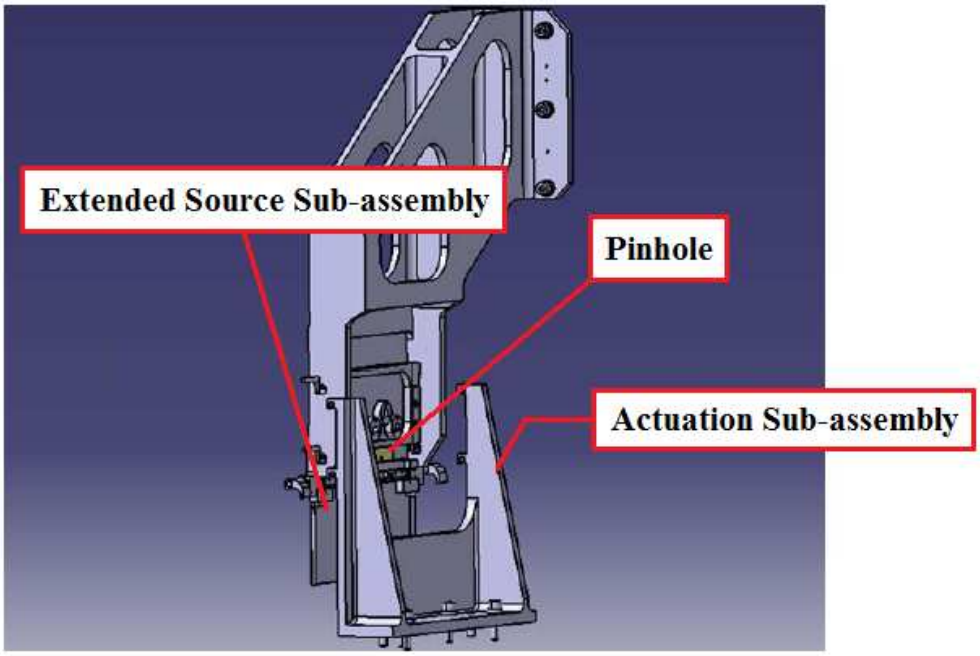

Figure 3.5: The Target Assembly and Actuation Sub-assemblies

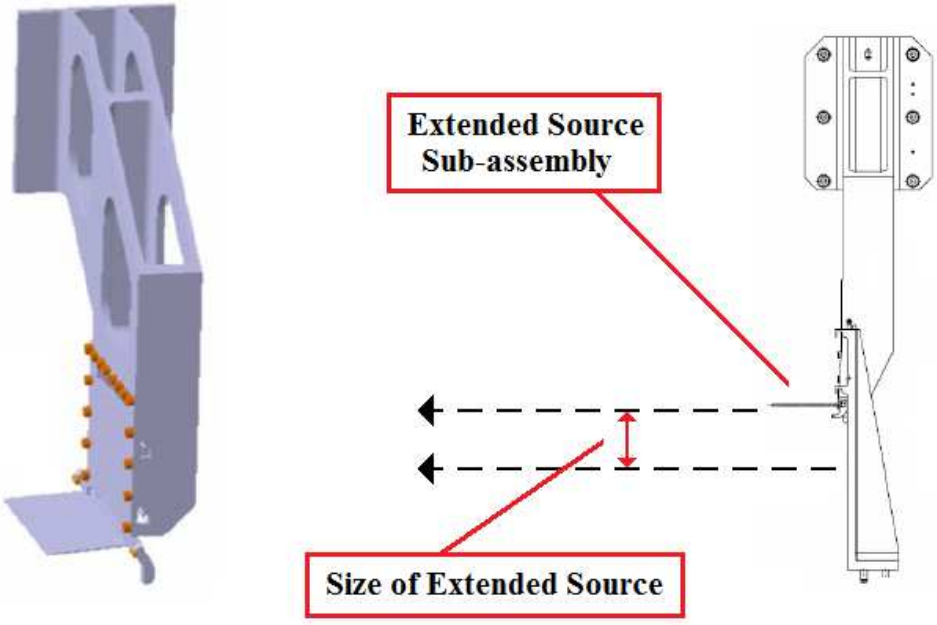

Figure 3.6: Extended Source Activation

The Linear Stages are three identical stages orientated orthogonally to one another (as per Figure 3.7) which are used to scan the point source across the MIRI field of view and to kinematically select the extended source. As the Main Optical System object surface is curved the linear stages are required to move the pinhole in three dimensions to scan the point source across the MIRI field of view. As a result it is the combined accuracy of the linear stages which must be investigated to determine if they will enable sufficient point source positional accuracy for the across slice diffraction loss investigation. The testing of the Linear Stages will now be outlined.

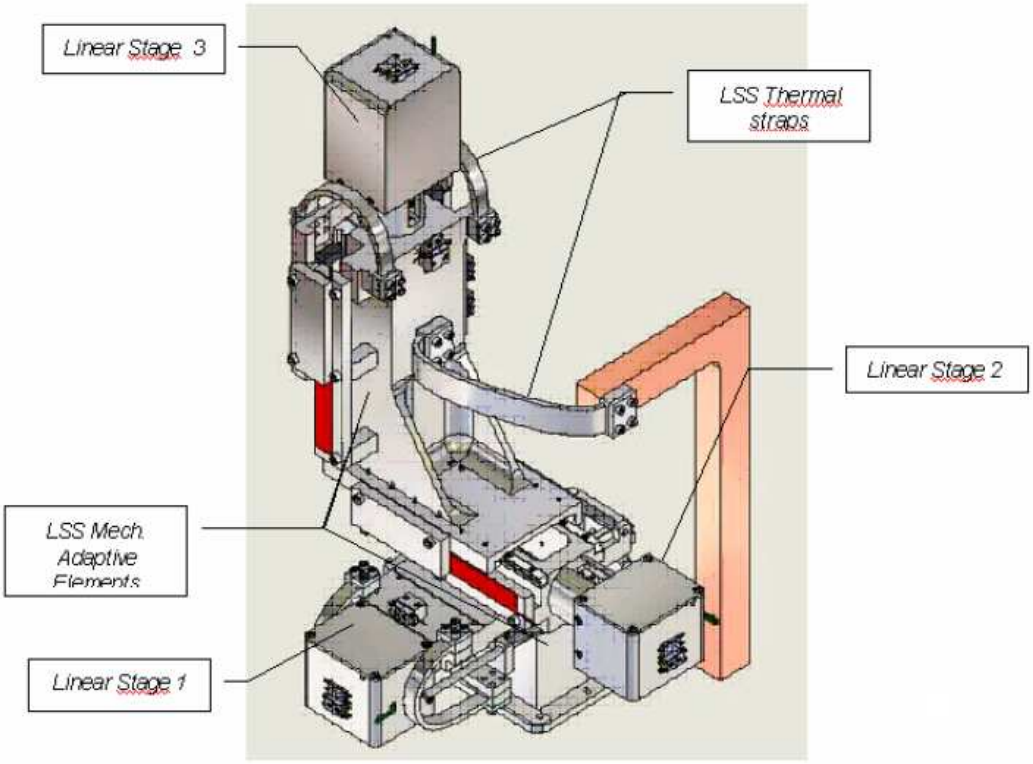

Figure 3.7: The Linear Stages Assembly

3.2 Testing of the Positional Repeatability and Run-out of The Linear Stages

It was required that the diffraction losses for a point source be measured at varying across slice positions. To perform this analysis it was necessary to ensure that the accuracy of the point source positioning on the image slicer would be sufficient to perform an incremental scan of the point source across a slice. This positioning was achieved using the Source Scanning System of the MIRI Telescope Simulator and in particular the Linear Stages. Section 3.1.2 outlined how the movement of a focussed point source across the MIRI field of view is achieved through the movement of three orthogonal linear stages.

To understand the stage movement there were three attributes of the stages which had to be measured. The first was the positional accuracy of the stages which gave a measurement of the poitional error in each stage movement. The second was the orthogonality of the linear stages to ensure that the movement of a stage only moved the pinhole along a single axis. The third was the stage run-out which measured the angular change in the plane of the Target Assembly during each stage movement. It will be shown that this angular drift will induce an offset in the placement of the pinhole from the nominal position on the Main Optical System object surface which will affect the position and focus of the point source on the image slicer.

Due to the importance of the Linear Stages and the Target Assembly for the image slicer diffraction analysis they were tested separately before integration onto the MIRI Telescope Simulator. I spent two months working at the Instituto Nacional de Técnica Aeroespacial (INTA) in Madrid during the summer of 2007 where I wrote the basic test procedure for the warm functional test of the Linear Stages. I also participated in the testing program. The test was carried out at ambient temperature in a Class 1000 cleanroom.

3.2.1 The Test Procedure

The test was designed to measure the positional accuracy, orthogonality and the run-out of the Linear Stages simultaneously as these are the attributes that will define

the errors involved in the positioning of the pinhole at the Main Optical System object surface. This error will induce offsets into the position and focus of the point source on the field of view reducing the ability to perform a fine scan of the point source across the image slicer. The attributes of each Linear Stage will be measured separately to investigate the offset produced by each on the pinhole position.

The movement of each stage was carried out in a forwards and a backwards motion to investigate any change in the relative alignment and positional error dependent upon the direction of movement of the stage. Each stage was investigated in linear integrations of 3mm as this divided the complete stage movement into $\sim$25 increments which was of a sufficient resolution to enable an accurate analysis of the stages. All measurements were taken from the Target Interface of the Linear Stages shown in Figure 3.8. This interface connects the Linear Stages and the Target Assembly and was scannable in three dimensions hence measurement of the attributes of all three stages could be achieved from its surface.

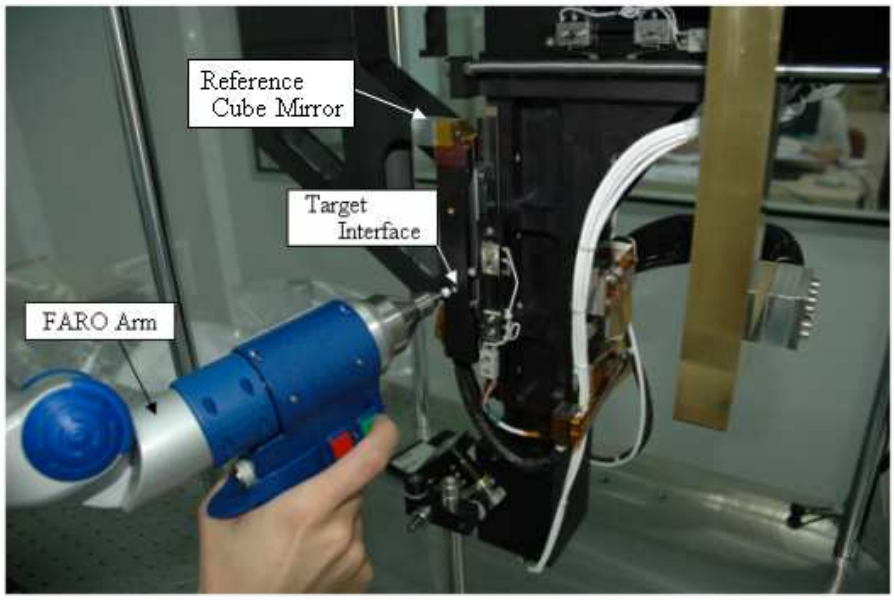

Figure 3.8: The Target Interface

The FARO Arm (a coordinate measuring machine) was used to define the stage position at each point after the stage movement. This enabled a calculation of the posi-

tional accuracy and the orthogonality of the stages. It was measured from a reference position in the side of the Target Interface.

A theodolite was used to measure the run-out of the stages by observing the change in angle of reflection from a reference cube mirror attached to the Target Assembly (as per Figure 3.9). Due to the different directions of stage movement three different methods had to be employed for the run-out measurements.

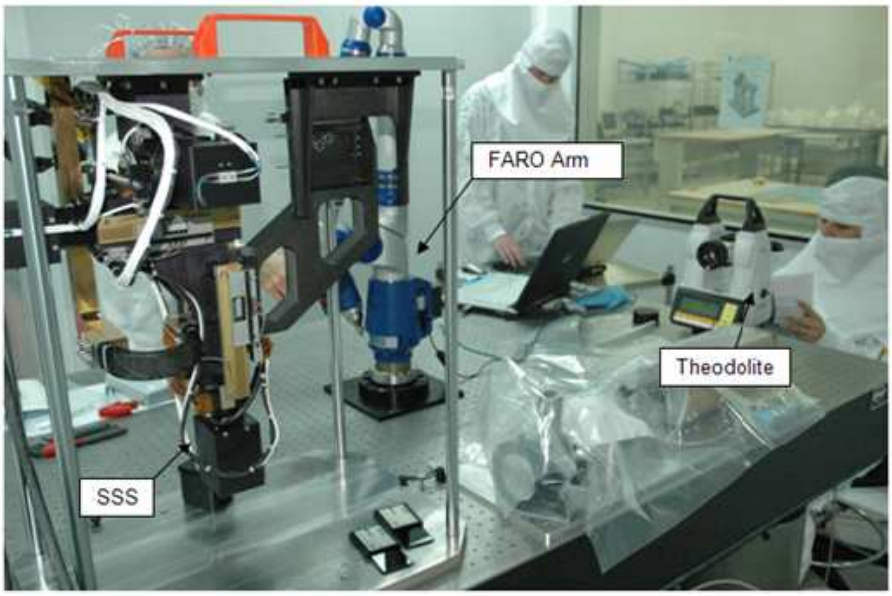

Figure 3.9: Theodolite Alignment in the Test Set-up

Method 1 enabled the run-out measurement of the Target Interface directly along the line of sight. It required the theodolite to be set up to observe the reference cube along the line of the stage movement which always presented the cube within the field of view of the theodolite. The cube mirror alignment could be determined over the complete movement of the stage without movement of the theodolite.

Method 2 enabled the run-out measurement of the Target Interface horizontally across the line of sight. The idea was to position the theodolite in the same orientation to the reference cube as per Method 1. The alignment was obtained initially and after each movement of the stage. However as the theodolite field of view was not sufficient to measure the alignment of the reference cube across the entire stage movement it was necessary to move the theodolite after several stage movements. A measurement of

the reference cube alignment before and after movement enabled the measurement in the change in theodolite coordinate system necessary to calibrate for the movement. A repeat of this process was required until the complete stage movement had been covered.

Method 3 enabled the run-out measurement of the Target Interface vertically across the line of sight. This method was similar to that of Run-out Method 2 except the Target Interface was moved in a vertical direction. As such it was the height of the theodolite which had to be adjusted when the reference cube moved to the edge of the theodolite field of view.

3.2.2 Results of the Linear Stage Investigation

To consider the effect of the run-out on the positioning of the pinhole at the Main Optical System object surface we must first consider the Target Assembly which can be seen in Figure 3.10. The Target Assembly was attached to the linear stages at the approximate position of the reference cube mirror from the surface of which the run-out of the linear stages was calculated. Any change in angle that is observed at the reference cube due to the run-out of the stages will also be seen at the surface of the Target Assembly. As the target assembly was attached to the linear stages at the reference cube position the change in angle due to the run-out will induce a change in position of the pinhole. The magnitude of this change in position is dependent upon the change in angle and the spatial offset of the pinhole from the point of rotation.

The run-out of each stage was calculated about the average orientation of the reference cube mirror to the theodolite. A measured vertical run-out of a stage by the theodolite coupled with the distance of the pinhole from the point of attachment of the Target Assembly (labelled Vertical Offset in Figure 3.10) defines an offset of the pinhole position from the nominal case of zero run-out. Similarly a measured horizontal run-out combined with the Horizontal Offset (again labelled in Figure 3.10) also defines an offset of the pinhole position from the nominal case of zero run-out.

Consider Figure 3.10. For a large vertical run-out the movement would induce a change in both the **x** (focus) and **z** (vertical) axes. However due to the small run-out angles measured it can be approximated that the run-out only induces a pinhole position offset in the direction of focus (**x**). Similarly the offset due to the horizontal

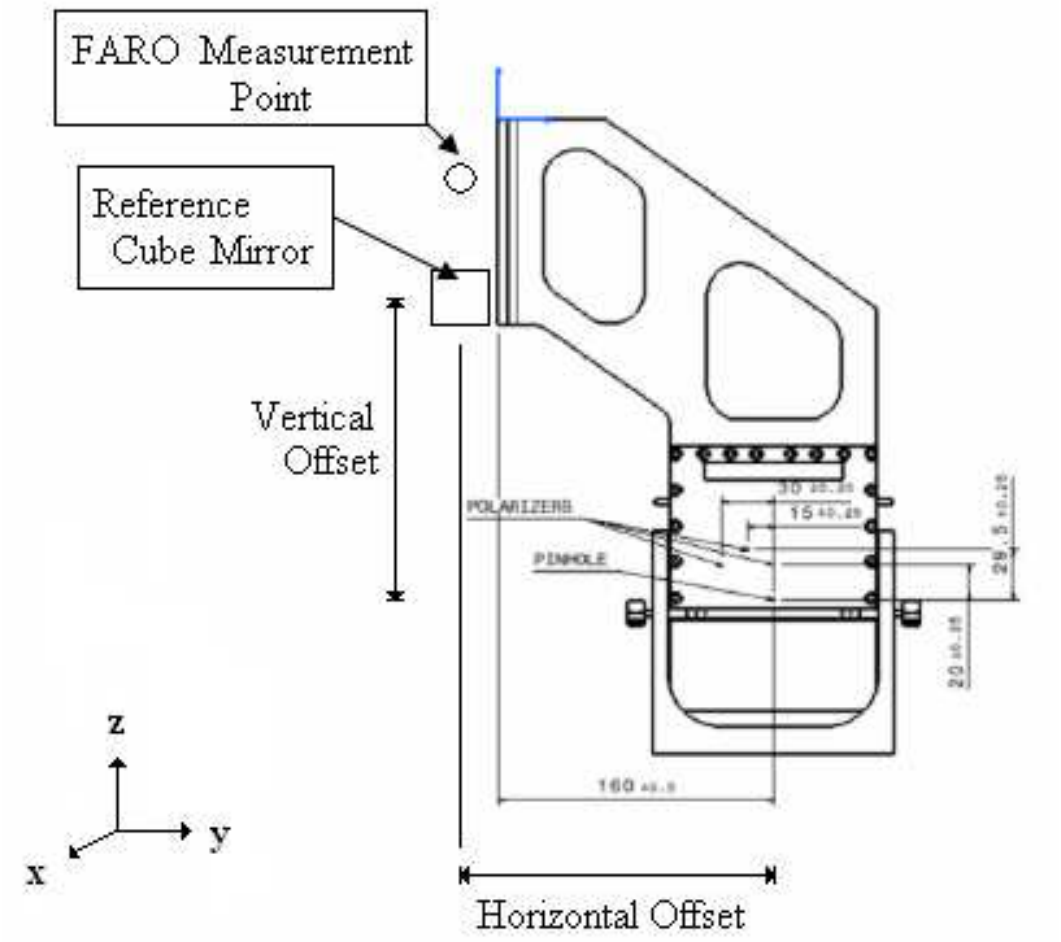

Figure 3.10: Measurement Positions on the Target Assembly

run-out again only offsets the position of the pinhole in the focus direction. As a result of the small values measured for the run-out of each stage only affects the focus of the point source incident on the Medium Resolution Spectrometer field of view.

There was a rotation around the **x** axis which could not be measured in this test setup. This would have accounted for movements in both **y** and **z** leading to a positional offset of the point source in the Medium Resolution Spectrometer field of view.

The worst case offsets applied to the focus position of the pinhole from the Main Optical System object surface due to the run-out of the stages are shown in Table 3.1. They are calculated from the addition of the worst run-out measured from the movement of each stage. Whilst it is possible that the stage positions to image the

point source upon the Medium Resolution Spectrometer field of view were the combination of those stage positions of worst measured run-out in practice this is unlikely.

	Run-out Induced Focus Change [mm]
Max Offset	0.11
Min Offset	-0.17

Table 3.1: Worst Case Focus Offset due to Combined Stage Run-out

The positional accuracy of the linear stages must be considered with the run-out induced focus offset to fully understand the errors associated with the positioning of the pinhole at the Main Optical System object surface. Table 3.2 shows the maximum positional error measured for each of the Linear Stages where **x** is indicative of the focus position and **y** & **z** represent the field of view axes. Note that the larger spread in repeatability of the z axis is explained because the movement is along the vertical axis and the stage must also hold position against gravity.

	x	**y**	**z**
Max Offset	15.4	29.6	108.7
Min Offset	-20.0	-6.9	-45.0
Standard Deviation	7.9	8.5	32.5

Table 3.2: Positional Repeatability of the Linear Stages [μm]

Through a combination of the focus offsets applied through the stage run-out and the positional repeatability along the focus direction an estimation of the maximum focus offset of the pinhole from the Main Optical System object surface was derived. This is shown in Table 3.3.

	Pinhole Offset at the Main Optical System Object Surface [mm]
Max Offset	0.13
Min Offset	-0.19

Table 3.3: Pinhole Offset at Main Optical System Object Surface

MIRI Telescope Simulator Requirement 511.03 states that "the MIRI Telescope Simulator pupil-focus, with nominal value 3017.561 $\pm$ 10mm, shall be within $\pm$2mm at any point in the MIRI field of view".

This requirement implies that the allowed error in the focus positioning of the pinhole to the Main Optical System object surface is $\pm$2mm. It was designed to set a limit at which the point source delivered to the MIRI field of view would still be in sufficient focus. It is evident that the combined positional errors along the focus axis for the pinhole at the Main Optical System object surface do not compromise the requirement and infact they are of a magnitude smaller than the requirement

There is a possibility that the positional error in the **y** & **z** axes could induce an additional focus offset of the pinhole position from the Main Optical System object surface due to its curved shape (Figure 3.2). Consider a pinhole positioned at focus **x** = 0 on a flat object surface orientated along the **y-z** plane. An offset applied along either of these two axes would change the position of the pinhole on the object surface but however it would not change the focus setting. Now consider a pinhole placed at nominal focus on the actual Main Optical System object surface which is curved. Deviations along the **y-z** plane would cause the pinhole to be offset from the nominal focus position. It is this offset that will now be considered.

The MIRI Telescope Simulator input is located to the side of the object surface shown in Figure 3.2. Due to the gradient at this position a small increment in the field of view position (**y** or **z**) could correspond to a large change in focus. It was necessary to calculate the offset that the **y** & **z** positional errors shown in Table 3.2 have on the position of the pinhole with respect to the Main Optical System optical surface. The Main Optical System object surface is defined by the following conic equation which relates the depth z to the radius r of a point on the surface of the conic (See Figure 3.2), where k is the conic constant = -0.53, and c = $\frac{1}{20.2}$ where 20.2mm is the Radius of Curvature.

$$z = \frac{cr^2}{1 + (1 - (1 + k)c^2r^2)^{0.5}} \tag{3.1}$$

The change in focus position was investigated for the worst case positional error occurring at the position of the object surface which corresponds to the Medium Resolution Spectrometer field of view. The induced focus offset was measured as $\pm$0.13mm.

Combined with the total run-out and **x** stage positional error this places the maximum offset of the pinhole from the Main Optical System as +0.26 / -0.32mm which is still well within the $\pm$2mm outlined in MIRI Telescope Simulator Requirement 511.03.

The positional errors in the **y** & **z** Linear Stages also correspond to a movement of the point source across the Medium Resolution Spectrometer field of view. Derived from the maximum **y** & **z** stage positional errors is an offset of $\sim$0.17 arcseconds on the field of view, approximately that of the Channel 1 slice width. If this pinhole offset was typical at the Main Optical System object surface at the position of the Medium Resolution Spectrometer then the accurate positioning of the point source on the image slicer would be difficult. This is a worst case analysis across the entire movement of the stages. On a scale relative to the size of the Medium Resolution Spectrometer field aperture the positional error is $\sim$0.03 arcseconds or $\sim \frac{1}{6}$ of a Channel 1 slice width and would enable a sufficient positional repeatability for the measurement of the diffraction losses of the point source being sliced at varying across slice positions.

The orthogonality between the stages (Eiriz and Gonzalez, 2007) is shown in Table 3.4. Whilst there was a measurable deviation from being perfectly orthogonal this will not be detrimental to the positioning of the pinhole on the Main Optical System object surface. This is because the angles are a constant error and the same at all positions of the stages hence they can be accounted for when the MIRI Telescope Simulator characterisation and calibration process is being performed.

Angle [degrees]	**z-x**	**y-z**	**x-y**
Measured	89.95	90.04	90.03
Error	0.05	0.04	0.03

Table 3.4: Orthogonality Between Linear Stage Axes

3.3 The Reduced Functionality of the MTS

The MIRI Telescope Simulator that was delivered to the Rutherford Appleton Laboratories for the Verification Model test campaign did not meet all of the requirement

specifications for its design. The major issue that affected the testing was that the MIRI Telescope Simulator had an incorrect focal length.

MIRI Telescope Simulator Requirement 511.03 states that "the MIRI Telescope Simulator pupil-focus, with nominal value 3017.561 $\pm$10mm, shall be within $\pm$2mm at any point in the MIRI field of view".

The focal length of the delivered MIRI Telescope Simulator was measured as 3002 mm which is outside of the specified range considering the error. As a result the pinhole needs to be offset along the focus axis from the Main Optical System object surface to create a focussed point source at the MIRI field of view aperture Unfortunately at the position of the Medium Resolution Spectrometer field of view this Linear Stage is towards the end of its range of movement and the offset cannot be achieved. As a result the point source incident upon the Medium Resolution Spectrometer is approximately 5mm out of focus which results in a substantial enlargement of the point source. This issue is compounded as the out of focus image is astigmatic. This is an optical aberration that elongates the point source either side of best focus. The combined result is that the point source imaged onto the Medium Resolution Spectrometer is oversized by a factor of approximately 35 and it is elliptical. Due to the diffuse nature of the incident point source longer integrations were necessary to achieve the same signal to noise as required for a true point source. This increased the time required to perform the tests on the Medium Resolution Spectrometer. The origin of the incorrect focal length is unknown however it is possible that one of the mirrors has been designed incorrectly. As yet this has not been ascertained.

The other design problem that affected the Medium Resolution Spectrometer Subsystem was that the illumination of the extended source of the MIRI Telescope Simulator did not extend to the Medium Resolution Spectrometer field of view aperture. This however was not an issue as the internal calibration source would provide a suitable substitute for the extended source.

Due to the increased size of the point source delivered to the Medium Resolution Spectrometer by the MIRI Telescope Simulator it was impossible to measure the diffraction losses of the slicing of the point spread function at different across slice positions (as per Section 2.9). In total it was still possible to run approximately 90% of the performance tests on the Medium Resolution Spectrometer Verification Model however the errors associated with the tests are increased in several cases. This presents a seri-

ous problem for the analysis of the test data however it is a feature of the Verification Model data that cannot be changed.

3.4 The MTS and Subsequent Testing

In conclusion the testing of the Linear Stages and Target Assembly have shown that the positional accuracy required in the placement of the pinhole on the Main Optical System object surface has been achieved. As such the diffraction loss investigation as a function of the point source slice position is possible. However due to the issues with MIRI Telescope Simulator and in particular the diffuse nature of the source this test was not possible during the Verification Model test campaign. In reality this is one of many tests which must be performed on the Mid-Infrared Instrument to verify its operation under flight conditions. Approximately 90% of the Medium Resolution Spectrometer tests could be performed however several of these including the one outlined in the next chapter have an increased error due to the diffuse nature of the point source.

Expectations of the Test Campaign

The purpose of building a Verification Model was twofold. Firstly it was essential to ensure that the sub-sections of the instrument could be assembled and aligned to the required accuracy and secondly it enabled various performance tests to be carried out to ensure that the instrument operated as expected. Channels 1 & 2 were operational in the Verification Model as any problems with with scattered light would be largest because of the lower operational wavelengths. It was intended that any observed discrepancies could be investigated and if necessary alterations could be made to the Flight Model as it was being built. A test team was assembled from the various institutions that were involved in the design of the Mid-Infrared Instrument whose function was to create a complete suite of tests to investigate the performance and characterise the instrument.

The Verification Model test campaign ran throughout August and September 2008 at the Rutherford Appleton Laboratories in Oxfordshire. The duration of the test campaign was required to be less than two months as there was only sufficient funding

to keep the instrument at operational conditions for this length of time. To extract the maximum information from the limited test duration the test team was designed to enable instrument testing 24 hours a day. This was achieved using three teams in shift patterns of $8\frac{1}{2}$ hours. The extra half hour was intended to see both teams working together to ensure that the handover between shifts was a smooth transition. It was also a good opportunity to discuss problems and contemplate solutions.

It was never intended that the Verification Model would enable a complete investigation of the instrument characteristics due to the restricted test duration and the problems with the MIRI Telescope Simulator. It was however intended to investigate the main features that would degrade the operation of the Flight Model.

I was heavily involved in the test team through helping to write the test procedures, performing the test procedures during the test campaign and also in reducing the subsequent test data. As I was involved with the image slicer integration into the Integral Field Units at the UK Astronomy Technology Center (whose design is noted in Section 2.2.2) I was best suited to analyse the transmitted field of view of the Medium Resolution Spectrometer Verification Model. The resultant data reduction and subsequent analysis is outlined in the next three chapters.

The Field of View Test Analysis and Findings

The findings of the field of view analysis are split between the next three chapters. Chapter 4 outlines the data reduction technique required to reconstruct the Verification Model field of view and compares the measured on-sky extents with the instrument requirements and the optical model. This chapter also details an amendment I made to a component in the Flight Model to increase the probability that the Flight Model field of view would exceed the instrument requirements.

Chapter 5 outlines a magnification of the slice lengths that was measured across the detector which induces an error into the spatial alignment of the reconstructed field of view. This chapter also details a performance test that I devised which must be carried out on the Flight Model to enable a full spatial calibration of the field of view.

Chapter 6 outlines the measurement of additional light at the Verification Model detector. In considering each case separately it enables a systematic analysis of the Medium

Resolution Spectrometer to investigate the origin. The resultant reduction in the signal to noise of the instrument due to the additional light is calculated and compared to the requirement.

CHAPTER 4

The Field of View of The JWST MIRI-MRS

The field of view analysis of the Medium Resolution Spectrometer Verification Model for both Channels 1 & 2 will be outlined. The reduction technique used to reconstruct images will be outlined and also the compact source in these reconstructed images will be shown to be consistent with that delivered by the MIRI Telescope Simulator considering the reduced functionality. A method to calculate the field of view of the spectrometer from the reconstructed images will be defined and the results compared to the instrument requirements. The on-sky alignment of the sub-spectra will be investigated and compared to the expected alignment measured in the lab to show that the alignment is unchanged due to vibration. The optical model will be compared with the on-sky position of the field of view and will be shown to have a close agreement indicating that the field position of the instrument is well understood. An investigation into the Flight Model field of view will be outlined including a change of a component necessary to enable the flight model field of view requirement to be met.

The design of the Medium Resolution Spectrometer for The Mid-Infrared Imager of the James Webb Space Telescope (JWST MIRI-MRS) was detailed in Chapter 2. Of

particular relevance to this chapter was the section outlining the field of view of the Medium Resolution Spectrometer (Section 2.7).

4.1 Data Reduction

The first stage in the analysis was to reduce all the raw data frames into data cubes. All of the frames used in this analysis are LVL2 data frames generated using miri_sloper +r2 -a 2 -n 1 -OR. This is an automated pipeline process which subtracts the pixel noise from the data. Each frame displays the 1024 by 1024 detector array separated into two for Channels 1 and 2. This is most easily seen in the flat field images created by the Spectrometer Calibration Unit. Shown in Figure 4.1 these display high signal and coverage over the entire field of view. The Spectrometer Calibration Unit was noted in Section 2.1.

In Figure 4.1 Channel 1 (21 slices) is on the left and Channel 2 (17 slices) is on the right hand side of each array. The separation between each slice on the detector (X-axis) is defined by the output slit mask in the Spectrometer Pre-Optics (Section 2.2.2, Figure 2.10). The slice extension in the wavelength direction (Y-axis) is caused by the diffraction grating in the Spectrometer Main Optics (Section 2.3.1).

Removal of the Wavelength Curvature from the Detector Frames

Scanning down the wavelength direction of the LVL2 data frames it is seen that the boundary positions for a given slice are not constant in x. In Figure 4.1 this is most obvious for the Channel 2 slices before flattening. The curvature occurs in the Spectrometer Main Optics which produces a different amount of curvature for each channel due to their different paths through the optics. According to the optical model the magnitude of this curved distribution is mirrored about the middle of the detector (y = 512 pixels) marked Baseline in Figure 4.1.

It was necessary to remove the curvature so that the data for each channel could be more easily investigated over any wavelength range. The curvature was removed by fitting a quadratic curve to the inner edges of the slices enabling an offset generated by the quadratic to be applied to each row to remove the curvature. To increase the

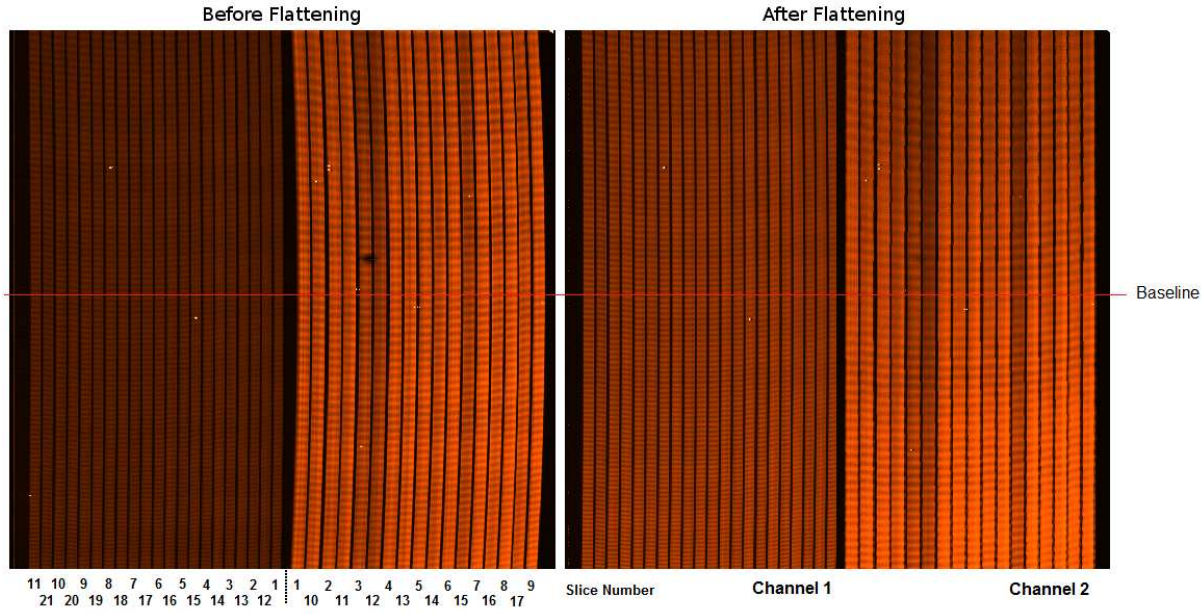

Figure 4.1: The LVL2 Frame Before and After Removal of the Wavelength Curvature

effectiveness of the straightening process the raw data frames were linearly interpolated to a 4096 by 4096 array. This enabled rows in the detector frame to be moved on a sub-pixel scale hence increasing the resolution and the smoothness of the edges of the rows after straightening.

Selection of Slice Boundaries

Figure 4.2 shows a cross-section of the slice profiles from a Channel 1 flat field observation. The 21 individual slices and the inter slice gaps can be clearly seen. The flux level at which to define the boundaries between slice and gap is an important variable in the reduction. Using a lower cut-off includes more of the signal but also an increasing signal to noise associated with the pixels at the extremities of the slices. It is approximated that a cut-off value of $\sim$10% that of the peak-trough difference (as per Figure 4.2) is a good compromise between inclusion of signal and exclusion of noise.

It is impossible to define the slice boundaries from a point source image because the point source does not illuminate all of the slices on the detector simultaneously. As the extended source was not available during the Verification Model Testing (noted in Section 3.3) flat field images were used for the slice cut-off analysis.

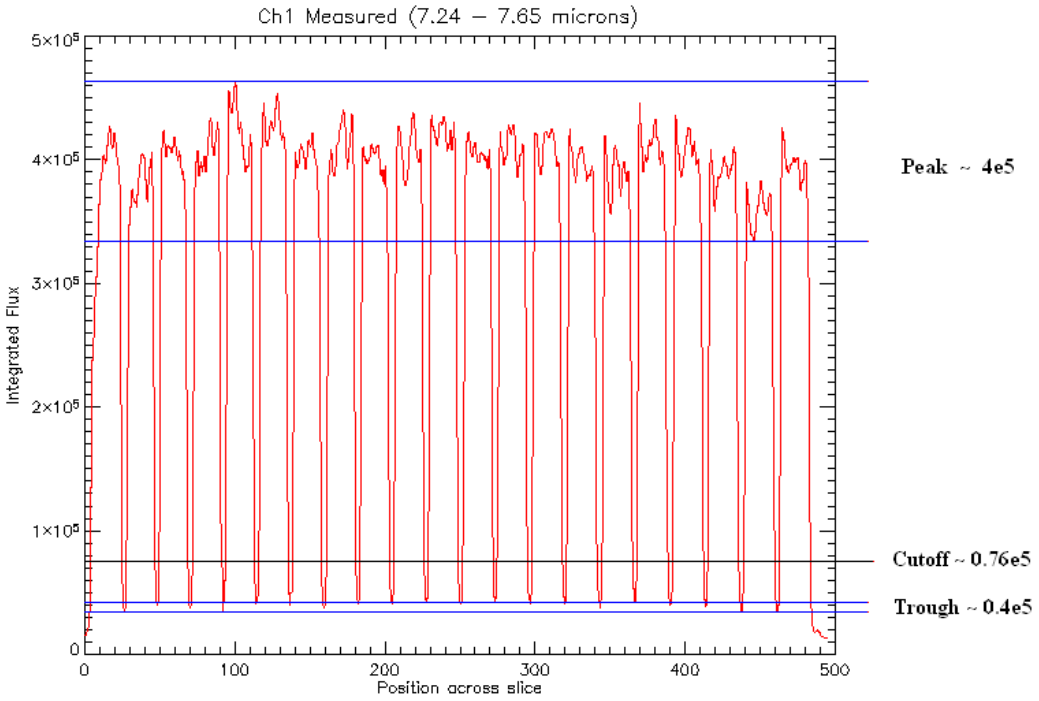

Figure 4.2: The Cut-off Method to define slice boundaries

For each dichroic configuration the pixel coordinates at which the cut-off was applied are different. This is due to the alignment errors of the dichroic filters in the Dichroic Wheel Assembly. The small misalignments result in an offset in the position of the field of view that each dichroic produces on the sky. The drift in the cut-off position of the slices is only a few pixels between dichroic observations but it necessitates that the slice cut-offs for each dichroic set be derived from a flat field image taken with the correct instrument configuration. The alignment errors in the field of view will be detailed in Section 4.5.

Opto-Mechanical Stability of the Spectrometer

It had to be determined whether the positioning of the slices on the detector changed after movement of the spectrometer and other telescope mechanisms. It was important to identify any drift in slice position on the detector because a low stability in slice position with time would require a regular measurement of the positions for accurate data reduction. If there was a shift of an amount greater than $\sim$0.5 pixels

then new cut-off boundaries for an image will need to be calculated from a flat field image taken either directly before or after the image (or on a timescale relating to the drift of the slices on the detector). To investigate this two flat field images taken several days apart with the same instrument configuration were compared. For each frame 13 rows were extracted from the same positions as per Figure 4.3. These rows were selected to sample the complete wavelength direction of the flat field images to highlight any wavelength dependant shifts in the positioning.

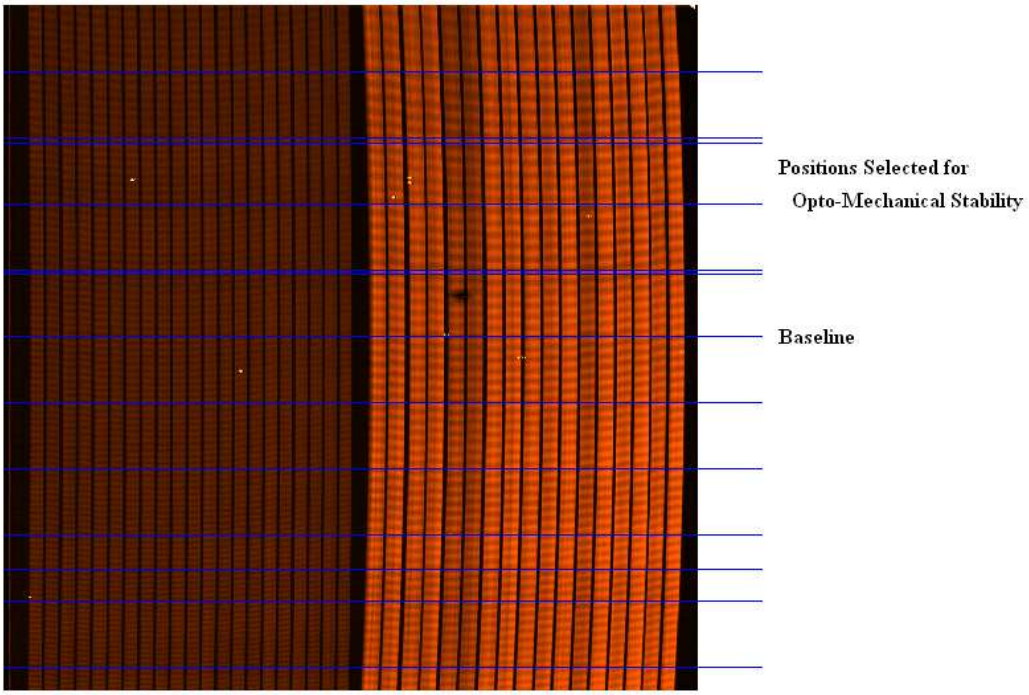

Figure 4.3: The Opto-Mechanical Data Selected for Analysis

To investigate the alignment between each sample position the frames were compared using a cross correlation routine in IDL. This firstly aligns the arrays and then offsets one with respect to the other in predefined increments. For each offset it calculates the correlation between the arrays and returns the offset value where the trends in the arrays are best aligned. Any shift in the positioning of the slices on the detector would be evident by an offset in the cross correlation. The arrays were linearly magnified by a factor of 10 to increase the resolution of the cross correlation analysis.

Between the two flat fields used in the analysis the time elapsed was 40 hours 48 minutes. The Medium Resolution Spectrometer Dichroic Wheel Assemblies were moved 17 times and the MIRI Imager Filter Wheel moved 9 times. The average offset of all positions was 0.07 pixels with a standard deviation of 0.05 pixels equating to an RMS positional variation $\sim$0.09 pixels. This instability is so small it can be assumed that the slice positions on the detector for each instrument configuration are constant over the timescale of the observations used in this analysis.

The RMS Opto-Mechanical Stability exceeds the requirement OBA-0653 (Bean, 2008) which states that "The along slice position of sub spectra shall vary by < 0.5 pixels root mean squared when the MIRI spectrometer mechanism is re-configured". This requirement was described so that the operation of the instrument would not require constant flat field observations to ensure accurate data reduction as this would reduce the time available for observing astronomical observations over the lifetime of the instrument.

4.2 Reconstructing the Field of View

Using the boundary positions of the slices on the detector the slice data can be extracted from a point source image. For image reconstruction the order of each slice on the detector is also required. This is shown in Figure 4.4. Note the large arrow shows the relative orientation of each channel with respect to the other. The slice order on the detector was derived from the continuity of the point source after an initial image reconstruction.

Aligning the slice numbers sequentially will correctly reconstruct the image of the point source as per Figure 4.5. Channel 2 however undergoes an extra reflection in the camera optics of the Spectrometer Main Optics (Section 2.3.2) which explains why the orientation of the slice numbering occurs in the opposite direction to Channel 1 in Figure 4.4. The extra reflection also causes the reconstructed image of Channel 2 to be inverted when compared to Channel 1. For this reason the Channel 2 reconstructed image shown in Figure 4.5 was flipped vertically to be in the same orientation as Channel 1. In each reconstructed image the individual slice lengths are indicative of the length that each slice covers on the detector.

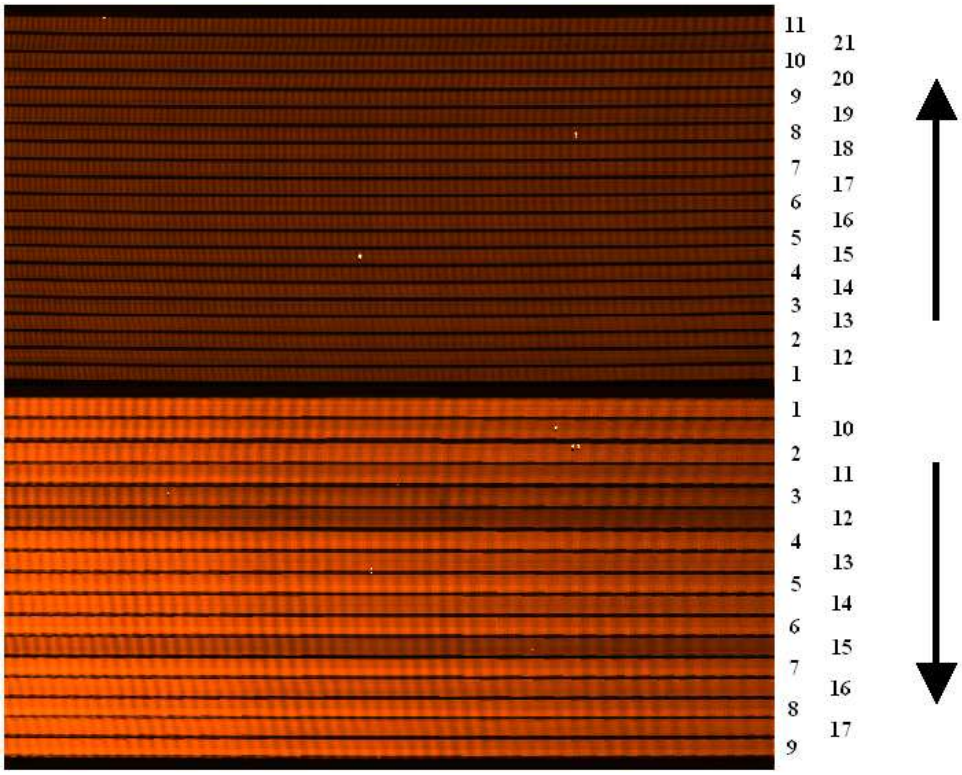

Figure 4.4: The Slice Numbering on the detector

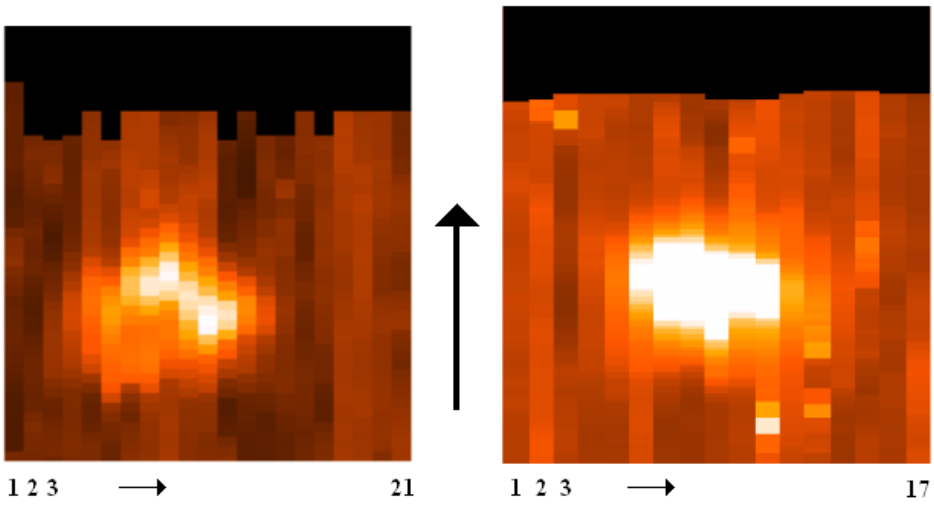

Figure 4.5: Initial Reconstruction of the Point Source Images

Defining the Field of View

The length of each slice projected onto the sky is defined by the attenuation of the ends of the slices at the slit mask (as per Section 2.2.2, Figure 2.10). As a result the field of view reconstruction should be of the same dimensions as the field of view transmitted by the Integral Field Unit (IFU) as it contains all the optics that both slice and define the extent of the field of view of each slice. During the IFU assembly it was found that back illuminating them (ie through the slit mask) with a diffuse source showed an image of the field of view transmitted through the IFU. This field image was produced in the input field aperture of the anamorphic pre-optics (noted in Section 2.2.2, Figure 2.5).

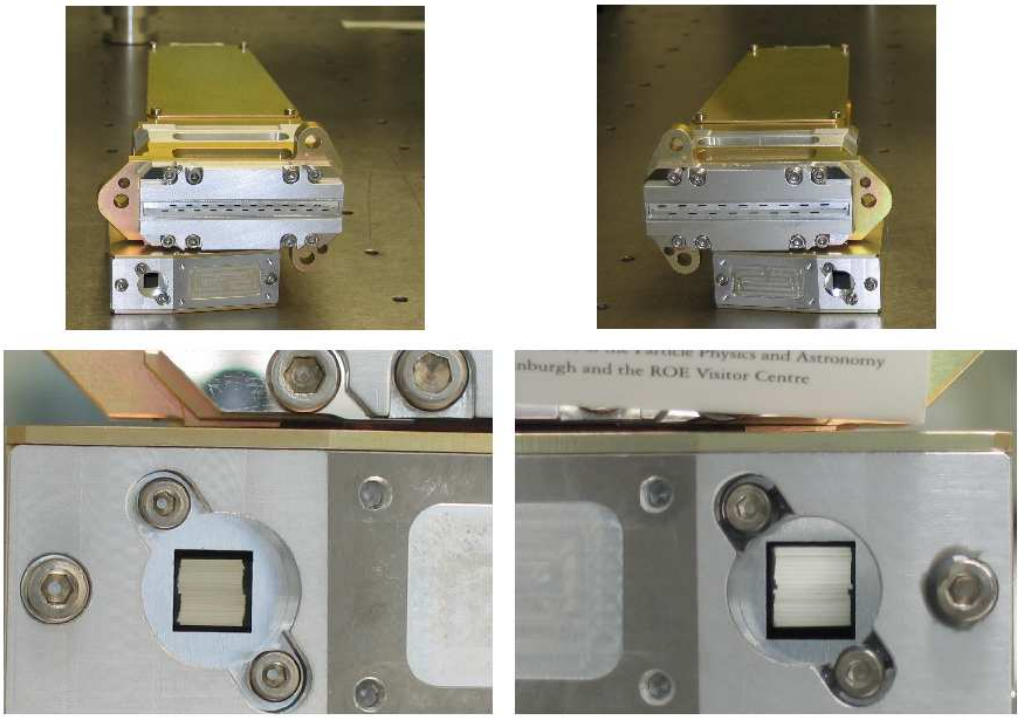

Figure 4.6: The Channel 1 & Channel 2 Integral Field Units and Transmitted Fields of View

The diffuse back illumination was achieved by holding a piece of white card at 45 degrees to the slit mask and shining a white light from above. The Channel 1 and 2 IFU's are shown in Figure 4.6 along with their back illuminated fields of view (the Channel 1 images are on the left). Note the card is just visible at the top of the Channel 2 back

illumination image. The diffuse card gave an approximately collimated beam of light (considering the small apertures) which is what the output of the IFU in operation will produce. As such the optical path followed by the light in the reverse path approximately traces that of the operational throughput and hence the field of view outlined is that which is actually transmitted.

The output slit mask dimensions were determined using an optical model where the slit mask of the IFU's were back illuminated and the slit mask was adjusted to create a square field of view on the sky. The deviation of the actual transmission from the optical model, that is the varying slice lengths and the slice offsets, are due to tolerances in the output slit mask and the re-imaging mirrors in the IFU. This will be covered in more detail in Section 4.5.

Resampling to Reconstruct the Field of View

At the output of the Integral Field Unit the slices are laid end to end for input into the Spectrometer Main Optics. An output slit mask is present at this image plane. Because it defines the along slice dimensions of each slice, the ratio of one slit length on the slit mask to another will be approximately the same as the ratio of the slice lengths on the sky for the same slices. These slice ratios must be applied to the reconstructed images to make the along slice plate scale in each slice identical.

Remember that the initially reconstructed field of view (Figure 4.5) depicts the relative slice lengths at the detector. If the spectrometer optics were perfect then the ratios of the slice lengths in the initially reconstructed field of view would match those transmitted by the Integral Field Unit (Figure 4.6). This is not the case. As a result we need to resample the initially reconstructed field of view slice lengths to match those transmitted by the Integral Field Unit. The individual slice offsets also need to be applied for complete field of view reconstruction.

Before reconstruction of the field of view the orientations of the slices sampled by the Integral Field Unit (Figure 4.6) have to be determined with respect to the slices in the reconstructed field of view (Figure 4.5). This was derived from the back illumination observations of the Integral Field Units taken during the Verification Model build. The transformations are shown in Figure 4.7. Each field of view shown below is orientated in the same manner as for Figure 4.5.

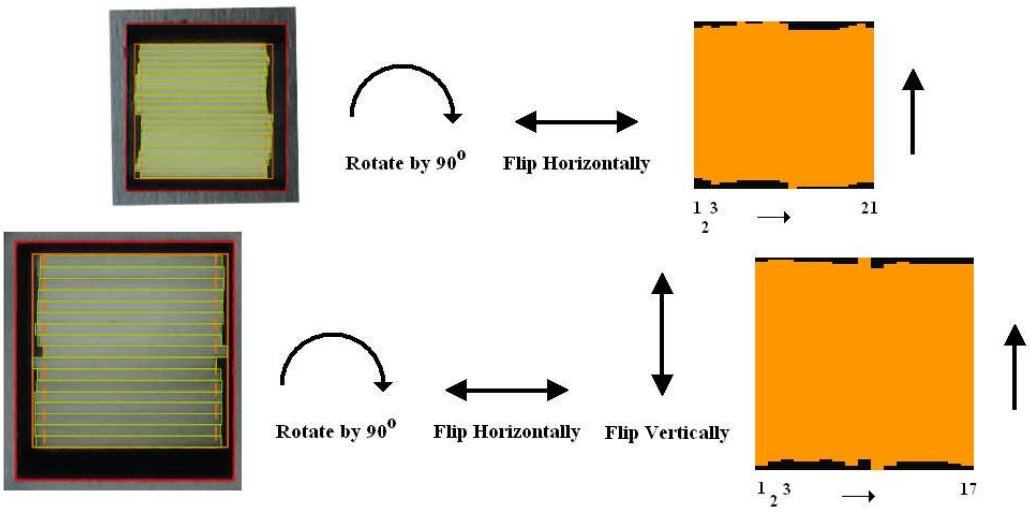

Figure 4.7: Orientation of the Transmitted and Reconstructed Fields of View

Having determined the orientation of the transmitted to the reconstructed field of view we can re-sample each slice and apply the offsets to the initial reconstruction to accurately reproduce the transmitted field of view dimensions.

For each channel the length of the slices transmitted by the Integral field Unit (IFU) varied on the scale of a few percent. This was due to tolerance errors in the IFU and especially those in the output slit mask. The length of a re-sampled slice was determined using the following Equation 4.1.

$$Length_n = \frac{FOV_n}{\overline{FOV_n}} * Baseline_n \tag{4.1}$$

$Length_n$ is the length of the re-sampled slice n, FOV_n is the length of slice n transmitted through the IFU, $\overline{FOV_n}$ is the most common slice length transmitted through the IFU and $Baseline_n$ is the average length of the slices in the initially reconstructed field of view. Effectively the re-sampled length is a fraction of the most common slice length transmitted by the IFU multiplied by the average slice length of the slices in the initial reconstruction. This method keeps the along slice plate scale (arcseconds per pixel) of the re-sampled field of view approximately the same as that in the initial reconstruction.

After the application of the re-sampling transform the slice offsets were then applied to the reconstructed image to reproduce the field of view of the instrument. This can

be seen in Figure 4.8. The re-sampled and slice aligned images are an improvement over the initially reconstructed images as the compact source is more continuous at slice boundaries, i.e. there are smaller offsets in the alignment of the compact source across neighboring slices.

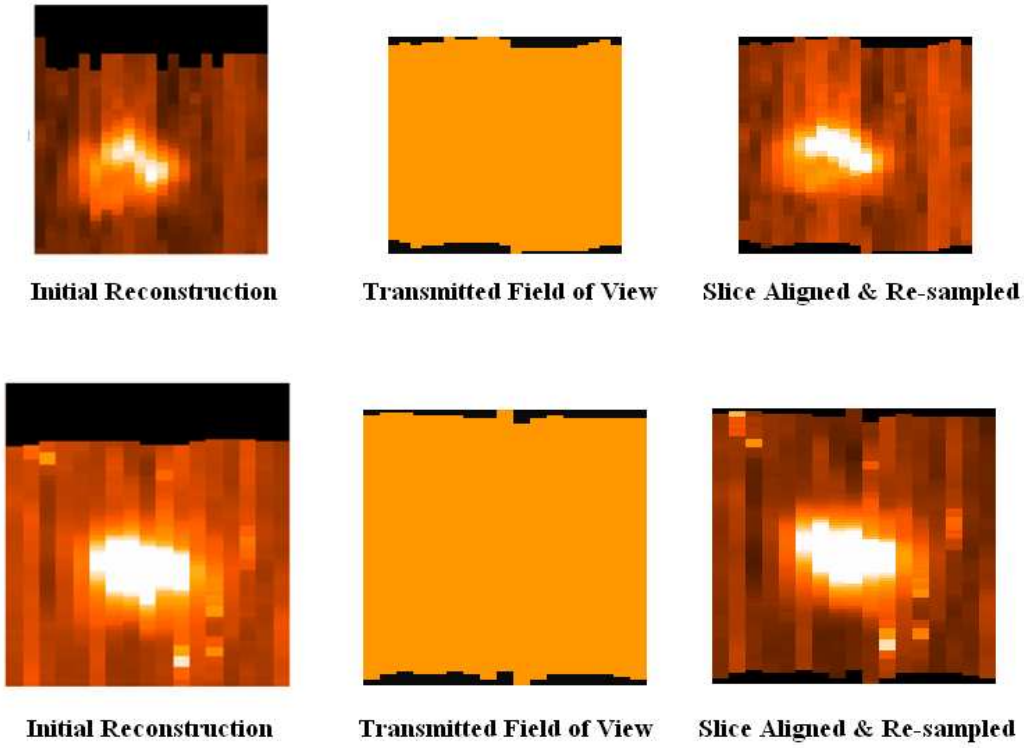

Figure 4.8: The Slice Aligning and Re-sampling Stages for Channels 1 & 2 (Top & Bottom)

4.3 Evaluating the Reconstructed Images

In order to fully evaluate the accuracy of the slice aligned image reconstruction we first need to understand what we expect to see in the reconstructed image. The reconstructed point source images show an elliptical source. The origin of this ellipticity must be investigated as it could be caused by some unforseen diffraction effects in the Medium Resolution Spectrometer. The most probable cause is that it is an artifact of the defocussed compact source imaged onto the input aperture of the Medium Resolution Spectrometer by the MIRI Telescope Simulator. In a good optical system an

out of focus point source will become a larger more diffuse circular pattern. However in a system where there are optical aberrations applied to the beam an out of focus point source can become elliptical. Astigmatism in particular causes a point source to become elliptical when out of focus with the major axis and minor axis of the ellipse swapping either side of best focus.

Optical Aberrations in the MTS Source

The defocus aberrations were investigated on a position at the center of the MIRI Imager field of view where there was sufficient movement of the MIRI Telescope Simulator point source either side of best focus. From images of the point source taken at several positions during a scan through best focus it was observed that there was astigmatism in the beam.

The Delivered MTS Compact Source

The optical model does not contain the point source astigmatism observed at the input to the Medium Resolution Spectrometer because it was unforseen. In order to evaluate the reconstructed field of view images the input point source with the correct defocus (compact source) is required. As the optical model can not reproduce the correct input it was decided to use the point source imaged onto the MIRI Imager (MIRIM) with the correct defocus. It is assumed that MIRIM images the point source onto the detector without imposing any additional aberrations to the beam. It was also necessary to assume that the linearity of the defocus was the same for a position at the center of the MIRIM field of view as at the Medium Resolution Spectrometer field of view.

Figure 4.9 compares the reconstructed compact source images with those expected from the defocussed input point source. The plate scale is identical for each image. In each case the model conforms with that expected, considering both the orientation of the ellipse and its size and eccentricity. Also for 'B' & 'C' the off-center peak in intensity of the ellipse can be seen. It is concluded that the elliptical form of the Medium Resolution Spectrometer compact source in the reconstructed images is due to the problems with the MIRI Telescope Simulator (in particular the defocus issue) and is not created by extra diffraction within the system.

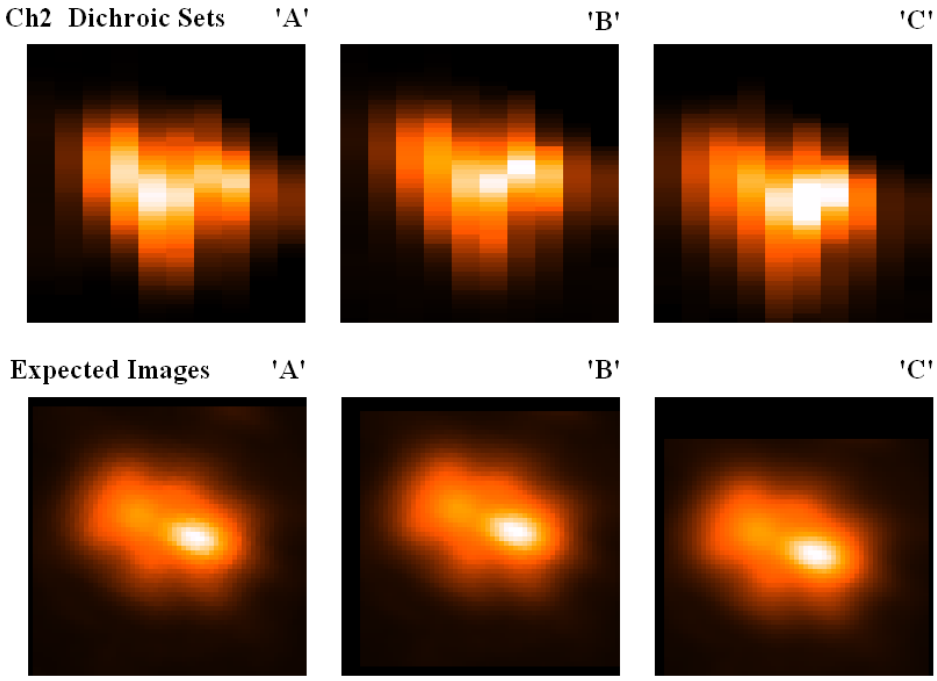

Figure 4.9: Comparison of The MTS "Point Source" with Channel 2 Dichroic Images

The Channel 1 reconstructed images show an additional scattered light component which increases with shorter dichroic configurations. This additional scattering can be seen by comparing the image for Channel 1 with that of Channel 2 in Figure 4.10 (left and right respectively). The Channel 1 compact source is more extended than its Channel 2 counterpart even though in a diffraction limited system the opposite would be the case. This additional scattering will be investigated in Section 6.3.

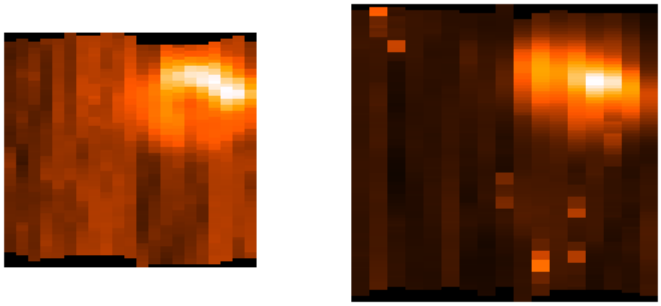

Figure 4.10: Reconstructed Point Source Images for Channel 1 and Channel 2

4.4 Measuring The Field of View

For each instrument configuration it was necessary to calculate the extent of the field of view in order to check that the requirement specifications were met. Requirement OBA-0641 (Bean, 2008) states that "The Integral Field Units shall have a common field of view of at least 3.5 by 3.5 arcsecs for all subsections of the spectrograph wavelength range". This field of view requirement was described with the intention that it would enable the fully sampled observation of typical spiral galaxies at z = 1 in a single set of exposures (as outlined in Section 2.2.1, Figure 2.4).

The method used to determine the extent of the field of view is identical for each sub-spectra. By extrapolating the values of the MIRI Telescope Simulator (MTS) coordinates at the corners of a reconstructed image the extent of the field of view can be defined in MTS coordinates. Converting the MTS coordinates into MIRI Imager Subsystem (MIRIM) pixel units enables an evaluation of the extent of the field of view as each MIRIM pixel is of side 0.11". It is necessary to assume that the MIRIM coordinate system holds out to the position of the Medium Resolution Spectrometer input.

Corner Position Extrapolation

During the Verification Model test campaign observations were made of the compact source in the approximate corners of the field of view for each sub-spectra in each channel. Figure 4.11 shows one such set of observations. For the purposes of this analysis it was necessary to evaluate the center positions of each compact source. An IDL centroid routine was not accurate as in Channel 2 Slices 3, 12 & 15 were less intense due to pupil undersizing in the IFU. Channel 1 was also problematic but for a different reason. In this case the image of the out of focus PSF was much more spread across the FOV than for Channel 2 (as in Figure 4.10) and the IDL routine was quite obviously making errors in the centroiding. For these reasons the centroid of each observation was taken by eye.

High wavelength images using $\sim$0.03% of the bandpass at the highest transmitted wavelength were used for this analysis. This was done to minimise any effects that may cause the compact source to appear more extended and hence reduce the accuracy of the centroiding. This could include apparent movement of the compact source

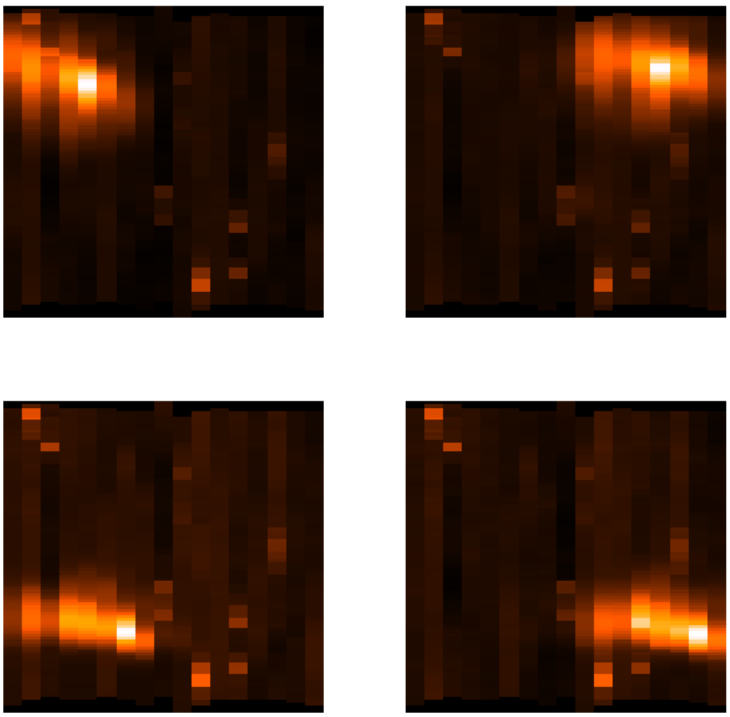

Figure 4.11: The Approximate Corner Observations for Channel 2 Dichroic "B"

in the along slice field of view due to limited resolution in the slice straightening technique where a single pixel offset in the along slice position of the compact source would equate to an approximate offset of 0.04 arcseconds in the along slice direction.

The extent of the field of view was calculated by extrapolating the MIRI Telescope Simulator coordinates at the corners of the field of view. This was done using the compact source MTS coordinates and the corresponding source positions on the field of view. Due to the relative alignment of the Medium Resolution Spectrometer (MRS) field of view and the MIRI Telescope Simulator coordinate system the MRS pixel axes are orientated at an angle of 12.69 degrees anticlockwise to the MIRI Telescope Simulator coordinate system. This orientation was calculated from the field of view allocations noted in Wells (2007). The MRS field points shown in Figure 4.12 denote the extrapolated corner positions of the MRS field of view of Channel 2 Dichroic "B" in MIRI Telescope Simulator coordinates.

Due to the angle that the Medium Resolution Spectrometer field of view makes with the MIRI Telescope Simulator coordinate axes, vector transformations must be ap-

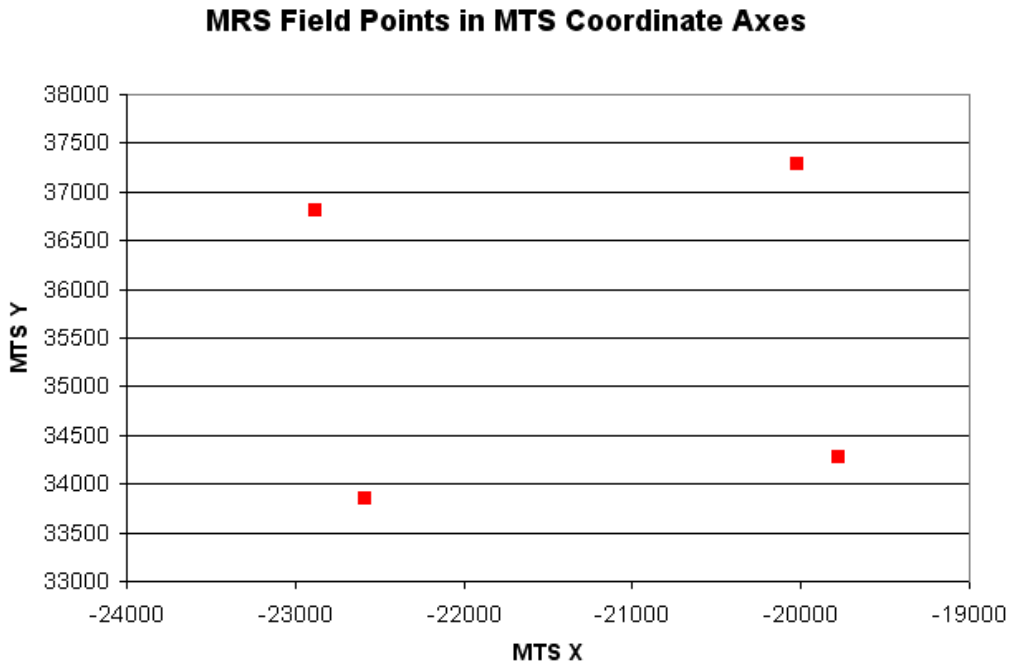

Figure 4.12: The Tilt of the MRS FOV to the MTS Coordinate Axes

plied to the corner extrapolation when converting field of view pixel offsets into MIRI Telescope Simulator (MTS) coordinate offsets. The vector transforms are shown in Table 4.1. $dMTS_x$ and $dMTS_y$ give the increments to be applied to a set of MTS coordinates required to reposition the compact source at the corner position. $Pix(x)$ and $Pix(y)$ are MTS coordinate units per pixel in X and Y of the field of view images, θ is the angle 0.213 radians (12.69 degrees), X and Y are the pixel coordinates of a compact source centroid in a field of view image where the image is a Channel 2 [102,99] array of spatial pixels.

Note the Channel 1 images extend [84,78] pixels. As such the Channel 1 corner extrapolation analysis requires that the values 102 and 99 be substituted for 84 and 78 respectively.

The MTS Coordinate System in MIRIM Pixel Units

To define the field of view in arcseconds it was necessary to convert from the MIRI Telescope Simulator (MTS) coordinates into MIRI Imager (MIRIM) pixel units, where

Bottom Left Field Point:	$dMTS_x = Pix_x * [(X * COS(\theta)] - [Y * SIN(\theta)]$ $dMTS_y = Pix_y * [(Y * COS(\theta)] + [X * SIN(\theta)]$
Bottom Right Field Point:	$dMTS_x = Pix_x * [((102 - X) * COS(\theta)] + [Y * SIN(\theta)]$ $dMTS_y = Pix_y * [(Y * COS(\theta)] - [(102 - X) * SIN(\theta)]$
Top Left Field Point:	$dMTS_x = Pix_x * [(X * COS(\theta)] + [(99 - Y) * SIN(\theta)]$ $dMTS_y = Pix_y * [((99 - Y) * COS(\theta)] - [X * SIN(\theta)]$
Top Right Field Point:	$dMTS_x = Pix_x * [((102 - X) * COS(\theta)] - [(99 - Y) * SIN(\theta)]$ $dMTS_y = Pix_y * [((99 - Y) * COS(\theta)] + [(102 - X) * SIN(\theta)]$

Table 4.1: The Corner Extrapolation Matrices for the MTS Coordinates

each pixel unit is of side 0.11 arcseconds. The coordinate transform is defined in Table 4.2, it is the inverse of a coordinate transform outlined in Glasse (2009b). X_{MIRIM} and Y_{MIRIM} are the MIRIM pixel units, MTS_X and MTS_Y are the corner field points in MTS coordinates, C_X = 659.13 and C_Y = 688.82 define the MTS coordinate origin in MIRIM Pixels, P_x and P_y are the MIRIM pixel units per MTS coordinates along x and y and θ is the angle 1.579 radians (90.46 degrees) which defines the rotational angle between the MIRI Telescope Simulator and the MIRI Imager coordinate axes. The coordinate transform can be seen in Figure 4.13.

$X_{MIRIM} = C_X + [MTS_X * P(x) * COS(-\theta) - MTS_Y * P(y) * SIN(-\theta)]$
$Y_{MIRIM} = C_Y + [MTS_X * P(x) * SIN(-\theta) + MTS_Y * P(y) * COS(-\theta)]$

Table 4.2: Conversion of the MTS Coordinate System into MIRIM Pixel Units

4.5 The On-Sky Field of View of the MRS Verification Model

The extent of the field of view was derived in arcseconds for each sub-spectra using the process outlined. Due to the design error of the MIRI Telescope Simulator (MTS) the errors involved in this analysis due to the centroiding accuracy of the defocussed source are larger than achievable with a fully operational MTS. Channel 1 had several additional problems. During the test campaign the Channel 1 automatic image

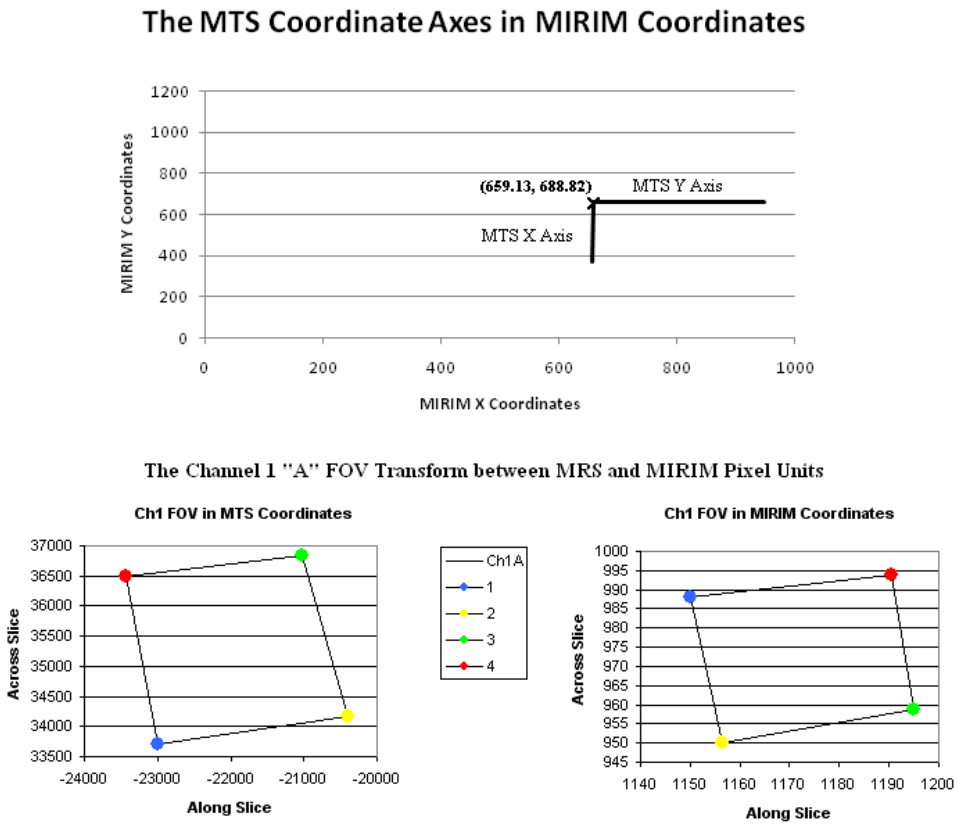

Figure 4.13: The MTS Coordinate Transform into MIRIM Pixel Units

reconstruction was not working correctly resulting in the field of view position being misunderstood. As such the images taken for Channel 1 were not in the corners of the field of view necessitating a larger corner extrapolation than for Channel 2. Also the Channel 1 compact source was more diffuse than that of Channel 2 as per Figure 4.10. Both of these additional problems will have induced further error into the Channel 1 analysis.

The Measured Field of View Alignments of the MRS

Figure 4.14 shows the overlaid field of view plots for each sub-spectra of the Medium Resolution Spectrometer Verification Model scaled in arcseconds. It is evident that the alignment is not perfect both in the case of the alignment between channels and that between sub-spectra within a channel.

The misalignments originate in the differing optics that the path of each sub-spectra traverse through the Spectrometer Pre-Optics. Within a channel the only change in the optics between sub-spectra is the different dichroic configuration used to select the correct wavelengths. The on-sky shift in alignment between the observations within a channel is therefore due to the relative alignment of the dichroic filters with respect to one another. The on-sky shift between Channel 1 and Channel 2 could also be due to a systematic offset applied by the orientation of the Channel 2 dichroic filters to those of Channel 1. This will be further investigated in Section 4.7.

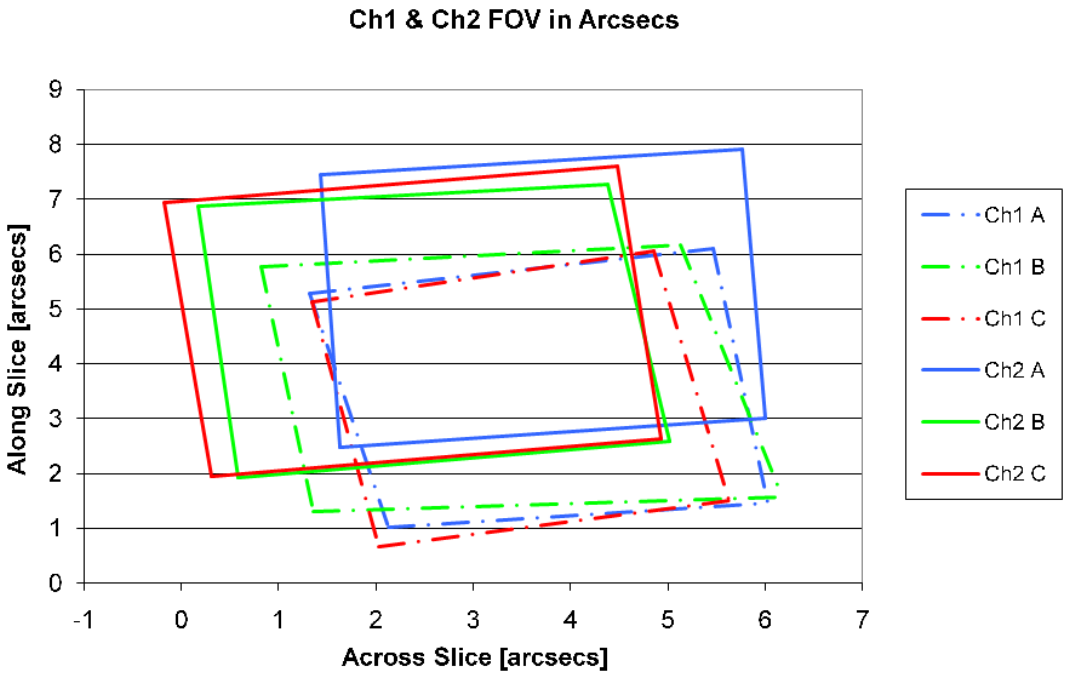

Figure 4.14: The Transmitted Fields of View for each instrument Configuration

Absolute Dimensions of the On Sky Field of View in Arcseconds

The extent of the Verification Model field of view measured for each channel can be determined from the plot in Figure 4.14 by taking an average of the along and across slice extents of each sub-spectra. The measured fields of view in arcseconds are shown alongside the requirements for the Medium Resolution Spectrometer in Table 4.3. The expected parameters are taken from a design description document

outlining the operational requirements of the spectrometer (Renouf, 2006).

	Measured		Expected	
	Across Slice	Along Slice	Across Slice	Along Slice
Channel 1	4.0	4.7	3.7	3.7
Channel 2	4.4	4.8	4.7	4.5

Table 4.3: The Measured and Expected Spectrometer Fields of View [arcseconds]

The sources of error in this analysis were noted in Section 4.5. With a fully operational MIRI Telescope Simulator the dominant error in the analysis is in the centroiding within a pixel expected to be approximately 3%. However due to the extended nature of the astigmatic compact source delivered this centroiding process is made more complicated. It is estimated that the errors in the centroiding will be approximately doubled to 6%. For Channel 1 the additional errors due to the larger corner extrapolation are expected to dominate over any centroiding errors. This additional error will now be calculated.

The errors measured for Channel 2 are 6% & 7% in the across and along slice direction respectively. These levels are consistent with the anticipated Channel 2 error due to the diffuse nature of the source. The errors measured for Channel 1 are 8% & 27% in the across and along slice direction respectively. As expected these errors are larger than for Channel 2. The heightened Channel 1 errors also explain the more varying shape between the Channel 1 sub-spectra in comparison to those of Channel 2.

The field of view requirement of at least 3.5 by 3.5 arcsecs was described with the intention that it would enable the fully sampled observation of typical spiral galaxies at z = 1 in a single set of exposures (as outlined in Section 2.2.1, Figure 2.4). Three conditions must be met in order to meet this requirement. The first is that most of the Channel 1 field of view (if not all of it) must be contained within that of Channel 2. The second is that the Channel 1 sub-spectra fields of view must be aligned to a high accuracy. The third is that the on-sky field of view transmitted by the Channel 1 Integral Field Unit does not degrade below a common 3.5 arcseconds due to the slice offsets in the along slice direction. Non-conformance in any of the three situations will reduce the common field of view below the required threshold. Note that there is much more tolerance between the alignment of the Channel 2 sub-spectra. Whilst

they must share a common field of view with Channel 1 this could be achieved with offsets of the order of 1 arcsecond between the Channel 2 sub-spectra.

Due to the large spatial offset of Channel 1 with respect to Channel 2 in Figure 4.14 it is concluded that Channel 1 is not sufficiently contained within Channel 2 for the field of view requirement to be met in the Verification Model. Also due to the large uncertainty associated with the Channel 1 sub-spectra it is unclear whether Channel 1 is aligned to the high accuracy required. It is possible however to deduce whether the common field of view sampled for Channel 1 meets the 3.5 x 3.5 arcseconds requirement. Figure 4.15 shows the Channel 1 Verification Model field of view transmitted by the Integral Field Unit. The on-sky offset of one slice from another gives the jagged alignment along the edge of the field of view which in itself could reduce the common field of view transmitted by the Integral Field Unit to below the 3.5 square arcseconds requirement. If this was the case then the field of view requirement could never be met for the Verification Model.

The Channel 1 Verification Model IFU Transmitted Field of View

The Channel 1 Verification Model field of view transmitted by the Integral Field Unit (IFU) is illustrated in Figure 4.15. In the along slice direction it can be seen that the slice offsets cause the common along slice field of view to be less than that of a slice length. This is illustrated as the blue square. Assuming that the average on-sky slice length sampled by Channel 1 is 3.7 arcseconds the square field of view sampled by the Channel 1 IFU was measured as 3.5 arcseconds in the along slice direction. There can be no error in the across slice direction as the field image is divided by the image slicer. The resultant field of view transmitted by the Channel 1 Verification Model IFU is 3.5 x 3.7 arcsecs (compared to the 3.5 x 3.5 arcseconds spectrometer requirement).

Whilst the along slice requirement is met for a single sub-spectra the Channel 1 dichroics must be perfectly aligned in the along slice direction to meet the requirement considering all sub-spectra. Whilst the actual Verification Model alignment of the Channel 1 dichroics could not be accurately ascertained due to the associated errors it can be assumed that they are not perfectly aligned considering the accuracy of the Channel 2 dichroic alignment. It is therefore argued that the common field of

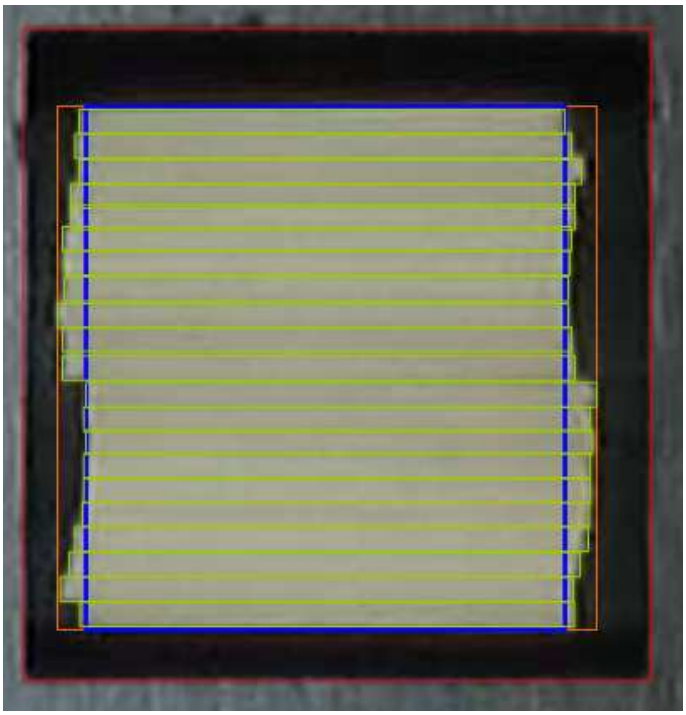

Figure 4.15: The Channel 1 Verification Model IFU Field of View

view of the Medium Resolution Spectrometer Verification Model does not meet the 3.5 square arcseconds requirement.

The on-sky slice offsets are caused by tolerances in several of the Integral Field Unit components, the main contributors being the re-imaging mirrors (Section 2.2.2, Figure 2.9) and the output slit mask (Section 2.2.2, Figure 2.10). Any positional error in the along slice direction of a re-imaging mirror will cause an along slice offset of the slice on the field of view. Similarly a positional offset in the along slice direction of a slit on the output slit mask will cause the on-sky slice to be offset from the nominal position. It is a combination of these two effects which cause the slice misalignments within a channel.

The Channel 1 Flight Model field of view transmitted by the Integral Field Unit contains slice offsets similar to the Verification Model. It is most important that the Flight Model meets the 3.5 square arcseconds field of view requirement. As such the same field of view analysis considering the slice offsets will be performed for the Flight Model. This analysis will be detailed further in Section 4.9.

4.6 The Expected Verification Model Field of View

During the assembly of the Verification Model (and the Flight Model) the relative alignment of the Channel 1 and Channel 2 fields of view was adjusted using two adjustable mirrors, one in the dichroic level optics for each channel (noted in Section 2.2.1). These mirrors enabled full adjustment of both the Channel 1 and Channel 2 fields of view to ensure that the on-sky field of view of Channel 1 was fully contained within that of Channel 2. Their adjustment required an alignment telescope to be placed along the optical axis of the telescope as per Figure 4.16 (Lee et al., 2007b). This was achieved by placing the alignment telescope perpendicular to the graticule using reflection and aligning the telescope with the graticule crosshair. Through the use of each adjustable mirror the Channel 1 and Channel 2 alignment was set such that the chief ray passed through the center of the anamorphic pre-optics field stop (noted in Section 2.2.2, Figure 2.8).

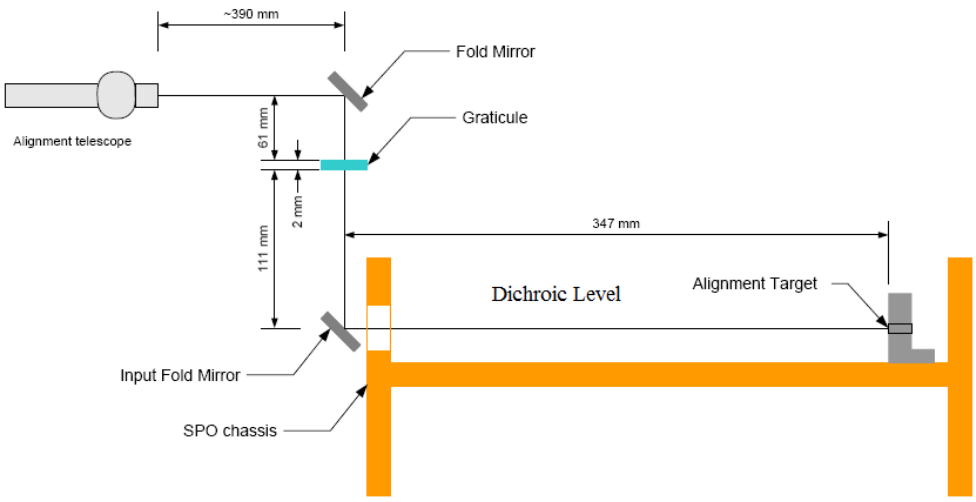

Figure 4.16: The Alignment of the Anamorphic Pre-Optics Field Stops

As this alignment was done optically at ambient environment it was necessary to use optically transparent filters as the filters designed for flight do not transmit at optical wavelengths. Cleartran filters with an approximate transmission of 0.70 at optical wavelengths were used (Lee, 2006a). These optically transparent filters will be referred to as OGSE Filters (Optical Ground Support Equipment).

The alignment of the Channel 1 & Channel 2 anamorphic pre-optics field stops was achieved using the Cleartran OGSE Filters. This does not however provide any information as to the relative alignment of the sub-spectra due to the dichroic filter alignment. Remember from Section 4.5 that the sub-spectra field of view misalignments are due to the small angular misalignments that the dichroic filters make with respect to the beam. It is expected that the dichroic filters will be orientated at slightly differing angles to the Cleartran OGSE Filters when they are fitted into the dichroic level. These orientations were measured in the lab during the Verification Model assembly to measure the sub-spectra field of view alignments (Lee, 2007c). Used in comparison with the sub-spectra alignments measured during the test campaign they enable an investigation into whether the relative dichroic alignments change after the complete instrument vibration.

The Relative Alignment of the Sub-spectra

For reference to this section the dichroic level was detailed in Section 2.2.1. The relative alignment of the dichroic sub-spectra was also measured using an alignment telescope placed along the optical axis. Even though the filters do not transmit at optical wavelengths each channel could be investigated as Channel 1 & Channel 2 are reflected from the front surfaces of their respective dichroic filters. Note that as Channel 2 is transmitted through the Channel 1 dichroic filter the Channel 1 Cleartran OGSE Filter must be fitted when investigating the Channel 2 sub-spectra alignment. Also the Cleartran OGSE blocking filters must be used in both the Channel 1 & Channel 2 dichroic chain to ensure transmission to the anamorphic pre-optics field stop.

The Channel 1 & Channel 2 Relative Alignment

The Channel 1 sub-spectra alignment was investigated in reflection from the Channel 1 filter on Dichroic Wheel Assembly A (DWA-A) as per Figure 4.17. In each case the offset on the alignment telescope required to position the alignment target at the center of the anamorphic pre-optics field stop was determined. As this is at a field image the measured offsets and the plate scale of the image provide a direct measurement of the relative on-sky alignment of the sub-spectra. The Channel 2 sub-spectra alignment was similarly measured in reflection from the Channel 2 filter

on Dichroic Wheel Assembly B (DWA-B) as shown in Figure 4.17. The sub-spectra alignments will be discussed in the following section.

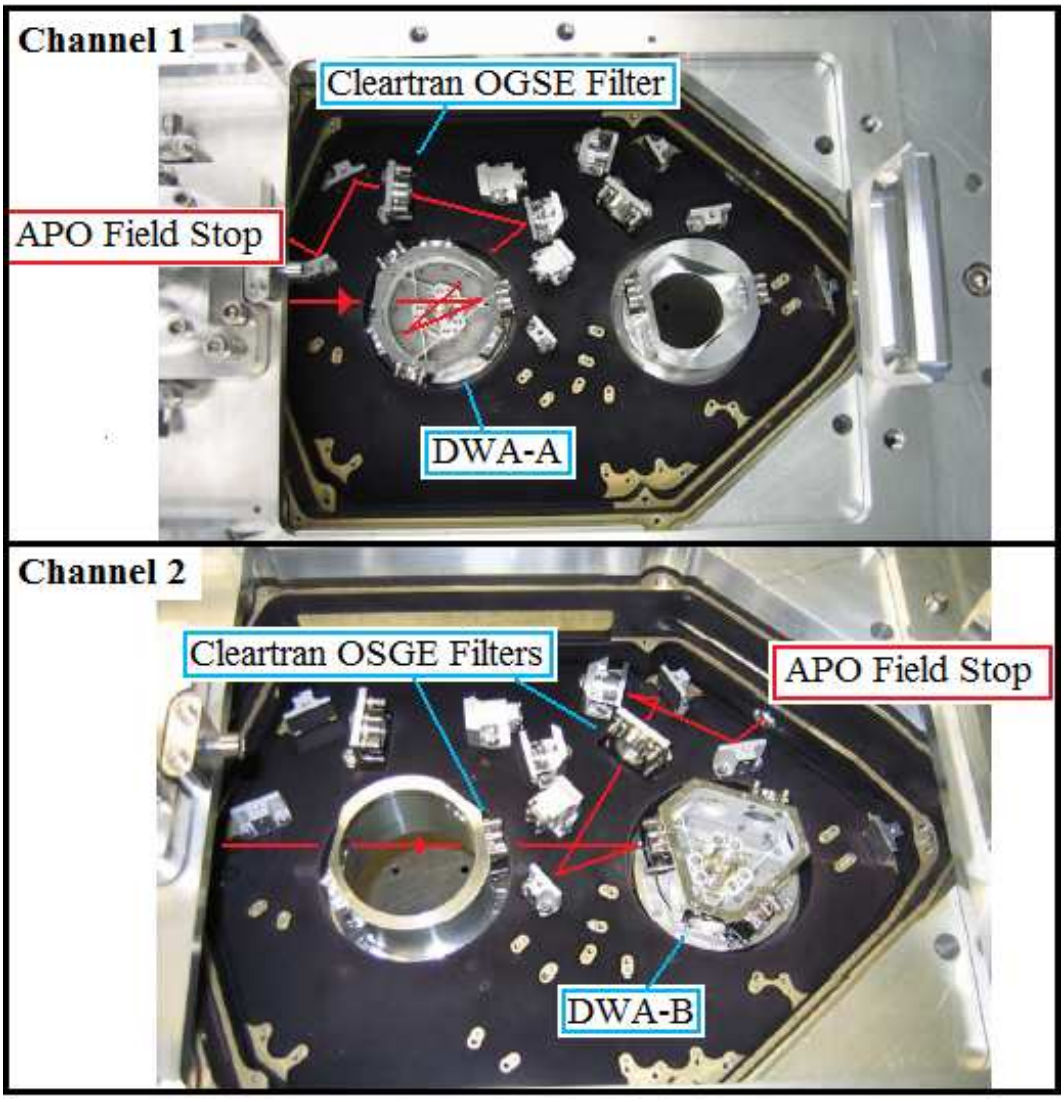

Figure 4.17: The Channel 1 & 2 Dichroic Alignment Test Set-up

4.7 Comparison of the On-Sky and Expected Fields of View

The expected sub-spectra alignments for the Verification Model are shown in Figure 4.18 (Lee et al., 2007b). Comparing Figure 4.18 with that of Figure 4.14 which shows the sub-spectra alignment measured during the Verification Model test campaign it can be seen that the major sub-spectra alignment characteristics observed match those expected. These are the global offset of the Channel 1 field of view from Channel 2 and the large offset of Channel 2A from 2B and 2C. As a result it can be concluded that the relative filter alignment on the dichroic wheel assemblies is unchanged after vibration. This is a very important result as it implies the alignment will not change during the launch phase of the instrument.

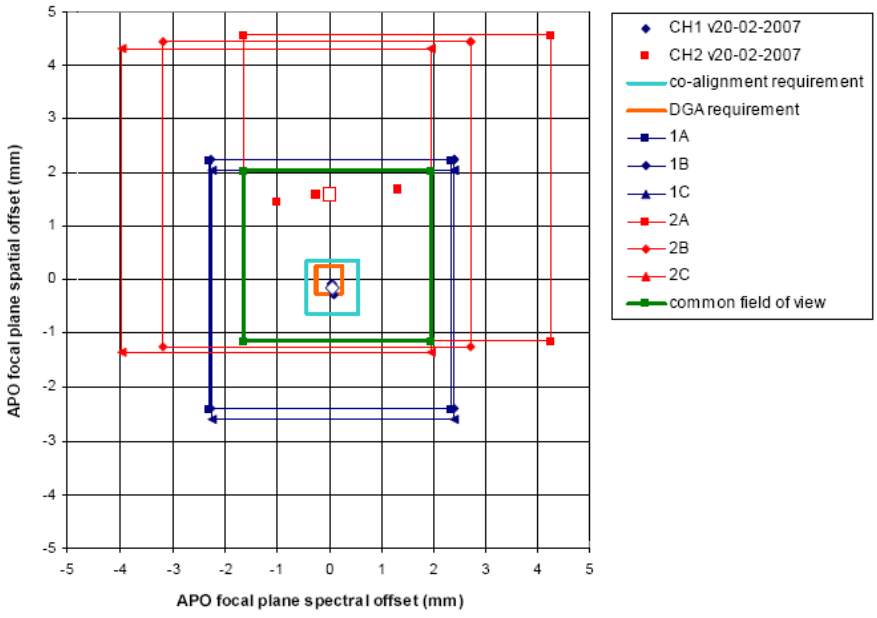

Figure 4.18: Lab Measurements of the Relative Alignment of the Field of View for each Instrument Configuration (Spectral = Across Slice, Spatial = Along Slice)

The expected offset of the Channel 2 field of view from that of Channel 1 is due to a systematic error in the rotational positioning of the Channel 2 dichroic wheel. This is a problem with the early design of the rotational stage and will be corrected in the Flight Model. Rotational error denotes a movement in the along slice direction as opposed

to pyramidal error which acts in the across slice direction. The expected across slice offset of Channel 2A from 2B and 2C is caused by a tilt in the alignment of the Channel 2 dichroic wheel. The magnitude of this error depends on how far the filter being measured is offset along the circumference of the wheel from the position of maximum tilt. Without these errors Channel 1 would be completely contained within Channel 2 necessary to meet the field of view requirement of the instrument.

4.7.1 The Channel 2 Field of View

The expected alignment of Channel 2 in Figure 4.18 shows Channel 2A offset by around $\frac{1}{4}$ of its field of view in the across slice direction. Along the same axis but on a smaller scale Channel 2C is offset from Channel 2B by around $\frac{1}{8}$ of its field of view. This sub-spectra alignment is also measured in the actual field of view extents as per Figure 4.14 though the smaller offset of 2B from 2C is less obvious. This discrepancy is most likely due to the 6% measurement error of the field of view extent due to the corner extrapolation and the centroiding used in the analysis.

4.7.2 The Channel 1 Field of View

Figure 4.18 shows that the Channel 1 sub-spectra are expected to be aligned to a much higher precision than for Channel 2. Channel 1 is also expected to be offset by around $\frac{1}{5}$ of its field of view in the along slice direction from Channel 2. The sub-spectra alignment shown in Figure 4.14 indicate that these features are present although there is some uncertainty in the magnitude of the measured offset. This is due to the large variation seen in the relative shapes of the Channel 1 sub-spectra fields of view in comparison to those of Channel 2 which appear more regular. This larger error was due to the Channel 1 analysis and in particular the larger corner extrapolation.

4.8 The Optical Model Field of View

The measured sub-spectra field of view alignments have been compared with the expected alignments and have been shown to be consistent with one another. The next

stage of the analysis was to compare the measured on-sky positioning of the sub-spectra with the optical model. This will enable an insight into how well the optical model understands the design of the Medium Resolution Spectrometer. The comparison was done in MIRI Imager pixel units as the sub-spectra fields of view have already been converted into these coordinates.

The optical model contains data for each detector pixel defining the on-sky position that it subtends. This position is given in V2-V3 coordinate axes (where V2 & V3 corresponded to the angles in x and y that the center of the detector pixel viewed on the sky make with the principal optical axis of The James Webb Space Telescope at the given wavelength). This V2-V3 coordinate system must be converted into MIRI Imager pixel units for the comparison.

Converting The Optical Model Data into MIRIM Pixel Units

The coordinate transforms to convert the optical model data into MIRI Imager (MIRIM) pixel units are outlined in Wells (2007). The first step in the reduction was in converting from the angular V2-V3 coordinate system into that of the angular MIRIM field of view. The origin of the angular MIRIM coordinate system is located at [-7.25, -1.53] on the V2-V3 coordinate axes and orientated at an angle of 4.555 degrees anticlockwise to it as per Figure 4.19.

The coordinate transform is shown in Table 4.4 where V2 and V3 are in arcminutes and θ is 0.0795 radians (4.555 degrees).

$X_{MIRIM}[arcmin] = [(V2 + 7.25) * COS(\theta) + (V3 + 1.53) * SIN(\theta)]$
$Y_{MIRIM}[arcmin] = [(V3 + 1.53) * COS(\theta) - (V2 + 7.25) * SIN(\theta)]$

Table 4.4: Conversion of V2-V3 Coordinates into Angular MIRIM Coordinates

To finish the conversion we need to convert from angular MIRIM coordinates ($X_{MIRIM}[arcmin]$) to a linear MIRIM coordinate system ($X_{MIRIM}[mm]$), then to a detector coordinate system ($X_{det}[mm]$) and finally into detector pixels ($X_{det}[pixels]$). The necessary transformations are shown in Table 4.5 (using the same transforms for y as in x). 0.0259 [arcmin per mm] is the plate scale of the MIRIM field of view (= 0.11

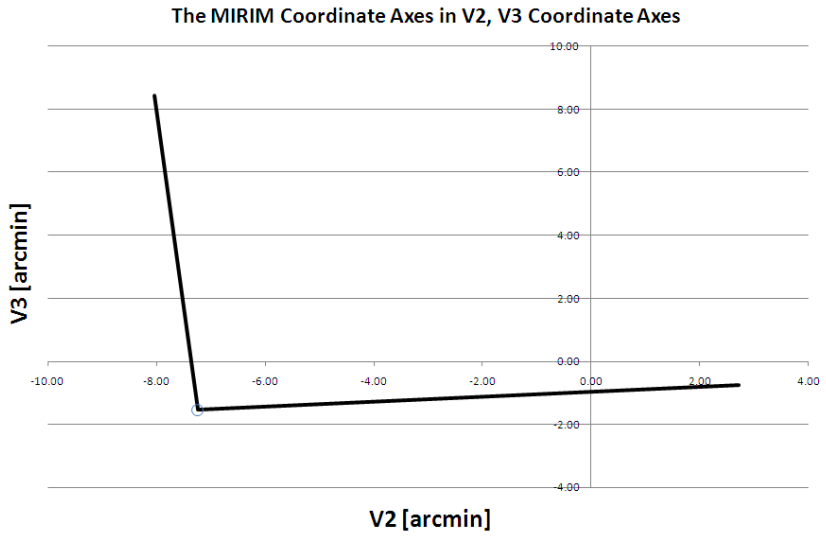

Figure 4.19: MIRIM Coordinate Axes in V2, V3 Coordinate Axes

* 40 / 60 / 2.8235) where the pixel pitch of 25 microns = 0.11 arcsecs at the detector and 2.8235mm is the magnification factor from the MIRIM field of view to the detector.

$X_{MIRIM}[mm] = X_{MIRIM}[arcmin]/0.0259$
$X_{det}[mm] = -X_{MIRIM}[mm]/2.8235$
$X_{det}[pixels] = (X_{det}[mm]/0.025) + 512$

Table 4.5: Conversion of the Angular MIRIM Coordinates into MIRIM Pixel units

4.8.1 The Channel 1 Optical Model Field of View

The on-sky position expected from the Channel 1 optical model is shown with the measured sub-spectra positions for Channel 1 in Figure 4.20. Note the Channel 2 optical model data is included for a positional comparison. The Channel 1 optical model shows a good understanding with the measured on-sky positions of the Channel 1 sub-spectra. There is a small rotation between the orientation of the optical model field of view and those of the measured Channel 1 sub-spectra. The origin of this rotation is possibly from the analysis errors in the corner position extrapolation.

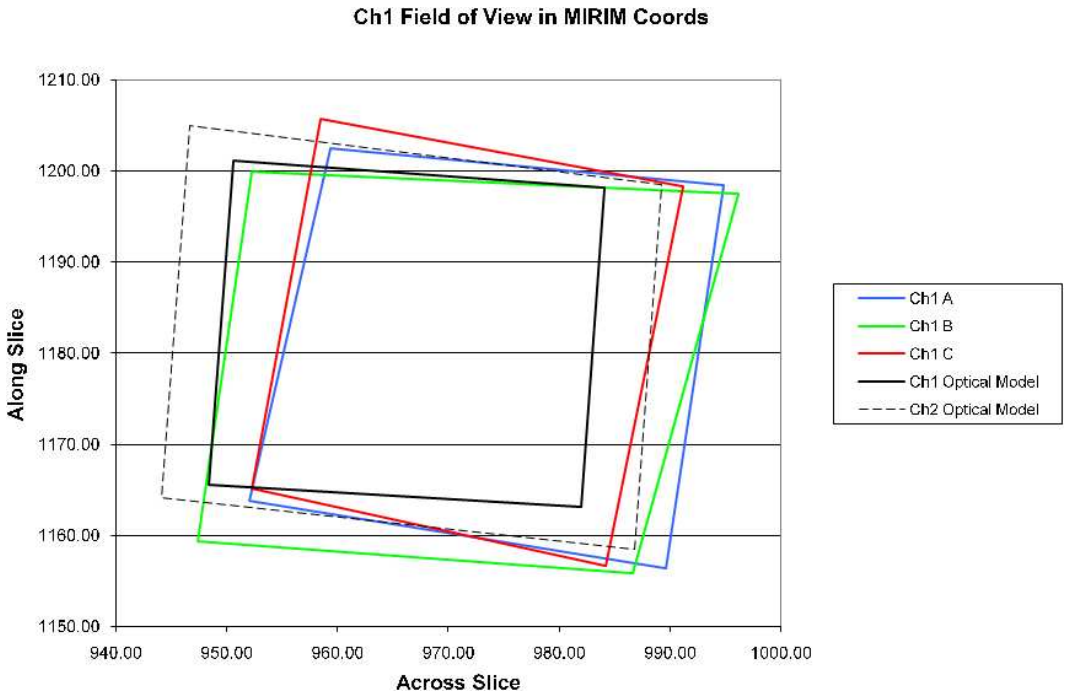

Figure 4.20: The Ch1 Transmitted FOV and the Zemax Model Data

4.8.2 The Channel 2 Optical Model Field of View

The on-sky position expected from the Channel 2 optical model is shown with the measured sub-spectra positions for Channel 2 in Figure 4.21. Again the Channel 1 optical model data is included for comparison. The Channel 2 optical model shows a large offset in the along slice direction to the on-sky position of the Channel 2 sub-spectra. This offset is well understood as being due to a systematic rotational error in the Channel 2 dichroic wheel as per Section 4.7. Accounting for the effects of the rotational error and the pyramidal error (which caused the Channel 2 sub-spectra to be misaligned in the across slice direction) the Channel 2 optical model shows a good understanding with the measured on-sky positions of the Channel 2 Medium Resolution Spectrometer sub-spectra. There is also small rotation between the optical model field of view and those of the measured Channel 2 sub-spectra however the rotation is less than that measured for Channel 2. It is probable that the rotation is due to the analysis errors which are smaller for Channel 2 than Channel 1.

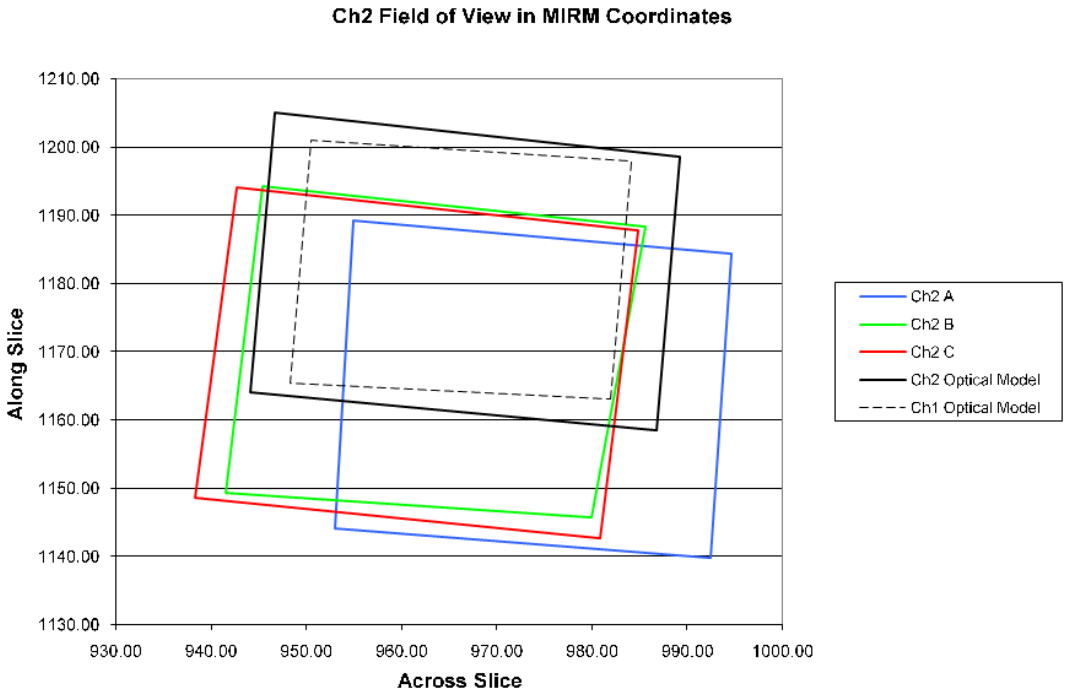

Figure 4.21: The Ch2 Transmitted FOV and the Zemax Model Data

Whilst the Channel 1 optical model more closely models the position of the Channel 1 sub-spectra there is a well understood origin for the offset in the optical model and sub-spectra positions for Channel 2. This shows that the instrument operation is well understood by the optical model with respect to the position of the fields of view.

4.9 The Channel 1 Flight Model Field of View

Investigating the Channel 1 transmitted field of view for the Verification Model (Section 4.5, Figure 4.15) it was shown that the slice offsets can degrade the along slice field of view to below 3.5 arcseconds which would make the field of view requirement of 3.5 square arcseconds impossible to achieve. As such it must be ensured that the Flight Model slice alignment is above this threshold.

Section 4.5 alluded to two other conditions necessary to achieve the field of view requirement. That the Channel 1 field of view must be contained within that of Channel 2 and that the Channel 1 sub-spectra must be aligned to a high accuracy. Due to the possibility of a misalignment between the Channel 1 sub-spectra it is prudent to en-

sure that the along slice field of view is greater than 3.5 arcseconds as this will relax the accuracy of the dichroic alignment necessary to achieve the field of view requirement.

The effect of both the on-sky slice alignment and the dichroic alignment will now be investigated and any sources of error that reduce the common field of view of the Flight Model will be minimised.

4.9.1 The Channel 1 Flight Model Slice Alignment

The Channel 1 Flight Model field of view transmitted by the Integral Field Unit (IFU) displays slice offsets similar to that of the Verification Model shown in Figure 4.15. The slice offsets are caused by tolerances in several of the IFU components with the main contributors being the re-imaging mirrors (Section 2.2.2, Figure 2.9) and the output slit mask (Section 2.2.2, Figure 2.10). The left hand image of Figure 4.22 shows the Channel 1 Flight Model field of view with the common square field of view enclosed by the blue box. Assuming the average length of the slices corresponds to 3.7 arcseconds the common square field of view extends ~3.41 arcseconds in the along slice direction. This along slice field of view is below that of the requirement and hence is not acceptable.

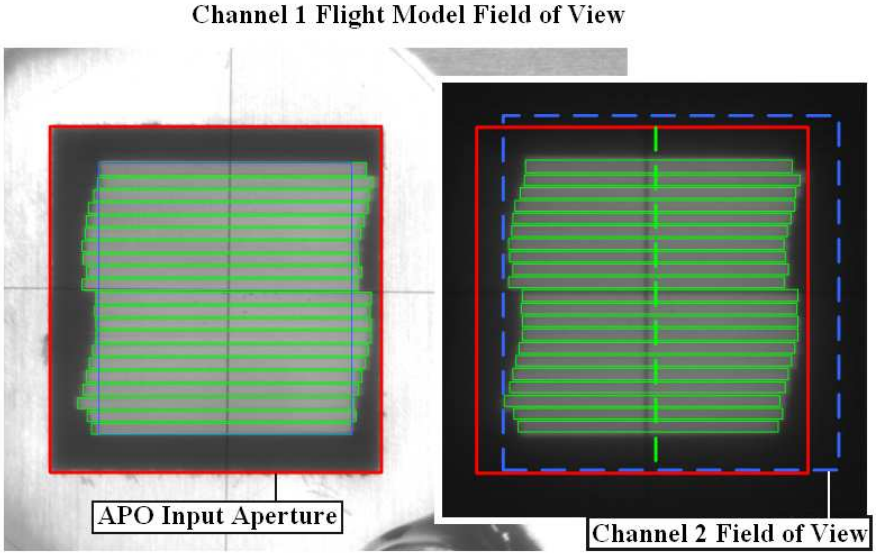

Figure 4.22: The Channel 1 Flight Model Field of View. The green line denotes the position midway between the APO input aperture and the edge of the Channel 2 field of view.

The slice offsets are caused by along slice positional tolerances in the re-imaging mirrors and the output slit mask. The slice offsets for the Flight Model field of view were be removed by changing the positions of the slits on the output slit mask (the re-imaging mirrors were kept constant) as this will move the on-sky position of the slice in the along slice direction. By creating offsets to the along slice positions of the slits on the output slit mask it was possible to remove the slice offsets in the Channel 1 field of view.

Whilst this would increase the square field of view transmitted by the Integral Field Unit it was necessary to ensure that the Channel 1 field of view was still contained within that of Channel 2 (in dashed blue) to meet the requirement. It was also required that the Channel 1 field of view be fully contained within the anamorphic pre-optics input aperture (in red) so that there was no attenuation of the Channel 1 field of view at the aperture. It was decided that the center of the Channel 1 slices be aligned along the dashed green line in the right hand image of Figure 4.22 as this was at the midpoint between the edges of the Channel 2 field of view on the left and the anamorphic pre-optics input aperture on the right.

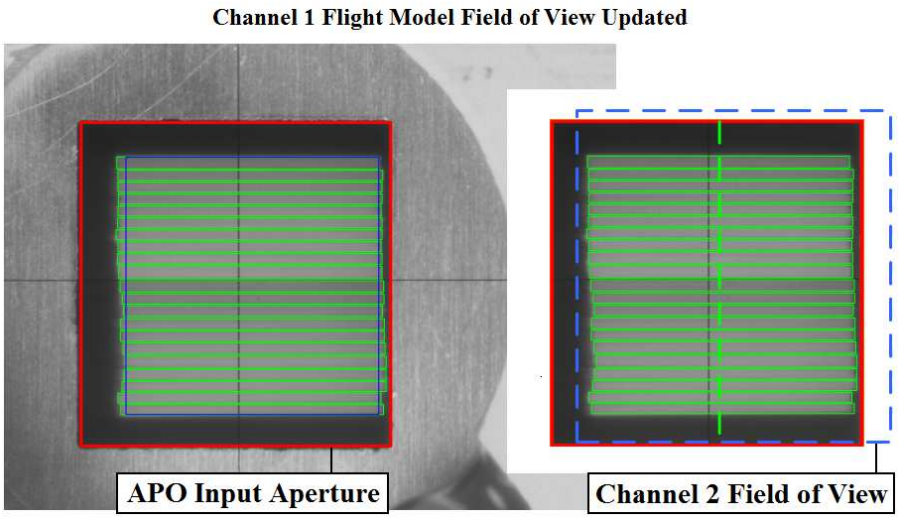

Figure 4.23: The Updated Channel 1 Flight Model Field of View. The green line denotes the position midway between the APO input aperture and the edge of the Channel 2 field of view.

The Flight Model field of view with the new output slit mask is shown in Figure 4.23. There are still slice offsets due to the machining errors in the output slit mask however

it can be seen that they are much smaller than in Figure 4.22. As required the Channel 1 field of view is contained within that of Channel 2 and is fully transmitted by the anamorphic pre-optics input aperture. The along slice field of view transmitted by the Channel 1 Flight Model Integral Field Unit is 3.6 arcseconds. This produces a Channel 1 sub-spectra field of view of 3.6 x 3.7 square arcseconds which enables the 3.5 square arcseconds field of view requirement to be met during flight with some tolerances in the on-sky sub-spectra alignment.

Diffraction Investigation of the New Slit Mask Dimensions

A check was done on the new slit mask dimensions to ensure they do not compromise another spectrometer requirement. OBA-0652 states "Spectra from different spectral/spatial ranges that are imaged onto the same two-dimensional detector array shall be separated by a gap of at least the diameter of the first dark diffraction ring as determined from the PSF generated by the segmented model in the Interface Requirement Document, at the longest wavelength in the spectral direction, to avoid overlap of the spectra at different orders" (Bean, 2008). Basically the slice spacing on the detector should be equal to the diameter of the PSF out to 1st minimum of the longest wavelength to be imaged onto the detector. This was so that there was no cross talk between neighboring slices on the detector which was necessary to maximise the signal to noise of an observation. It was possible that the new slit mask dimensions, as they define the slice spacing on the detector, would not meet this requirement.

A diffraction analysis of the expected detector slice profiles for the new Flight Model slit mask was carried out and compared with the expected slice profiles for the old slit mask. These slice profiles were used to model the flux levels between two slices. This enabled an investigation into whether there were heightened flux levels at any between slice positions as this would indicate that the slices were too close together. The method for the derivation of the slice profiles will be outlined in Section 5.1. Figure 4.24 shows the slice profiles for the new slit mask dimensions in blue and compares the inter slice minima levels with those for the old slit mask represented by the red line. There are no obvious between slice positions where there is a large flux increase so it can be concluded that the new output slit mask dimensions are compliant with the slice spacing requirement at the detector.

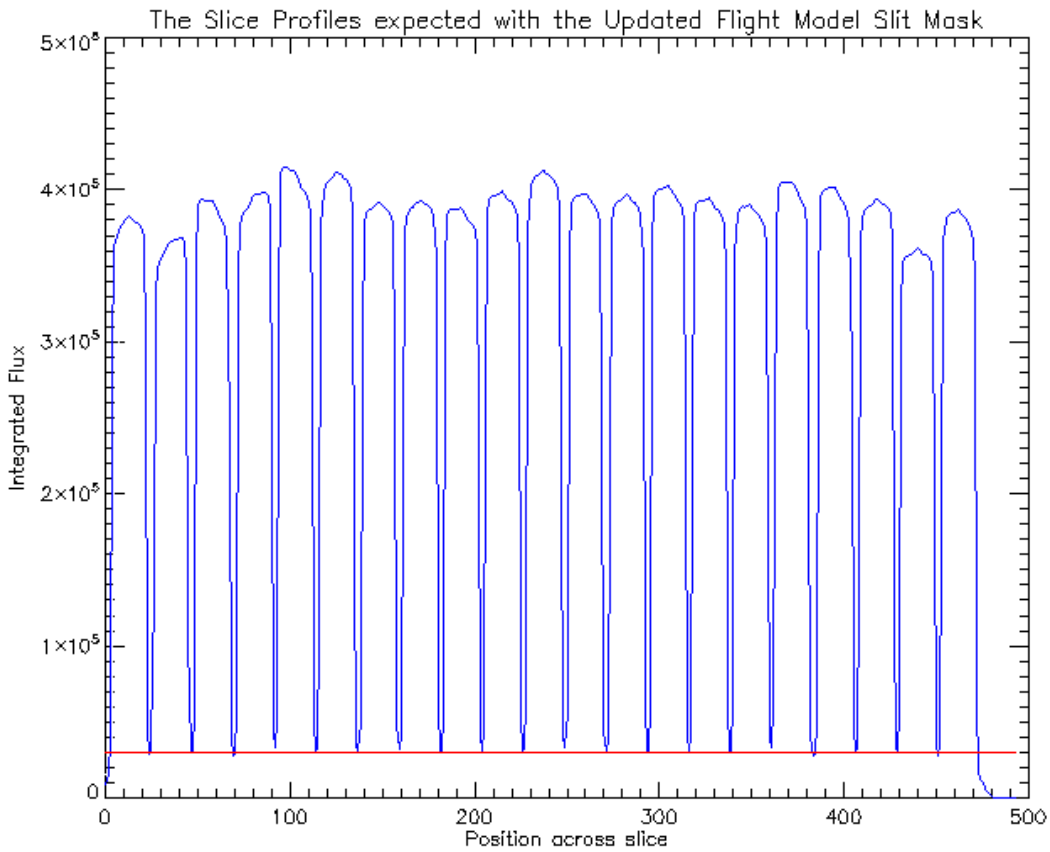

Figure 4.24: The Channel 1 Flight Model Expected Slice Profiles

4.9.2 The Channel 1 Sub-spectra On-sky Alignment

The new output slit mask has aligned the slices on the sky to produce a 3.6 x 3.7 arcseconds field of view. It has also been shown that the Channel 1 on-sky field of view is contained within that of Channel 2. This implies that two of the three conditions for the field of view requirement to be met are satisfied (as per Section 4.5). The final condition is that the Channel 1 sub-spectra must be aligned to a degree on the sky that does not reduce the common field of view to below 3.5 square arcseconds.

It was noted in Section 4.7 that the relative dichroic alignment will change the sub-spectra field of view alignment on the sky. The Flight Model dichroic alignment was investigated to check that they would reduce the common field of view to below the 3.5 square arcseconds requirement.

The Dichroic Considerations

At the time of writing it was impossible to actually measure the relative alignment of the dichroic observations within each channel for the Flight Model as was done for the Verification Model in Section 4.7. This was because the dichroic wheel mechanisms had not been delivered and as such the dichroic wheels could not be positioned within the Spectrometer Pre-Optics as they will during flight. It was however possible to calculate the expected alignments from direct measurements of the filters and mirrors on the dichroic wheels. The dichroic measurements and alignment results are outlined in Lee et al. (2008). The Dichroic Wheel Assemblies shown in Figure 4.25 were measured in turn using the same method.

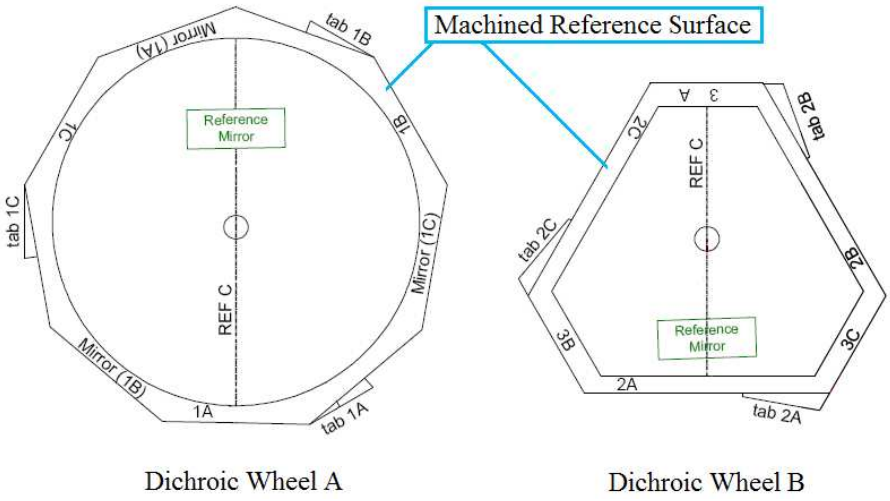

Figure 4.25: The Flight Model Dichroic Wheel Assemblies

The two interactions which will change the downstream path of a beam incident upon the wheel are reflection and transmission interactions. The dominant change in the position of a field of view was caused by reflection from the surface of a dichroic at an incorrect orientation to the beam. The field of view offset of a beam transmitted by a dichroic incorrectly orientated by 1 degree was measured as less than a 2% movement of the field of view on the sky. As the typical tilt angles are of the order of 250 times smaller the change in the transmitted field of view can be ignored. As such to calculate the sub-spectra on-sky alignment it was only necessary to consider the angles that the dichroic filters used in reflection made with the nominal case.

Measurement of the Dichroic Alignment

The top surface of each dichroic wheel is a diamond machined reference surface on the same plane as the wheel mounting surface. For measurement each wheel was mounted on a tip-tilt stage on a rotary stage. The tip-tilt stage enabled the wheel to be aligned on the same plane as the rotary stage which was intended to reduce any pyramidal errors during measurement. These arise when the mounting surface of the wheel is inclined at an angle to the plane of the rotational stage. The pyramidal error (noted in Section 4.7) was reduced by observing the top surface of a dichroic wheel using an interferometer to measure the change in the vertical tilt of the surface during the stage rotation. Through plotting the measured vertical tilt of the reference surface as a function of the stage rotation angle an insight into the angular position of the maximum pyramidal error could be derived. The tip-tilt stage could then be used to minimise the pyramidal error.

Once the test set-up had been calibrated a theodolite was used to measure the relative alignment of the dichroic filters in reflection (as well as the backs of the mirrors mounted on the Channel 1 wheel). This alignment was calculated relative to a reference tab on each wheel (Tab 1A or 2A). Note that the relative alignment of Dichroic Wheel A with respect to Dichroic Wheel B was calculated using the a reference mirror on the dichroic wheel mount which was used for both wheels.

Consider Figure 4.26 which shows both the nominal case and that with a filter offset. The angular difference between the nominal reflected beam and that from the offset filter is 2dθ where dθ is the angle that the filter is offset from the nominal case [radians]. The offset in the field of view **x** [mm] can be determined from the angular offset dθ of the filter and the downstream distance **D** to the anamorphic pre-optics field stop (approximately 350 mm).

Considering small angles Equation 4.2 shows how the tip-tilt offset measured at a dichroic was converted into an offset at the anamorphic pre-optics input field stop. This offset could be converted into an on-sky offset using the plate scale of 0.795 arcseconds per mm at the field stop (calculated as per Section 1.2.1) where the focal ratio is 39.37 and the telescope diameter 6595 mm (Section 2.1).

$$\mathbf{x} = 2\mathbf{D}d\theta \tag{4.2}$$

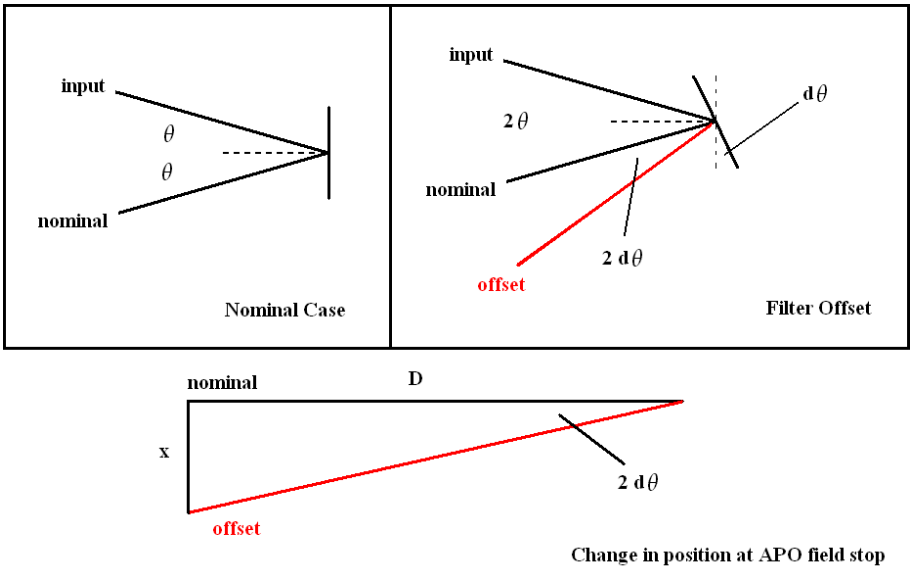

Figure 4.26: Dichroic Filter Alignments and the Field of View Offset

The Relative Alignment of the Dichroic Filters

The relative alignment of the dichroic filters in Figure 4.27 shows an offset in the spectral direction (across slice) of sub-spectra 1C with respect to 1B and 1A. This offset reduces the common Channel 1 field of view in the across slice direction to 3.34 arcseconds. The offset of the 1C sub-spectra may however arise from a pyramidal error in the analysis as this could not be completely removed during the calibration. The RMS error for the component alignment on the Channel 1 wheel was ∼50 arcseconds although the contribution of the pyramidal error to this is unknown. Remembering that the Channel 1 beam is reflected off both a dichroic filter and a mirror on Dichroic Wheel A (as per Figure 4.17) accounting for an error of 30 arcseconds in both the dichroic filter and mirror of Channel 1 is required to increase the common field of view to 3.5 arcseconds.

In the along slice direction the common field of view is 3.62 arcseconds. However considering the 0.1 arcsecond loss due to the slice misalignment (as per Section 4.9) the common along slice field of view is 3.52 arcseconds. This is greater than the 3.5 arcseconds requirement which necessitated the redesign of the output slit mask. As such it can be concluded that the redesign of the output slit mask was a success.

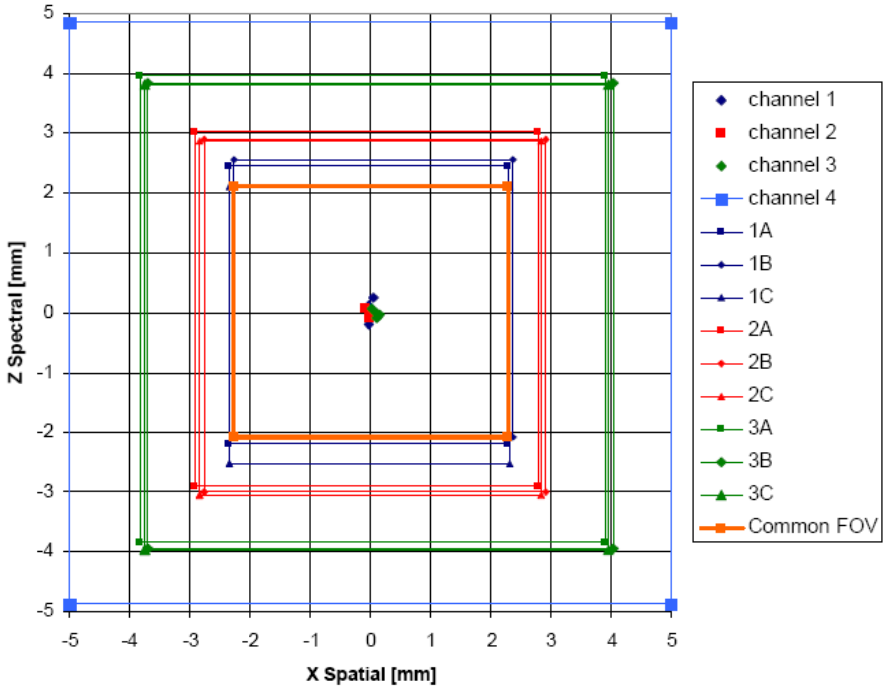

Figure 4.27: Expected Field of View Alignment for the Flight Model (Spectral = Across Slice, Spatial = Along Slice)

4.9.3 The Complete MRS Flight Model Field of View

The expected field of view of the flight model is 3.52 x 3.34 arcseconds without accounting for error. The field extent in the across slice direction does not exceed the requirement by a factor of 5%. However due to the along slice direction exceeding 3.5 arcseconds the common field of view is only 4% smaller than the requirement. The field in the across slice direction may increase from 3.34 to 3.5 arcseconds if the pyramidal error influencing the measurement of dichroic filter and mirror 1C is of the order 30 arcseconds. In such a case the field of view requirement of 3.5 square arcseconds will be met. Remember that that the field of view requirement of 3.5 x 3.5 arcseconds was designed to enable the fully sampled observation of typical spiral galaxies at z = 1 in a single set of exposures (as outlined in Section 2.2.1, Figure 2.4). Whether this will be achieved during flight will have to be derived when the filter alignment can be measured using the filter mechanisms for placement and rotation. In such a test set-up the pyramidal error of the previous alignment will not be present however it

is expected that these mechanisms will introduce their offsets to the filter orientations due to machining tolerances.

4.10 Conclusions of the Field of View Analysis

The method to reconstruct the field of view for the Medium Resolution Spectrometer has been defined along with an investigation into the opto-mechanical stability of the slices on the detector. The stability was found to be very high which enabled a single flat field observation to be used for several days observations to define the slice positions on the detector.

The field of view requirement of at least 3.5 by 3.5 arcsecs was described with the intention that it would enable the fully sampled observation of typical spiral galaxies at z = 1 in a single set of exposures (as outlined in Section 2.2.1, Figure 2.4). Three conditions must be met in order to meet this requirement. The first is that most of the Channel 1 field of view (if not all of it) must be contained within that of Channel 2. The second is that the Channel 1 sub-spectra fields of view must be aligned to a high accuracy. The third is that the on-sky field of view sampled by the Integral Field Unit in the along slice direction does not degrade below a common 3.5 arcseconds due to the slice offsets. Non-conformance in any of the three situations will reduce the common field of view below the required threshold.

For the Verification Model the field of view requirement was not achieved mainly due to the on-sky dichroic alignment. However whilst the the on-sky alignment for each of the sub-spectra in Channels 1 and 2 was not of the accuracy required the measured sub-spectra alignment (shown in Figure 4.14) closely followed that of the lab measurements (shown in Figure 4.18) and was well understood. Whilst the alignment between the sub-spectra was not perfect it did not change noticeably due to vibration. This is an important result as it implies that once the Flight Model dichroic filters have been sufficiently aligned there should not be a shift due to vibration.

Section 4.9 details a modification carried out on the Flight Model output slit mask to increase the common along slice field of view transmitted by the Integral Field Unit from 3.41 arcseconds to 3.6 arcseconds and kept the Channel 1 field of view within that of the on-sky Channel 2 position. This redesign made it possible to achieve the

3.5 square arcseconds field of view required for the Flight Model with some tolerances in the alignment of the Channel 1 dichroic filters.

The expected sub-spectra alignment for the Channel 1 Flight Model was investigated through the dichroic filter alignment. The analysis showed that the expected field of view for the Flight Model was measured as 3.52 x 3.34 arcseconds (across and along slice respectively) however this may increase to 3.52 x 3.5 arcseconds if the error introduced into the measurement of dichroic and mirror 1C was of 30 arcseconds. It cannot be ascertained if this was the case however a further dichroic alignment analysis will be done with the dichroic wheel mechanisms which will reduce the error in the analysis and enable a more accurate measurement of the expected common field of view.

Further Investigation Required

Section 4.2, Figure 4.7 showed that the ratio of the slice lengths sampled by the Integral Field Unit are different from the same slice length ratios measured on the detector. This implies that the slices at the detector have been magnified within the Spectrometer Main Optics. Chapter 5 will describe this magnification of the slice lengths and investigate its impact on the operation of the instrument. The magnification will be shown to induce an error into the spatial alignment of the reconstructed Verification Model field of view. It will also detail a performance test that I devised which must be carried out on the Flight Model to enable a full spatial calibration of the field of view.

The Channel 1 reconstructed images show an additional component close to the Channel 1 compact source which increases in size and intensity with shorter dichroic configurations. This can be seen by comparing the image for Channel 1 with that of Channel 2 in Figure 4.10 (left and right respectively). The Channel 1 image is more extended than its Channel 2 counterpart even though in a diffraction limited system the opposite would be the case. This would indicate that there may be light scattering in the system which may reduce the efficiency of the instrument. To investigate its impact this scattering will be investigated in Chapter 6.

CHAPTER 5

Slice Magnification

It was noted in the previous chapter that the ratio of the slice lengths presented for input to the Spectrometer Main Optics at the output slit mask are different from the same slice length ratios measured at the detector (as per Section 4.2, Figure 4.7). The change in slice lengths between the output slit mask and the detector will be investigated for Channels 1 & 2 and it will be shown that there is a changing magnification observed in the slice lengths across the detector which must have occurred in the Spectrometer Main Optics. This magnification will also be shown to be present in the optical model. The impact of the magnification on the operation of the spectrometer will be investigated and it will be shown that it must be considered to achieve an accurate spatial calibration of the field of view. It will be shown that the worst case field of view alignment error observed is approximately 0.28 arcseconds between two adjacent slices in a Channel 1 field of view reconstruction. This offset is approximately 8% of the along slice dimension or 2 pixels uncertainty in the 22 pixel along slice dimension. To remove this alignment error for all channels in the Flight Model I devised a method of calibrating the Medium Resolution Spectrometer so that the reconstructed images could be fully spatially aligned. This calibration procedure which will be outlined is required for flight to accurately measure the spatial distribution when observing an extended target.

5.1 Measuring the Magnification Effect

The slices transmitted by the Integral Field Unit are presented for input to the Spectrometer Main Optics at the image plane defined at the output slit mask (Section 2.2.2, Figure 2.10). The magnification was investigated by comparing the along slice extent of the slices at the output slit mask (that which defines the length of and the spacing of the slices on the detector) with the actual placement and extent of the slices on the detector. The output slit mask dimensions will be referred to as ″Theoretical Measurements″ and the spacing of the slices on the detector will be ″Observed Measurements″. If the ratio of two observed slice lengths deviate from the theoretical slice lengths then the cause is a magnification originating in the Spectrometer Main Optics.

Figure 5.1 shows the observed and theoretical slice profiles for Channel 2 ″A″ between 8.07 - 9.05 microns. The observed slice profiles [red] were derived by integrating the straightened slices on the detector over the indicated wavelength range. The theoretical slice profiles [blue] were used to model the expected slice profiles on the detector without the magnification. By comparison the effects of the magnification on the slice profiles at the detector can be observed. The theoretical slice profiles were derived from several stages of analysis which will be described below. Integrated flux is a linear measure of the total flux contained within the wavelength range and the position across slice is measured in pixels on the detector. The across slice detector position and pixel numbering for each channel in is shown in Figure 5.2.

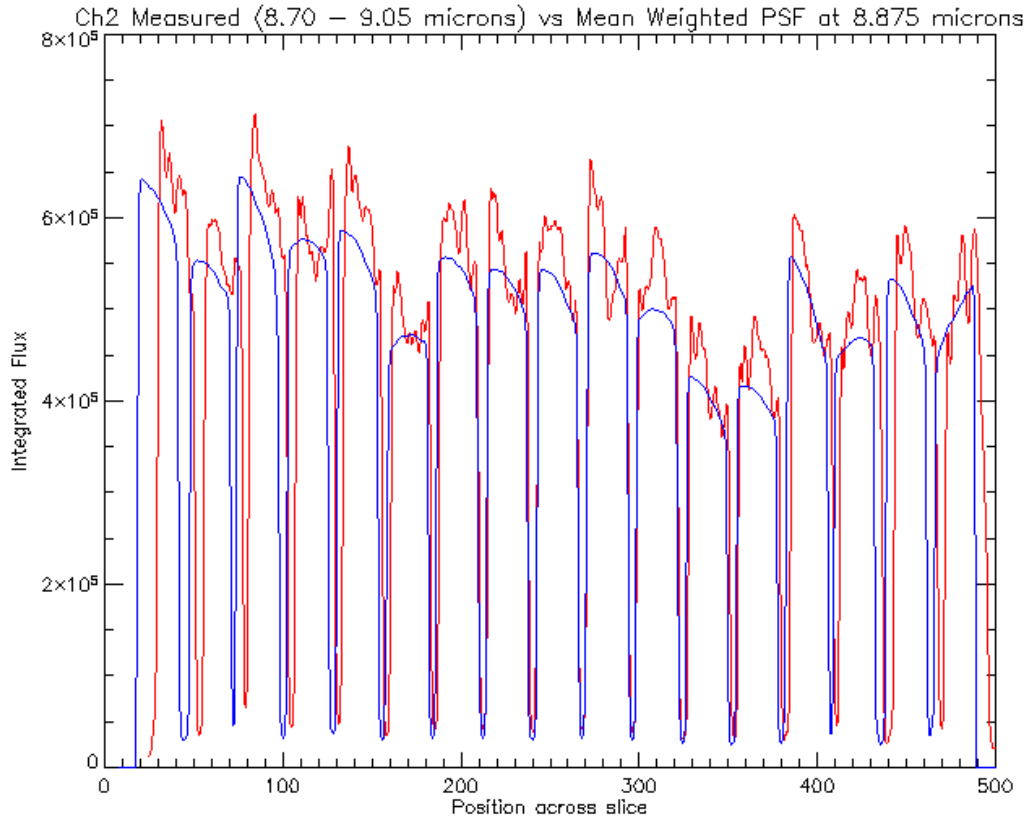

Figure 5.1: The Observed & Theoretical Slice Profiles: Channel 2, Dichroic A (Red = Observed, Blue = Theoretical)

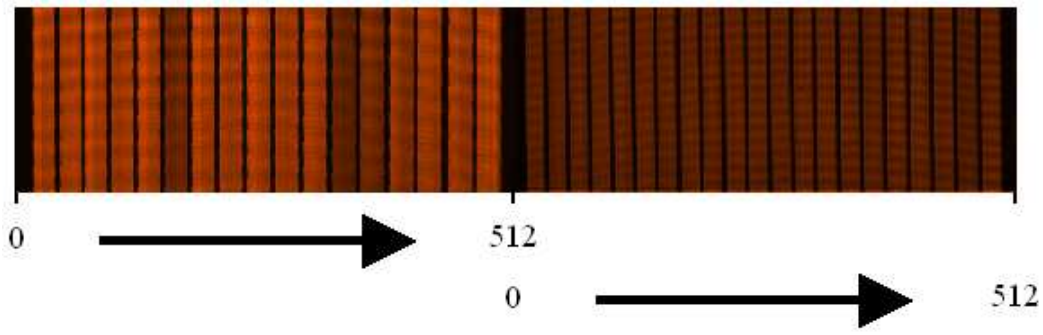

Figure 5.2: The Across Slice Detector Position and Pixel Numbering for Each Channel

Evaluation of the Theoretical Slice Profile

The theoretical slice profiles were constructed from the output slit mask and the observed slice profiles as measured on the detector. This was done using IDL and is outlined in Figure 5.3. Firstly an array of the theoretical profiles was constructed using the spacing measured from the output slit mask. Then to enable a direct comparison with the observed slice profiles measured at the detector the theoretical slice profiles were scaled in (x) to match the extent of the observed slices on the detector.

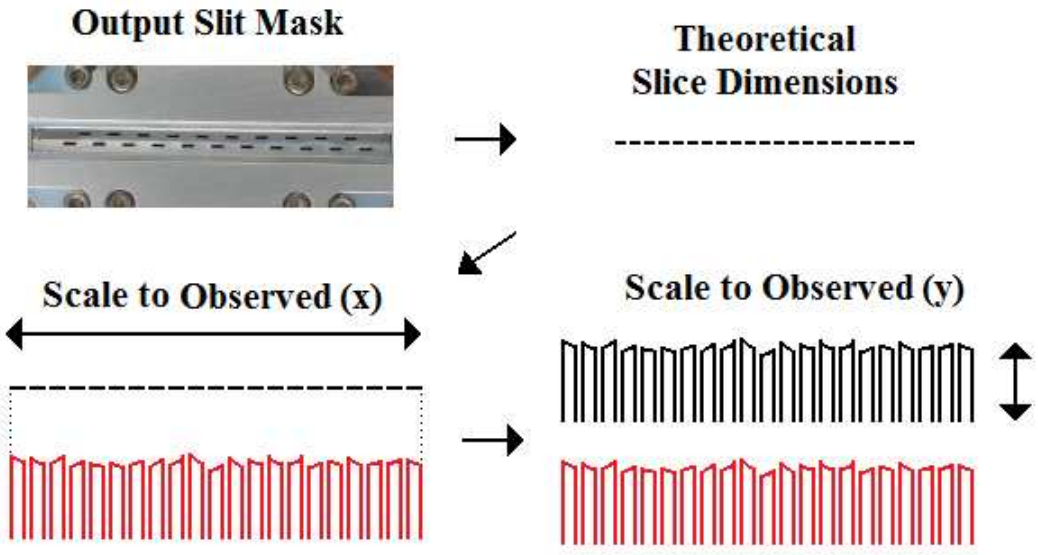

Figure 5.3: The Construction of the Theoretical Slice profiles

Next the the integrated flux (y) of each expected slice profile was scaled to that of the observed slice profiles. This was achieved by matching the flux levels at the boundaries of a theoretical slice to those at the boundaries of the matching observed slice. The flux levels within a theoretical slice were taken as an interpolation between the two edge values. Finally the theoretical slice profile was convolved with the MIRI point spread function (PSF) at the investigated wavelength to mimic the diffraction effect of the instrument. This convolution was done using the MIRI PSF diffraction pattern supplied from the optical model. As such the theoretical slice profiles model the diffraction limited performance of the instrument at the detector. Integrations over small wavelength increments were investigated to more fully match the PSF over the complete wavelength range.

5.2 The Channel 2 Combined Slice Profiles

The observed slice profiles used for the Channel 2 analysis were derived from an integration over the same detector pixels for each sub-spectra. This was to ensure that the beam used for each roughly followed the same paths through the spectrometer. The Channel 2 combined slice profiles are shown in Figures 5.4 to 5.6 where the observed slice profiles are red and the theoretical blue.

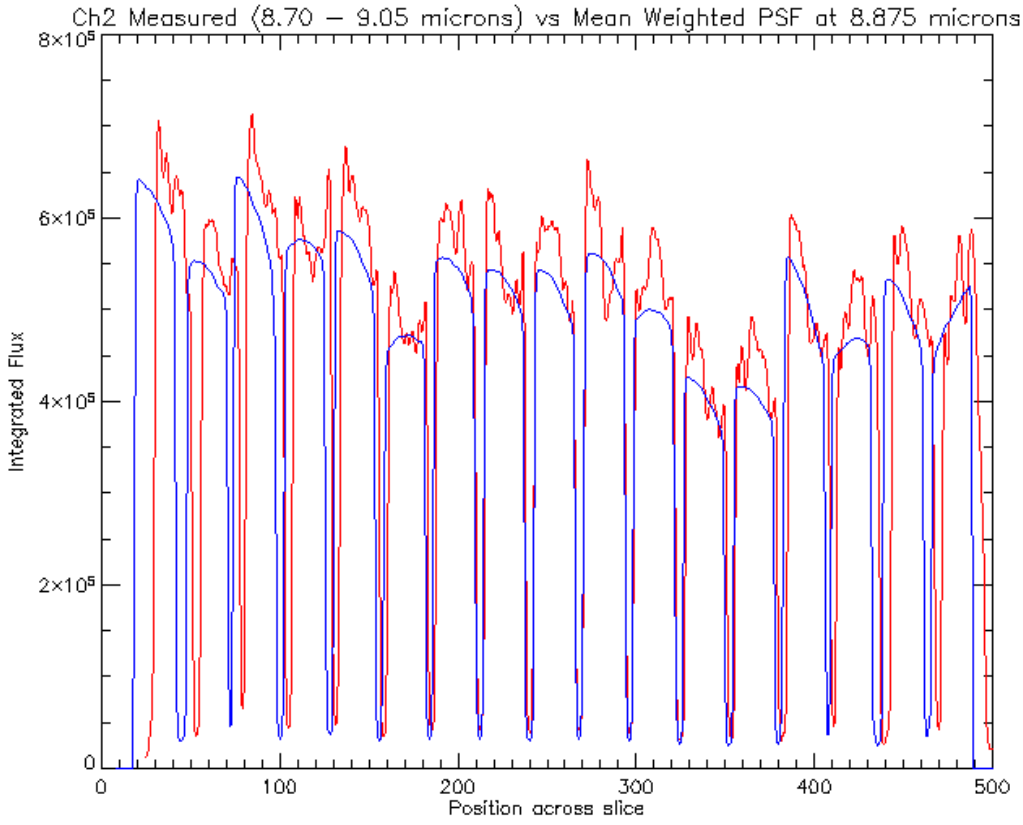

Figure 5.4: The Observed (Red) & Theoretical (Blue) Slice Profile: Channel 2, Dichroic A

The positions of the between slice minima mark the boundaries between two slices. As such a slice length can be approximated as the distance between two adjacent minima. The deviation between the theoretical and the observed slice lengths can be seen in Figure 5.5 for Channel 2 Dichroic B. It can be seen at low x that the positions of the observed minima seem to be squeezed towards the center of the detector from the theoretical positions whereas at high x the opposite is the case. This is a direct measurement of the along slice magnification of the slices by the Spectrometer Main Optics. It shows that the observed slice magnification changes with slice position across the detector. This same trend can also be seen in Channel 2 Dichroics A and C (Figures 5.5 & 5.6).

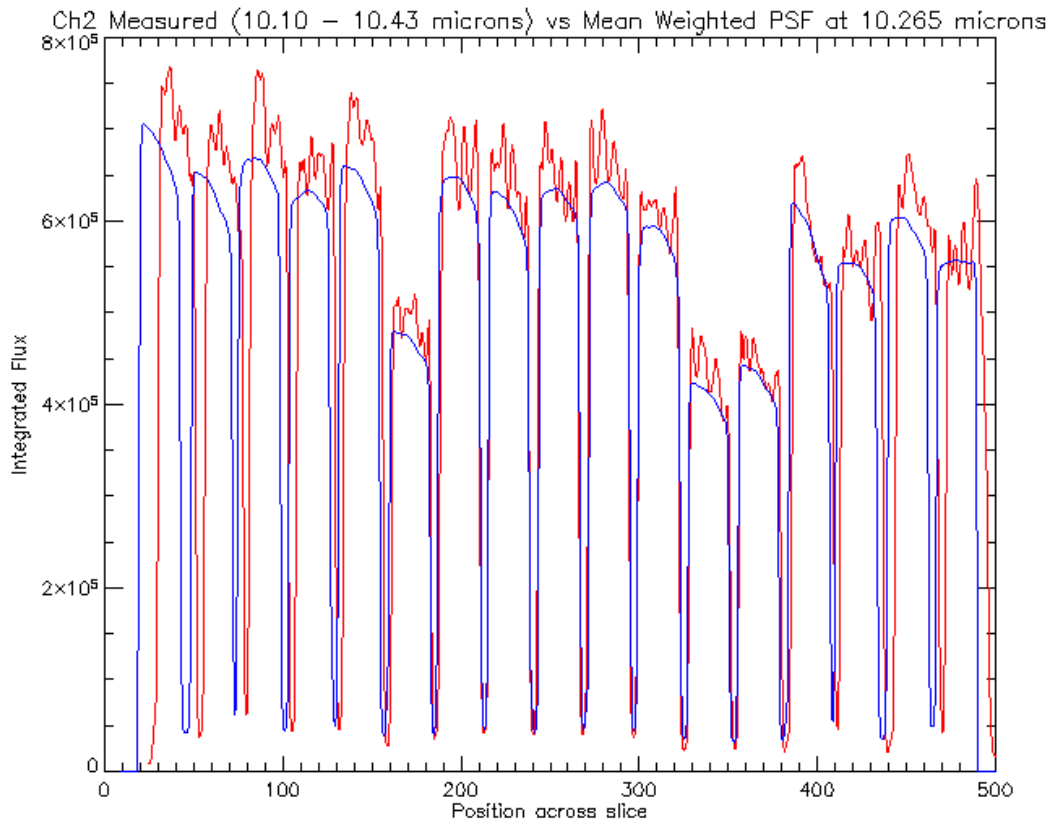

Figure 5.5: The Observed (Red) & Theoretical (Blue) Slice Profile: Channel 2, Dichroic B

The between slice minima flux level of the theoretical slice profiles match closely to those of the observed slice profiles for Channel 2. This is true for all sub-spectra. This shows that the observed between slice flux levels are consistent with those predicted by the theoretical slice profiles which are diffraction limited. It can be concluded that for Channel 2 there is no additional light measured at the detector which may degrade the efficiency of the instrument.

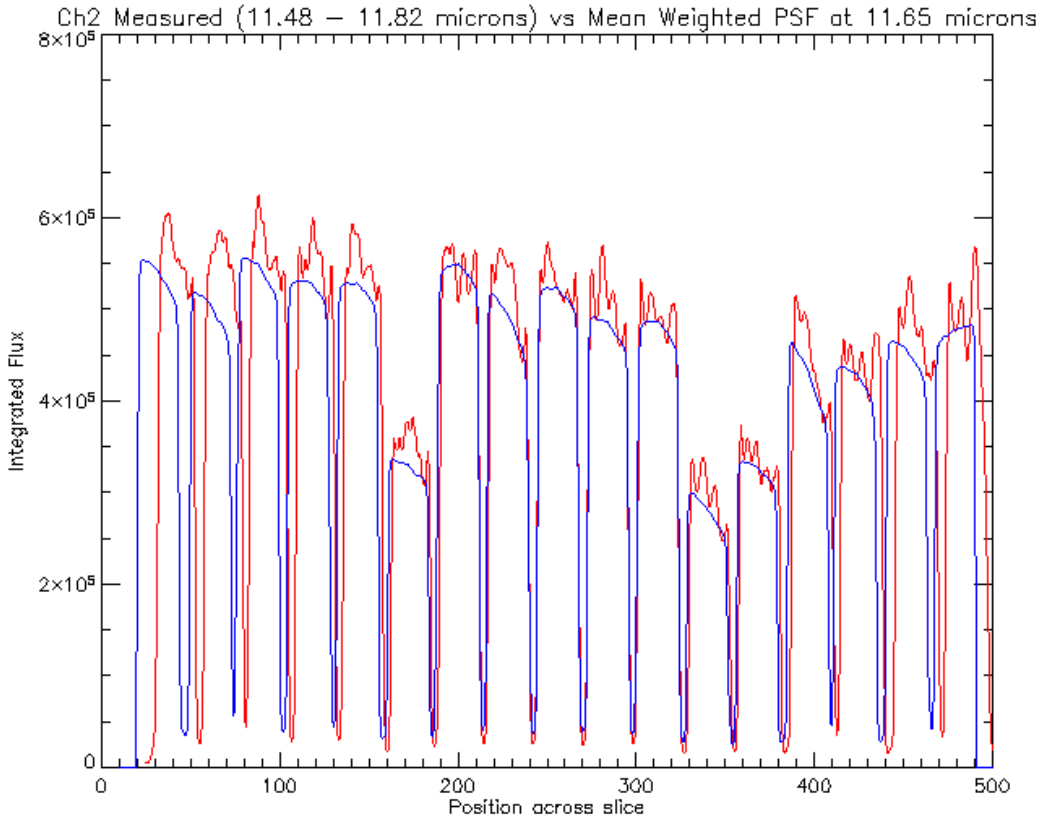

Figure 5.6: The Observed (Red) & Theoretical (Blue) Slice Profile: Channel 2, Dichroic C

5.2.1 The Channel 2 Magnification Gradient

In order to quantify the magnification of the slice lengths across the detector the ratios of the observed to the theoretical slice lengths were calculated from Figures 5.4 to 5.6. The result for Channel 2 Dichroic A can be seen in Figure 5.7. At small x the observed slices are smaller than theoretical and at high x the opposite is the case.

Note the magnification factor is unity at $\sim$ 220 pixels which indicates that there is no slice magnification at the approximate center of the slices on the detector. The error associated with the Channel 2 magnification is originated from the uncertainty in the measurement of the theoretical slice lengths. This uncertainty causes a measurement error in the magnification of $\sim \pm 3\%$ for Channel 2.

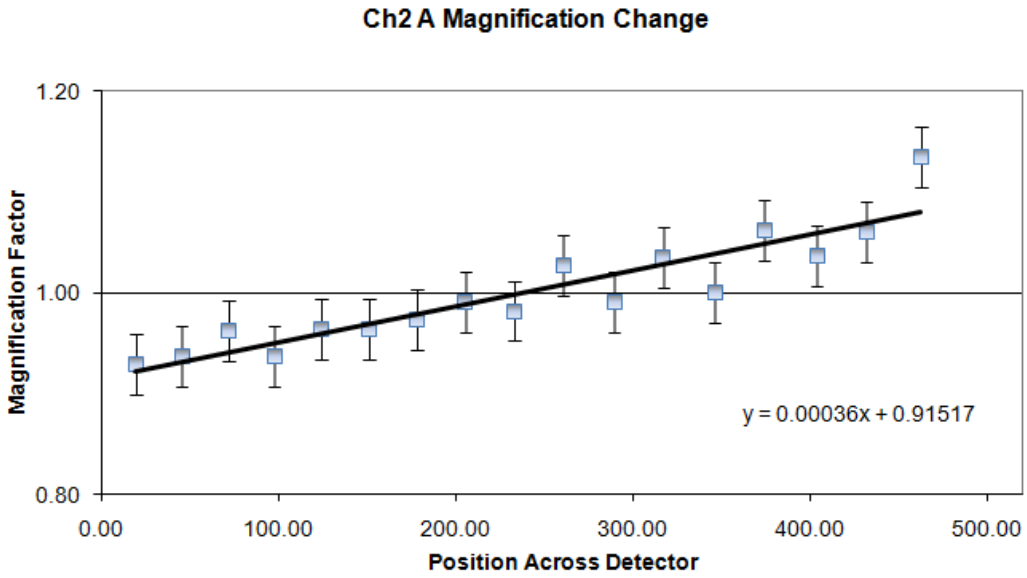

Figure 5.7: The Magnification Gradient for Channel 2 Dichroic A

Figures 5.8 and 5.9 show the slice magnification across the detector for Channel 2 Dichroics B & C. In each case the slice magnification can be approximated by a linear gradient across the detector. The slice magnification gradients measured for Channel 2 were approximately the same for each sub-spectra. This is not unexpected because using the same detector pixels for the investigation of each sub-spectra implies the beam path through the Spectrometer Main Optics will be the same.

The largest change in the gradient of 6% was measured between Dichroics A and C. The measured field of view of these two sub-spectra are the most offset on the sky of any combination of the Channel 2 dichroics (See Figure 4.21). As a result the positions that these sub-spectra present their slice data to the detector are also the most offset of any of Channel 2. This may account for the measured difference in the magnification gradient as the path followed through the Spectrometer Main Optics

will also be the most offset of any of the Channel 2 sub-spectra. This proposal could not be investigated using the optical model.

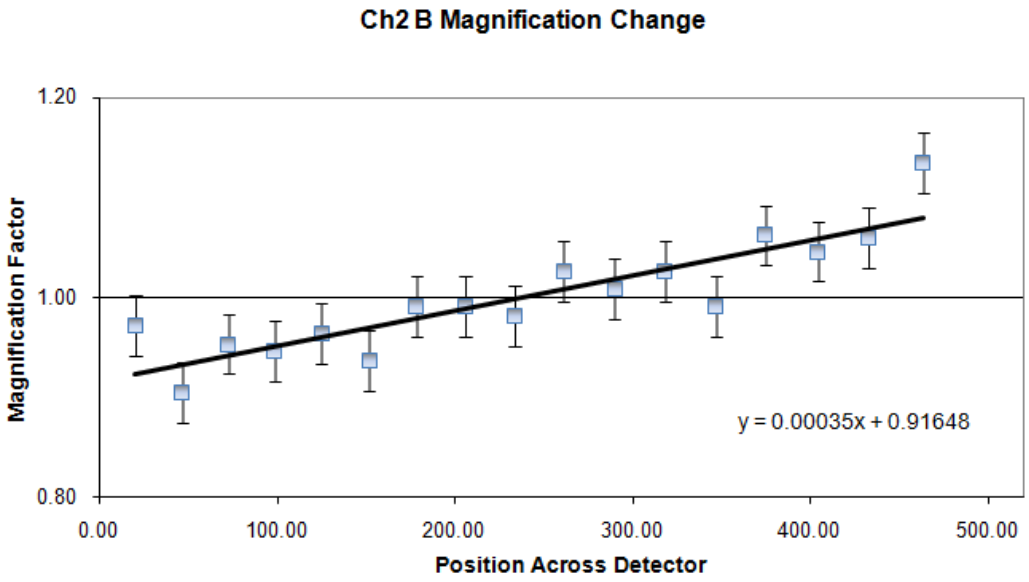

Figure 5.8: The Magnification Gradient for Channel 2 Dichroic B

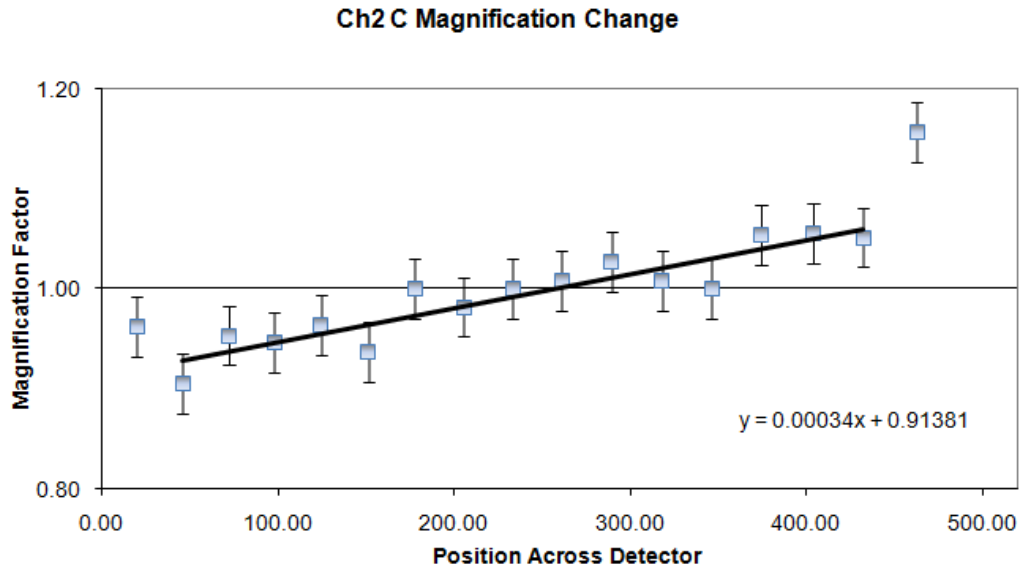

Figure 5.9: The Magnification Gradient for Channel 2 Dichroic C

A slice with a magnification factor that falls above the gradient is longer at the detector than is expected via the linear gradient. The deviations of the individual slice magnifications from those expected by the linear gradient imply that the gradient does not totally model the magnification measured at the detector and as such a higher order consideration may need to be applied.

The Channel 2 along slice extent of ∼29 pixels defines the resolution of this investigation which can not be increased because nothing of the magnification within a slice can be extracted from the slice profiles. In effect each slice depicts the average magnification across 29 pixels.

The magnification plot in Figure 5.10 shows the combined plots of Figure 5.7 to 5.9. A line was drawn between the points for each of the dichroics to more easily distinguish between each data set. It indicates that there are some similarities in the higher order magnification trends of the sub-spectra across the detector. This suggests that the slice magnification deviations from the linear gradient could be an observed measurement of a higher order magnification trend as opposed to being noise in the measurements. The investigation will be carried out in Section 5.6.

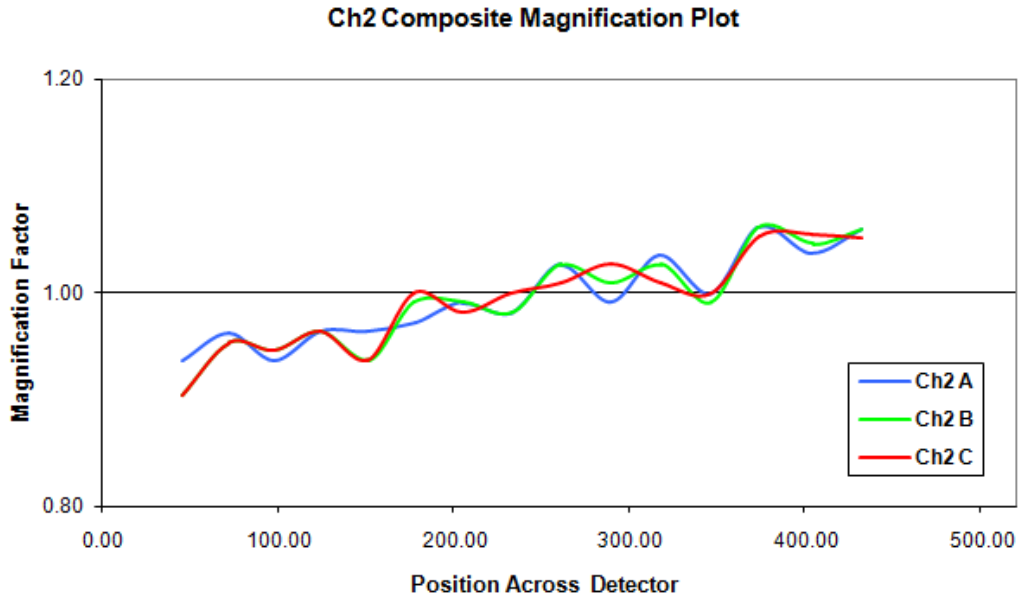

Figure 5.10: The Magnification Gradient for Channel 2, All Dichroics

5.3 The Channel 1 Combined Slice Profiles

The observed slice profiles for the Channel 1 analysis were also derived from an integration over the same detector pixels for each sub-spectra to ensure that the beam used for each roughly followed the same paths through the spectrometer. The combined slice profiles for Channel 1 shown in Figures 5.11 to 5.13 were calculated in the same manner as for Channel 2. The deviation between the positions of the theoretical and the observed minima can be seen in Figure 5.11 for Channel 1 Dichroic A. As for Channel 2 it can be seen at low x that the positions of the observed minima seem to be squeezed towards the center of the detector from the theoretical positions whereas at high x the opposite is the case. This trend is also observed in Channel 1 Dichroics B and C (Figures 5.12 and 5.13). It is worth noting that the rate of divergence between the theoretical and the observed minima seems to be different than for Channel 2.

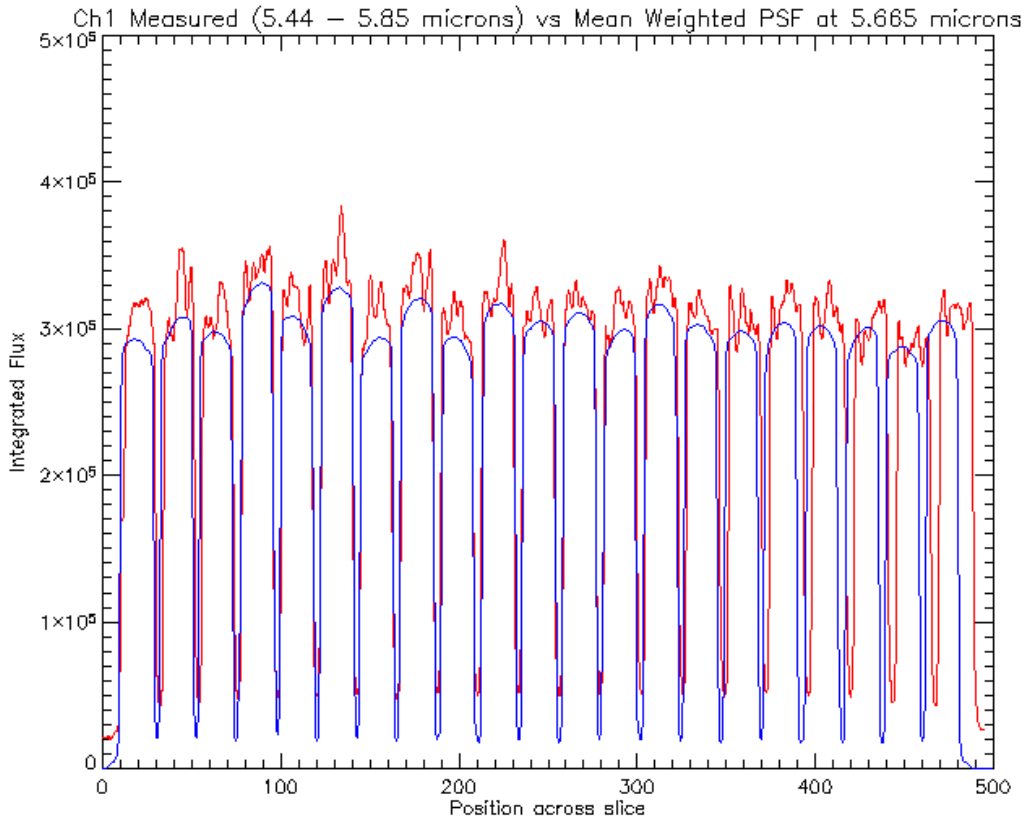

Figure 5.11: The Observed (Red) & Theoretical (Blue) Slice Profile: Channel 1, Dichroic A

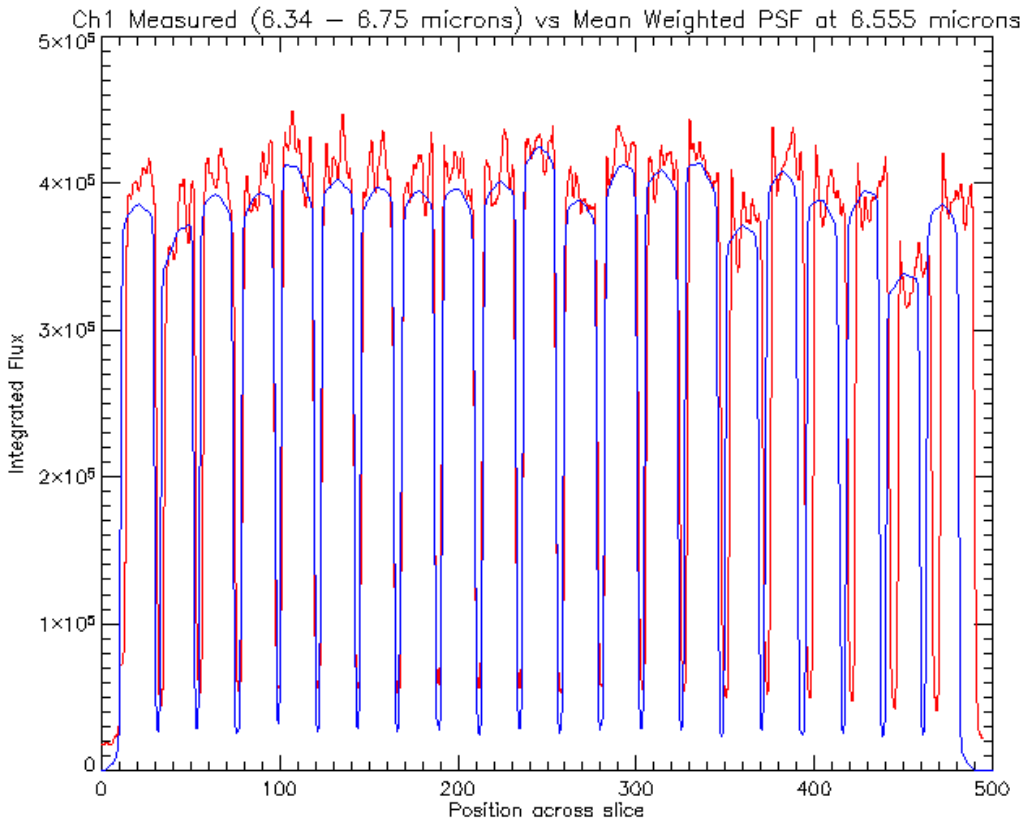

Figure 5.12: The Observed (Red) & Theoretical (Blue) Slice Profile: Channel 1, Dichroic B

The between slice minima flux level of the theoretical slice profiles is substantially less than the flux levels measured from the observed slice profiles for Channel 1. This indicates that there is more flux reaching the inter slice positions at the detector than can be explained by the diffraction limited theoretical model. This inter slice flux excess is greater for the shorter wavelength sub-spectra which may indicate that there is an issue with scattered light in Channel 1. This inter slice flux excess will be investigated in Chapter 6.

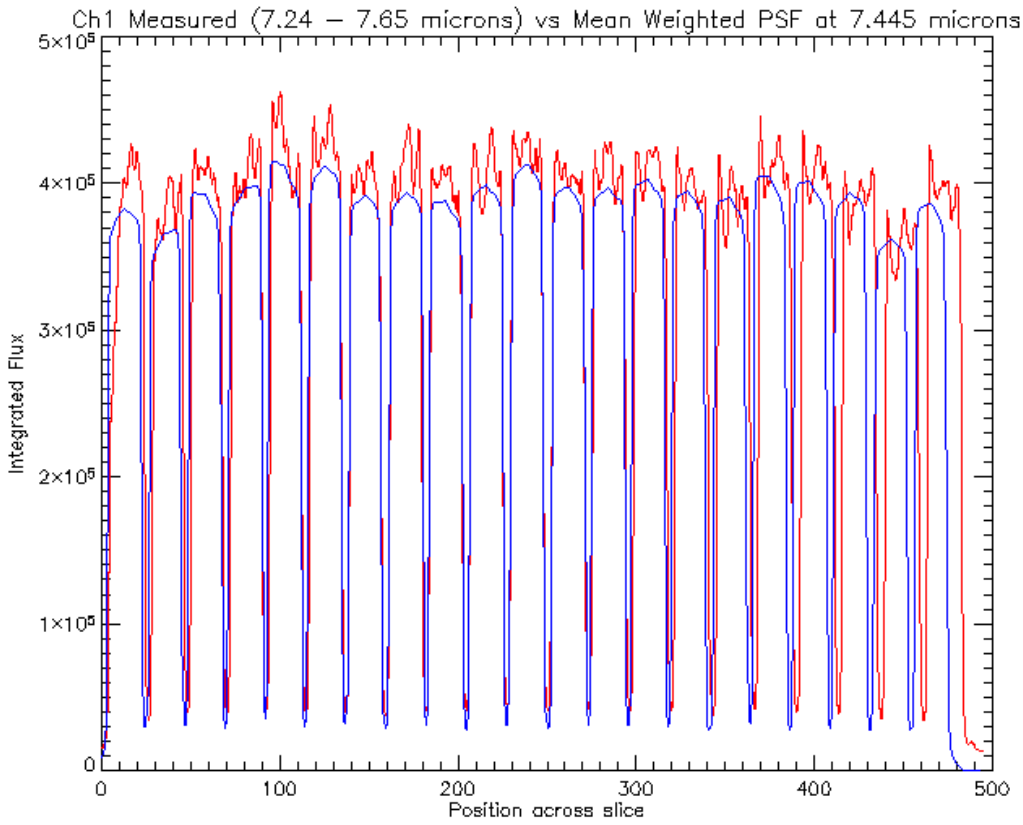

Figure 5.13: The Observed (Red) & Theoretical (Blue) Slice Profile: Channel 1, Dichroic C

5.3.1 The Channel 1 Magnification Gradient

To quantify the magnification the ratios of the observed to the theoretical slice lengths were calculated from Figures 5.11 to 5.13. As with Channel 2 the magnification can be approximated by a positive linear gradient across the detector however the slice magnification is unity at $\sim$ 150 pixels which is a different detector position than for Channel 2. The error associated with the Channel 1 magnification is originated from the uncertainty in the measurement of the theoretical slice lengths. This uncertainty causes a measurement error in the magnification of $\sim \pm 4\%$ for Channel 1.

Figures 5.15 and 5.16 show the slice magnification across the detector for Channel 1 Dichroics B & C. The slice magnification gradient for Channel 1 is approximately a factor of 2 larger than that measured for Channel 2. As they follow different paths

through the Spectrometer Main Optics this is not unexpected. As for Channel 2 the slice magnification gradients measured for Channel 1 were approximately the same for each sub-spectra.

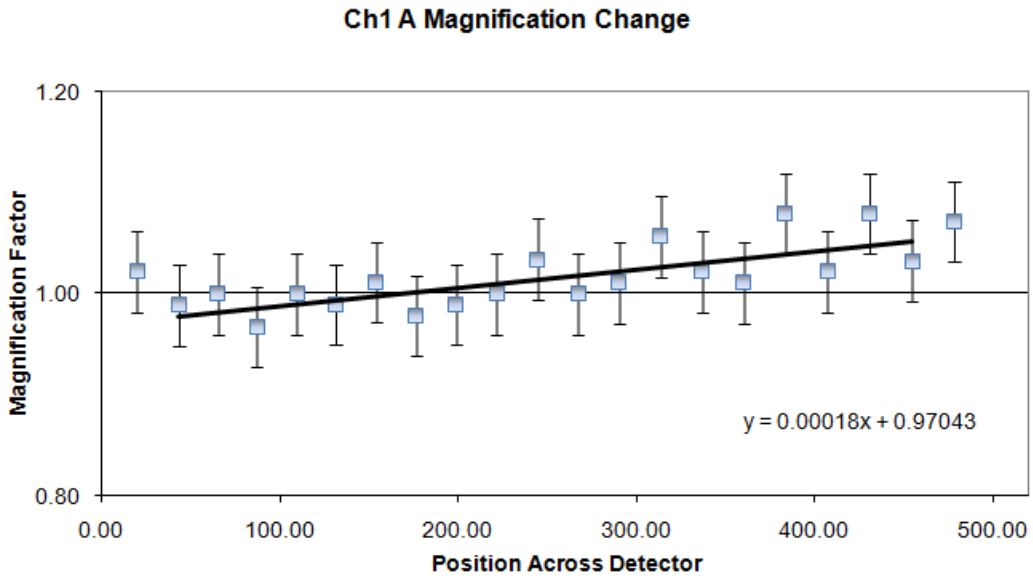

Figure 5.14: The Magnification Gradient for Channel 1 Dichroic A

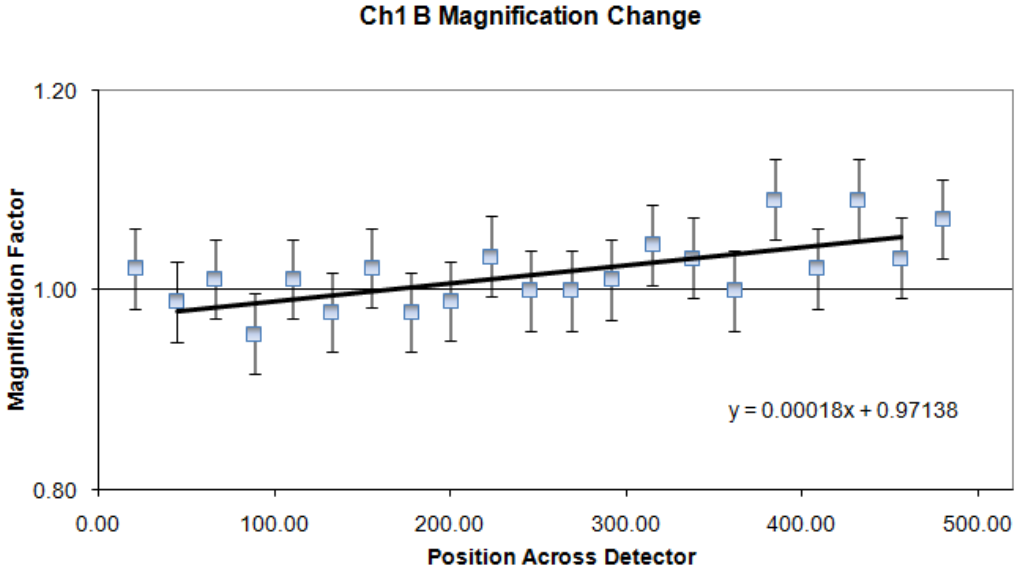

Figure 5.15: The Magnification Gradient for Channel 1 Dichroic B

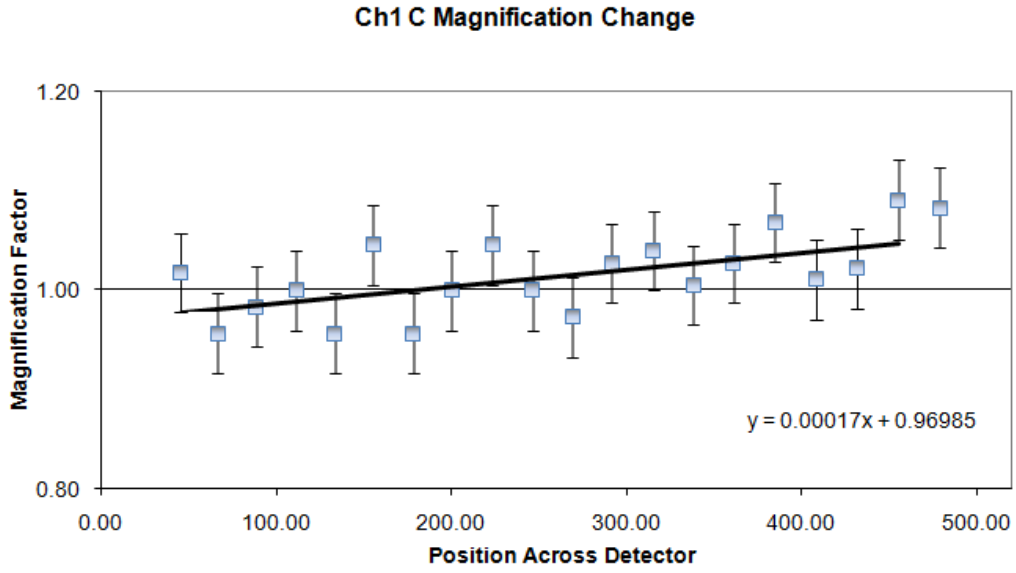

Figure 5.16: The Magnification Gradient for Channel 1 Dichroic C

The largest change in the gradient of 6% was measured between Dichroics A & C. Unfortunately the Channel 1 field of view analysis contained significantly more error than for Channel 2 due to several factors outlined in Section 4.5 which made it impossible to determine whether the measured field of view of these sub-spectra were also the most offset on the sky. This is the same set of dichroics across which the maximum gradient change for Channel 2 was measured. Section 4.9.2 noted that there is a negligible change in the field of view alignment from nominal of a beam transmitted through a misaligned dichroic filter. As such the cause of the maximum deviation between Dichroics A & C for Channel 2 can not also be caused by the Channel 1 dichroic filter and is just coincidental.

The Channel 1 along slice extent is ∼22 pixels. There is a deviation between the individual slice magnifications from those expected by the linear gradient. The deviations from linearity observed in the Channel 1 analysis supply further evidence towards a higher order magnification of the slices across the detector.

The magnification plot in Figure 5.17 shows the combined plots of Figures 5.14 to 5.16. A line was drawn between the points for each of the dichroics to more easily distinguish between each data set. As for Channel 2 there is an indication that there are some similarities in the higher order magnification trends of the sub-spectra across

the detector. This suggests that the slice magnification deviations from the linear gradient could be an observed measurement of a higher order magnification trend as opposed to being noise in the measurements. This will be further investigated in Section 5.6.

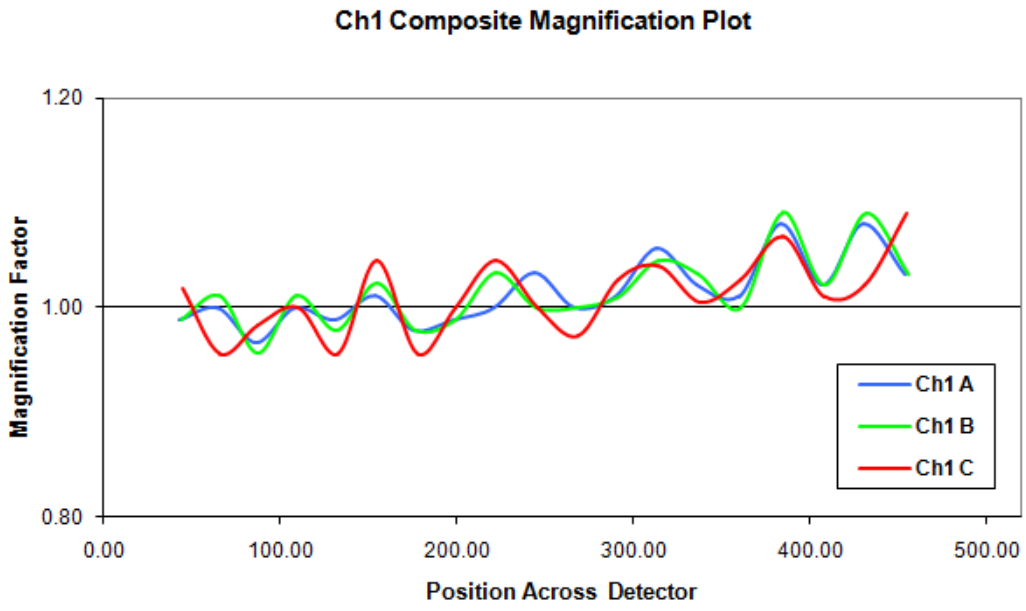

Figure 5.17: The Magnification Gradient for Channel 1, All Dichroics

5.4 Wavelength Investigation of the Linear Magnification Gradient

The previous magnification investigations were done over a constant range of detector pixels (in wavelength) for each channel. As such the beam used for each sub-spectra investigation of a channel followed approximately the same path through the Spectrometer Main Optics. This was done because any slice magnification that was dependant upon detector wavelength position would be constant across the sub-spectra.

To fully understand the operation of the instrument it was necessary to determine if such a variation in the detector wavelength position caused a change in the measured along slice magnifications at the detector. If such a variation was observed it would

imply that the slice magnification is dependant upon the path of the beam through the Spectrometer Main Optics. This ”wavelength dependent” investigation was done with a constant instrument configuration of Channel 1 Dichroic C at three positions chosen to be in the middle and at either end of the wavelength range covered.

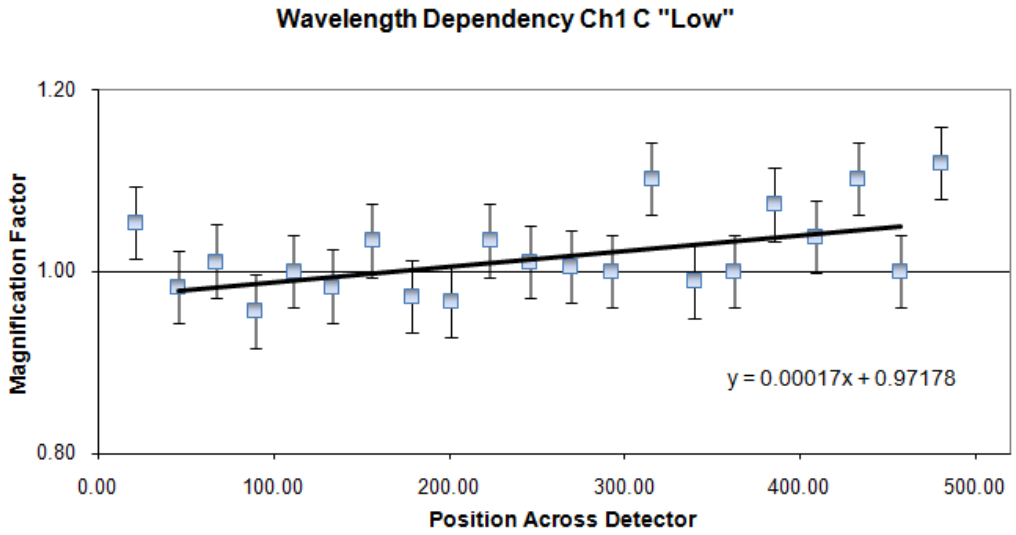

Figure 5.18: The Magnification Gradient for Channel 1 C Short Wavelength

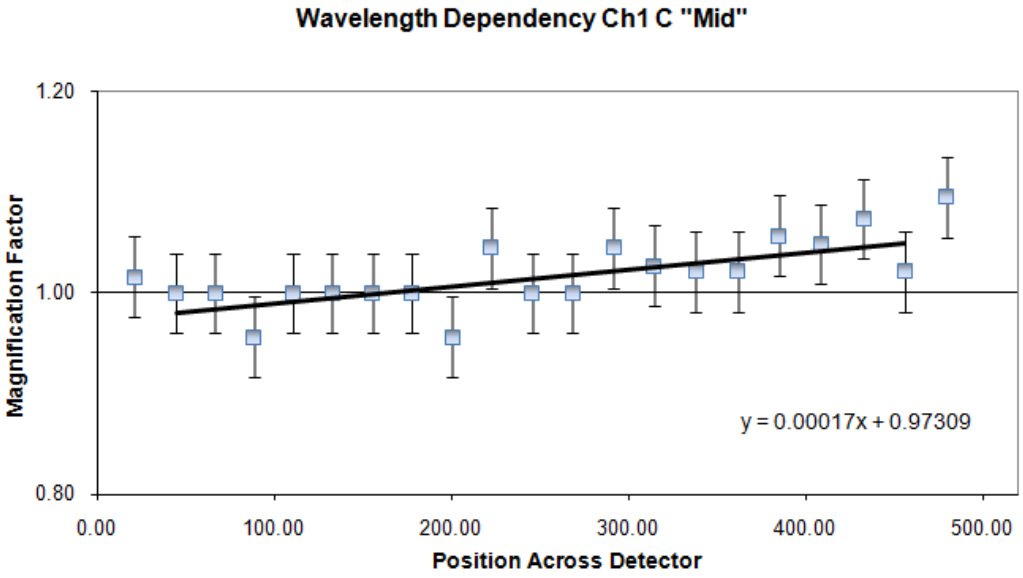

Figure 5.19: The Magnification Gradient for Channel 1 C Medium Wavelength

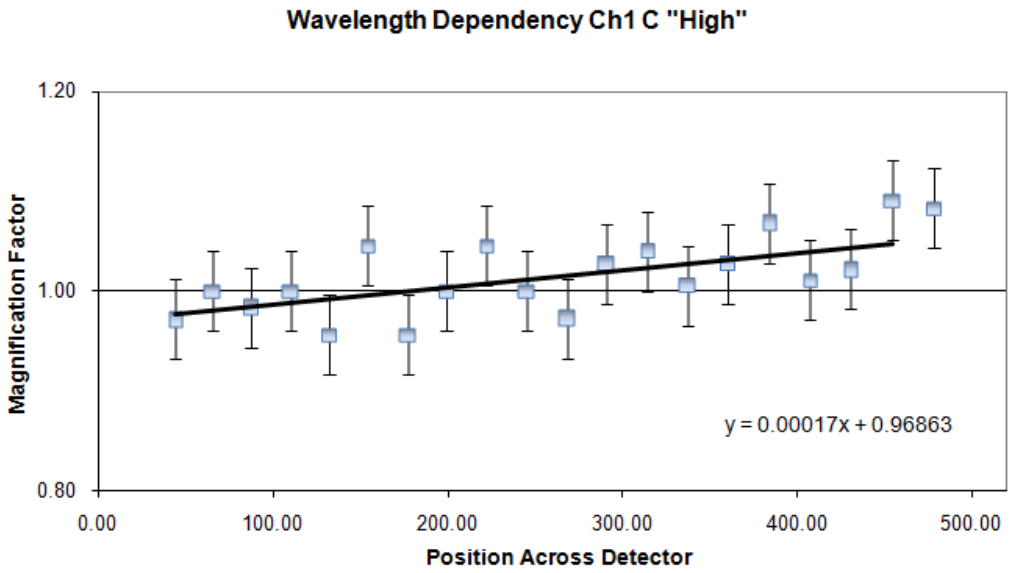

Figure 5.20: The Magnification Gradient for Channel 1 C Long Wavelength

The gradient analysis graphs are shown in Figures 5.18 to 5.20. In each case the gradient remains constant and the intercept changes on a scale of less than 1% (with the Channel 1 measurement error of $\sim \pm 4\%$, Section 5.3.1). This shows a good wavelength stability of the slice magnification across the detector. The magnification gradient of 0.00017 is the same as that measured earlier for the Channel 1 Dichroic C. It is concluded that the magnification gradient of the slices measured across the detector shows a high wavelength stability. This implies that the along slice magnification is not dependant upon the path of the beam through the Spectrometer Main Optics.

5.5 Magnification Gradient Measured from the Optical Model

For each channel it has been shown that there is an along slice magnification of the slices which is measured at the detector that occurs in the Spectrometer Main Optics. This slice magnification has been approximated as a linear gradient across the detector which is constant across the sub-spectra within a channel and in wavelength (as per Sections 5.2, 5.3 & 5.4). There is evidence however that the slice magnification is of

a higher order trend due to similarities in the deviations of slice magnifications from those expected by the linear gradient within each channel (as per Figures 5.10 & 5.17).

It is possible to investigate whether this slice magnification gradient is also present in the optical model. Figure 5.21 shows the optical model slice lengths plotted in V2-V3 angular on-sky coordinates. As well as the on-sky coordinates the optical model defines the corresponding detector pixel. Through sampling the detector at constant wavelength the length of each slice in detector pixels and the corresponding on-sky slice length can be determined. The detector plate scale [arcseconds per pixel] can be used to investigate the relative magnification of the slices.

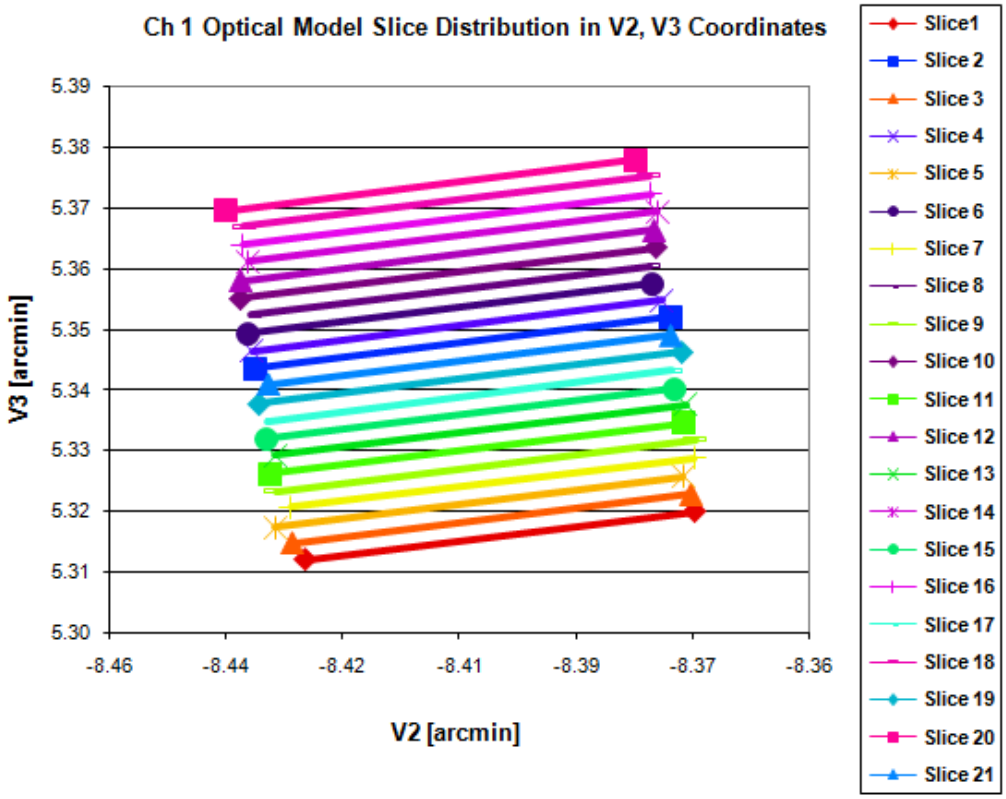

Figure 5.21: The Channel 1 Optical Model Slice Lengths

5.5.1 The Channel 1 Optical Model

The optical model considers only perfect optics. Figure 5.22 shows the slice magnification at the detector expected for Channel 1 by the optical model at 5 microns. The relative slice magnification was calculated from the pixel scales using slice 6 (positioned at the center of the detector) as a baseline for the analysis.

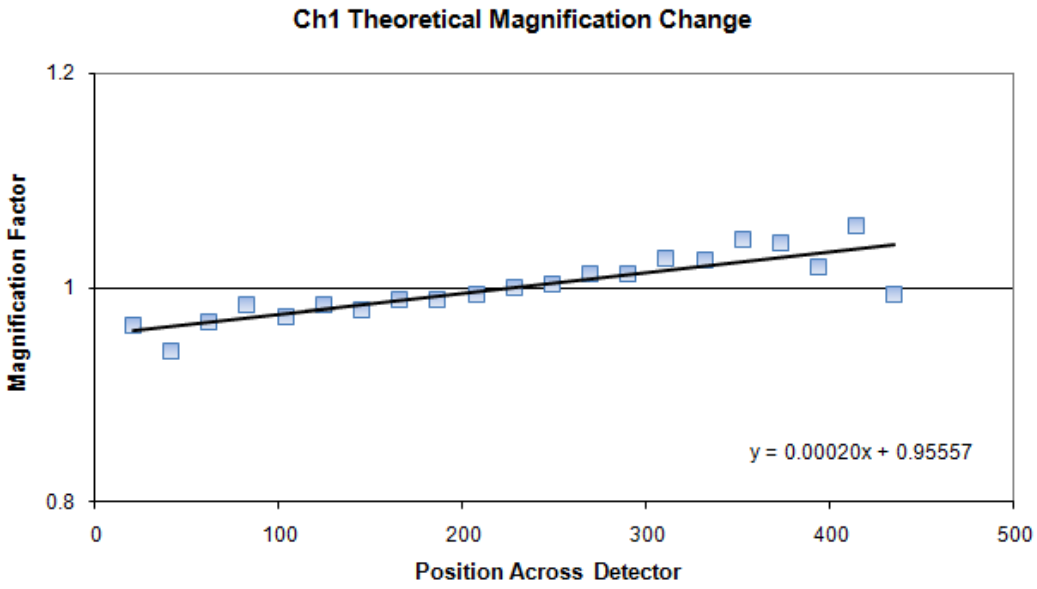

Figure 5.22: The Channel 1 Magnification Gradient from The Optical Model

The most important result is that the optical model does expect the slice magnification. This was not known before the analysis. Furthermore considering perfect optics the optical model shows deviations of the slice magnification from that expected by the linear gradient. This is further evidence that the magnification trend is of a higher order across the detector. This will be considered in Section 5.6.

The optical model magnification gradient can be compared to all of Channel 1 as it has been shown that the gradient within a channel is not wavelength dependent. The gradient expected from the optical model of 0.00020 can be compared with those measured for Channel 1 (0.00018, 0.00018 & 0.00017). It was noted that the errors in the measured magnification of an individual slice were ∼4%. This cannot account for the difference between the optical model magnification gradient and those measured. The

consistently lower measured gradients may imply that the model is not completely accurate or there is an influence on the magnification gradient that the optical model does not understand.

5.5.2 The Channel 2 Optical Model

Figure 5.23 shows the slice magnification at the detector expected for Channel 2 by the optical model at 7.7 microns. The relative slice magnification was calculated from the pixel scales using slice 5 (positioned at the center of the detector) as a baseline for the analysis.

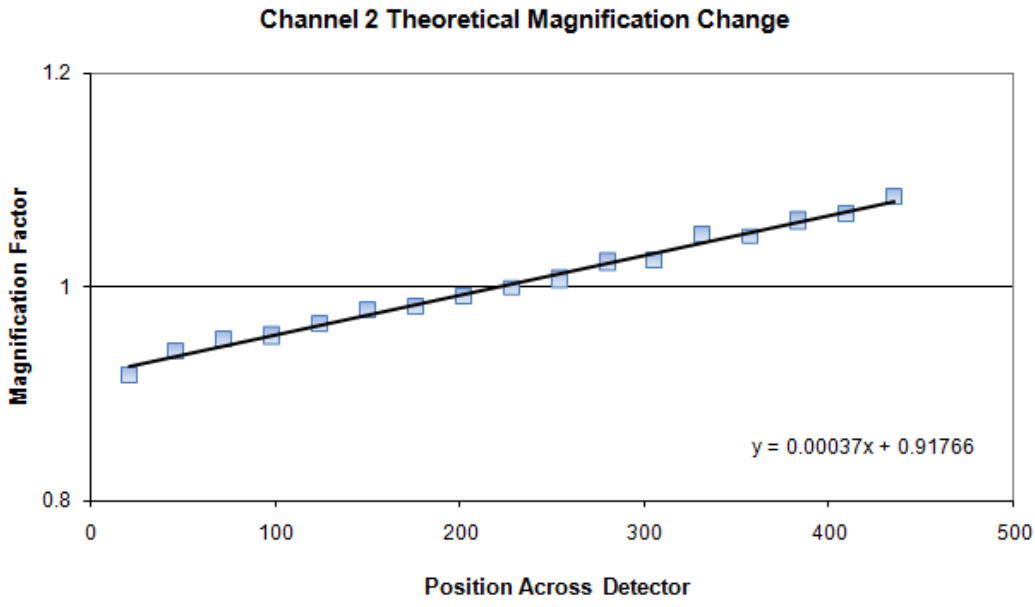

Figure 5.23: The Channel 2 Magnification Gradient from The Optical Model

The Channel 2 optical model implies that the magnification is of a higher order as the slice magnifications show deviations from that expected by the linear gradient however they are not as pronounced as for Channel 1. This higher order magnification will be considered in Section 5.6 along with that of Channel 1.

The optical model magnification gradient can be compared to all of Channel 2 as it has been shown that the gradient within a channel is not wavelength dependent. The

gradient expected from the optical model of 0.00037 can be compared with those measured for Channel 2 (0.00036, 0.00035 & 0.00034). It was noted that the errors in the measured magnification of an individual slice were $\sim$3%. Again this cannot account for the difference between the optical model magnification gradient and those measured. As for Channel 1 the measured gradients are consistently lower which may be further evidence that the model is not completely accurate or there is an influence on the magnification gradient that the optical model does not understand.

Optical Model Conclusions

For both channels is has been shown that the magnification gradients are anticipated by the optical model and the measured gradients are consistent with those expected. The optical model which considers perfect optics also showed that there were expected deviations of the measured slice magnifications from the linear gradient. That the deviations from linearity are present theoretically in perfect optics provides further evidence towards a higher order magnification of the slices across the detector. This magnification will now be considered.

5.6 Slice Deviations from the Linear Magnification Gradient

The deviations of the individual slice magnification from that expected by the liner magnification gradient was seen in Channels 1, 2 & the optical model (Sections 5.2.1, 5.3.1 & 5.5). The appearance of these deviations in the optical model which considers perfect optics is a strong indication that there is a real higher order magnification trend and its measurement is not due to machining errors in the components of Channels 1 & 2.

This higher order magnification can account for the discontinuity of the compact source between slices in the reconstructed images (as per Figure 4.9). Its effect and the procedure necessary to fully spatially calibrate the field of view during image reconstruction will be considered in Section 5.7.

The standard deviation of the individual slice magnifications from the linear gradient in the observations has been measured at ∼7.9% in Channel 1 and ∼7.1% for Channel 2 at a level of 3 sigma. In the optical model the standard deviation of the individual slice magnifications from the linear gradient is ∼4.3% in Channel 1 and ∼1.4% for Channel 2 also at 3 sigma. It is unknown why the slice deviations within the optical model are larger for Channel 1 than for Channel 2 whilst the measured deviations for Channel 1 & 2 are very similar. It is possible that machining errors in the components input additional offsets in the slice magnification. The design of the Spectrometer Pre & Main Optics will now be considered to highlight any areas in which the magnification of the slices could be changed due to machining tolerances.

5.6.1 Magnification Issues with the Spectrometer Pre-Optics

The principal components of an Integral Field Unit (IFU) (as per Section 2.2.2) are the powered image slicer and the re-imaging mirrors. The remaining components are fold mirrors or apertures and excluding diffraction will not change the speed of the beam. The normal and basic diagram of the Integral field Unit is shown in Figure 5.24. The magnification of the field applied by the re-imaging mirror is $\frac{y}{x}$.

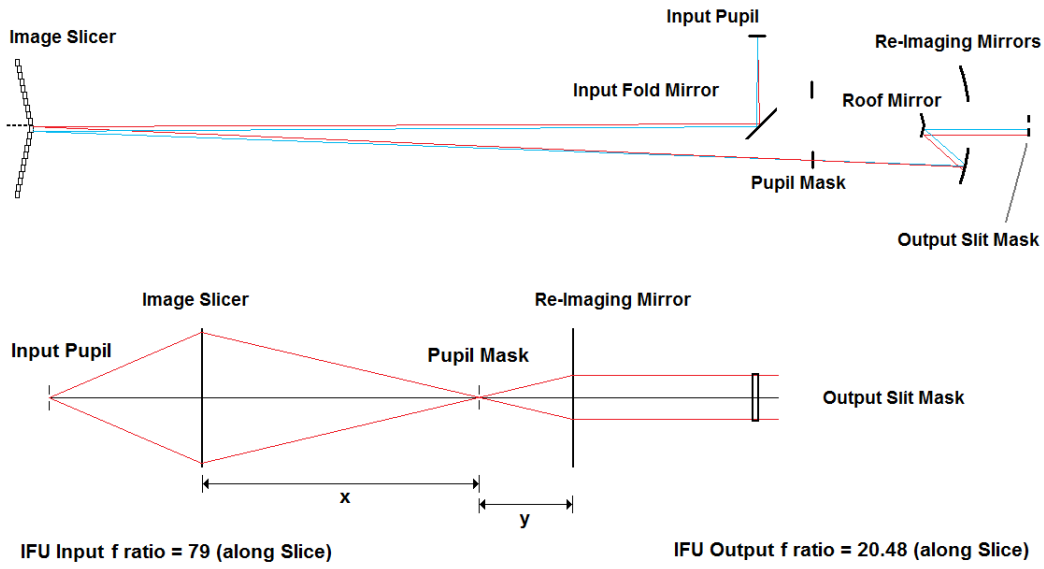

Figure 5.24: The IFU Design and the Nominal Magnification

Machining tolerances in the IFU components will cause deviations in the position of the pupil within the IFU. These deviations can be seen in Figure 5.25 where the beam defines the maximum extent of transmission. It is assumed that the field image delivered by the anamorphic pre-optics is in the correct position at the slicer.

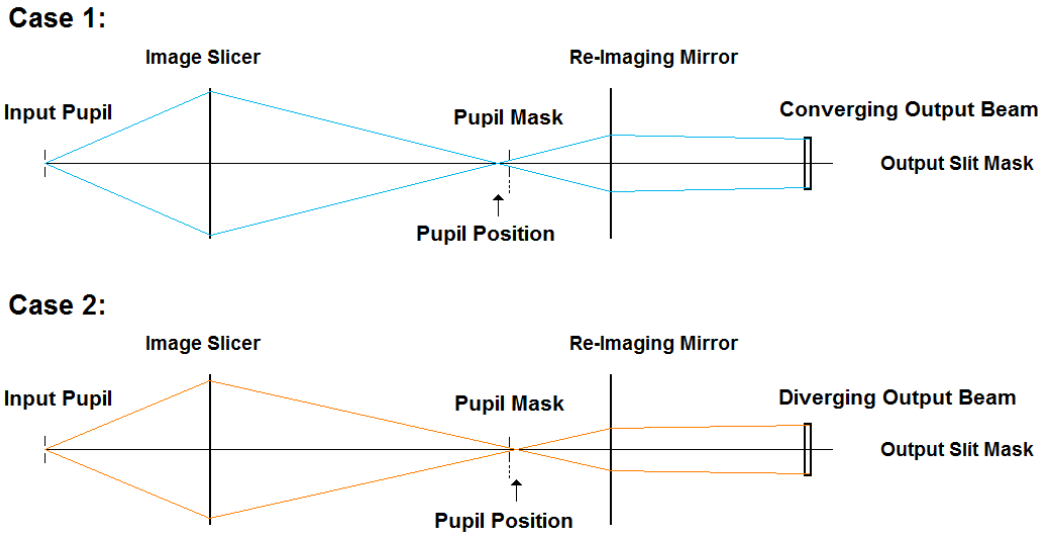

Figure 5.25: The Magnification Change due to Tolerances in the IFU

An incorrect radius of curvature of the slicer will cause a pupil offset from the nominal position whilst an incorrect radius of curvature of the re-imaging mirror will cause an apparent pupil offset from nominal. Either condition will change the plate scale of the slice at the output slit mask.

Case 1 occurs when the radius of curvature of the image slicer or the re-imaging mirror is reduced. The effect is at a maximum when both cases are true. A converging output beam is produced which increases the plate scale at the output slit mask from the nominal case. Effectively the re-imaging mirror is overpowered and increases the along slice extent that is transmitted through the output slit mask.

Conversely Case 2 occurs when the radius of curvature of the image slicer or the re-imaging mirror is increased. Again the effect is at a maximum when both cases are true. In this case a diverging output beam is produced and the plate scale at the output slit mask is reduced. Effectively the re-imaging mirror is underpowered and decreases the along slice extent that is transmitted through the output slit mask.

For Case 1 and Case 2 when the tolerances of the components are at a maximum and the effects are cumulative the change in the along slice field of view is ∼3% from the nominal case however it is also possible that the machining errors in the components cancel each other out.

It has been shown that tolerances in the image slicer and re-imaging mirrors can introduce a change in the plate scale in the along slice direction of the slices at the output slit mask. It should be noted however that any such change from nominal will not cause the measured deviations from the linear magnification gradient seen in Figures 5.10 & 5.17. This is because changing the plate scale of the slice images as the output slit mask does not have any effect on the size of the slices as these are defined by the output slit mask. As such it will not influence the magnification of the slices within the Spectrometer Main Optics. It will however will have an influence on the plate scale of slices in the reconstructed images which will be considered further in Section 5.7.

5.6.2 Magnification Issues with the Spectrometer Main Optics

It has been determined that the along slice magnification measured across the detector occurs in the Spectrometer Main Optics (as per Section 5.1). This slice magnification can be approximated by a linear gradient across the detector which is constant for the sub-spectra within a channel and with wavelength. There are however deviations of the slice magnification from the linear gradient in both the measured data and the optical model for both channels. These can be seen in Figures 5.10, 5.17, 5.22 & 5.23.

In each case the slice magnifications have been calculated from the slice profiles at the detector. These investigations are limited to the resolution of an along slice length which is ∼22 pixels for Channel 1 and ∼29 for Channel 2. It is argued that the slice magnification deviations from the linear gradient are indicative of a higher order magnification of the slices across the detector. Unfortunately there is no additional analysis that can be done with the Verification Model test observations to further this hypothesis because nothing can be deduced about the magnification within a slice. This higher order magnification is however an issue for properly aligning the field of view and will be considered further in the next section.

5.7 Field of View Reconstruction Considering the Magnification Effects

It has been shown that there are two sources of magnification that will change the plate scale of the individual slices in the reconstructed images. That which occurs in the Spectrometer Pre-Optics which may increase or decrease the along slice extent of each slice by up to 3% (as per Section 5.6.1) and that which occurs in the Spectrometer Main Optics and will cause a non-linear magnification of the slices across the detector (as per Section 5.6.2). The reconstructed images show a discontinuity of the compact source between slices (as per Figure 4.9) which is due to the slice magnification. The effect that this magnification has on the reconstructed images will now be considered.

The dominant magnification on the field of view alignment is from the non-linear magnification in the Spectrometer Main Optics. This causes a deviation of the slice lengths from those expected of approximately 8% at a level of 3 sigma for both channels. It is proposed that the non-linear magnification varies across a scale smaller than a slice length. Consider Figure 5.26.

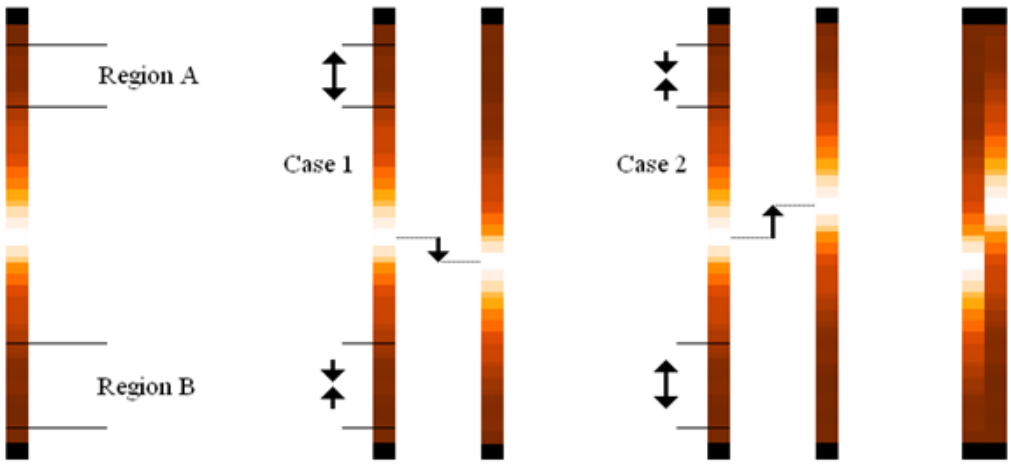

Figure 5.26: The Along Slice Magnification Problem

The left hand image depicts a nominal unmagnified slice as it exits the front of the output slit mask. In Case 1 Region A is positively and Region B negatively magnified. This results in the center of the PSF to be offset from its correct position on the slice.

Now consider Case 2 where the opposite magnification occurs. The center of the PSF will move in the opposite direction. If these two slices were situated next to each other on the field of view then there will be a step in the alignment like that shown in the right hand image and the reconstructed (Figure 4.9).

To quantify this offset consider Channel 1 which extends 22 pixels on the detector. Now assume that 11 pixels at one end of a slice were positively magnified and the 11 pixels at the opposite end were negatively magnified. Considering a magnification of 8% the PSF offset between slices of Channel 1 $\sim$0.29 arcseconds whereas the same analysis for Channel 2 yields an offset of $\sim$0.38 arcseconds. As such a small change in the magnification within a slice can cause a significant spatial offset.

The magnification induced by component tolerances in the Spectrometer Pre-Optics are much less important to the relative slice alignment. In a worst case scenario they change the on-sky length of a slice by approximately 3% however as this magnification is constant within a slice the offsets will be relatively small compared to the non-linear magnification.

Actual Alignment of the Reconstructed Images

The alignment of the reconstructed images is evaluated from the source continuity between slices. In practice some reconstructed images are better aligned than others however it is proposed that this is due to the source being positioned on slices that are magnified in different manners. The resolution at which the slice magnification can be measured with the current data is not sufficient to apply the higher order magnification to the slices. As such the full spatial calibration of the images can not be achieved. In the worst case measured spatial alignment between adjacent slices in a Channel 1 image the PSF was offset by 0.28 arcseconds which is consistent with the 8% slice magnification error outlined previously. Whilst this was the worst alignment observed it is possible that the alignment was worse in positions on the detector where the compact source had not been observed.

Whilst the higher order magnification could not be measured the image reconstruction process was designed to include the linear magnification gradient to the slice resampling. This was achieved by re-magnifying each pixel along a slice by incremental amounts determined by the gradient. The linear magnification slice reduction did not

have a noticeable effect on the relative slice alignment due to the small magnification changes which were applied across each slice.

It is expected that being able to resample a slice using the higher order magnification that varies within the slice would greatly increase the alignment of the images. Unfortunately there was insufficient data to carry this out because the magnification was an unexpected feature of the reconstructed images. It is my belief that the full spatial calibration of the Flight Model images is of a high priority. As such I will outline a new test procedure to enable complete calibration of the magnification which is to be submitted to the test team for implementation in the testing of the Flight Model.

5.8 Along Slice Magnification Characterisation for The Flight Model

The Verification Model test campaign did not provide suitable measurements to analyse the non-linear magnification within each slice. The result is that there was substantial error in the spatial alignment of the reconstructed images. For the Flight Model this magnification must be measured to create astronomical images that are fully spatially aligned across the entire field of view. As such a new test procedure must be defined which will enable the measurement of the variation in the magnification within each slice.

The New Flight Model Test Procedure

It is expected that the MIRI Telescope Simulator will be fully functional for the testing of the Flight Model enabling the delivery of a point source to the Medium Resolution Spectrometer. The measurement of the magnification within each slice is possible by incrementally scanning the point source along a slice and comparing with the movement of the source in the reconstructed image. This procedure must be done for each slice. The length of the magnification investigation is dependant upon the number of observations to be taken in the along slice direction and the length of an observation to achieve sufficient signal to noise. As the investigation is potentially time intensive steps can be taken to increase the efficiency of the procedure.

Between Slice Point Source Scanning

By scanning the point source along the position between two slices it is possible to simultaneously investigate the relative movement in the along slice direction of two slices. If the magnitude of the movement of the point source in the along slice direction differs from that of its neighbor (between the same two observations) then the relative size of the movements is a direct measurement of the change in the magnification between the slices. The issue with scanning the point source along the between slice position is that the position of the slices must be well known to enable the MIRI Telescope Simulator to accurately increment movement in the along slice direction. Any error in the movement of the point source in a vector that is not along the slice boundary could remove the point source from one or both of the slices to be investigated.

Resolution of the Along Slice Investigation

The investigation in the along slice direction should be of sufficient resolution to fully characterise the non-linear magnification. However as an increase in the resolution will increase the number of observations required for the investigation a balance must be achieved. The most economic method is to use the central position of the point source and also its profile in the along slice direction. The point source can be properly characterised without any magnification using the MIRI Imager. Any deviations of the point source profile in the along slice direction from the profile measured on the MIRI Imager indicates a magnification effect. With the observation time large enough to ensure the FWHM of the PSF is easily measurable it will be possible to fully characterise a complete slice in 21 observations for Channel 1 and 17 for Channel 2.

The Problems of the Spatial Alignment for Observing

If the field of view spatial alignment is not achieved to a sufficient level then the exact positions and extents of observed features can not be determined from any future extended targets observed with the Medium Resolution Spectrometer. In the worst case the offset measured was 0.28 arcseconds. Whilst this is the maximum positional error that was measured between two slices from the Verification Model data it is

possible that the maximum possible error is larger than this. To consider what impact this misalignment would have on scientific observations we shall consider Figure 5.27 which depicts a typical spiral galaxy of approximate diameter 3.5 arcseconds. This corresponds to the approximate size that a spiral galaxy would subtend at a redshift z = 1 and also to some of the larger galactic structures observed in the Hubble Ultra Deep Field alluded to in Section 1.1.1.

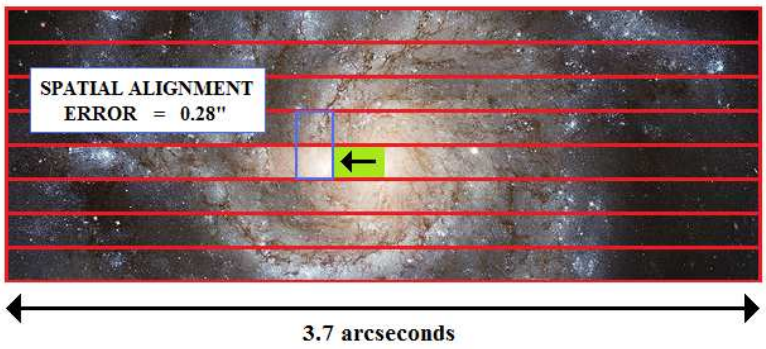

Figure 5.27: The Along Slice Magnification Impact on Scientific Observations

An average spiral galaxy of diameter 50kpc subtends approximately 3 arcseconds at z = 1 hence the field of view alignment error of 0.28 arcseconds corresponds to $\sim$5 kpc. This would cause a large problem for mapping the distribution of materials in nearby spiral galaxies. It can be seen in Figure 5.27 that the 0.28 arcseconds spatial offset applied to the galactic core will spatially offset the core of the galaxy to a position on one of the spiral arms. The resultant spectral analysis of the field image could show for example the broad line region of a Seyfert 1 galaxy normally measured at the galactic core situated within a spiral arm containing shocked gas and star forming regions. Such a field of view alignment error would include uncertainty in the positional knowledge of any extended source observations. As such the calibration procedure must be carried out during the Flight Model test campaign as the procedure could be best done in laboratory conditions.

The Preferred Test Procedure

A balance must be struck between properly characterising the magnification for complete spatial calibration and the time required to complete the test procedure. The

time is a big consideration because it will cost approximately £10000 per day to keep the Flight Model at flight conditions and the project does not have an unlimited test budget. It is my belief that this investigation will command a high priority because it is a very important feature to understand to enable accurate image construction and one which would be more difficult to characterise when the James Webb Space Telescope is on orbit. Performing the calibration observation on-orbit would also reduce the amount of scientific observations possible over the lifetime of the instrument.

The test procedure requires a scan of the point source along each slice of the image slicer for each channel. It was decided that this scan would be done at the between slice position to investigate two slices simultaneously. Table 5.1 shows the required number of scans for the complete magnification analysis of each channel.

	Between Slice Scans	Observations per Scan	Total Observations
Channel 1	11	21	231
Channel 2	9	17	153
Channel 3	8	16	128
Channel 4	6	12	72

Table 5.1: Observations Required to Calibrate a Single Dichroic Field of View

At each scan position the point source must be well positioned at the center of the between slice position where an observation must be taken. The observation must be of sufficient time to make the FWHM of the point source readily measurable so that the along slice profile of the source can be accurately measured.

In total Channel 1 requires 693 observations to obtain complete coverage at all the slice positions for all dichroic observations. Additional time will be required for movement of the MIRI Telescope Simulator point source between observations. This procedure must be done for each Channel which increases the number of observations to 1752.

The required time for the test procedure can be approximated from the expected reduction in observation time due to a more concentrated point source being incident on the Medium Resolution Spectrometer. The extent of the incident point source will approximately a factor of 30 - 40 smaller than the compact source incident during the Verification Model test campaign.

To achieve the signal to noise of the Verification Model observations which required an integration of 20 minutes the Flight Model observation time will be approximately 35 seconds (derived by considering the expected reduction in the size of the delivered compact source). A downtime of 30 seconds between observations is deemed adequate for movement of the MIRI Telescope Simulator point source and to prepare the detector for another observation. Changing dichroics in the Medium Resolution Spectrometer takes approximately 1.5 minutes hence each dichroic will be fully investigated before moving onto the next. It is assumed the same length of observation will be required for each channel. In total this test procedure requires a time of $\sim$32 hours for completion.

5.9 Conclusions of the Slice Magnification Analysis

The magnification of the slices on the detector has been investigated for both Channels 1 & 2. The magnification was dependant upon the position of the slice across the detector and could be approximated by a linear gradient. This magnification gradient for Channel 2 (Figure 5.7) was measured to be approximately twice that for Channel 1 (Figure 5.14) however as each channel follows different paths through the Spectrometer Main Optics it is not expected that the magnification gradient should be similar between channels. The magnification gradient of sub-spectra within a channel was approximately constant. By comparing each of the sub-spectra within a channel it was observed that there were similarities in the measured deviations of the slice lengths from those expected by the linear gradient (Figures 5.10 & 5.17). This implies that the deviations from the gradient are a real feature and not due to tolerances in the components of the spectrometer. As such the magnification may be better modelled by a higher order trend.

A wavelength investigation of the linear gradient was done for Channel 1C by measuring the gradient at three wavelength positions (Low, Medium & High). In each case the magnification was measured to have the same gradient. This showed a good wavelength stability of the slices within a sub-spectra concluding that the data collected from any position on the detector will return the same linear gradient measurement.

Whilst it was not known that there would be a magnification of the slices in the Spectrometer Main Optics a subsequent investigation of the optical model showed that in both the case of Channel 1 & 2 the magnification was present. Furthermore the optical model data also showed deviations of the slice lengths from the linear gradient. This is further proof that the linear magnification gradient does not entirely describe the magnification of the slices across the detector. It is expected that Channels 3 & 4 will also have a magnification of the slices across the detector as their design is synonymous with that of Channels 1 & 2.

As the slice magnification was unexpected at the time of the Verification Model test campaign the Verification Model data does not contain sufficient information to investigate the magnification of the slices on a sub-slice scale. However the effect of a variable magnification acting across the detector has been shown to be the probable cause of the discontinuities of the compact source between slices in the reconstructed images (Figure 5.26) providing further evidence that the variable magnification is a real feature.

The effect of the magnification on the reconstructed images results in errors in the spatial alignment between slices. This has been quantified in Section 5.8 at Figure 5.27 where the measured worst case offset between slices is 0.28 arcseconds. I devised a calibration procedure such that the error can be removed from the reconstructed images in order to enable the Medium Resolution Spectrometer to fulfill its potential. Whilst this calibration procedure is time intensive it must be done during the Flight Model test campaign at the Rutherford Appleton Laboratories to enable the full spatial calibration of the Flight Model observations.

Further Investigation Required

Chapter 6 outlines the measurement of additional light at the Verification Model detector. This additional light includes that observed in Figures 5.11 to 5.13 of this chapter and also that of Chapter 5 which was observed near the Channel 1 point spread function in Figure 4.10. In considering each case separately Chapter 6 outlines a systematic analysis of the Medium Resolution Spectrometer to investigate the origin of the additional light. The resultant reduction in the signal to noise of the instrument due to the additional light is also calculated and compared to the requirement.

CHAPTER 6

Additional Light at the Detector

Channels 1 & 2 were operational in the Verification Model as any problems with the design of the instrument that caused scattered light at the detector would be largest because of the lower operational wavelengths. There are three cases where there was additional light detected in the observations. An investigation of the background level at the detector with the contamination control cover closed showed that there were no light leaks in the instrument. It was therefore concluded that the origin of the additional light was not due to an external source. The additional light was separated into 3 classifications. Type I refers to the case where additional light was measured at the Channel 1 inter slice positions on the detector. Illustrated in Figure 6.1 it shows that the level of excess light was measured to be approximately constant at the inter slice positions across the entire detector. Type II refers to the case where there is a ghost image close to the compact source in the Channel 1 reconstructed images as illustrated in Figure 6.2. The direction of the ghost from the compact source was approximately constant though the intensity of the ghost increased with decreasing wavelength sub-spectra. Type III refers to the case where there was a higher diffuse background measured in the Channel 1 reconstructed field of view as illustrated in Figure 6.3. This chapter will deal with the origin of the excess light and the impact it will have on the performance of the instrument.

The MIRI Telescope Simulator issues which caused the diffuse compact source outlined in Section 3.3 will induce the largest error into the analysis of the Type II ghost. Types I and III represent scattered light at the detector which is less dependant upon the defocus of the beam produced by the simulator.

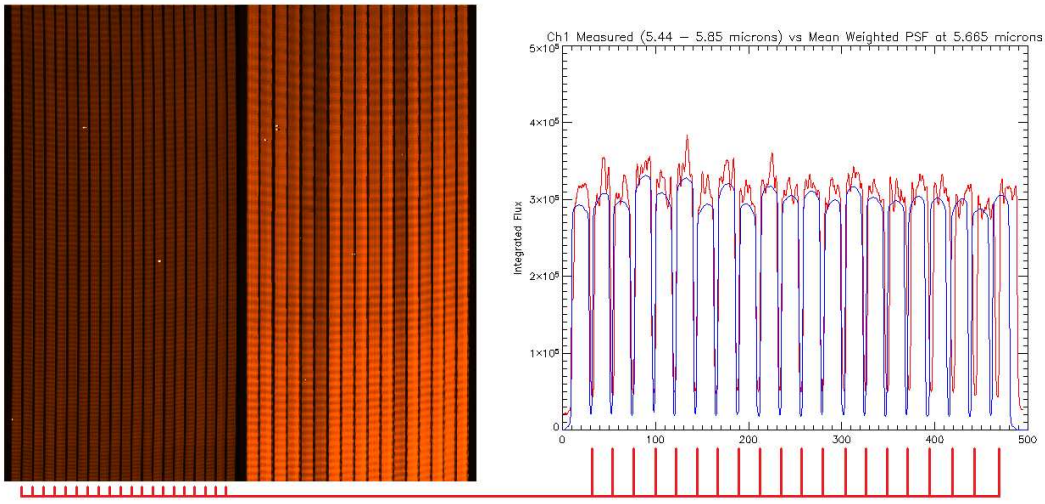

Figure 6.1: Type I: Channel 1 Inter Slice Flux Excess

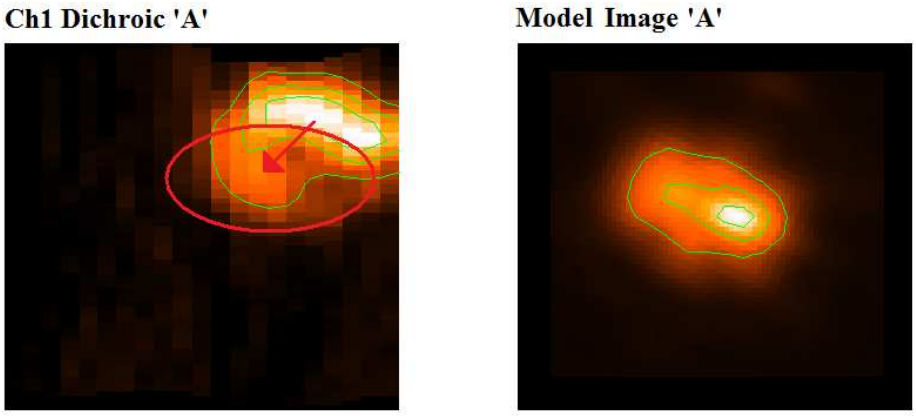

Figure 6.2: Type II: Ghost Near the Channel 1 PSF

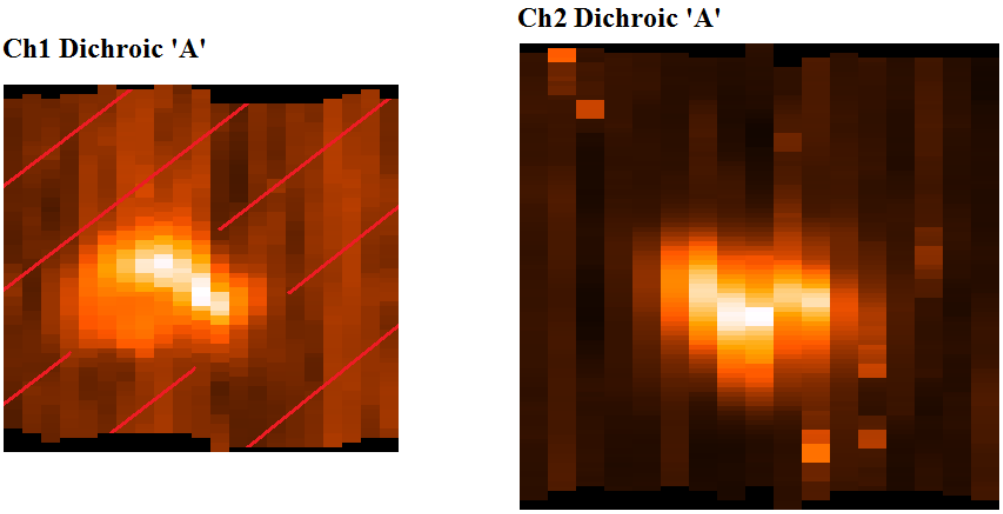

Figure 6.3: Type III: General Background Increase in the Channel 1 Field of View

6.1 Type I: The Channel 1 Inter Slice Flux Excess

The Channel 1 slice profiles on the detector were described in Section 5.3. In each case the observed flux measurements were compared with theoretical expectations where the theoretical inter slice minimum describes the flux level that the diffraction limited PSF will reach at the between slice position on the detector. Any excess between the observed inter slice flux level and the theoretical model indicates additional flux from another source. This additional flux would reduce the signal to noise of the observations hence degrading the performance of the instrument. The origin of this between slice flux excess will be investigated in this section.

The Channel 1 observations showed a flux excess between the observed inter slice flux level and the theoretical level. This flux excess is shown in Figure 6.4 which is a montage of the lowest flux levels of the slice profile images shown in Figures 5.11 to 5.13. The red profiles indicate the observed measurements and the blue indicate the diffraction limited theoretical model. It can be seen that the flux excess for Channel 1A is larger than for 1C, with 1B being at an intermediate stage.

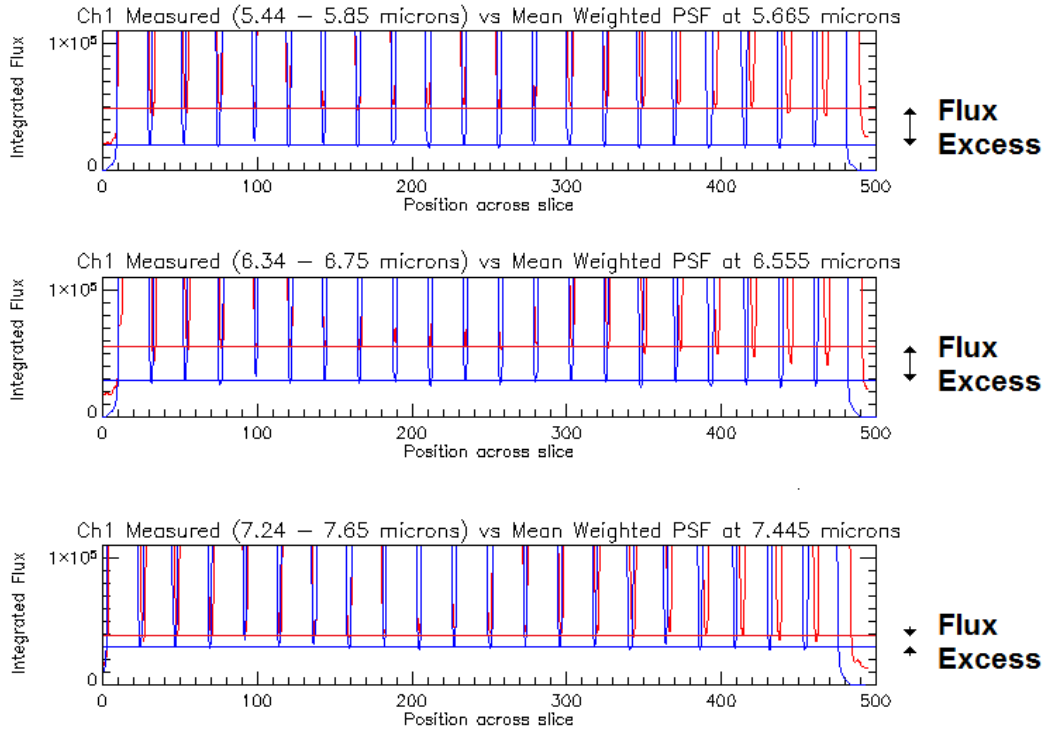

Figure 6.4: The Inter Slice Flux Excess for Channel 1 A, B & C (Red = Observed, Blue = Theoretical)

In a diffraction limited situation the measured inter slice flux level will decrease when moving from a longer to a shorter wavelength observation because the FWHM of the PSF is smaller and as such the flux level requires a smaller distance to reduce to the same level as that of the longer wavelength case. As the gap size is constant it is the level of the flux that varies with wavelength.

In practice the inter slice flux levels for Channel 1 increase with decreasing wavelength which indicates that the Medium Resolution Spectrometer is not diffraction limited for Channel 1. Consider the normalised flux excesses which are 42553 for Channel 1A, 29050 for Channel 1B and 7692 for Channel 1C described in units of integrated flux which is a linear scale defined by the detector. A more useful measure is to quantify the inter slice flux as a percentage of the general flux level within a slice as in Table 6.1.

	Channel 1A	Channel 1B	Channel 1C
Inter Slice Flux Excess	11%	8%	2%

Table 6.1: The Channel 1 Inter Slice Flux Excess

6.1.1 The Channel 1 Slice Profiles Considering the Flux Excess

Section 5.1 outlined the method used to derive the diffraction limited theoretical slice profiles from the observed slice profiles at the detector. However the Channel 1 theoretical slice profiles calculated in Section 5.3 did not account for the flux excess measured in Channel 1. As the excess flux is approximately constant across the inter slice positions on the detector it will be assumed that it is approximately constant across the entire detector.

The theoretical slice profiles were recalculated to account for the excess flux at the detector in Channel 1. This was achieved by scaling the flux level of the theoretical slices to the magnitude of the observed slice profiles minus the excess. This is illustrated in Figure 6.5.

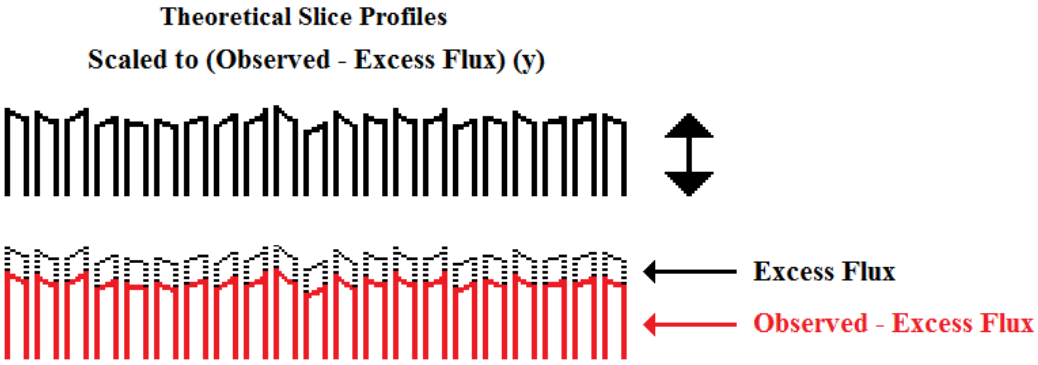

Figure 6.5: Derivation of the Theoretical Slice Profiles Accounting for the Excess Flux

The inter slice flux levels are shown for each sub-spectra in Figure 6.6 each calculated considering an excess flux level across the entire detector. It can be seen by comparing this image with that of Figure 6.4 that the excess inter slice flux is no longer present.

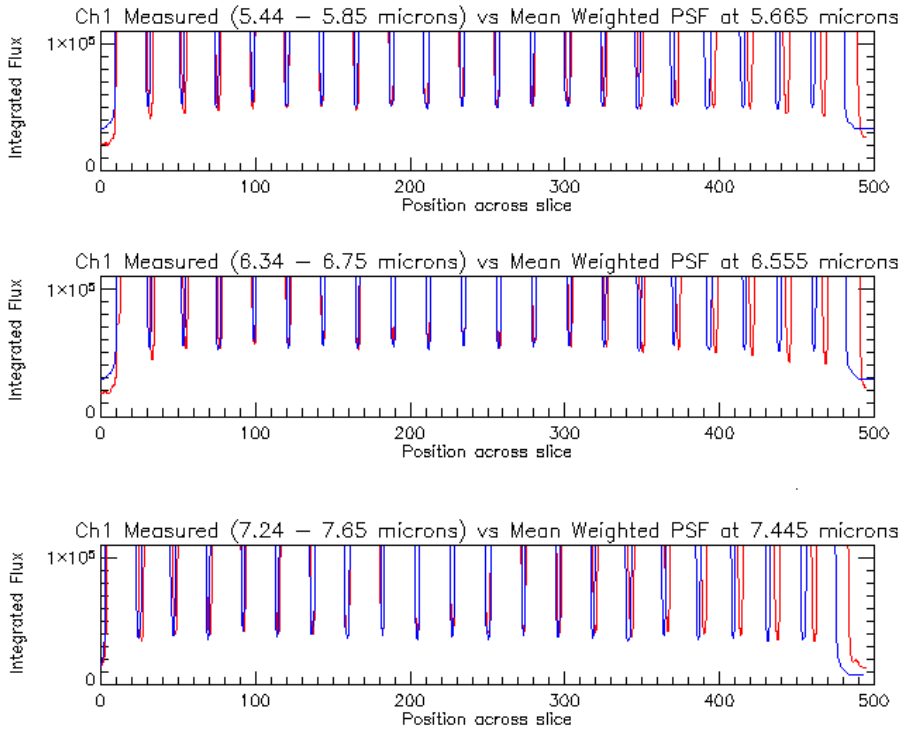

Figure 6.6: Channel 1 A, B & C Slice Profiles Accounting for Excess Flux (Red = Observed, Blue = Theoretical)

The theoretical slice profiles in Figure 6.6 closely match the observed slice profiles measured across the detector for each of the Channel 1 sub-spectra. This implies that the model which assumes a constant level of excess flux present across the entire detector is consistent with the measurements. This origin of this excess flux must now be investigated.

6.1.2 The Origin of the Flux Excess

To ascertain the origin it first had to be understood in which sub-system of the spectrometer the excess inter slice flux was inserted. Consider the output slit mask where the inter slice gap was defined. For reference the design and operation of the output slit mask was detailed during the overview of the Integral Field Units in Section 2.2.2. The re-imaging mirrors were also noted in this section.

The output slit mask defines the slice spacing at the detector including the length of the gaps because the image plane defined at the output slit mask is imaged directly onto the detector. A scattered light analysis of the Integral field Unit (Lee, 2006b) showed that the Integral Field Unit is a well baffled system and the expected out of field scattered light is expected to be less than 1% scattered at angles of >10 degrees. These angles correspond to out of field stray light scattered off a re-imaging mirror which exit the output slit mask through a different aperture. In effect the nominal beams reflect off a re-imaging mirror and exit through the corresponding slit mask aperture whereas the out of field stray light reflecting off the same re-imaging mirror will exit through a different slit mask aperture. However as the output slit mask is at an image plane any out of field stray light that is transmitted to the detector will be imaged back into the same position at the detector. As such this stray light cannot account for any of the inter slice flux excess.

Consider Figure 6.7 which shows the output slit mask operation. It is not possible that any flux which is transmitted through the Integral Field Unit is present at the inter slice position because the mask is made of opaque aluminium. There is a low probability that flux is reflected back onto the front of the output slit mask from the Spectrometer Main Optics which would illuminate the inter slice region. However the angle that the mask subtends to any incident light from the Spectrometer Main Optics is designed to direct the incident light towards the black anodised low reflectivity surfaces in the Spectrometer Pre-Optics. This would effectively remove any such light from the system. It can therefore be assumed that the inter slice flux excess measured at the detector is not present at the Integral Field Unit output slit mask and therefore it is injected into the beam after this point. This reduces the origin of the inter slice flux excess to the output fold mirror of the Spectrometer Pre-Optics and all of the Spectrometer Main Optics. The output fold mirror is a diamond machined flat mirror (noted in Section 2.2.2) which is within specification and the design of the Spectrometer Main Optics (detailed in Section 2.3) was also constructed from components within specification.

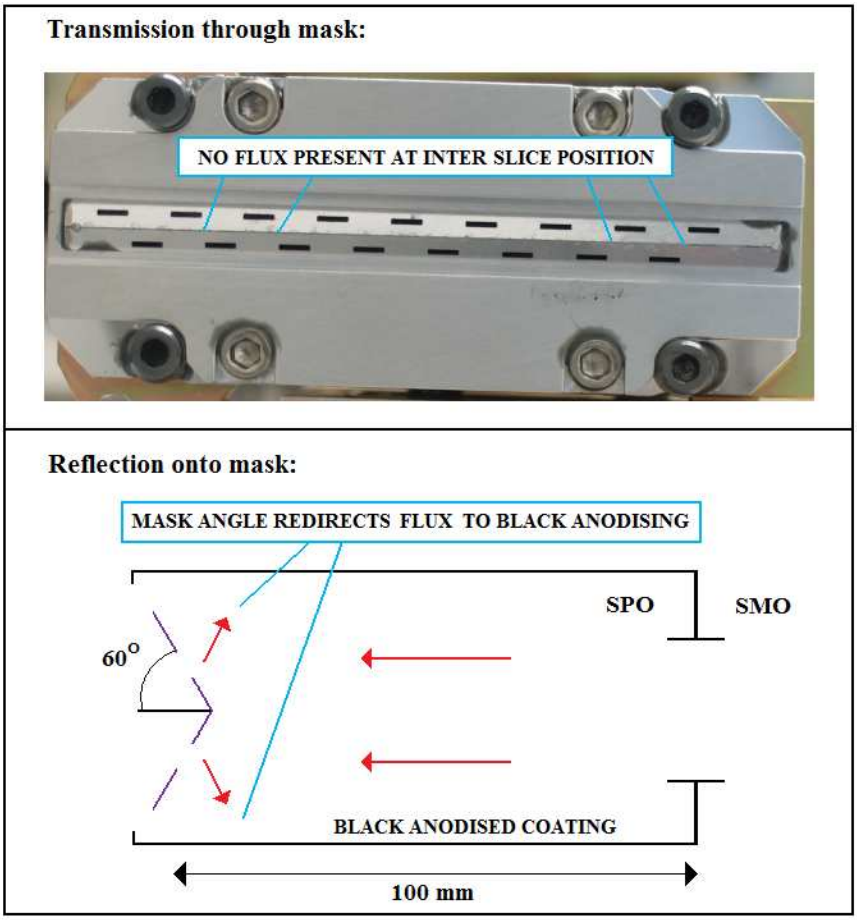

Figure 6.7: Inter Slice Flux at the Output Slit Mask

The Total Integrated Scatter

Whilst the amount of excess flux does increase with lower sub-spectra there is no measured wavelength dependency within a sub-spectra observation. This indicates a low likelihood that the origin of the excess flux is due to scattering at the optical surfaces. The Total Integrated Scatter (TIS) is a measure of the amount of scattered light from an optical surface. It is defined in Equation 6.1 (Stover, 1995) where σ is the root mean square (RMS) surface form error of the optical surface and λ is the wavelength under question. $\sigma Cos\theta_i$ is indicative of the roughness of the surface apparent to the beam, with increasing angle of incidence θ the surface becomes more flat. For the purposes of this scattering investigation $\theta_i = 0$ will be considered, this is the angle at which the Total Integrated Scatter is at a maximum. For Channel 1 λ = 5.5 to 7.7 μm and the typical values of σ for the mirrors in the Spectrometer Pre-Optics were $\sim$25 nm root

mean squared. It was assumed that these values were indicative of the flatness of the rest of the mirrors in the Channel 1 optics. As such the Total Integrated Scatter from a single optical surface in Channel 1 increases from $\sim$ 0.2% to 0.3% of the total incident light with decreasing wavelength. This equation is only valid whilst $\lambda \ll 4\pi\sigma Cos\theta_i$ (the smooth surface requirement).

$$TIS = \left(\frac{4\pi\sigma Cos\theta_i}{\lambda}\right)^2 \tag{6.1}$$

The proposal is that the scattering into the inter slice position occurs after the output slit mask of the Integral Field Units which implies that only scattering from the 7 optical surfaces between the mask and the detector could redirect light into the inter slice position. These 7 surfaces are the fold mirror from the Output Fold Level (Section 2.2.2) and the 6 optical surfaces (the collimator, grating & 4 camera mirrors) in the Spectrometer Main Optics (each described in Section 2.3). The expected Total Integrated Scatter (TIS) from this region in the spectrometer is shown in Table 6.2.

	Channel 1A	Channel 1B	Channel 1C
TIS (post-slit mask)	2.1%	1.6%	1.2%
Inter Slice Flux Excess	11%	8%	2%

Table 6.2: The Total Integrated Scatter & Flux Excess for Channel 1

From a comparison of the expected Total Integrated Scatter and the preciously measured inter slice flux excess it is concluded that the Total Integrated Scatter from the optical surfaces in the Spectrometer Main Optics could not solely account for such elevated flux levels, though it will contribute to the measured levels. As a result the majority of the measured excess flux must originate elsewhere in the Spectrometer Main Optics. The fold mirror from the Output Fold Level and the collimator and the camera optics were all eliminated from the investigation as the method of fabrication is well understood and they could not be possible sources of the excess flux. As a result the component most likely to be at fault is the grating.

Scattered Light at the Gratings

The operation of the gratings in the Spectrometer Main Optics was outlined in Section 2.3.1. With a grating efficiency of 55%, 45% of the light incident upon them is not included into the useful output (Meijers et al., 2006). This is an obvious possible source of the excess inter slice flux. The gratings have been designed to reduce spectral ghosts due to ruling inaccuracies and to reflect only in the zeroth and 1^{st} orders. Since the 1^{st} order is used for observations the zeroth order should be completely removed from the system, this is achieved through the use of a light trap.

The optical design of the grating system shown in Figure 6.8 is synonymous with that shown in Figure 2.11 in Section 2.3.1. Due to the beam geometry the zeroth order light trap is also housed in the Spectrometer Pre-Optics. The Mirror M1 depicts a mirror from the camera optics.

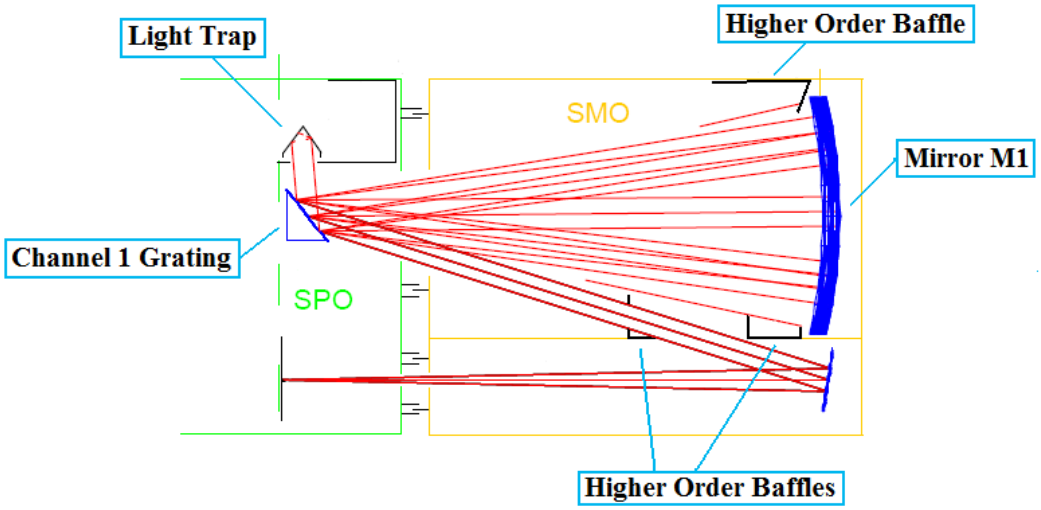

Figure 6.8: Spectral View of the Collimator, Grating and Light Trap

The 45% of incident light directed into the zeroth order must be removed from the system by the light trap. Any errors in the design of the zeroth order light trap could result in an increase in scattered light within the system. There are additional areas for concern. The rulings in the grating could produce ghosts whilst any scattering into the beam from the grating surface would result in a general background flux across the entire detector as the grating is at a pupil plane. There is also the possibility

that higher grating orders are present from lower wavelengths (ie 2.7 micron light will produce 2^{nd} order spectral lines at the same position on the detector as 1^{st} order spectral lines from 5.4 microns). The separate components of the grating system shall now be considered as possible sources of the excess flux.

The Grating

The Channel 1 and Channel 2 gratings were both supplied by Zeiss. In a mechanical design report (Nelles, 2007) which details the surfaces of the gratings there are several issues highlighted with regards to the surfaces of the gratings. These were classified into three types: those that occurred over small areas as shown in Figure 6.9, over large areas as shown in Figure 6.10 and other issues as shown in Figure 6.11.

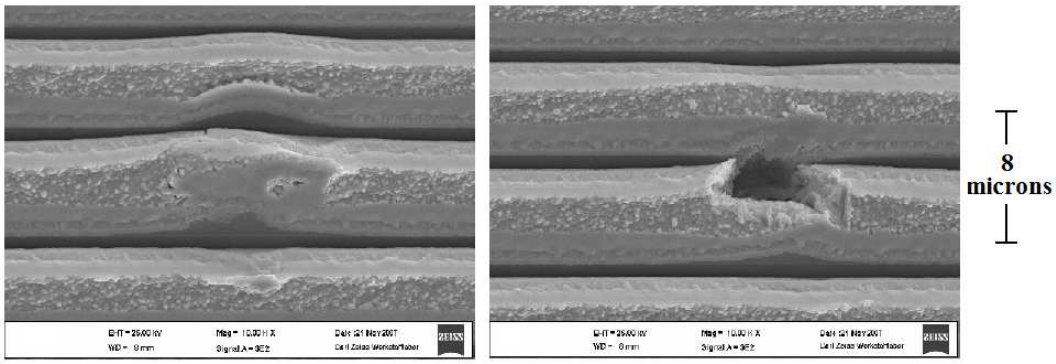

Figure 6.9: Small Area Grooving Inhomogeneities

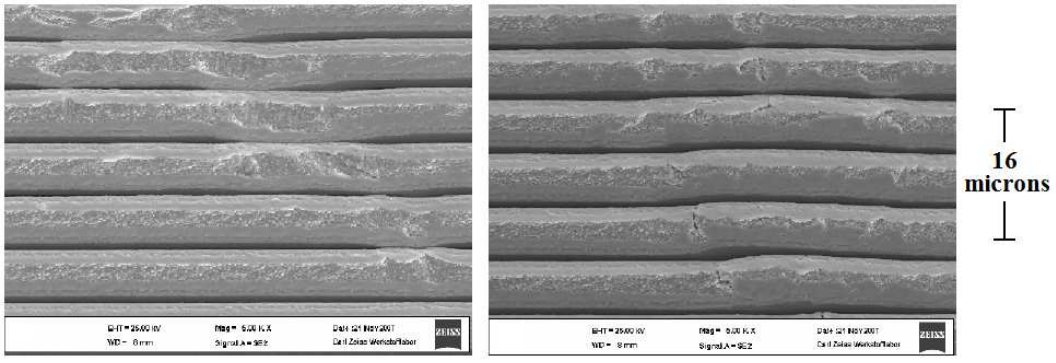

Figure 6.10: Large Area Grooving Inhomogeneities

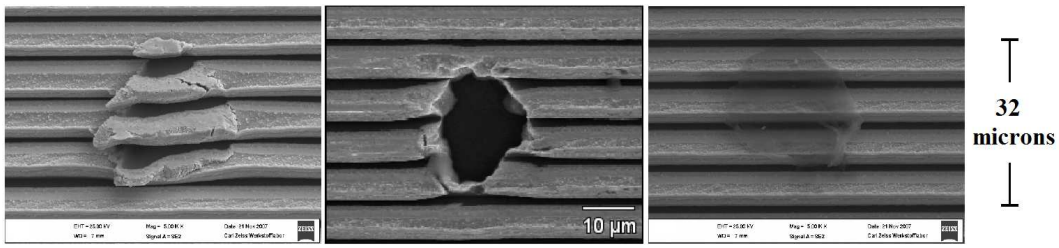

Figure 6.11: Grooving Defects, Holes and Contamination

From the images of the grating surfaces it is evident that there were areas of the gratings which were deformed. Nelles (2007) states that besides the "already known defects, which are typical for a grating" there were new defects of an unknown origin. These defects were thought to be originated in contamination and corrosion of the surfaces. The regularity at which each defect occurs across the grating is not defined though it does state that the holes and the large area inhomogeneous ruling appearance are the most common issue across the grating surface. Unfortunately it does not detail any measurements of the gratings in operation.

The pupil image footprint on the grating is an ellipse covering an area of approximately 25 x 41 mm, or 3140 mm^2. For the holes in the grating to cause an 11% scattering level they would need to cover approximately 285 mm^2 of the footprint of the pupil image (assuming that the entire scatter was directed towards the detector). Modelling each hole as a circle of radius 10μm just over 3 million holes would be required to account for the inter slice flux excess. Whilst the regularity of the holes is unknown it is not expected that there will be a population of 3 million holes in such a small area. The contribution of the holes to the inter slice flux excess as such is expected to be much less than 1%.

Consider the grooving inhomogeneities shown in Figures 6.10 and 6.9. The deviations of the rulings from parallel and the issues with the groove surfaces in the along slice direction could induce scattering into the system. The result at the detector would depend on the type of scattering that was observed. Consider a single spectral line If the errors in the grating surface were systematic then it is possible that a spectral ghost would be created that would be reflected at a different angle to that of the nominal line from the grating. This is shown in Figure 6.12.

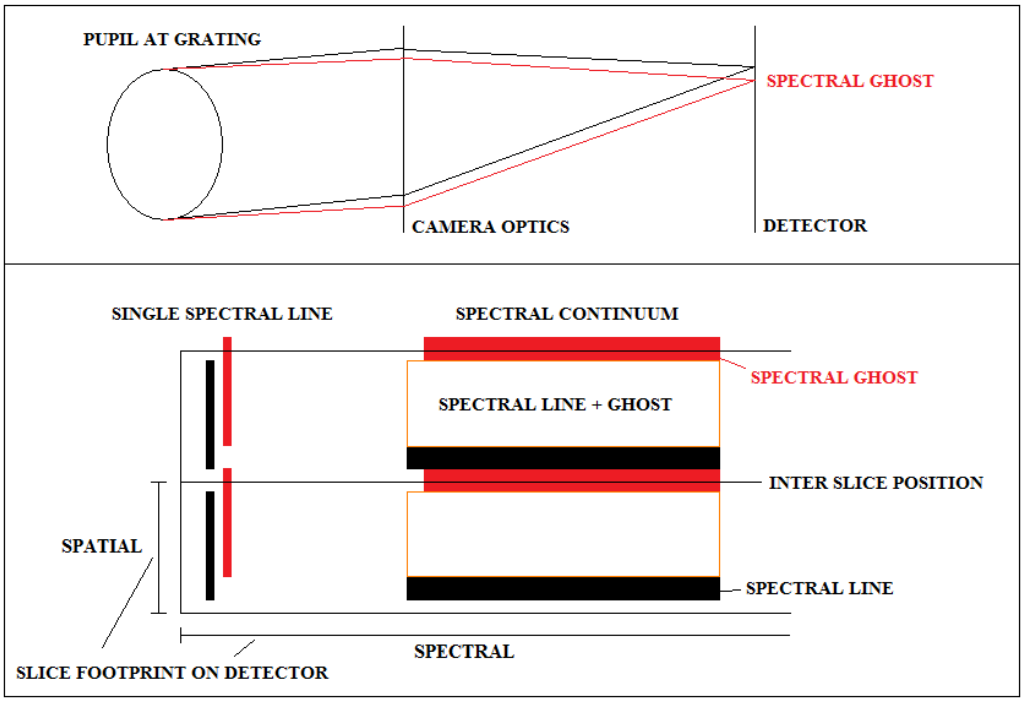

Figure 6.12: Consequences of a Spectral Ghost at the Detector

The result of such a spectral ghost at the detector would be a ghost spectral line offset from the nominal spectral line where the relative intensities of each would be dependant on the fraction of the flux that entered the ghost angle at the grating. The spectral ghost could be shifted in both the along slice and across slice direction at the detector. Figure 6.12 models the nominal line and its spectral ghost on two slices of the detector. It also shows the result of such a spectral ghost when a spectral continuum such as the flat field is incident on the grating. It can be seen that with a spectral ghost offset in the along slice direction the inter slice position is illuminated by the spectral ghost. This is a possible mechanism by which the flux excess can be injected into the inter slice positions.

Now consider the case where the grating did not preferentially reflect a ghost into a single spectral offset from the nominal reflection angle of a spectral line but into an open angle about it. In this case there would be a low level extended background about the spectral line at the detector. If such a low level background extended to the inter slice position then as for the previous case this would explain the observed inter slice flux excess measured with the flat field.

Using observations taken with etalons the spectral lines produced at the detector were investigated for Channel 1 as per Figure 6.13.

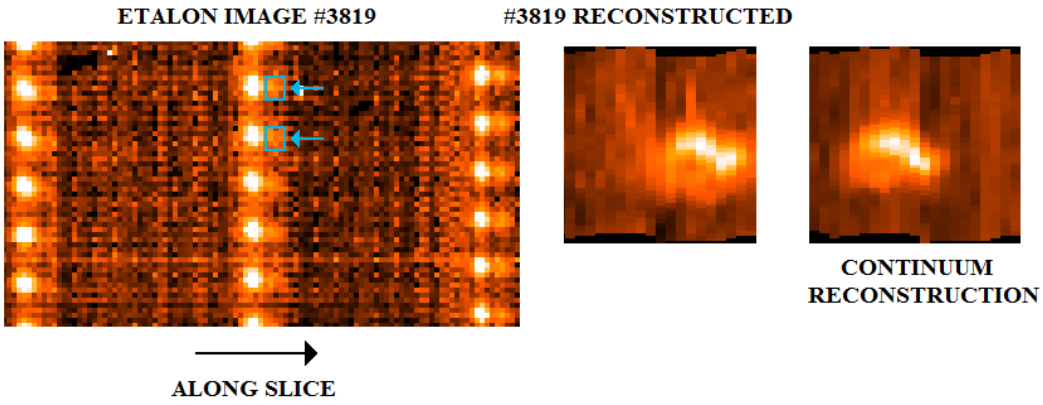

Figure 6.13: The Channel 1A Etalon Lines and Continuum Comparison

It can be seen in the etalon lines that there is an additional feature in the along slice direction (as noted by the blue boxes) which could account for the inter slice flux if it were present at the inter slice position. However reconstructing the field of view (using the process outlined in Section 4.2) from the etalon observation and comparing this with a continuum observation shows that the features observed in the etalon observation are indicative Type II Ghost of Channel 1A (which also occurs in the along slice direction as will be noted in Section 6.3). As such the 11% inter slice flux level for Channel 1A was not observable which was also the case for Channels 1B & 1C however this could indicate that the light scattered at the grating is dispersed over a large area on the detector. As a result of this and a lack of data from the grating suppliers it is difficult to determine whether the gratings are the source of the excess inter slice flux. If however the large area grooving inhomogeneities were indicative of 11% of the surface of the grating and the light scattered from these surfaces reached the detector then it is possible that the origin of the inter slice excess flux is the grating.

Out of Band Light at the Grating

Out of band light refers to light incident on the grating of a wavelength not within a channels passband. Due to the wavelength dependant beam interaction at the grating any such out of band light could be directed towards the detector.

Any higher wavelength light incident on the grating will be directed towards the higher order baffles which will effectively remove this light from the system as these non optical surfaces in the Spectrometer Main Optics are coated in a black anodising with ∼10% reflectivity (Renouf, 2006). There are concerns however of higher grating orders being present from lower wavelengths (ie 2.7 micron light will produce 2^{nd} Order spectral lines at the same position on the detector as 1^{st} Order spectral lines from 5.4 microns). Whilst such an occurrence would reduce the signal to noise of a spectrum at the detector as it is being polluted by additional spectral features it is not likely that this flux would be present at the inter slice position as there is no wavelength dependant deviation in the along slice direction.

To investigate the possibility of out of band light the reflectivity and transmission profiles of the Channel 1 dichroics and the blocking filter (Glasse, 2005) were investigated. These are shown in Figure 6.14. Their operational passbands and placement in the instrument are detailed in Section 2.2.1.

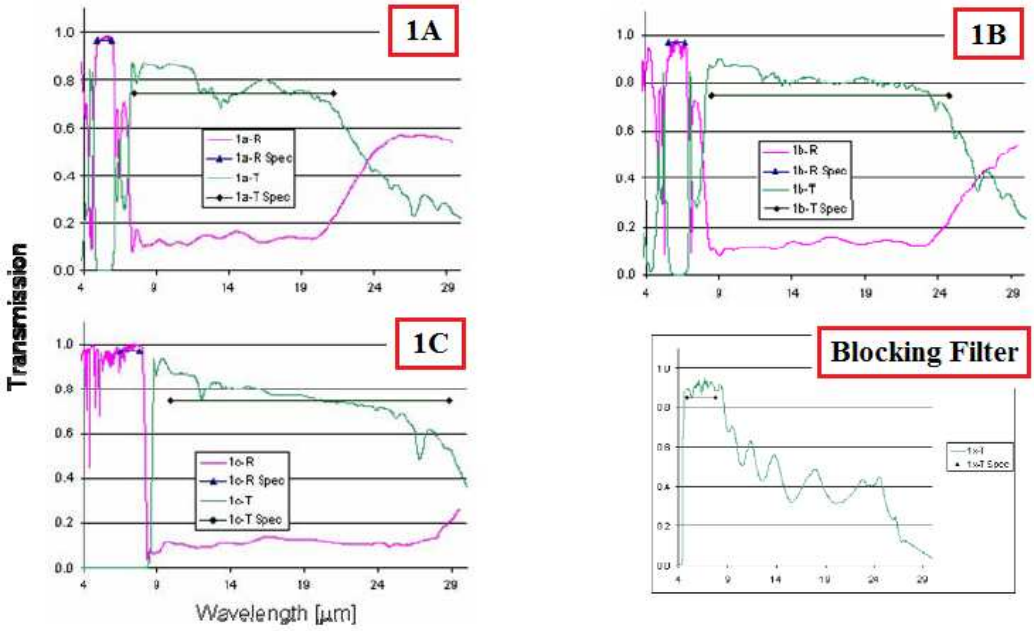

Figure 6.14: Measured Transmission & Reflectivity for the Channel 1 Filters

The reflection profiles of the dichroics are listed in Table 6.3 for each Channel 1 filter (except the blocking filter which shows the transmission profile). They show the

bandwidth across which each filter reflects $> 40\%$ of the incident flux to the grating.

	λ_{min} [microns]	λ_{max} [microns]
Dichroic 1A	5.0	7.2
Dichroic 1B	5.9	7.9
Dichroic 1C	4.0	8.2
Blocking Filter	4.9	14

Table 6.3: The Filter Passbands for $> 40\%$ Flux Reflection to the Grating

The blocking filter sees a very quick reduction to zero transmission for wavelengths less than 5μm. This is a good wavelength cut-off as it quite abruptly reduces the transmission of the out of band light to zero. It does not create such a sharp cut-off for longer wavelengths with the transmission to the grating gradually reducing to zero at around 29μm.

Due to the abrupt cut-off of the blocking filter at 5μm it is concluded that the out of band straylight for lower wavelengths at the grating is not an issue. Looking at the transmission profiles for the Channel 1 dichroics at longer wavelengths it is evident that there is a low level transmission of $\sim$15% at longer wavelengths which sees a sharp rise towards 20μm for dichroic 1A, 24μm for dichroic 1B and 28μm for dichroic 1C. These long wavelength transmissions of the dichroic filters will not be completely removed by the blocking filter. Longer wavelength light however would not be incident upon Mirror M1 in Figure 6.14 as the angle of the 1^{st} diffraction order produced would be greater than that of the expected bandwidth and hence would be directed towards the higher order baffles. It is therefore argued that the stray light is not originated from either lower or higher order diffraction from the grating.

Reflection of the Zeroth Order from the Light Trap

It has been noted in Sections 2.3.1 & 6.1.2 that the zeroth order from the grating is directed towards a light trap in the Spectrometer Pre-Optics. The removal of this light from the system will now be considered. The ray diagram of a light trap can be seen in Figure 6.15 (Lee et al., 2007a). It consists of a cone within an inverted cone with an open angle of $\sim 22.6^o$. Light incident upon the aperture of the light trap must undergo

several reflections before which it is redirected out of the light trap. The exact number of reflections is dependant upon the angle of incidence that the beam makes with the surface of the light trap at the primary reflection. From the orientation of the zeroth order light trap with the zeroth order beam it is expected that approximately 7 reflections will be required. The surfaces of the light trap itself are coated in a low reflectivity coating over the range 5 - 28.3μm.

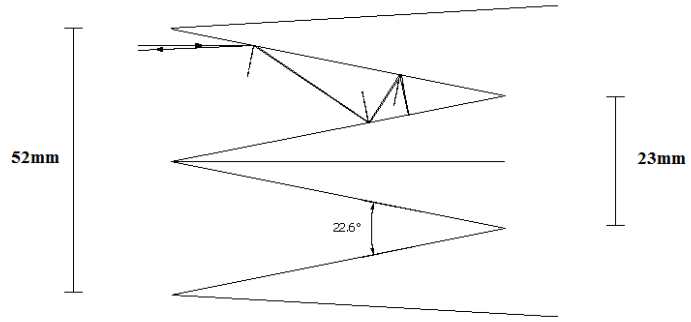

Figure 6.15: The Medium Resolution Spectrometer Light Traps

The high number of reflections coupled with the low reflectivity from a surface serve to substantially reduce the total flux output from a light trap. The expected level of attenuation of a beam that a light trap produces can be calculated from Equation 6.2, where x is the reflectivity of a surface and n is the number of reflections required to redirect the beam out of the trap.

$$Attenuation = x^n \tag{6.2}$$

The low reflectivity coating which is a black anodising had not been perfected for the Verification Model resulting in reflectivities of $\sim$44% for Channel 1A, $\sim$23% for 1B and $\sim$10% for 1C. A graph of the reflectivity of the Verification Model anodising can be seen in Figure 6.16 (Lee, 2007b). It is expected that for the Flight Model the black anodising reflectivities in the Spectrometer Pre-Optics will have been reduced to $\sim$10%.

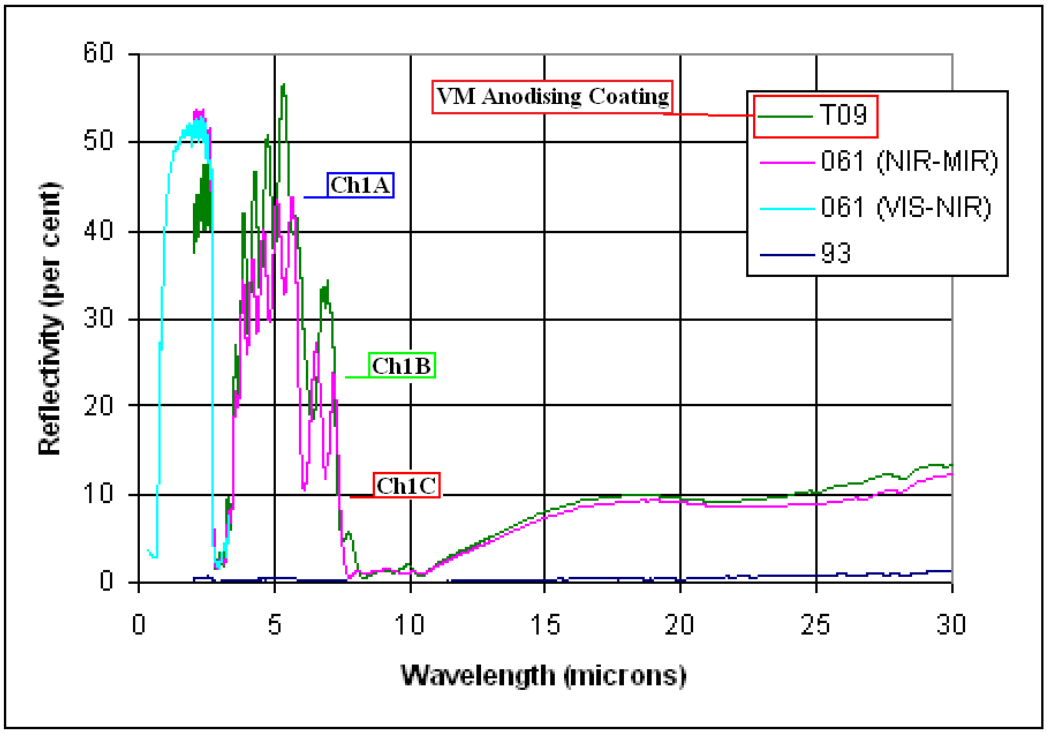

Figure 6.16: Reflectivity of the SPO Blackened Surfaces

Whilst the reflectivity for Channel 1A was a factor of 4.4 greater in the Verification Model than designed, the reflected flux from the light trap was still expected to be less than 1% that of the incident flux. This was calculated from Equation 6.2 using 7 reflections and 0.44 reflectivity. At this level it is not expected that the reflected light would have a noticeable effect on the inter slice flux levels at the detector.

It is very unlikely, however possible, that the surfaces on the inside of the light trap deviated in some way from the design so that only a single reflection was necessary for a part of the beam to exit the light trap. This would most likely occur either from a flat surface at the tip of the cone or at the interface between the two cones.

The following outlines a basic analysis which was done to calculate the fraction of the pupil which must be reflected directly back out of the light trap to cause an 11% inter slice flux level. It was assumed that the reflected light was directed towards the detector with no losses and created a general background across the Channel 1 detector.

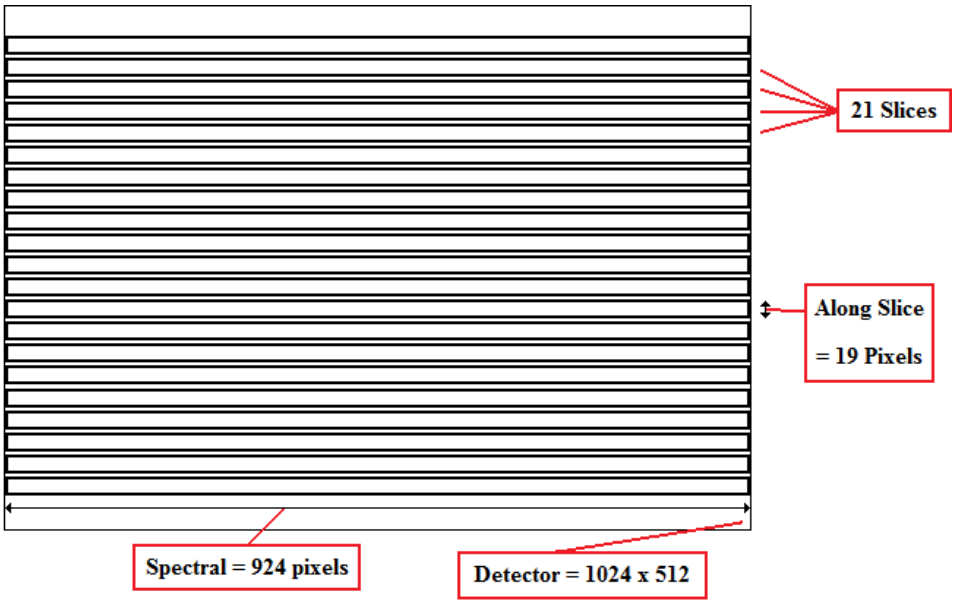

Figure 6.17: Packing Fraction of the Channel 1 Detector

Consider Figure 6.17 which depicts the 21 spectral footprints on the Channel 1 detector. Each Channel 1 spectrum is of 1024 pixels in length and 19 pixels in width (as noted in Sections 2.6 & 2.7) resulting in a spectrum packing fraction on the detector of 0.7. Assuming that the 55% in the 1^{st} order is evenly distributed between the spectral footprints an effective flux per pixel of $\frac{55}{0.7}$ or 78% of the total flux for each pixel incident at the grating is achieved. An 11% background level of this will require 9% of the total flux for each pixel incident at the grating.

Now consider the fraction of the zeroth order which must be reflected from the light trap to achieve this background level (the zeroth order contains 45% of the flux per pixel incident on the grating). Assuming there is no attenuation in the beam due to the black anodising it is required that 20% of the zeroth order light being reflected from the light trap. However the black anodising has been shown to reduce the beam to 44% of incident at Channel 1A wavelengths. This requires that 45% of the zeroth order light must be directed towards the detector after a single reflection. Consider Figure 6.17 which depicts the entrance aperture of the light trap. To achieve this level of flux there must be a substantial defect in the construction of the light traps which were optically checked for such defects and no problems were noticed. As a result it is concluded that errors in the light traps could not account for the additional flux

measured across the detector. It should be noted that even if a sizeable reflection of flux was reflected from the light trap the cone within a cone design would be expected to scatter the reflected light into a large open angle further diluting scattered flux that would be incident on the detector.

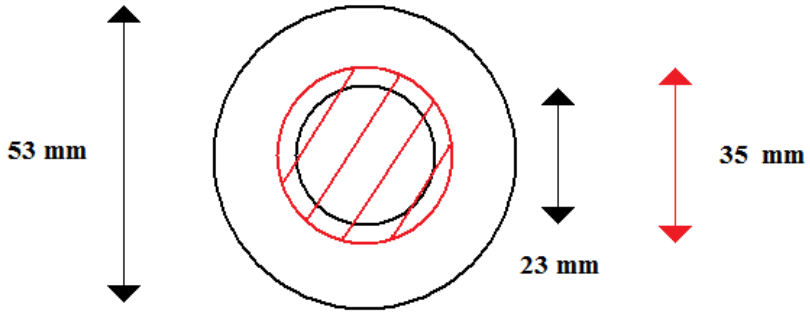

Figure 6.18: Trap Defect Needed to Account for Flux Excess

Alignment of the Zeroth Order and the Light Trap

The total flux of a beam reflection from the light trap was less than 1% of that incident. However any misalignment between the zeroth order pupil image and the light trap would cause an increase in the flux reflected back into the system. This would arise in the case when part of the zeroth order pupil image falls outside the input aperture for the light trap. The area surrounding the light trap was also coated in black anodising though only a single reflection was required in this case to redirect flux back into the system. This alignment need also be investigated.

Lee (2008) outlines a vignetting analysis that was done for the spectrometer. The analysis showed no vignetting for any of the Channel 1 dichroic beams on either the light trap or the collimator or grating. The beam footprint on the Channel 1 light trap is shown in Figure 6.19. The beam footprint is expected to be the same for each of the Channel 1 dichroic observations as they each reflect off the grating at the same angle. The circular green line depicts the input aperture of the light trap and the solid white area the beam footprint. It is evident that there is some tolerance in the alignment of the zeroth order and the input aperture of the light trap. As such it is argued that the excess flux is not injected into the system either from a direct reflection of the beam

from the light trap or due to a misalignment between the zeroth order and the input aperture of the light trap.

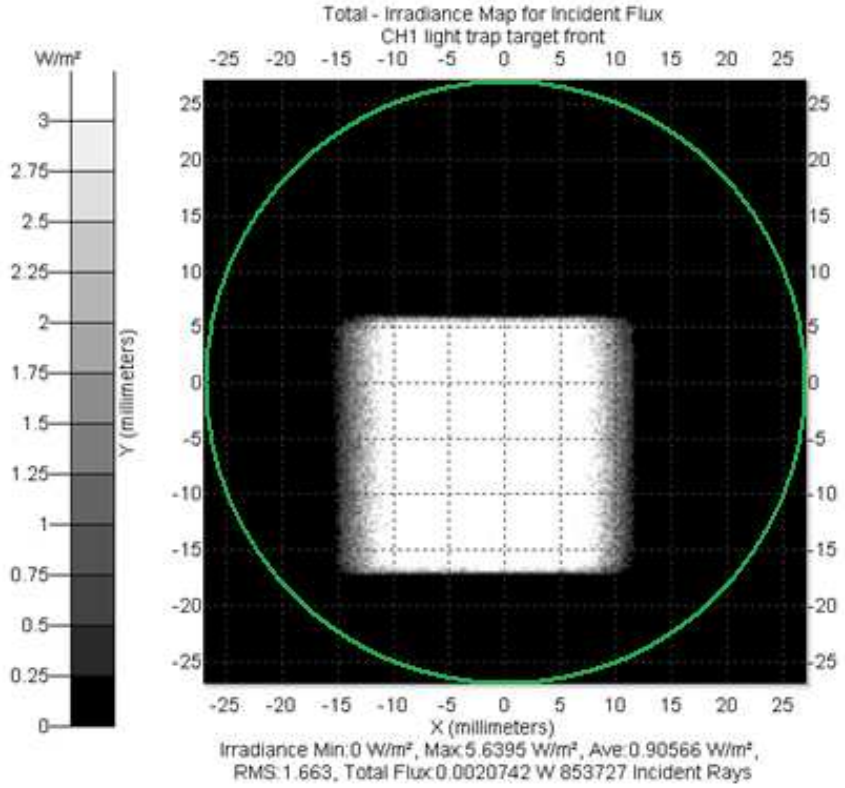

Figure 6.19: Channel 1 Beam Footprint at the Light Trap

Reflection from the Detector

It was possible that the detector was reflecting part of the flux incident upon it back into the beam which was somehow redirected back towards the detector. Figure 6.20 (Glasse, 2006) shows the reflectivity of the anti-reflective coating applied to the Channel 1 detector. The reflectivity is <8% over the bandwidth covered by Channel 1. Also the observed trend of increasing excess with reducing wavelength is not followed by the reflective coating making it unlikely that the origin of the inter slice flux is from a reflection of part of the incident flux from the surface of the detector.

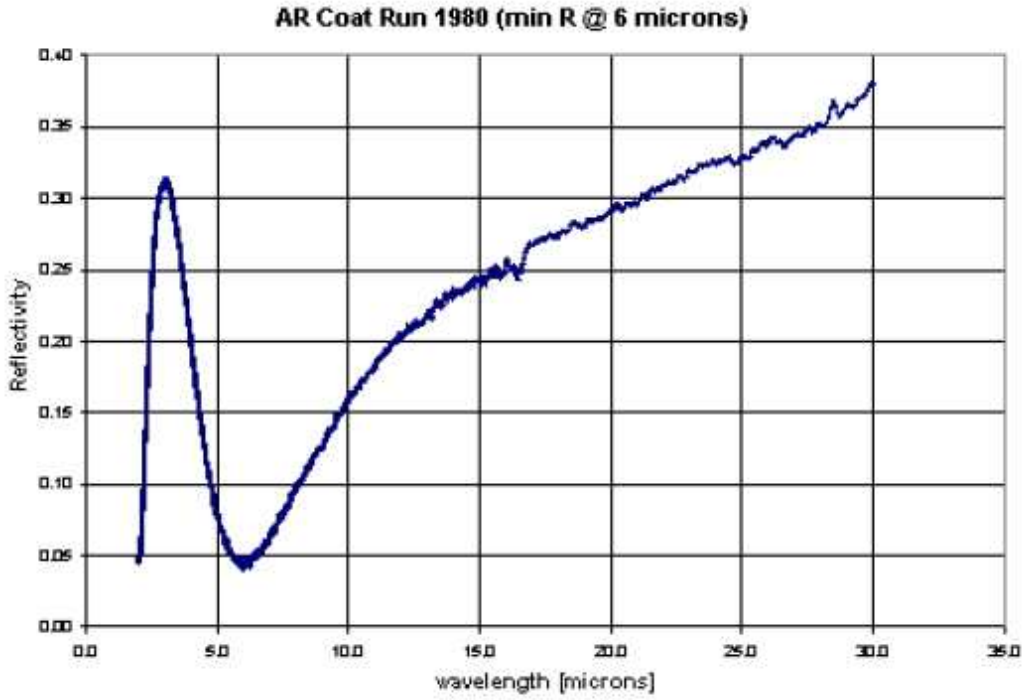

Figure 6.20: The Reflectivity of the Channel 1 Detector Coating

The Verification Model Black Anodising

Consider the reflectivities of the black anodising used for the non-optical surfaces in the Verification Model and also the measured levels of flux excess shown in Table 6.4.

	Channel 1A	Channel 1B	Channel 1C
VM Anodising Reflectivity	44%	23%	10%
Inter Slice Flux Excess	11%	8%	2%
Re-based VM Anodising R	11%	5.8%	2.5%

Table 6.4: VM Anodising Reflectivities and the Inter Slice Flux Excess

The trend between the dichroic values within each data-set seems to be approximately the same, ie large gap between 1A & 1B and smaller gap between 1B & 1C. To investigate this further the VM Anodising Reflectivity values were re-based to those of the inter slice flux excess using a factor of $\frac{11}{44}$. This re-based reflectivity also shown in Ta-

ble 6.4 provides a direct comparison with the measured flux excesses. These values show a close agreement with the measured inter slice flux excess.

Whilst this trend may indicate that the inter slice flux excess could be caused by the black anodising in the Spectrometer Pre-Optics Verification Model it is highly unlikely that this is actually the case. This is because the output slit mask defines the image field plane at which the inter slice flux is zero. Downstream of this mask the only component that utilises the Spectrometer Pre-Optics black anodising are the zeroth order light dumps and it has been shown that even with the larger reflectivities at the surfaces of the light trap the incident beam is attenuated to below 1% of that incident.

6.1.3 Conclusions of the Channel 1 Inter Slice Flux Excess

The purpose of this test was to investigate the origin of the inter slice flux excess which has been shown to be of a constant level across the entire detector. It was intended that the origin of this flux be understood so that it may be removed from the Flight Model as such a feature could reduce the signal to noise of any observations that are taken. The effect of such a reduction in the signal to noise on the telescope operations will be considered in Section 6.2

It has been shown that the inter slice flux excess measured for Channel 1 was injected into the beam after the output slit mask. This was deduced because the mask was opaque and present at the image field plane at the output of the Spectrometer Pre-Optics. The inter slice flux excess was shown to increase with decreasing wavelength though the rate of decrease was not linear with wavelength. The measured levels of the excess flux is shown in Table 6.5

	Channel 1A	Channel 1B	Channel 1C
Inter Slice Flux Excess	11%	8%	2%
TIS (post-slit mask)	2.1%	1.6%	1.2%

Table 6.5: The Flux Excess & Total Integrated Scatter for Channel 1

Table 6.5 also outlines the expected Total Integrated Scatter (TIS) from the 7 Channel 1 mirror surfaces located after the output slit mask. Whilst not responsible for the entire

inter slice flux it is expected that the Total Integrated Scatter does contribute by the expected levels.

Out of band stray light output from the Integral Field Unit had been shown to be less than 1% that of the total flux, scattered at angles > 10 degrees (Lee, 2006b). This large angle would direct the out of band stray light into the black anodised surfaces of the Spectrometer Pre-Optics resulting in an attenuation of the light to less than 0.5%. In practice there would also be scattered light that was transmitted within the paths of each slice through the Integral Field Unit. However at the image plane defined at the output slit mask this in band stray light was not present at the inter slice gap. The stray light and out of band stray light from the Integral Field Unit is discounted from the investigation.

A mechanical design report of the gratings (Nelles, 2007) showed that the surfaces of the gratings had flaws, the most common of which were holes and inconsistencies in the rulings. Whilst holes would have caused scattering at the pupil which would increase the background flux across the detector the number of holes required to cause such a scattering was deemed much too large ($\sim$ 3 million holes in an area of 3140mm^2).

The ruling inconsistencies in the grating, both deviations of the rulings from parallel and the issues with the groove surfaces in the along slice direction could have induced either a ghost pupil offset or a general scattering into a small angle. The exact type would be dependant on the beam interaction at the grating which can not be known without further data from the grating suppliers. The ghost pupil offset would induce a ghost spectral line at the detector whilst the general scattering would induce a low level scattering of light about the spectral line at the detector. Both a ghost spectral line at the grating and a low level general scatter about a spectral line could account for the excess total flux measured at the inter slice position of the flat field measurement. This is because each spectral line will undergo the same interaction at the grating and the resultant mosaic of the spectral line ghost or low level scattering would create a general background level at the detector

The etalon lines in Channel 1 were investigated to look for a measurement of a ghost spectral line however due to the Type II ghost near the PSF it could not be ascertained if any was present. The non appearance of a ghost spectral line could be indicative

that the grating scatters into a large open angle towards the detector and the general background flux would only be apparent with an incident extended source.

The possibility of higher order light being directed towards the detector from the grating was investigated. It is not anticipated that there was any higher grating orders output towards the camera optics by the grating. This is because the blocking filter is very efficient at blocking off light shorter than the Channel 1 minimum wavelength. As such any out of band stray light will be of a higher wavelength than the dichroic observation. Longer wavelength light however would not be incident upon the detector as the angle of the 1^{st} diffraction order produced would be greater than that of the expected bandwidth. It would however be incident upon the Higher Order Baffles present in the same figure.

The higher order baffles, as with the rest of the Spectrometer Main Optics, were coated in a black anodising that reduced the reflectivity at the Channel 1 operational wavelengths to $\sim$10%. It was possible that there was a path to the detector from the Higher Order Baffles that requires several reflections off optical and non-optical surfaces. Due to the baffling design of the Spectrometer Main Optics, if there was such a reflection it would have required more than one reflection off an anodised surface. Two reflections would have reduced the flux level of the higher order beam to $\sim$1% that of the initial flux and would be expected to effectively remove such light from the system.

The possibility of partial beam reflection from the zeroth order light traps was also investigated. The light traps were investigated to calculate their efficiency at removing the zeroth order light from the system. They were shown to be most effective, producing a reflection back into the system of $< 1\%$ even with a black anodising that had an increased reflectivity from what was intended. The alignment of the zeroth order and the light trap was also investigated. They were expected to be aligned to a high accuracy and between dichroic observations the angle of reflection of the zeroth order from the grating was identical. If the alignment of the zeroth order pupil and the light trap was correct then it is not expected that the excess inter slice flux could have originated at the light trap. If however there was a misalignment between the zeroth order pupil and the light trap, the fraction of the pupil that would not be incident on the light trap would be the same for each dichroic. The relative intensities of the resulting reflection back into the system due to any misalignment would be $\sim$44% for Channel 1A, $\sim$23% for 1B and $\sim$10% for 1C (reflectivities of the black anodising). It has been

shown however there is a low probability of a misalignment of the zeroth order and the input aperture of the light trap because of the large alignment tolerances due to the oversized input aperture of the light trap.

The final possibility for the origin of the excess inter slice flux was a part reflection of the Channel 1 dichroic observations from the surface of the detector. The reflectivity of the Channel 1 detector coating showed a reflectivity of $< 8\%$ over the Channel 1 dichroic wavelengths. The highest reflectivity of the detector coating occurs for Channel 1C which was measured with the smallest excess inter slice flux of the Channel 1 observations. Neglecting the incorrect wavelength dependance of the detector reflection to the inter slice flux excess the detector reflection is not expected to contribute as the reflected beam will retrace its path back into the Spectrometer Pre-Optics. It should be reflected off the front of the output slit mask to be incident on the black anodised surface, effectively removing it from the system.

It was deduced that the flux excess occurs in an interaction of the beam somewhere within the Spectrometer Main Optics. This restricts the origin to seven reflections off diamond machined optical surfaces including one grating, there is also a light trap and several light baffles to reduce unwanted flux levels. Whilst the origin of the Channel 1 inter slice flux excess can not be attributed in complete confidence it is expected that it is a direct result of a combination of both the Total Integrated Scatter from the optical surfaces after the output slit mask and the defects in the gratings. This is because the other components in the Spectrometer Main Optics are not expected to scatter light or otherwise affect the beam.

The Flight Model will not be of exactly the same construction as the Verification Model, most importantly the gratings used for Channels 1 & 2 will contain less defects (the best gratings were chosen for the Flight Model) and the black anodising in the Spectrometer Pre-Optics will have a lower reflectivity at the Channel 1 wavelengths. It is expected that the improved gratings will reduce the excess inter slice flux though whether the lower black anodising reflectivity in the Spectrometer Main Optics will have an effect on the excess flux levels is unknown.

With a fully functional MIRI Telescope Simulator (as is expected for the Flight Model) it will be possible to investigate the origin of the excess flux further if it is still present. The ability to position both a true point source will enable an insight into the origin of the inter slice flux excess that was not possible with the Verification Model. This

can be achieved primarily from investigating a spectral line taken with an etalon at a high signal to noise. Such an image of a spectral line at the detector should show either a spectral line ghost or a general low level scatter about the spectral line (or both) however with the improved gratings I expect the levels to be reduced.

6.2 The Performance Impact of the Inter Slice Flux Excess

The previous section has shown there is excess flux present at the inter slice positions at the detector for the Channel 1 dichroic observations which is not seen in Channel 2. If this observed feature of the Channel 1 observations is present in the Flight Model then there will be an associated reduction in the Signal to Noise of the scientific observations. This is because the excess background flux will add extra noise into the reduced images. The impact of the increased background levels will now be considered.

6.2.1 The Method of Background Subtraction

A common method for the removal of extended background radiation is to make two observations and subtract one from the other. One observation should be of an astronomical object of interest [1] and the second observation should be taken with a small on-sky offset applied [2]. Due to the small offset for [2] the background light should be approximately the same as for [1]. Also making the observations closely separated in time should ensure the internal emissions from the telescope surfaces are also similar as the internal temperatures will be the same. Ideally for background subtraction the background in [1] would be exactly the same as that of [2]. This would result in a perfect background subtraction leaving all pixel values except those of the object as zero. This however is not what happens in practice due to Shot Noise. An increasing background flux is associated with an increase in the associated Shot Noise resulting in a reduction in the Signal to Noise of the observation. The temperature change of the telescope will also have an effect on the background but this will be excluded from this analysis.

Shot Noise originates from the variation in the number of photons that arrive at a detector pixel in a given time interval. Consider a detector where the mean number of photons per integration that arrive per pixel = n. Now consider a single pixel, whilst it is most likely that n photons will arrive during the observation there will also be a probability that the number of photons will not equal n. The probability distribution is described by Poisson Statistics. Equation 6.3 describes the Poisson Distribution, where n is the expected number of photons (the mean) and k is the actual number of photons arriving at the a pixel. $f(k;n)$ describes the probability that k photons will arrive at a pixel knowing that the mean number to arrive per pixel is n. For large populations the Poisson Distribution approximates to the Gaussian Distribution.

$$f(k;n) = \frac{n^k e^{-n}}{k!} \tag{6.3}$$

The parameter n is not only the mean outcome of the distribution but it is also the Variance (σ^2) of the distribution. This originates from Equation 6.4 where X denotes the number of pixels on the detector array (ie the number of samples of k). The Standard Deviation (σ) which is a measure of the noise of the distribution is simply equal to the squared root of the Variance.

$$\sigma^2 = \frac{\sum(k-n)^2}{X} \tag{6.4}$$

The background subtraction in effect subtracts the Poisson distributed noise in [2] from that in [1]. When subtracting two Gaussian Distributions the Variance of the new distribution is simply the sum of the Variances of the two input distributions. As such the standard deviation of the new distribution (σ_{new}) which denotes the measurement of the noise in the background subtracted observation is shown in Equation 6.5. Note $\sigma_1^2 = \sigma_2^2 = \sigma^2$ indicates that the standard deviation of the Shot Noise in observations [1] and [2] are the same.

$$\sigma_{new} = \sqrt{\sigma_1^2 + \sigma_2^2} = \sqrt{2}\sigma \tag{6.5}$$

By increasing the exposure length of the astronomical object the effect of the Shot Noise can be reduced. Consider the Signal to Noise ratio (S/N) of an observation. The Signal is proportional to the number of photons that arrive n and the Noise, measured

by the Standard Deviation is equal to $\sqrt{n}$. As such the Signal to Noise Ratio of the astronomical object increases as $\sqrt{n}$ with an increase in the number of photons of n. An illustration of the background subtraction process can be seen in Figure 6.21.

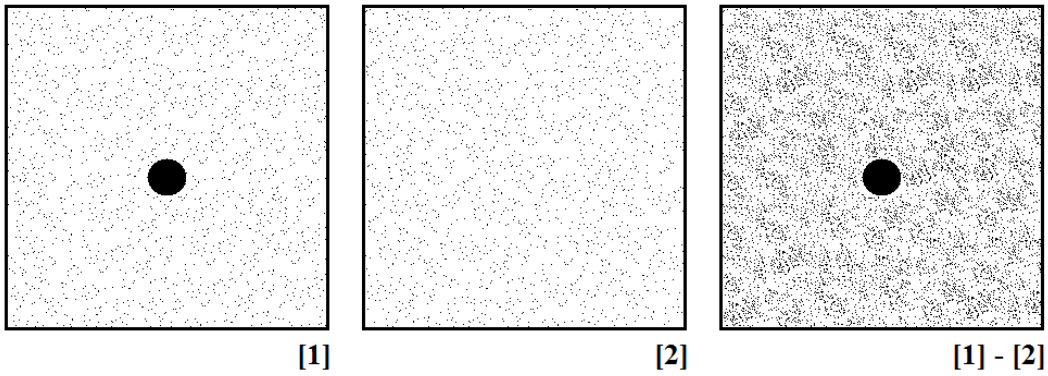

Figure 6.21: Process of Background Subtraction

6.2.2 The Background Noise Increase in the Channel 1 Observations

It has been shown that an increase in background level will cause an increase in the shot noise of the observation. The background should be kept to a minimum to reduce the integration time required for an object to achieve a required signal to noise.

Section 6.1.1 confirmed that an excess inter slice flux being present across the detector by an amount measured in Figure 6.4 was consistent with the observations. The measured increase in the Channel 1 background flux and the associated increase in noise are shown in Table 6.6. The background increase is measured as a fraction of the average total flux within a slice.

	Channel 1A	Channel 1B	Channel 1C
Background Level Increase	1.11	1.08	1.05
Shot Noise Level Increase	1.05	1.04	1.02

Table 6.6: The Excess Flux Induced Noise for the Channel 1 Observations

If the background noise was the only source of noise in the Channel 1 observations then the 5% increase measured for Channel 1A would require an on target increase in the integration time of 11% to achieve the same signal to noise as the nominal case. That of 1B and 1C will require increases of 8% and 5% respectively. This however is not the case as there is additional noise in the observations due to the detector. This will now be considered.

6.2.3 The Total Noise Increase in the Channel 1 Observations

The increase in the background noise has been derived from the excess inter slice flux measured at the detector. However to determine the effect this background noise increase has on the total noise one must also consider the dark noise and read noise from the detector. The total background noise σ_{total} of an observation is shown in Equation 6.6 and is equal to the addition in quadrature of the variance in the background, dark and read noise respectively. It was noted in the previous section that the variance is equal to the mean number of photons per integration that arrive per pixel.

$$\sigma_{total} = \sqrt{\sigma_{back}^2 + \sigma_{dark}^2 + \sigma_{read}^2} \tag{6.6}$$

Figure 6.22 (Glasse, 2009a) shows the expected contributions of the background and dark current to the total photocharge per pixel at the detector in a 960 second observation for the Flight Model. Photocharge is equal to the number of photons incident multiplied by the quantum efficiency of the detector hence the photocharge contribution for each noise component can be approximated as the variance of the noise distribution for each component at the detector.

The excess inter slice flux was measured from a 1200 second observation. To aid comparison the photocharge levels measured from Figure 6.22 for the background and the dark current were scaled by $\frac{1200}{960}$. The expected photocharge in a 1200 second integration for the spectrometer background (the Nominal Background Charge) is noted in Table 6.7 and the dark current of 0.03 electrons per second equates to 36 electrons in a 1200 second exposure. The read noise for the Flight Model detector of 20 electrons is constant over exposure length.

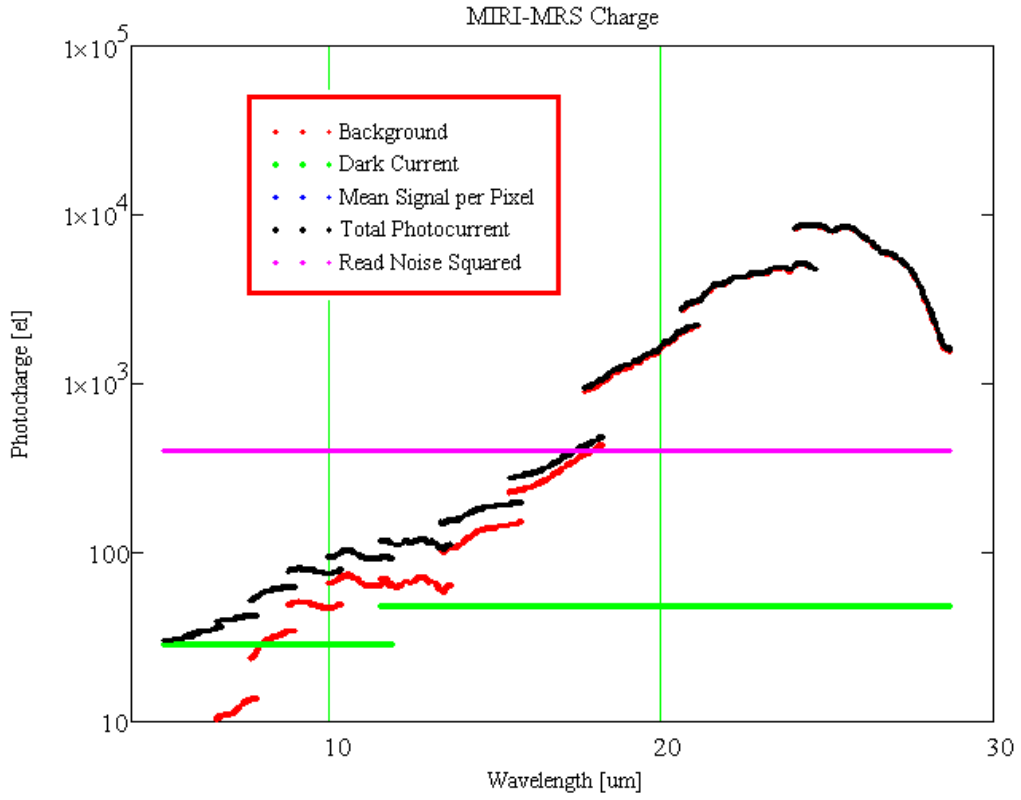

Figure 6.22: Noise Contributions in the Medium Resolution Spectrometer

Due to the excess flux at the detector the actual or increased background charge is a product of the nominal background charge and the inter slice flux excess. This is shown in Table 6.7 where the inter slice flux excess is that measured in Section 6.1 and denotes the background flux increase measured at the detector.

	Channel 1A	Channel 1B	Channel 1C
Nominal Background Electrons	2.6	8.3	16.5
Inter Slice Flux Excess	1.11	1.08	1.05
Increased Background Elecrons	2.9	8.9	17.3
Percentage Increase in Noise Level	1.0003	1.0007	1.0009

Table 6.7: The Channel 1 Background and Noise Increase considering Excess Flux

The noise increase can be calculated as per Equation 6.6 considering the increased background charge due to the excess inter slice flux shown in Table 6.7. The variance of the dark current is 36 electrons and the variance of the read noise is 400 electrons.

Requirement OBA-0589 is a requirement placed upon the background flux in the Medium Resolution Spectrometer. It states that "internal photon sources shall not raise the background flux by 1.2 to raise the noise floor by 1.1" (Bean, 2008). This means that the background flux should not be increased by 20% from its nominal value as this results in a shot noise increase of $\sim$10%. This requirement was designed to set an upper limit on the scattered light allowance in the Flight Model so that the observation times for any given source will only require a maximum of 120% of the nominal observation time. This was to ensure that the instrument is capable of observing a large number of targets in its operational lifetime.

The background increase of 11%, 8% and 5% for Channel 1 was less than the requirement however the total noise increase is negligible as the read noise is dominant in Channel 1. The background increase will only be important when it is of the order of the read noise. It can be concluded that the inter slice flux excess which is indicative of a general background increase across the detector will not impact on the exposure lengths required for observation.

6.3 Type II: The Ghost Near the Channel 1 PSF

The Channel 1 images show a directional low level extension of flux from the compact source. Figure 6.23 shows the comparison of the field of view reconstruction for each dichroic observation (Section 4.2) with the model compact source incident upon the Medium Resolution Spectrometer. The model images were derived from an out of focus image of the point source at the center of the MIRI Imager (Section 4.3). For each image the contours depict the 75, 50 & 25% levels of the flux from the maximum. From a direct comparison of the dichroic observations it is clear that the amount of excess light present increases with decreasing wavelength.

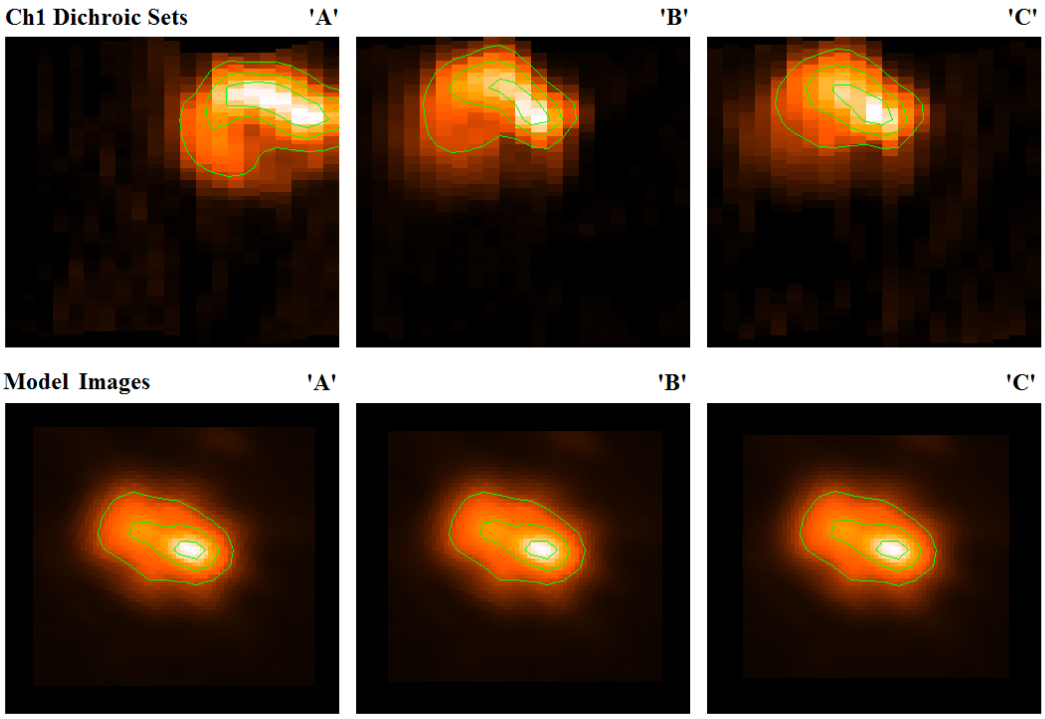

Figure 6.23: Channel 1 Images Compared with the Delivered Compact Source

The Ghost Impact on Science

Consider the implication if such a feature were present in the Flight Model observations. If the ghost feature extended the incident point source across twice as many pixels as the unaberrated point source would subtend then the signal to noise of the observation would reduce by a factor of $\sqrt{2}$ as per the reduction in photons arriving at each pixel (noted in Section 6.2.1). It is possible that the ghost effect could be deconvolved from the field reconstruction but the effectiveness of this process would depend on the ghost. If the ghost was constant across the field of view for a dichroic observation or even if the ghost varied but it was constant in a given position over time then the effect could be deconvolved. It was not possible to determine whether the ghost was constant across the field of view as the errors in the spatial alignment of the field outlined in Section 5.8 caused a variation in the shape of the ghost feature across the field. By comparing the two Channel 1 Dichroic A observations in different field positions shown in Figure 6.24 it can be seen that the ghost feature is very similar. This may or may not imply that the ghost feature is constant across the field.

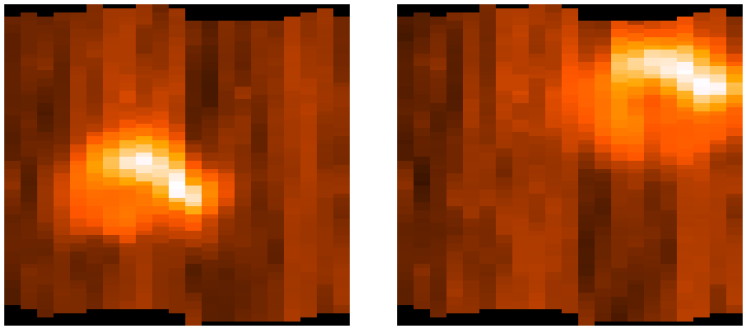

Figure 6.24: Channel 1 Dichroic A Positional Ghost Comparison

6.3.1 The Origin of the Channel 1 Ghost

Before the origin of the Channel 1 ghost can be determined it must first be ascertained in which sub-system of the spectrometer the ghost is offset from the beam. Due to the excess light being present in the Channel 1 images but not in those of Channel 2 (Shown in Figure 4.9) it is argued that the light is injected into the beam after the Channel 1 dichroic filter which defines the position at which the Channel 1 and Channel 2 beams separate. This channel separation occurs in the Dichroic Level of the Spectrometer Pre-Optics which was detailed in Section 2.2.1. Furthermore it is also argued that since a component of the additional light seems to be propagated in the across slice direction from the compact source this propagation must occur before the images are sliced. The image slicing occurs in the Integral Field Units which were described in Section 2.2.2.

Consider Figures 6.25 & 6.26 which shows the spatial separation of slices pre and post image slicing. Post image slicing the slices become more spatially separated until they reach the output slit mask in the Integral Field Unit (depicted in Figure 6.26 for three spatially adjacent slices in the field of view). The output slit mask is also described in Section 2.2.2. Transferring flux between two adjacent slices pre-slicing is much more straightforward than transferring flux between the same slices post-slicing as it is expected that flux transfer between two post-slicing would not be confined to the area around the compact source. The Channel 1 observations all show the ghost to be found close to the compact source position therefore it is likely injected into the beam after the Channel 1 dichroic but before the Channel 1 image slicer.

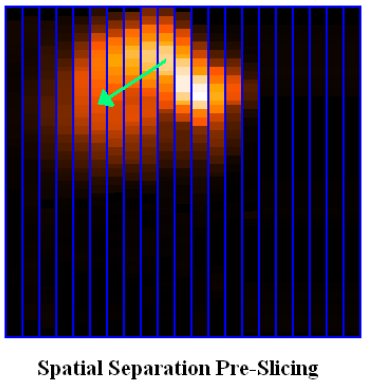

Figure 6.25: Channel 1 Spatial Slice Separation Pre-Slicing

Figure 6.26: Channel 1 Spatial Slice Separation Post-Slicing

The section of the instrument in question contains the Channel 1 relay optics in the Dichroic Level, the Anamorphic Pre-Optics and a flat fold mirror in the Integral Field Unit. The Channel 1 relay optics consists of four fold mirrors, a blocking filter and a light trap. The Anamorphic Pre-Optics consists of four powered mirrors and a fold mirror. The final mirror in the Integral Field Unit is a fold mirror. This section occurs within the Spectrometer Pre-Optics, the complete design of which can be found in Section 2.2.1 & 2.2.2. Note that all the mirrors are gold coated, diamond machined Al6061 and were tested to be within specifications.

A further test of the origin of the Channel 1 ghost is to investigate whether the ghost flux is present at the inter slice position when the ghost is at the edge of the field of view. Section 6.1.2 and Figure 6.7 showed that the excess inter slice flux cannot originate upstream of the Spectrometer Pre-Optics as the mask which defines the inter slice gaps is opaque. In the same manner it is possible to determine whether the ghost originates upstream or downstream of the output slit mask by whether the ghost flux is observed in the inter slice gap. The ghost was not observed to extend into the inter slice gap hence indicating that it originated before the output slit mask. This is consistent with the region of the instrument outlined previously.

Scattered Light

As the size and intensity of the ghost is seen to increase with decreasing wavelength it would indicate that the cause is scattered light from the beam interaction with the surfaces of the mirrors. A calculation was done to estimate the percentage of flux measured in the excess region for each Channel 1 dichroic observation. This was achieved by using the model images shown in Figure 6.23 as an analysis mask with which to investigate the dichroic images shown in the same figure. A two dimensional cross correlation routine in IDL was written to align the model images with the dichroic observations however this would not return an accurate alignment for the investigation. For this reason the model image and the dichroic observations were aligned by eye.

The investigation was carried out down to a level of 20% of maximum flux as this was deemed low enough to include the excess flux region whilst rejecting the noise in the observations. The amount of flux in the observation above the 20% of maximum level was taken as the total flux. The amount of flux that fell outside the 20% level of the model image but above the 20% level of the observation was taken to be the total excess flux. A ratio of the excess flux to the total flux returned the percentage of the flux scattered into the excess region. The results of the investigation are shown in Table 6.8.

	Channel 1A	Channel 1B	Channel 1C
Ghost Region Flux	24%	15%	10%

Table 6.8: The Percentage of Flux Scattered into the Ghost Region

There were some limitations to the investigation. The model image was derived from an out of focus observation of the point source at the center of the MIRI Imager Subsystem. It is indicative of the compact source imaged onto the Medium Resolution Spectrometer but is not the same. It is possible that there were additional features in the compact source at the entrance to the spectrometer that did not occur at the observed position on the MIRI Imager. This could induce a systematic error into the analysis. Whether this was the case is unknown. Also if the ghost extended beneath the compact source in an observation the ghost flux from this region would be included in the flux of the compact source, this would reduce the excess flux levels measured in the ghost. Whether this was a factor in the analysis is unknown. The largest source of error in the analysis originated in the relative alignment of the slices. The effects

of the alignment errors due to the variable along slice magnification applied in the Spectrometer Main Optics were outlined in Section 5.8. They resulted in sections of the compact source being mistaken for excess flux because the offsets placed this flux outside the analysis mask. To measure the approximate error in the excess flux levels the same analysis was done for Channel 2. As there was no measured excess flux for Channel 2 there should be a zero excess flux measured. Any measurement of excess flux would give an indication into the error associated with slice misalignments. The compact source in the Channel 1 reconstructed images (Figure 6.28) is seen to be more consistent between observations than that of the Channel 2 images (Figure 6.29). It is expected that because of the larger magnification gradient measured for Channel 2 (a factor of 2 greater than for Channel 1) the alignment errors are larger for Channel 2. The average excess flux measured for Channel 2 was $\sim$12%, it is expected that the error is larger than would be expected for Channel 1 though whether this is also by a factor of 2 is unknown.

The Total Integrated Scatter

The percentage of flux excess measured for Channel 1 increases with decreasing wavelength indicating that the origin of the flux excess could be from scattered light. To investigate the likelihood that the excess flux was caused by scattered light the Total Integrated Scatter (TIS) was calculated over the complete Channel 1 optics before slicing for each dichroic. The Total Integrated Scatter was detailed in Section 6.1.2. The results are shown in Table 6.9.

	Channel 1A	Channel 1B	Channel 1C
TIS (pre-slicer)	8%	5%	3%
Ghost Region Flux	24%	15%	10%

Table 6.9: The TIS for Channel 1 (Pre-Image Slicer) & Ghost Region Flux

It is clear that even if all the Total Integrated Scatter was beamed directly into the excess position it could not account for all the excess flux that was observed. If the total integrated scatter of the compact source was beamed into a ghost region of $\frac{1}{3}$ size of the compact source then the Total Integrated Scatter could account for the ghost region flux. However this is not how Total Integrated Scatter works. The open angle

into which the scattering is projected is dependant upon the surfaces of the mirrors. A Specular Reflection is one where there is zero scatter out of the beam as would be for a perfect mirror. A Lambertian Reflection is one where the scatter is projected with uniformly into an open angle of 2π. The diamond machined mirrors in the spectrometer would cause the reflected beam to be most like that of a Specular Reflection which implies that the open angle of the scatter will be concentrated around the reflected beam. This type of scattering can not account for the directional ghost offset observed in the field of view.

Ghost Reflection in the Blocking Filter

In all of the Channel 1 observations the ghost is always offset by approximately the same amount and in the same direction. It is argued that its origin is not in a grazing reflection off a surface in the Spectrometer Pre-Optics as the ghost offset in this case would not be expected to track with the compact source. Excluding the Total Integrated Scatter over the mirror surfaces it is expected that there would be no issues with the mirrors as they were all measured to be within specification. If the ghost origin is not in any of the mirrors in the section of the instrument in question then the only other components are the blocking filter and the light trap. The most obvious source of the ghost in these two components is that it originates from a double reflection in the Channel 1 blocking filter.

As noted in Section 2.2.1 the Channel 1 blocking filter was orientated at 10 degrees to the beam to enable the reflected part to be directed towards a light dump. Figure 6.27 shows the ray diagram of a double reflection ghost created by the filter. The ghost offset corresponds to a 0.87mm offset at the anamorphic pre-optics field stop. At this field stop the approximate along slice extent measures 4.35mm of the 5.7mm aperture. This 0.87mm offset therefore extends approximately 0.36 arcseconds in the along slice direction.

The ghost offset was measured from the Channel 1 observations however its centroid was difficult to determine as it was unknown whether the ghost extended into the detector area where the compact source was observed. It was attempted to remove the compact source from an observation by subtracting a properly aligned model image of the type shown in Figure 6.23. This did not return the low level ghost

distribution due to the alignment errors between the observation and model images that originated in the along slice magnification which were outlined in Section 5.8.

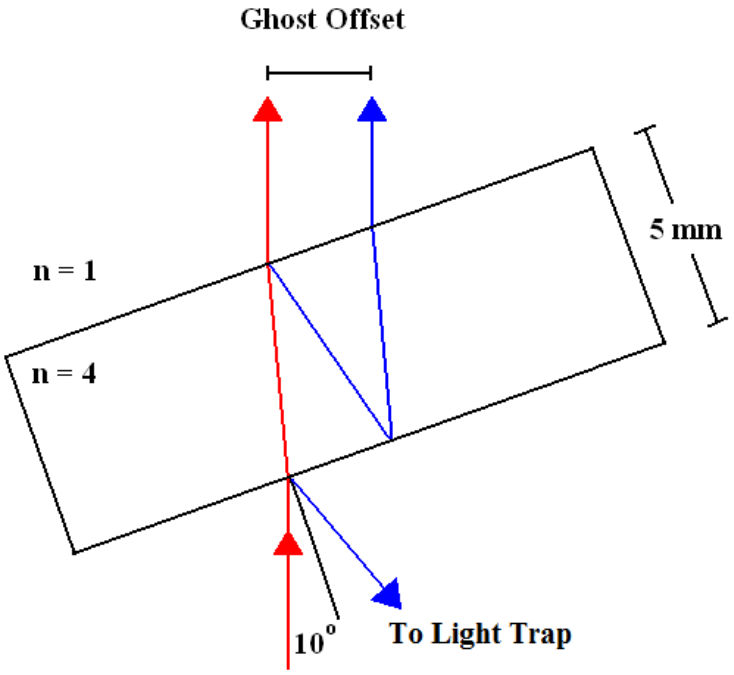

Figure 6.27: Double Reflection Ghost Offset at Dichroic

The ghost centroid was evaluated by eye using a best guess as to its extent. The analysis placed the ghost at an approximate offset of 0.20 arcseconds along slice and 0.45 arcseconds across slice for Dichroic 1C increasing to an offset of 0.25 arcseconds along slice and 0.56 arcseconds across slice for Dichroic 1A. Remember that the blocking filter angle could create a ghost offset by approximately 0.36 arcseconds in the along slice direction. There is a negligible vertical tilt on the blocking filter so there can be no across slice movement imparted on the ghost. It is clear that this blocking filter reflection cannot account for the across slice offset of the ghost from the compact source.

Remember from Section 6.3.1 that the ghost flux (measured as a total percentage of the compact source flux) was ∼24% for Channel 1A, ∼15% for 1B and ∼10% for 1C. Glasse (2005) states that the blocking filter redirects ∼13% of the in band incident light upon it to the light trap from a coating of the front surface. If ∼21% of the light incident on the blocking filter went into the ghost reflection for Channel 1A then this could account for the amount of flux measured in the ghost (where $\frac{21}{87} = 24$). It can not

however account for the across slice offset of the ghost measured in all the Channel 1 observations. There was no data specified for the internal reflectivities of the blocking filters.

Reflection from the Light Trap

Glasse (2005) states that the blocking filter redirects ∼13% of the incident light upon it to the light trap. The possibility of the light trap as the origin of the ghost shall now be considered.

The light traps which were described in Section 6.1.2 (Figure 6.15) are designed as a cone within a cone which necessitates the incident light to be reflected off several surfaces before being redirected back into the Spectrometer Pre-Optics. The exact number of reflections is dependant upon the angle of incidence that the beam makes with the surface of the light trap at the primary reflection. From the orientation of the light trap with the reflected beam it is expected that approximately 7 reflections will be required. The surfaces of the light traps themselves have been treated with a black anodising which is designed to have a low reflectivity ∼10%. In the Verification Model however this black coating had not been perfected (See Figure 6.16) producing reflectivities of ∼44% for Channel 1A, ∼23% for 1B and ∼10% for 1C. Whilst these reflectivities are in some cases much higher than will be found in the Flight Model, even for Channel 1A after the 7 reflections necessary to escape the light trap the reflected flux will be approximately 0.04% of the flux level initially incident upon the blocking filter. Coupled to that the light reflected from the light trap would need to be subsequently transmitted through the well baffled system to the detector however due to the offset of the light trap from the optical path if the reflected light was redirected towards the blocking filter it would not be transmitted by the optics.

Due to the transmissive properties of the blocking filter 87% of the light incident will be transmitted through the coating on the front surface. If the light trap operates as expected then the secondary transmission through the blocking filter will be a negligible amount of flux. If however by some operational defect the light trap only attenuates the incident flux by a single reflection (worst case) then the reflected secondary flux towards the blocking filter will be approximately 6% of that initially incident on the light trap (equal to the anodising reflectivity in Channel 1A of 44% times the flux of

13% which was initially reflected towards the light trap). These amounts could not account for the measured flux in the ghost as such it is very unlikely that the light trap reflection is the origin of the ghost.

Ghost Reflection in the Dichroic Filter

A similar analysis as for the blocking filter was done for the dichroic filter in Dichroic Wheel A from the front of which the Channel 1 beam is reflected. The Dichroic Wheel is also detailed in Section 2.2.1. This analysis returned an along slice offset of $\sim$0.55 arcseconds but in the opposite direction to the blocking filter. Each Channel 1 dichroic filter supplied from the manufacturer has an approximate reflectivity of 0.98 over the in band wavelength range (Glasse, 2005). Even if all the light not reflected in the first instance was reflected off the back surface of the dichroic and back into the beam with the calculated offset, there would be a further reduction in the flux due to the blocking filter. It is expected that any such flux that reached the detector would be of such a low level that it can be ignored as a possible source of the ghost.

6.3.2 Conclusions Regarding the Ghost Near the Ch1 PSF

The purpose of this test was to investigate the origin of the Channel 1 ghost as the extension of the incident point source across n times as many pixels as the unaberrated point source will reduce the signal to noise of the observation by a factor of $\sqrt{n}$. This would require an increase in the observation of n times the original observation period to achieve the same signal to noise. Any increase in the observation time will reduce the capability of the instrument enabling less observations over the operational lifetime. This is unwanted.

Due to the directionality of the ghost offset it has been shown that the ghost region flux in the Channel 1 observations must originate between the Channel 1 dichroic filter mounted on Dichroic Wheel A and the Channel 1 image slicer. The measured percentage of flux scattered into the ghost region and the expected Total Integrated Scatter from all the optical surfaces pre-image slicer are shown in Table 6.10.

	Channel 1A	Channel 1B	Channel 1C
Ghost Region Flux	24%	15%	10%
TIS (pre-slicer)	8%	5%	3%

Table 6.10: The Ghost Region Flux & TIS for Channel 1 (Pre-Image Slicer)

The flux level of the ghost could be explained if the Total Integrated Scatter concentrated the scatter from the compact source into a ghost region of $\frac{1}{3}$ size of the compact source however as per the nature of the Total Integrated Scatter this is not possible. As such it is expected that the Total Integrated Scatter does not account for any of the ghost region flux (except possibly for a low level background flux which would be approximately constant across the entire field of view). Excluding the Total Integrated Scatter over the mirror surfaces it is expected that there would be no issues with the mirrors as they were all measured to be within specification. As the only other components in the section of the instrument in question that were not mirrors the blocking filter, dichroic filter and the light trap were investigated as possible sources of the ghost.

Ghost reflections in the blocking filter, from the light trap and in the dichroic filter in Dichroic Wheel A were investigated. The expected contribution to the flux level of the ghost at the detector was deemed insignificant for both the reflection from the light trap and the reflection from the dichroic filter in Dichroic Wheel A. There was however a possibility that the ghost could be caused by a double reflection in the blocking filter as the measured ghost flux could be explained by 21% of the light incident on the blocking filter being input into a double reflection. This double reflection however could only account for an offset of the ghost from the compact source in the along slice direction. Measurements of the Channel 1 observations showed the ghost to be offset by a factor of 2 more in the across slice direction than in the along slice direction. This offset was calculated from the centroid of the ghost in which there could have been a systematic offset as it was unknown how far the ghost extended in the region of the compact source. It should be noted however that whilst there could be errors in the exact magnitude there was a definite across slice offset of the ghost from the compact source. The origin of this across slice offset cannot be ascertained at this time.

The ghost tracks across the field of view of the observations at the same rate as the compact source. For this reason it is highly unlikely that the ghost is caused by a

grazing reflection off a surface in the Spectrometer Pre-Optics. If this was however the case then it is expected that the ghost will be present in the Flight Model to the same degree. If however the grazing reflection was off a black anodised surface then the intensity of the ghost in Channel 1A would be reduced by a factor of 4.4 at 5 microns due to the black anodising reflectivity in the Flight Model being reduced from $\sim$44% to $\sim$10%.

There is one final explanation for the ghost which is that is it a real feature in the MIRI Telescope Simulator compact source delivered to the Medium Resolution Spectrometer. The model images shown in Figure 6.23 were extracted from an out of focus image at the center of the MIRI Imager, taken with a 7.7 micron filter. This was the lowest wavelength filter available for observations on the MIRI Imager in the Verification Model. It is possible that the compact source sees a spatial degradation at shorter wavelengths than this or when positioned at the input aperture to the Medium Resolution Spectrometer as it is at a different position on the Main Optical System Object Surface within the MIRI Telescope Simulator (Section 3.1.1). Quite why the compact source degradation would be so directional and wavelength dependant is unknown but it cannot be ruled out as a possibility. The MIRI Telescope Simulator is currently being fixed so this cannot currently be investigated.

Having looked at the design of the instrument the section in which the ghost is thought to originate is between the Channel 1 dichroic filter mounted on Dichroic Wheel A and the Channel 1 image slicer. Each of the mirror components were measured to be within specification and as the technique is well understood any mirrors were eliminated from the list of potential ghost sources. The only two components left in the section where the ghost was thought to arise were the dichroic and blocking filter. The dichroic filter was also eliminated from the investigation because any ghost reflection it would produce would be of a negligible intensity. The dichroic filter was shown to be able to produce a ghost offset in the along slice direction of the approximate size measured however it could not produce the across slice offset. The other possible source of the ghost is that it is a real feature in the compact source supplied by the MIRI Telescope Simulator due to the diffuse nature of the source. Whether this is the case is unknown. It is possible that the blocking filter does produce a ghost via a double reflection however as the filter has been optimised to operate over 5 - 7.7 microns it is not likely that the 21% level required to account for the ghost flux is input into the ghost.

In conclusion the ghost has to be either originated in a double reflection of the blocking filter or an actual feature in the compact source delivered by the MIRI Telescope Simulator. Whether it will be present in the Flight Model is unknown though it is quite possible that it will not be a factor as a fully functional MIRI Telescope Simulator should be supplied.

If the ghost is still an issue for the Flight Model then the complete field of view investigation outlined in Section 5.8 will provide adequate observations to characterise the ghosts properties. If the ghost is constant across the field of view for a dichroic observation or even if the ghost varied but it was constant in a given spatial position over time then the effect can be deconvolved. However the spreading of flux across additional pixels will reduce the effectiveness of the deconvolution. The combined effect could reduce the signal to noise of the observations which would require a longer integration time for observations to achieve the required signal to noise.

6.4 Type III: The General Background Increase in the Channel 1 Field of View

There was a general background level present in each of the reconstructed images. This background varied mostly between channels with a smaller variation in the background level between dichroic observations within a channel. Figures 6.28 & 6.29 show typical reconstructed images for each channel (from Section 4.2). In each case the left hand images are Dichroic A, the middle Dichroic B and the right hand images Dichroic C. The background level could originate in any sub-system of the Medium Resolution Spectrometer indicating that any of the previously noted origins of excess light in this chapter could be a contributing factor. Any further potential causes of this light will now be considered.

It is seen in the Channel 1 reconstructed images that there are constant features of the background between each of the images. These took the form of a general agreement between which slices appeared darker or lighter than their neighbors. This trend was also evident for the Channel 2 reconstructed images. As the slices followed different paths through the spectrometer their beams reflected off different mirrors. As such it is not surprising that the flux levels across the slices varies due to the different losses

associated with the changing mirror surface features. It is the average level of the background in an image that is used in the analysis.

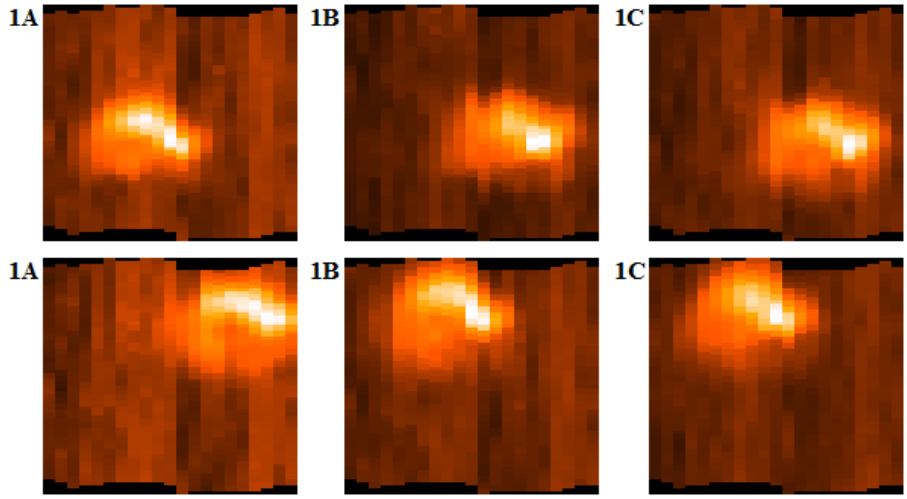

Figure 6.28: Channel 1 Images for Background Comparison (See Caption Below)

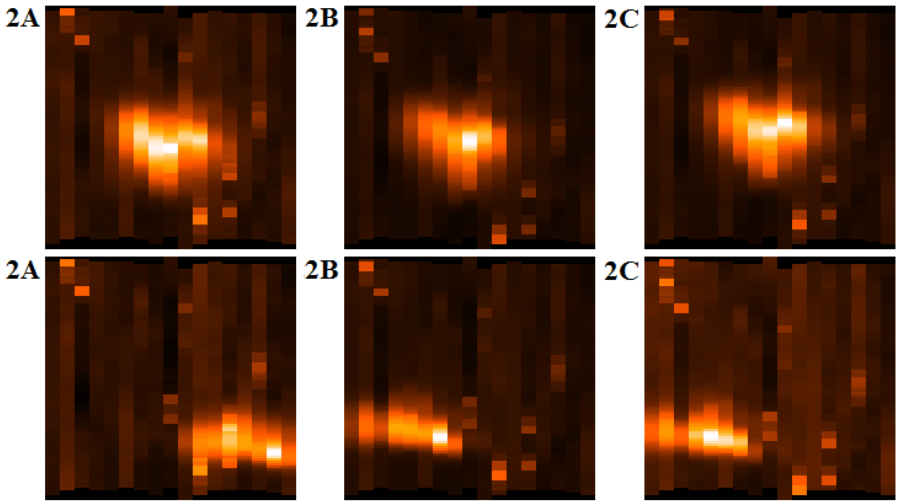

Figure 6.29: Channel 2 Images for Background Comparison (See Caption Below)

The Channel 1 and Channel 2 background images are depicted above. There are similarities in the relative flux levels of the slices within a channel, these are due to the differing paths of the channels through the instrument. The background level in Channel 1 is higher than that of Channel 2, pointing to additional scattered light in this channel at the detector.

For each Channel 1 and Channel 2 image the background flux level was measured as a percentage of the maximum flux value in the image. The average results for each Channel 1 & 2 dichroic observation are shown in Table 6.11.

	Dichroic A	Dichroic B	Dichroic C
Channel 1	19%	15%	14%
Channel 2	8%	6%	7%

Table 6.11: The Measured Background Flux Levels in Channels 1 & 2

The approximately constant background level in Channel 2 indicates that the background is not wavelength dependant. Considering also that Section 5.2 showed that the Channel 2 slice profiles closely matched that expected from the diffraction model it is concluded that the background measured for Channel 2 is approximately that of the background limit of the instrument. The Channel 1 background level is wavelength dependant and much higher than that of Channel 2 indicating that there is additional flux measured in the background of Channel 1.

6.4.1 The Total Integrated Scatter

The end to end model shows both the Channel 1 & 2 beam comes into contact with 30 optical surfaces between the primary mirror and the detector. These mirrors include the primary and secondary mirrors and also the Input Optics and Calibration, the Spectrometer Pre-Optics and Spectrometer Main Optics which were outlined in in Chapter 2. Considering all the optical surfaces for each channel as mirrors of surface roughness as measured for the Spectrometer Pre-Optics mirrors, the expected Total Integrated Scatter in shown in Table 6.12. This was calculated assuming that each optical surface was of approximately the surface roughness measured for the mirrors in the Spectrometer Pre-Optics which was $\sim$25nm RMS.

The open angle into which the scattering is projected is dependant upon the surfaces of the mirrors. A Specular Reflection is one where there is zero scatter out of the beam as would be for a perfect mirror. A Lambertian Reflection is one where the scatter is projected with uniformly into an open angle of 2π. The diamond machined

	Dichroic A	Dichroic B	Dichroic C
Channel 1	9%	7%	5%
Channel 2	4%	3%	2%

Table 6.12: The Total Integrated Scatter for Channels 1 & 2 (all surfaces)

mirrors in the spectrometer would cause the reflected beam to be most like that of a Specular Reflection. That is the open angle of the scatter will be concentrated around the reflected beam. Unfortunately there have been no measurements of the scattering so it is unknown into what open angle the scattering is projected. The Total Integrated Scatter is a summation over the complete number of optical surfaces in Channels 1 and 2. These surfaces occur in different sub-sections of a well baffled system and depending upon the position of the mirror within the system the effect of the scattering at an image plane will vary.

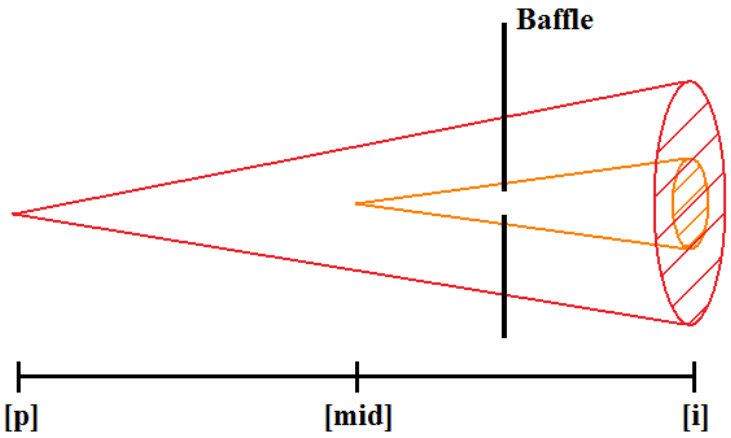

Figure 6.30: General Background and Losses associated with Scattering. [p] represents a pupil and [i] an image plane

Consider Figure 6.30 which shows scattering occurring at a pupil plane [p] and the mid-point between the pupil and image plane [i]. Whilst there is a constant open angle and total flux for the scattering at the two mirrors the scattering is more diffuse at the detector for the scattering from the pupil than the scattering from the mid-point. Also baffling within the system attenuates more scattered light from the pupil than from the mid-point.

Scattering from a mirror at the image plane will not induce an increase in the background level at the detector because the scattered light will be present at its position of origin at any subsequent image plane. There will however be a reduction in flux at the detector depending on how much of the scattered light from the image plane is transmitted through the baffling.

As a result of the unknown open angle of scattering it can not be exactly determined what the effect of the Total Integrated Scatter will be on the flux levels at the detector, it can however be used as a rough guide to the expected levels at the detector.

6.4.2 Over Illumination of the Image Slicers

The image slicers are over illuminated to allow for alignment tolerances in the Integral Field Unit. Figure 6.31 shows the footprint of the Anamorphic Pre-Optics input field aperture on the image slicer for Channel 1 which were both outlined in Section 2.2.2. In the along slice direction the individual slices are oversized. Even so the along slice illumination at the image slicer represents a longer field of view than is transmitted through the spectrometer as the along slice extents are attenuated at the output slit mask. The mask is made of aluminium so it can be assumed that the attenuated signal is reflected back into the Integral Field Unit (as per Section 6.1.2) where it will be reduced to zero following reflections at black anodised surfaces. In the across slice direction the footprint of the Anamorphic Pre-Optics input field aperture is oversized with respect to the across slice extent of the slices on the image slicer. As a result there is a direct illumination of the lambertian surface as indicated in Figure 6.31.

For Channel 1 the ratio of the footprint of the anamorphic pre-optics input field aperture which falls on the lambertian surface to that which falls on the slices is $\sim$19%. As for Channel 1, Channel 2 has oversizing in the along slice direction at the slicer and undersizing in the across slice direction in comparison to the footprint of the anamorphic pre-optics input field aperture. As for Channel 1 $\sim$19% of the total footprint falls on the lambertian surface.

The lambertian surface by definition reflects any flux incident upon it into an open angle of 2π. It is unlikely that a component of the background levels measured for Channel 1 & 2 are caused by the beam interaction at this surface because the Lambertian Scattering happens at an image plane. It is scattering of light at or near a pupil

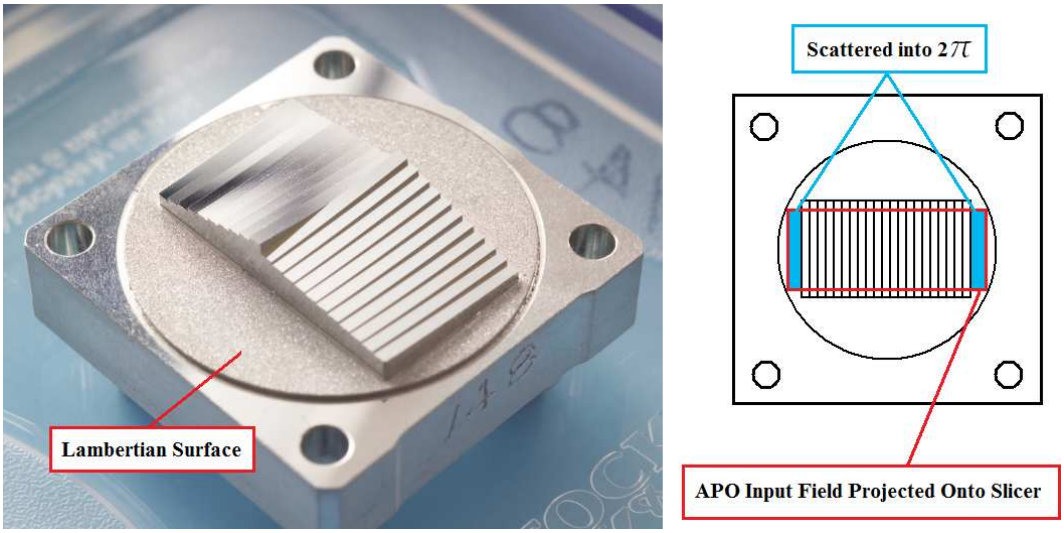

Figure 6.31: APO Input Field Aperture Footprint on the Channel 1 Image Slicer (Not to Scale)

plane that would cause the increase in the background flux levels. It is however possible that some Lambertian Surface scattered light did add to the general background level. However this would have required several reflections off surfaces to direct it towards the detector and it is likely that some of the surfaces encountered would be black anodised. It is expected that scattering from this surface will cause a negligible increase in the flux levels at the detector.

6.4.3 Other Possible Sources of Background

It has been shown that the levels of background measured both for the Channel 1 and Channel 2 reconstructed images could not be solely caused by the Total Integrated Scatter expected in each channel. The illumination of the image slicer was also noted to be a possible cause of additional background but due to the image slicer being at a field image it is not expected that there will be any contribution towards the background flux. As a result it is possible that the origin of the background flux does not occur within the Medium Resolution Spectrometer. Outside of this the background could be injected into the beam by hot surfaces within the cryostat or additionally the background could already be present in the MIRI Telescope Simulator output beam.

Flux Injection from Hot Surfaces in the MTS

As has previously been noted the flux injection could have originated from a hot surface in the MIRI Telescope Simulator which was described in Chapter 3. Whilst the blackbody was operating at 800K for the test observations this is unlikely because the MIRI Telescope Simulator had temperature sensors all over the assembly and especially on surfaces close to the beam path. During the observations taken for this study the temperature sensors were well below their operational limit. This indicates that there should be negligible flux injection from hot surfaces. It is possible that there was an additional path from the hot source to the input aperture of the spectrometer but as the wavelength dependant background was not measured for Channel 2 this explanation is unlikely.

Excess Background in the MTS Output Beam

The final possible explanation for the excess background is that it was already present in the beam when incident upon the Medium Resolution Spectrometer input field aperture. It has already been noted in Section 3.3 that there were several issues with the MIRI Telescope Simulator (MTS). It would be expected however that any background levels present in the output beam from the MTS would be wavelength dependant. As for the previous argument it is unlikely that the beam supplied from the MIRI Telescope Simulator would cause such a discontinuity between the background levels measured for Dichroics 1C & 2A as they as are similar in wavelength. Whilst the general background level of Channel 2 and a corresponding amount of Channel 1 could be originated in the MIRI Telescope Simulator the additional background flux excess for Channel 1 must be originated in the spectrometer (with a small component from scattering of optical surfaces in the MIRI Telescope Simulator).

6.4.4 Type I and Type II Background Sources

It is possible that the measured background flux for Channel 1 is also caused in the same way as the excess flux near the Channel 1 PSF covered in Section 6.3. In particular multiple reflections within the blocking filter would be a possible origin of a low level of flux in the background. However the blocking filter can only account for a

movement of flux in the along slice direction whereas the increased background is observed across the entire field of view coverage and not just in the along slice direction from the compact source. Also the reduced flux in the further reflections make this an unlikely explanation due to the relatively high background measured for Channel 1.

It is more likely that the origin of the Channel 1 inter slice flux excess covered in Section 6.1 is a contributing factor to the background level. This is because it was noted in Section 6.1 that the Channel 1 inter slice flux excess (Type I) was indicative of a general background flux applied across the entire detector. As a result the measured levels of the inter slice flux excess will also be present within a slice. Taking this into consideration the Channel 1 background levels that are still unaccounted for are shown in Table 6.13, where the Channel 1 background level is taken from Table 6.11 and the inter slice flux excess from Table 6.5. Note that the inter slice flux excess is originated after the output slit mask.

	Dichroic 1A	Dichroic 1B	Dichroic 1C
Channel 1 Background (Type III)	19%	15%	14%
Inter Slice Flux Excess (Type I)	11%	8%	2%
Channel 1 Unaccounted Background	8%	7%	12%

Table 6.13: Channel 1 Background Excepting the Inter Slice Flux Excess

It was argued that the Channel 2 background level was indicative of the ambient background of the compact source incident on the Medium Resolution Spectrometer as there was no obvious wavelength dependency. It would however have included the Total Integrated Scatter Component of the complete Channel 2 optics. It is expected that the ambient background level of Channel 2 is indicative of the expected ambient level of Channel 1. Again the measured background for Channel 1 would include the Total Integrated Scatter Component of the complete Channel 1 optics. As the inter slice flux excess already accounts for the mirror surfaces after the output slit mask, only the mirror surfaces before the output slit mask need be considered. Table 6.14 shows the Channel 2 background level taken from Table 6.11 and the expected Total Integrated Scatter. It also contains the expected Total Integrated Scatter for the Channel 1 optical surfaces before the output slit mask.

	Dichroic A	Dichroic B	Dichroic C
Channel 2 Background (Type III)	8%	6%	7%
Channel 2 *TIS* (all surfaces)	4%	3%	2%
Channel 1 *TIS* (pre-slit mask)	7.1%	5.3%	4.1%

Table 6.14: Channel 2 Background and Total Integrated Scatter

The ambient background level for Channel 2 is that given by the Channel 2 background level minus the Total Integrated Scatter from the Channel 2 optical surfaces. The resulting ambient level for Channel 2 is approximately 4% measured as a percentage of the peak flux. It is expected that the ambient level for the Channel 1 background will be approximately the same. Combining the Channel 1 ambient background level with the Total Integrated Scatter before the output slit mask gives the background level contribution of the instrument before the output slit mask. Table 6.15 compares this Channel 1 background with the Unaccounted Channel 1 background from Table 6.13 and shows them to be in general agreement across the Channel 1 dichroic observations.

	Dichroic 1A	Dichroic 1B	Dichroic 1C
Channel 1 Background (pre-slit mask)	11.1%	9.3%	8.1%
Channel 1 Unaccounted Background	8%	7%	12%

Table 6.15: The Channel 1 Pre-Image Slicer and the Unaccounted Backgrounds

Combining the pre-slit mask background with the Inter Slice Flux Excess gives the expected Channel 1 background. This is presented for comparison with the measured Channel 1 background in Table 6.16.

	Dichroic 1A	Dichroic 1B	Dichroic 1C
Channel 1 Background (Type III)	19%	15%	14%
Expected Channel 1 Background	22.1%	17.3%	10.1%

Table 6.16: The Measured and Expected Channel 1 Background

As such it is proposed that the measured background levels in the Channel 1 observations are due to a combination of the Type I inter slice flux excess, the Total Integrated Scatter over the Channel 1 optical surfaces and the ambient background. The average of both the measured and expected backgrounds are approximately 16% that of the peak flux. There is however an obvious scatter of the expected background levels about the measured levels. The amount of attenuation of the Total Integrated Scatter at the internal baffles will include error into the analysis. Other factors which were variable between the Channel 1 dichroic observations would induce further error. These included different dichroic filters and varying reflectivities of the black anodised surfaces in the instrument with wavelength.

6.4.5 Conclusions of the General Background Increase

The purpose of this test was to investigate the origin of the Channel 1 background measured within the reconstructed images and to determine its effect on the Medium Resolution Spectrometer Flight Model. The Type I inter slice flux excess in Channel 1 (as per Section 6.1) was consistent with a general background flux applied across the entire detector. As such this is a contributing factor the Type III background measured within the slices. The other contributing factors to the background within an observation were determined to be the Total Integrated Scatter and the ambient background level of approximately 4% which was measured from the Channel 2 observations.

It was shown that during the illumination of the image slicer that approximately $\sim$19% of the beam falls on a lambertian surface. However that this interaction had a negligible increase on the background level as it occurred at an image plane and it is likely that the black anodised surfaces would remove the scattered light from the system before it could be reflected back into the beam. The possibility of flux injection into the beam from the MIRI Telescope Simulator was also investigated. This was also expected to have a negligible contribution to the flux levels at the detector due to the temperature sensors on the surfaces close to the beam being within the expected levels.

It was concluded that the heightened Channel 1 background level was principally due to the errors in the grating construction that presented itself as a Type I intra slice flux excess. The secondary source was in the Total Integrated Scatter which would

not reach the detector at the levels outlined in Table 6.12 due to the expected losses at baffles within the instrument. The level of transmission of this scattering to the detector is therefore dependant upon the open angle of scattering about the nominal beam which was unknown.

Section 6.2 alluded to the impact of the Type I inter slice flux excess on the instrument performance. The Type III investigation however has shown that there was a additional background flux present within the slices on the detector that was not included in the instrument performance analysis.

The total background measured within a slice can be found in Table 6.16 labelled Channel 1 Background (Type III). However this background is not the background excess as the ambient background levels of approximately 4% are also included. Table 6.17 shows the increased background charge due to the background level increase on the nominal background charge (as per Table 6.7).

The noise increase can be calculated as per Equation 6.6 considering the total background increase measured from the Type III investigation and the dark and read noise for a 1200 second observation. This is shown in Table 6.17. Again the variance of the dark current is 36 electrons and the variance of the read noise is 400 electrons.

	Channel 1A	Channel 1B	Channel 1C
Nominal Background Charge	2.6	8.3	16.5
Background Level Increase	1.15	1.11	1.10
Increased Background Charge	3.0	9.2	18.2
Percentage Increase in Noise Level	1.0004	1.0010	1.0018

Table 6.17: The Total Noise in Channel 1

Requirement OBA-0589 was defined to keep the noise levels below an acceptable threshold. It states that internal photon sources shall not raise the background flux by 1.2 to raise the noise floor by 1.1, Bean (2008). This requirement was designed to set an upper limit on the scattered light allowance in the Flight Model so that the observation times for any given source will only require a maximum of 120% of the nominal observation time. This was to ensure that the instrument is capable of observing a large number of targets in its operational lifetime.

The total background increase of 15%, 11% and 10% for Channel 1 was less than the requirement however the total noise increase is negligible as the read noise is dominant in Channel 1. The background increase will only be important when it is of the order of the read noise. This will be good news for the operation of the instrument in space as lower noise levels result in a shorter time on integration to achieve the same signal to noise.

CHAPTER 7

Conclusions

The Medium Resolution Spectrometer is nearing the end of the Flight Model assembly stage. Here at the UK Astronomy Technology Center we have just received the Spectrometer Pre-Optics back from the thermal cycling and vibration testing. Currently we are checking that the wavefront error of each channel and the general field of view alignment has not changed since the previous measurements which were taken immediately before the thermal cycling. Once the Spectrometer Pre-Optics has been completed it will be sent to the Rutherford Appleton Laboratories where the assembly and integration and verification stage will commence. This stage will culminate in the functional testing of the Medium Resolution Spectrometer Flight Model in a cryostat with the MIRI Telescope Simulator.

The test analysis that I performed on a Channel 1 prototype image slicer (detailed in Section 2.8) was the first actual measurement of the diffraction losses due to slicing. This measurement was required to verify that the operation of the image slicer was well understood at 5 microns as it was possible that the optical model was incorrect as image slicing at this wavelength had never been performed before. Unfortunately due to the problems associated with the source supplied by the MIRI Telescope Simulator (detailed in Section 3.3) the diffraction losses due to slicing in the complete Medium Resolution Spectrometer could not be measured. This will finally be achieved on the

Flight Model with a fully functional MIRI Telescope Simulator however no problems are anticipated due to the very good agreement between the prototype image slicer and the optical model.

The Medium Resolution Spectrometer Verification Model was tested at the Rutherford Appleton Laboratories (RAL) during August and September 2008. I was a member of the test team whose purpose was to create a suite of tests that would enable the complete calibration of the entire MIRI instrument including the Medium Resolution Spectrometer. I was also heavily involved during the test campaign at RAL spending around a month on site performing the tests and the preliminary analysis on the data.

The Verification Model Field of View

Due to my involvement with the assembly of the image slicing components at the UK Astronomy Technology Center I was best equipped to analyse the data to investigate the field of view of the Medium Resolution Spectrometer. The data reduction procedures that I wrote to reconstruct the field of view of Channels 1 & 2 are detailed in Chapter 4 along with the measured field of view extents for each sub-spectra in arcseconds (as per Figure 7.1).

The errors in the field of view analysis were larger due to the issues with the MIRI Telescope Simulator and in particular the diffuse compact source delivered to the Medium Resolution Spectrometer. This increased the errors in the analysis from 3 to 6% however for Channel 1 there was an additional error as the automatic image reconstruction during the test campaign misunderstood the the position of the field of view. This required a larger extrapolation to the corner positions of Channel 1 (as per Section 4.4) which further increased the error in the analysis.

There was a requirement that the Medium Resolution Spectrometer field of view achieved a common 3.5 x 3.5 arcseconds across all sub-spectra. The alignment of the Verification Model sub-spectra (as per Figure 7.1) does not achieve this. This was expected as the alignment was not sufficient during the assembly stage. More importantly however the Verification Model sub-spectra alignment that was measured during the test campaign was approximately the same as that measured during the assembly stage. This implies that once the filters are properly aligned for the Flight Model

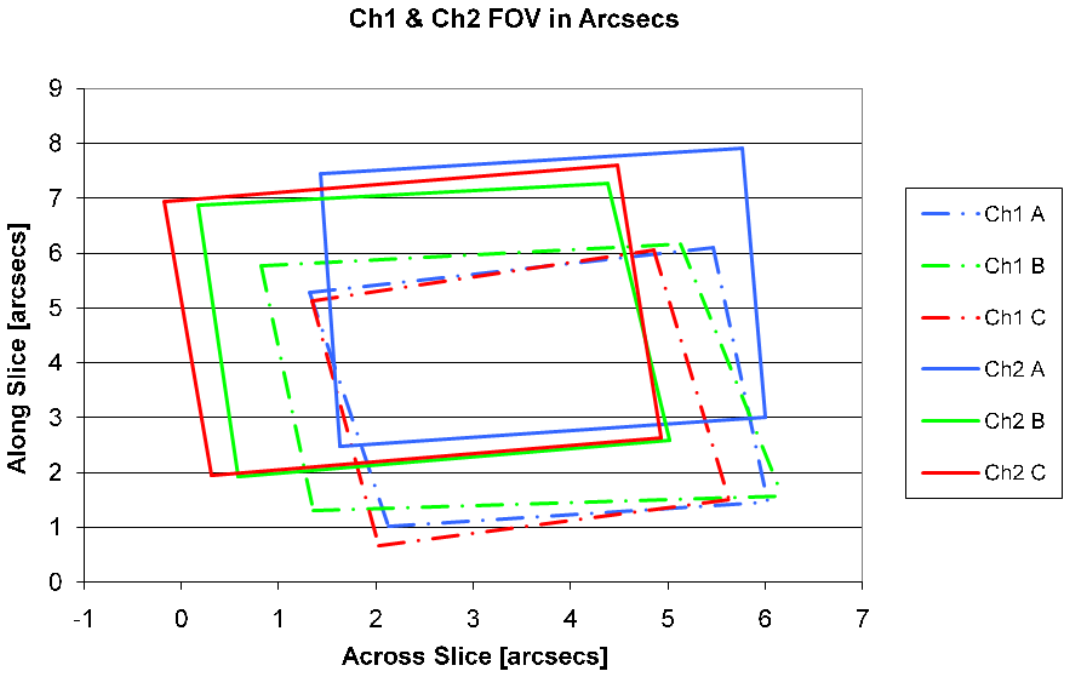

Figure 7.1: The Transmitted Fields of View for each instrument Configuration

the sub-spectra alignment will not change during vibration and hence the alignment for the Flight Model will not change from that required during launch.

The Flight Model Field of View

In an attempt to investigate the likelihood that the common field of view for the Flight Model would exceed the 3.5 square arcseconds instrument requirement an analysis was performed on the field of view sampled by the Channel 1 Flight Model Integral Field Unit which can be seen in Figure 7.2.

Whilst each slice extends 3.7 arcseconds in the along slice direction, the misalignments between the slices reduces the square field of view to ∼3.41 arcseconds in the along slice direction. As this misalignment would make the common field of view of 3.5 square arcseconds impossible to achieve I redesigned the Channel 1 output slit mask to improve the relative slice alignment (as per Section 2.2.2). This redesign of the output slit mask has increased the square field of view to ∼3.6 arcseconds in the along slice direction making it possible to achieve the field of view requirement for the Flight Model.

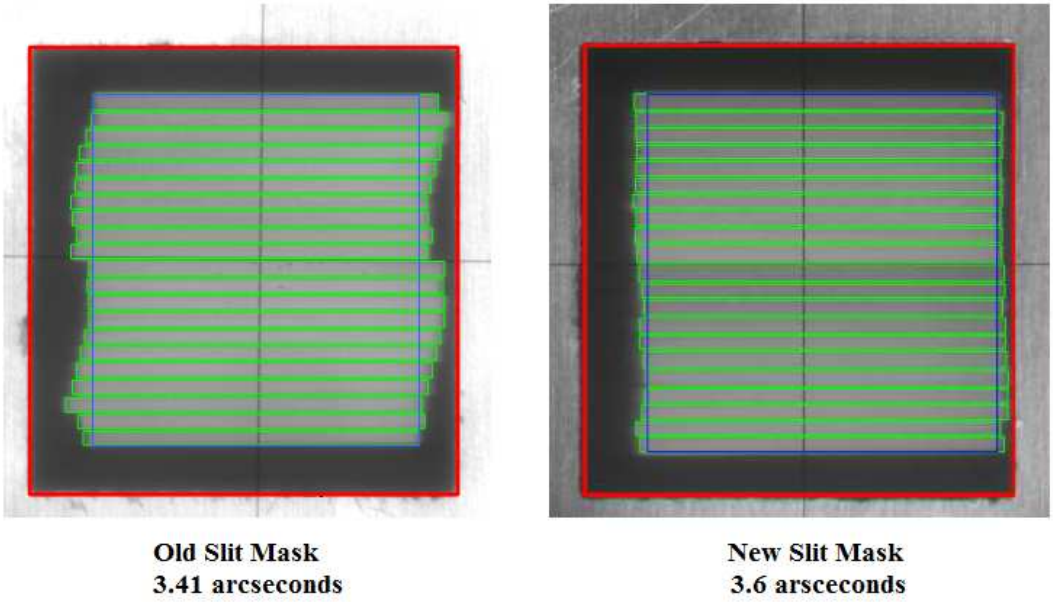

Figure 7.2: The Channel 1 Flight Model Field of View

The Slice Magnification

The analysis of the slice magnification at the detector showed that the slice lengths could be approximated by a linear magnification gradient across the detector. This gradient was different for each channel but approximately constant for the sub-spectra within a channel. A field of view reconstruction program was written to resample the slices to remove the magnification so that the along slice plate scale of each slice was constant in the reconstructed images. This however did not completely remove the discontinuity of the compact source between adjacent slices in the reconstructed images (as per Figure 4.8).

The magnification data for the sub-spectra within a channel showed an agreement in the deviation of the slice lengths from the linear magnification gradient at several positions across the detector (as noted in Section 5.6). As these deviations were also present in the optical model it is proposed that the deviations of a slice length from that expected by the magnification gradient could be a real measurement of a non-linearity in the magnification which would explain the source discontinuity between slices in the reconstructed images.

The largest source discontinuity observed was measured as 0.28 arcseconds in Channel 1 which amounts to a positional uncertainty of ∼5.4 kpc at redshift z = 1. Such a positional uncertainty is undesirable for the Flight Model during operation as this would reduce the quality of the science with the instrument (as per Section 5.8). I devised a calibration technique which must be performed on the Flight Model to remove this spatial error (as per Section 5.8). As this reduction technique is vital to the accurate spatial calibration of the Medium Resolution Spectrometer images it will be carried out during the Flight Model test campaign.

The Additional Light

There were several types of additional light measured at the detector which had been shown not to be due to a light leak in the instrument. They had been split into three types which shall now be considered.

Type I Inter Slice Flux Excess

There was an excess inter slice flux measured in the Channel 1 observations of approximately 11% of the average slice flux for Channel 1A, 8% for 1B and 2% for 1C. The analysis of this excess flux suggested that the flux was injected into the beam somewhere after the output slit mask (as per Section 6.1.2) and was consistent with an excess flux level being present across the entire detector. The Total Integrated Scatter over all optical surfaces in this section was not able to account for the measured flux. Each of the components in the section except the grating were diamond machined mirrors whose fabrication is well understood. As such they were eliminated from the investigation. On further investigation the grating seemed like the likely candidate both because of the flaws on the surface of the gratings (Section 6.1.2) and the requirement that the zeroth order light from the grating (45% of that incident) be removed from the system by a light trap (Section 2.3.1). The operation of the light trap was expected to remove greater than 99% of the light incident upon it resulting in the elimination of the zeroth order light from the investigation.

The ruling inconsistencies in the grating which included deviations of the rulings from parallel and issues with the groove surfaces in the along slice direction could have induced either a ghost pupil offset or a general scattering into a small angle (as per

Figure 6.12). The exact type would be dependant on the beam interaction at the grating which can not be known without further data from the grating suppliers.

Whilst the origin of the Channel 1 inter slice flux excess can not be attributed in complete confidence it is expected that it is a direct result of the defects in the grating with a small contribution from the Total Integrated Scatter from the optical surfaces after the output slit mask. This is concluded because the other components downstream of the output slit mask, which is the section of the instrument where the excess flux is injected into the inter slice positions, are diamond machined mirrors. Apart from the scatter due to the beam interaction on the mirror surfaces which has been accounted for in the Total Integrated Scatter these mirrors are not expected to otherwise alter the beam.

Type II The Channel 1 Ghost

There was a ghost measured near the Channel 1 PSF which contained approximately 24% of the total flux of the PSF for Channel 1A, 15% for 1B and 10% for 1C. The investigation of the ghost suggested that it was injected into the beam somewhere between the Channel 1 dichroic filter and the image slicer (as per Section 6.3.1). This section of the instrument contained a dichroic filter, a blocking filter, a light trap and 10 diamond machined mirrors. The mirrors were eliminated from the investigation as the Total Integrated Scatter due to the beam interaction could not cause a directional ghost like that observed and the mirrors are not expected to otherwise alter the beam as their fabrication is well understood. The cause of the ghost as light reflecting back into the system from the light trap was evaluated and eliminated from the investigation as the flux levels which it would reflect back into the system were much less than 1% of that incident upon it. Similarly a double beam reflection in the dichroic filter was eliminated from the investigation as the flux levels produced at the detector by such an interaction would also be much less than 1%.

The most likely source of the ghost was in a double reflection in the blocking filter. If 21% of the light incident on the filter were input into the double reflection then the flux level measured in the ghost could be accounted for. However this type of reflection could only account for the movement of the ghost in the along slice direction but not in the across slice direction as is also observed (Section 6.3.1).

The final explanation is that the ghost is an actual feature of the compact source delivered to the Medium Resolution Spectrometer by the MIRI Telescope Simulator. This is plausible because of the issues with the compact source outlined in Section 3.3. Whilst the ghost was not observed in a suitably out of focus image of the compact source on the MIRI Imager (Section 4.3) the lowest wavelength filter available was 7.7 microns which falls within the Channel 2 bandwidth and the ghost is not present in the Channel 2 reconstructed images. As a result it is possible that the feature is present at lower wavelengths though the process by which it would occur is unknown as it is not expected that any aberrations in the beam would be wavelength dependant.

Whilst the origin of the Channel 1 ghost can not be determined in complete confidence it is not thought that the double reflection in the blocking filter is the cause. This is because the ghost flux level requires 25% of the flux transmitted through the filter to be injected into the double reflection. Whilst there is no data from the filter suppliers this seems like too large a fraction to occur in an filter that is supposed to be optimised for high throughput of useful wavelengths. Considered with the inability of the double reflection to account for the offset of the ghost in the along slice direction the ghost originating in the double reflection is unlikely. As there are no other components which could cause the ghost reflection it is possible that the ghost is a feature in the MIRI Telescope Simulator. The process by which it is injected into the beam is unknown but with a fully functional MIRI Telescope Simulator for the Flight Model it is possible that the ghost will no longer be an issue.

Type III The General Background Increase

There was a wavelength dependant background level measured in the Channel 1 observations but not in that of Channel 2 (Section 6.4). The levels measured were 19% of the peak pixel flux for Channel 1A, 15% for 1B and 14% for 1C. The heightened background in the Channel 1 images was shown to be a combination of the Total Integrated Scatter from the beam interactions with the optical surfaces, the ambient background and the inter slice flux excess which extended across the entire detector and not just the inter slice positions. It is the inter slice flux excess which is the main contributor to the Channel 1 background level.

It is expected that the Total Integrated Scatter will be approximately the same for the Flight Model but at Lagrange Point 2 the ambient background should be less. Whether the inter slice flux excess which is due to the gratings will be of the same flux levels in the The Flight Model is yet to be determined however the gratings will be of a higher quality than those used in the Verification Model and a reduction in the flux level is expected. As a result it is expected that the general background level measured in the Verification Model will be worst than that expected for the Flight Model.

The heightened background flux level of the Verification Model reconstructed images was measured as 1.15 above nominal for Channel 1A, 1.11 for Channel 1B and 1.10 for Channel 1C. Whilst these are relatively large background increases the read noise of the detector dominates at Channel 1 wavelengths resulting in an increase in the total noise levels of the observations of much less than 1%. As such it can be concluded that whilst there is additional light levels present they do not affect the signal to noise of the observations. If similar levels of background are measured in the Flight Model this will not be an issue. In reality it is expected that the background levels will reduce for the Flight Model as the best components were kept for its construction.

Thesis Synopsis

In conclusion the design of the Medium Resolution Spectrometer which has been optimised for low diffraction losses has been shown to be well understood by the optical modelling. This is important as it means that there will be a high throughput of the spectrometer which as a result will require smaller exposure times to achieve a given signal to noise for an observation than for a spectrometer with larger diffraction losses. This increased sensitivity will enable more observations to be taken over the lifetime of the instrument.

The common field of view of the Verification Model did not meet the 3.5 square arcseconds requirement however this was never to be the case as the dichroic wheels were of an early design and the proper alignment had not been achieved in the cleanroom. More importantly however is that the alignment of the each sub-spectra did not change between the alignment measurements taken in the cleanroom and the measurements made when the Spectrometer Pre-Optics had been assembled. This implies

that once the Flight Model sub-spectra have been correctly aligned in the cleanroom the alignment will still be correct after vibration.

I redesigned the output slit mask of the Flight Model as during my investigation of the field of view sampled by the Channel 1 Integral Field Unit the common field of view was measured as 3.41 arcseconds in the along slice direction. I achieved an alignment of 3.6 arcseconds which ensures that the minimum common field of view of 3.5 square arcseconds is possible to achieve.

The change in the slice magnification at the detector induced a large uncertainty into the spatial alignment of the reconstructed field of view images. I devised a calibration test using a very fine scan of the point source across the field of view which would enable the complete spatial calibration of the field of view for each channel. This test will be carried out during the Medium Resolution Spectrometer Flight Model test campaign as it will be much easier to perform under test conditions.

There was additional light measured in the Verification Model observations. The source of this additional light has been investigated and the principal source was determined to be due to the errors associated with the grating surfaces in the Spectrometer Main Optics. The other source that contributed to the general background level measured within the Channel 1 observations were in the combined Total Integrated Scatter from the optical surfaces in the spectrometer. As the best components were kept for the Flight Model it is expected that these contributions to the background flux levels will decrease for the Flight Model.

The ghost near the Channel 1 PSF was investigated and the only possible cause in the spectrometer which could have caused a ghost of this magnitude was determined to be a double reflection in the blocking filter. This interaction however could not account for the offset of the ghost in the across slice direction. Due to the errors in the delivered MIRI Telescope Simulator it is possible that the ghost is a feature of the compact source delivered to the Medium Resolution Spectrometer however the process by which it would be visible in the Channel 1 observations but not those of Channel 2 is unknown. Nevertheless it is expected that with a fully operational MIRI Telescope Simulator the ghost may not be present in the Flight Model. If present however it is expected that the ghost may be well calibrated out of the observations as it scans in tandem with the compact source.

Even if the additional light levels in the Flight Model are the same as those measured for the Verification Model then the impact on the operation of the Medium Resolution Spectrometer will be minimal as the heightened background levels induced much less than a 1% increase in the total noise of the observations.

With a field of view meeting the requirement and an accurate spatial calibration of the field images provided during the Flight Model test campaign the James Webb Space Telescope Medium Resolution Spectrometer will be in a prime position for making new discoveries when the first science observations commence in 2014.

Bibliography

Aricha, A., Canchal, R., and Diaz, E.: 2006, *MIRI Telescope Sumulator Design Report*, Technical report, Instituto Nacional de Técnica Aeroespacial

Bean, E.: 2008, *MIRI-RS-00001-AEU, Optical Bench Assembly Requirements Document*, Technical report, Astrium

Caputi, K., Dunlop, J., McClure, R., and Roche, N.: 2004, *A deeper view of extremely red galaxies: the redshift distribution in the GOODS/CDFS ISAAC field, Monthly Notices of the Royal Astronomical Society, Vol 353, Issue 1, pp 30 - 42*

Dressler, A.: 1998, *Scientific Goals and Technical Challenges for the NGST, The Next Generation Space Telescope: Science Drivers and Technical Challenges, 34th Liege International Astrophysics Colloquium*

Eiriz, V. and Gonzalez, L.: 2007, *MIRI-RP-000XX-INT, LSS Run-Out and Orthogonality Test Report (Warm)*, Technical report, Instituto Nacional de Tecnica Aeroespacial (INTA)

Glasse, A.: 2003, *MIRI-TN-0001-ATC, The Choice of Slice Width for the MIRI IFU*, Technical report, UK Astronomy Technology Center

Glasse, A.: 2005, *MIRI-TN-00020-ATC, Spectrometer Filter Transmission Compliance*, Technical report, UK Astronomy Technology Center

Glasse, A.: 2006, *MIRI-IF-00003-ATC, Focal Plane Module Interface Control Document*, Technical report, UK Astronomy Technology Center

Glasse, A.: 2009a, *MIRI-TN-00061-ATC, Sensitivity Modelling of the MIRI Flight Model*, Technical report, UK Astronomy Technology Center

Glasse, A.: 2009b, *MIRI-TR-00027-ATC, VM Performance Test Report Measurement of the MIRIM Field of View*, Technical report, UK Astronomy Technology Center

Lee, D.: 2006a, *MIRI-PR-00020-ATC, Integration and Alignment of the MIRI Spectrometer Pre-Optics*, Technical report, UK Astronomy Technology Center

Lee, D.: 2006b, *MIRI-RP-00019-ATC, MIRI SPO: Scattered and Stray Light Analysis*, Technical report, UK Astronomy Technology Center

Lee, D.: 2007a, *MIRI-RP-00015-ATC, Channel 1 IFU Design*, Technical report, UK Astronomy Technology Center

Lee, D.: 2007b, *MIRI-RP-00031-ATC, Report on Black Surface Treatments*, Technical report, UK Astronomy Technology Center

Lee, D.: 2007c, *MIRI-TN-00042-ATC, Testing the Dichroic Grating Assembly Verification Model Alignment*, Technical report, UK Astronomy Technology Center

Lee, D.: 2008, *MIRI-TN-00053-ATC, Vignetting in the SPO and SMO*, Technical report, UK Astronomy Technology Center

Lee, D., Briggs, M., Montgomery, D., and Parr-Burman, P.: 2008, *MIRI-TR-00019-ATC, Dichroic Wheel Asembly, Flight Model*, Technical report, UK Astronomy Technology Center

Lee, D., Gallie, A., and Parr-Burman, P.: 2007a, *MIRI-RP-00012-ATC, MIRI SPO: Layout of Dichroics and Fold Mirrors*, Technical report, UK Astronomy Technology Center

Lee, D., Glasse, A., and Parr-Burman, P.: 2007b, *MIRI-TR-00009-ATC, Spectrometer Pre-Optics Verification Model Test Report*, Technical report, UK Astronomy Technology Center

Meijers, M., Oudenhuysen, A., and Stam, A.: 2006, *MIRI-DS-00003-NLC, Spectrometer Main Optics Design Description*, Technical report, Astron

NASA: 2004, *JWST-RQMT-002558, The James Webb Space Telescope Science Requirements Document, National Aeronautics and Space Administrationm, Goddard Space Flight Center*

Nelles, B.: 2007, *MIRI-RP-00045-ZEO, James Webb Space Telescope Mid-Infrared Instrument Gratings 1 and 2*, Technical report, Zeiss

Ramsay-Howat, S., Sharples, R., Wright, G., Hastings, P., Wells, M., Cunningham, C., Schmoll, J., Content, R., and Robertson, D.: 2003, in *Instrument Design and Performance for Optical/Infrared Ground-based Telescopes*

Rees, M.: 1998, *Probing the "Dark Age" with NGST, The Next Generation Space Telescope: Science Drivers and Technical Challenges, 34th Liege International Astrophysics Colloquium*

Renouf, I.: 2006, *MIRI-DD-00001-AEU, Optical Bench Assembly Design Description*, Technical report, Astrium

Sonneborn, G.: 2007, *Imaging and Spectroscopy with the James Webb Space Telescope, Proceedings of the International Astronomical Union, Symposium S250, Vol 3, pp 483 - 490*

Stover, J.: 1995, *Optical Scattering, Measurement and Analysis*, Spie Press

Wells, M.: 2007, *MIRI-IF-00005-ATC, Optical Interface Control Document*, Technical report, UK Astronomy Technology Center

Wells, M., Browning, R., Ferlet, M., and Lim, T.: 2004, *MIRI-RS-00002-RAL, MIRI Telescope Simulator Requirement Specification*, Technical report, Rutherford Appleton Laboratories

Wells, M., Lee, D., Oudenhuysen, A., Hastings, P., Pel, J.-W., and Glasse, A.: 2006, in *Society of Photo-Optical Instrumentation Engineers (SPIE) Conference Series*, Vol. 6265 of *Presented at the Society of Photo-Optical Instrumentation Engineers (SPIE) Conference*

Wright, G., Bortoletto, F., Bruce, C., van Dishoeck, E., Karnik, A., Lagage, P., Larson, M., Lemke, D., Oloffson, G., Miller, E., Henning, T., Heys, S., Ray, T., Rodriguez, J., Serabyn, E., and Walters, I.: 2003, in *Society of Photo-Optical Instrumentation Engineers (SPIE) Conference Series*

Wright, G., Rieke, G., Barella, P., Boeker, T., Colina, L., van Dishoeck, E., Driggers, P., Goodson, G., Greene, T., Heske, A., Henning, T., Lagage, P., Meixner, M., Norgaard-Nielsen, H., Oloffson, G., Ray, T., Ressler, M., Thatcher, J., Waelkens, C., Wright, D., and Zhender, A.: 2008, in *Society of Photo-Optical Instrumentation Engineers (SPIE) Conference Series*

Wright, G., Rieke, G., Colina, L., van Dishoeck, E., Goodson, G., Greene, T., Lagage, P., Karnik, A., Lambros, S., Lemke, D., Meixner, M., Norgaard, H., Oloffson, G., Ray, T., Ressler, M., Waelkens, C., Wright, D., and Zhender, A.: 2004, in *Society of Photo-Optical Instrumentation Engineers (SPIE) Conference Series*

Appendix A

Acronyms and Abbreviations

APO: Anamorphic Pre-Optics

ATC: UK Astronomy Technology Center

FM: Flight Model

FARO: A Coordinate Measuring Machine

FWHM: Full Width at Half Maximum

HWHM: Half Width at Half Maximum

IFU: Integral Field Unit

IOC: MIRI Input Optics and Calibration Sub-system

JWST: James Webb Space Telescope

MIRI: Mid-Infrared Instrument

MIRIM: Mid-Infrared Imager Sub-system

MRS: Medium Resolution Spectrometer Sub-system

MTS: MIRI Telescope Simulator

OBA: Optical Bench Assembly

OGSE: Optical Ground Support Equipment

PSF: Point Spread Function

RMS: Root Mean Squared

SMO: Spectrometer Main Optics

SPO: Spectrometer Pre-Optics

TIS: Total Integrated Scatter

VM: Verification Model